Dynamic Properties of Colloidal Silica Soils using Centrifuge Model Tests and a Full-Scale Field Test

A Thesis

Submitted to the Faculty

of

Drexel University

by

Carolyn T. Conlee

in partial fulfillment of the

requirements for the degree

of

Doctor of Philosophy

April 2010

ACKNOWLEDGEMENTS

There are numerous people that have contributed to my success. I would especially like to thank my graduate advisor, Patricia Gallagher, who has not only served as my mentor, but has also been a great friend to me. I would like to express gratitude to my undergraduate advisor, Andrea Welker, who encouraged me to pursue a higher degree in Civil Engineering. Special thanks is extended to many of the graduate students that I had the pleasure of meeting and the opportunity to work with including Ronnie Kamai, Rachelle Howell, Murat Hamderi, Jeff Cucura, Antonio Marinucci, and Nicholas Malasavage. A heartfelt thanks is extended to Ross Boulanger and Glenn Rix who provided valuable guidance and insight regarding my research. I would also like to acknowledge Seiji Kano, Ellen Rathje, Dan Wilson, and the staff at UC Davis for their assistance as well.

I would like to express my deep appreciation for the love, support, and encouragement of my parents who have been such an inspiration throughout my life. They have always emphasized the value of education and demonstrated the personal dignity attained through hard work. It is by learning through their example that I have been able to tenaciously complete this work.

This material is based on work supported by the National Science Foundation (NSF) under Grant Nos. CMS-0530478 and CMS-0402490. Any opinions, findings, and conclusions or recommendations expressed in this material are those of the author and do not necessarily reflect the views of the National Science Foundation. Recent upgrades have been funded by NSF award #CMS 0086566 through the George E. Brown, Jr. Network for Earthquake Engineering Simulation (NEES).

Table of Contents

LIST OF TABLES

LIST OF FIGURES

Abstract

Dynamic Properties of Colloidal Silica Soils using Centrifuge
Model Tests and a Full-Scale Field Test
Carolyn T. Conlee

Traditional ground improvement methods to mitigate the effects associated with liquefaction damage are often not feasible in developed areas. Commonly used soil improvement methods can have adverse affects on the surrounding infrastructure and less invasive methods are therefore required. Passive site stabilization is a non-invasive grouting technique where a stabilizing material can be injected at the edge of a site and delivered to target locations through the groundwater. As the stabilizer flows through the subsurface, it displaces the pore water and subsequently forms a permanent gel that binds to soil particles, resulting in a stronger soil formation.

Based on its unique characteristics, colloidal silica has been selected as an ideal material for passive site stabilization. For purposes of liquefaction mitigation, the dynamic behavior of colloidal silica soils was studied through centrifuge model tests and a complementary, full-scale field test. The centrifuge tests provided comparisons of the response for untreated sands and sands treated with 4%, 5%, and 9% colloidal silica concentrations (by weight) subjected to a sequence of dynamic shaking events. To complement the model tests, a full-scale field test was conducted to compare the response of a liquefiable soil formation to a soil grouted with colloidal silica. Permeation grouting techniques and field procedures were developed in order to treat an approximately 1.5 m (5 ft) thick liquefiable soil layer.

The centrifuge model tests and field test both show that colloidal silica soils reduce settlement, lateral spreading, and shear strains induced when subjected to large dynamic loads. For purposes of developing soil models, shear modulus degradation curves were developed and

relationships that govern unloading-reloading behavior were identified in centrifuge model tests. Amplification in the acceleration response and increases in excess pore pressure ratios were determined to be direct indications of treatment levels. Large transient changes observed in pore pressure response were shown to describe the behavior of stress transmittal between the soil and gel during cyclic loading. Additionally, the hysteretic response of colloidal silica soils exhibited greater hysteretic damping and cyclic mobility consistent with dense sands. The response also revealed a lower degree of cyclic degradation for higher concentrations of colloidal silica.

CHAPTER 1: INTRODUCTION

1.1. Research Motivation

When loose, saturated soils are subjected to earthquake loading, excess pore water pressures develop and liquefaction may occur. Liquefaction results in a rapid and dramatic loss in soil strength and stiffness. Liquefaction-induced ground failures cause large deformations and settlements of the ground. The results can be catastrophic to infrastructure and have caused structural damage, floating of buried structures, and loss of foundation support (Figure 1.1).

(a) after Niigata Earthquake, 1964 **(b) after Haiti Earthquake, 2010**

Figure 1.1 Liquefaction-induced damage

Traditional ground improvement methods to mitigate the potential of liquefaction damage at developed sites, such as soil compaction, are often not feasible because of adverse effects on adjacent structures due to vibration, densification, and increased lateral stresses. Passive site stabilization is an innovative, non-invasive technique where a stabilizer solution is injected at the edge of a site (via soil grouting) and delivered to target locations through augmented groundwater flow (Figure 1.2). As the stabilizer flows through the formation, it displaces the pore water and subsequently forms a permanent gel that binds the soil particles. Based on performance criteria,

colloidal silica has been selected as an ideal material for passive site stabilization. Treatment with colloidal silica results in a stronger and stiffer formation that is much less susceptible to liquefaction-induced damage associated with loose, saturated sands.

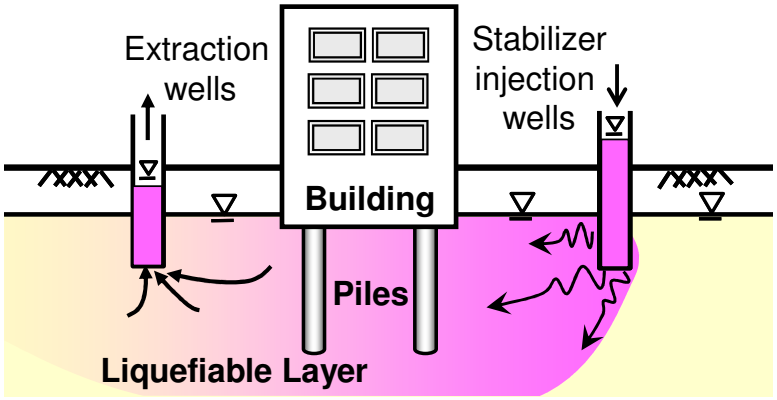

Figure 1.2 Passive site stabilization concept

With limited field studies of colloidal silica grouting for liquefaction remediation, there is a further need to improve grouting techniques with colloidal silica and quantify improvement by geotechnical and geophysical methods on large-scale projects. Development of grouting methods/procedures and verification techniques of soil improvement can optimize treatment in field applications. Additionally, a greater understanding of the dynamic response of colloidal silica treated soils is required to accurately define parameters that predict material behavior. With well-defined material parameters, numerical modeling methods can be implemented to predict the behavior of colloidal silica soils subjected to earthquake motions.

1.2. Scope of Research

The overall objective of this research is to evaluate the effectiveness of colloidal silica for purposes of liquefaction mitigation and ground improvement using centrifuge model tests and full-scale field testing. Two centrifuge tests were performed on various concentrations of colloidal silica and compared to an untreated soil deposit. The test was performed using the geotechnical centrifuge located at the Center for Geotechnical Modeling (CGM) at the University of California at Davis (NEES@UCDavis). The centrifuge model tests were later complemented with a full-scale field test. The field test utilized permeation grouting techniques to grout a soil deposit and compare the response to an untreated soil deposit. Shaking was induced using both a vibratory mandrel and a mobile shaker from the University of Texas (NEES@UTexas).

Two centrifuge tests were conducted at UC Davis. The purpose of the model tests was to study the effectiveness of colloidal silica for liquefaction mitigation. The tests compared an approximately 5m (16 ft) thick liquefiable layer saturated with varying concentrations of colloidal silica versus an untreated layer. The behavioral response of each soil was quantified in terms of accelerations, shear strains, pore pressures, displacements, and cone penetration testing. Additionally, dynamic response analyses from the centrifuge tests were utilized to study effects of shear modulus and hysteretic behavior of colloidal silica soils versus untreated soils.

To complement the centrifuge model tests, a full-scale field test was conducted. The main objective of the field test was to compare and quantify the behavior of a 1.5m (5 ft) thick liquefiable soil layer versus a similar liquefiable soil layer saturated with colloidal silica stabilizer. The effectiveness of the improvement mechanism for colloidal silica stabilizer was analyzed in terms of accelerations, pore pressure response, shear strains, and cone penetration testing. The second objective of the field test was to investigate and develop proper field procedures, such as batching techniques, optimal injection methods, and proper grouting procedures with colloidal silica.

This research is part of a collaborative, multi-institutional project funded by the National Science Foundation entitled “Seismic Risk Mitigation for Port Systems” led by Glenn Rix at Georgia Institute of Technology. The NEESR Grand Challenge encompasses experimental and numerical simulation approaches in understanding soil-foundation-structure systems of port facilities and soil improvement techniques to reduce seismic risk. Additionally, it utilizes the George E. Brown Network for Earthquake Engineering Simulation (NEES) to develop geotechnical and structural mitigation and repair strategies.

1.3. Organization of Dissertation

The research presented in the following chapters consists of two main studies. Although a literature review is generally provided in a separate chapter, it will be incorporated throughout the dissertation as the topics discussed become more relevant to previously published literature. In Chapter 2, a general background of the research topic is presented where the concept of passive site stabilization is explained, colloidal silica properties are defined, and applications of colloidal silica are discussed. Chapters 3 through Chapter 5 discuss the centrifuge model tests. In Chapter 3, the details such as model preparation and soil properties are discussed. The results and discussion of these tests are presented in Chapter 4. The results in Chapter 4 include lateral spreading, settlement, pore pressure, and acceleration response. Chapters 5 and Chapter 6 focus on shear modulus and stress-strain hysteretic behavior of colloidal silica treated soils. In Chapter 5, an overview of the dynamic response at small and large strains of soils, chemically grouted soils, and colloidal silica treated soils are discussed. Two methods for determining shear wave velocity in centrifuge model tests are also described. Additionally, methods for obtaining the hysteretic behavior and determining stress-strains along a soil profile are provided. Chapter 6 discusses the results of shear wave velocity and the stress-strain hysteretic behavior of colloidal silica treated soils. Chapter 7 and Chapter 8 focus on the field test study. In Chapter 7, details of the field test, such as site characterization, grouting procedures, and test layout are presented. In

Chapter 8, signal processing techniques from ground motion records are discussed in detail along with finite element analysis methods used for obtaining shear strains. The results of the field test study are also presented in Chapter 8. Finally, Chapter 9 discusses the main conclusions found in the study along with recommendations for future work.

CHAPTER 2: BACKGROUND

2.1. Passive Site Stabilization

Liquefaction is a phenomenon marked by a rapid and dramatic loss of soil strength, which can occur in loose, saturated soil deposits subjected to earthquake motions. Liquefaction-induced ground failures can cause large deformations and settlements, resulting in structural damage, floating of buried structures, and loss of foundation support. Traditional ground improvement methods, such as soil compaction, to mitigate liquefaction damage at developed sites are often not feasible because of adverse effects on adjacent structures due to vibration, densification, and increased lateral stresses.

Passive site stabilization is an innovative, non-invasive technique where a stabilizing material is injected at the edge of a site using permeation grouting methods. The stabilizing material is delivered to target locations through augmented or natural groundwater flow (Figure 1.2). As the material flows through the formation, it displaces the existing groundwater within the pore spaces and forms a permanent gel that binds to soil particles. Passive site stabilization results in a stronger and stiffer formation that is much less susceptible to liquefaction-induced damage associated with loose, saturated sands.

The stabilizer material for passive site stabilization must meet several performance criteria. Among the performance criteria are:

- low initial viscosity
- long induction period
- controllable gel times
- environmentally benign
- permanent over the life of the project
- cost competitive with other materials

Several potentially suitable materials have been evaluated to determine whether they were applicable to passive site stabilization. The materials included microfine cement grouts,

sodium silicate grout, acrylamide grout, and colloidal silica. Among the materials, colloidal silica was reported to be an ideal stabilizer in passive site stabilization because it met the essential performance criteria (Gallagher, 2000).

2.2. Colloidal Silica

The stabilizing material presented in this study is colloidal silica (CS) and will be denoted as *CS* in the chapters that follow. Colloidal silica is an aqueous dispersion of microscopic silica particles (7-22nm) produced from saturated solutions of silicic acid. The CS modlecules are spherical in shape with negatively charged surfaces (Figure 2.1). Some of the basic properties of the colloidal silic used ini this research study are summarized below in Table 2.1. It should be noted that the specified colloidal silica concentrations in the chapters that follow will represent concentrations by weight (not volume).

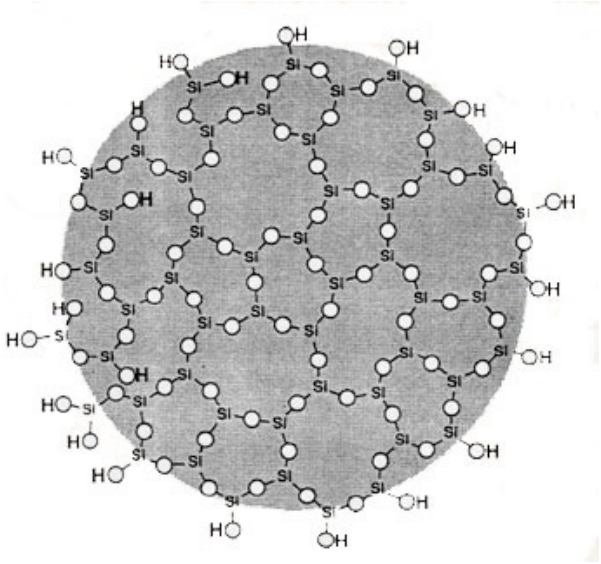

Figure 2.1 Colloidal Silica Particle (Silco International, 2005)

Table 2.1 Typical Properties of Ludox Colloidal Silia (DuPont)

Typical Properties of Ludox® Colloidal Silica	
Stabilizing counter ion	Sodium
Particle charge	Negative
Av. Particle diameter (nm)	7
Specific surface area (m2/g)	345
Silica as SiO2 (% by weight)	30
pH (25°C, 77°F)	10
Viscosity (cP)	5.5
Specific Gravity (25°C, 77°F)	1.22

2.2.1. Gel Characteristics and Gel Time

During manufacturing, colloidal silica solutions are stabilized against gelation using alkaline solutions, such as sodium hydroxide, which cause the particles to ionize and repel each other at high pH (Figure.2.3). Gelation can be induced by reducing the repulsive forces in a controlled manner, which allows the colloidal particles to interact and form siloxane (Si-O-Si) bonds as shown in Figure.2.3.

The bridging agents that allow siloxane bonds to form include monovalent cations (e.g. sodium) and divalent cations (e.g. calcium). When gelled, colloidal silica particles are linked together into branched chains that fill the volume of the solution. The overall medium is solidified by a coherent network of particles that retain the liquid solution (Iler, 1979). The chains that form these gel networks are illustrated in Figure 2.2. In soils, colloidal silica particles bond to themselves as well as the soil particles. It is believed that the bonds formed between colloidal silica particles and sand particles are created by the presence of cations in the soil.

Colloidal silica was selected to be an ideal candidate in passive site stabilization because when diluted, solutions have a low initial viscosity and long, controllable gel times. Gel times of colloidal silica can range from minutes to several months. Gel times depend on the rate of particle

to particle interaction, which depends on several variables including colloidal silica concentration, ionic strength, and/or the pH of the solution. Gel time decreases with increasing percent silica, decreasing particle size and increasing ionic strength. Higher ionic strengths will have larger effects on gel time because the addition of salt to the colloidal silica dispersion shrinks the double layer around the particles, increasing the probability of inter-particle collisions and reducing gel time. With respect to pH, a broad minimum gel time is exhibited in a near neutral range of 5<pH<7. Gel times can increase significantly outside this range (DuPont 1997, Gallagher 2000).

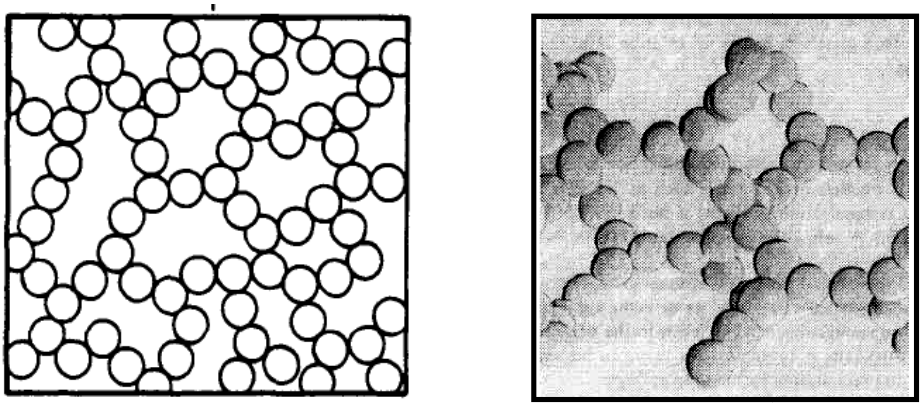

Figure 2.2 Representation of bonded colloidal silica gel particles

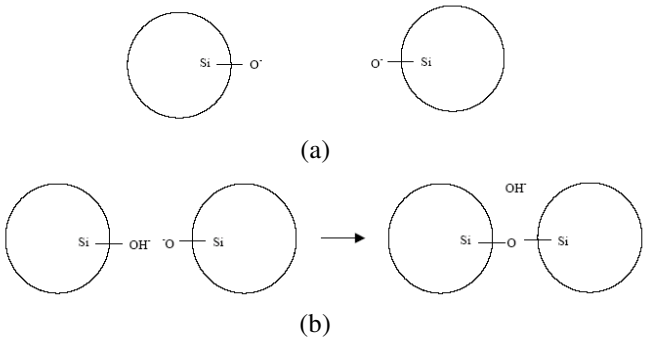

Figure.2.3 (a) O^- stabilizes solution, causing particles to repel each other (b) siloxane bond forms between molecules to induce gelation.

The shape of the gel time curve is similar regardless of gel time (Figure 2.4). It is characterized by an initial period, where the viscosity stays low and is followed by a rapid increase in viscosity and subsequent gelation. When diluted, the viscosity of colloidal silica solutions is similar to water (≃1 cP) and behaves as a Newtonian fluid. As the viscosity begins to increase rapidly, the behavior becomes non-Newtonian. Persoff et al. (1999) provides a chart of gel state descriptions with corresponding viscosities that range from gel state 1 (≈2 cP) to gel state 11 (≈2500 cP). The gel state descriptions are shown in Table 2.2. From Figure 2.5, gel State 1 is the period during which the viscosity of the catalyzed solution remains virtually unchanged (≈2 cP). During gel state 2, the viscosity gradually begins to increase (up to ≈ 10cP). At the initiation of gel state 3, the solution begins to rapidly progress at an exponential rate through several states including a flowing gel state, a non-flowing gel, a rigid gel, and a ringing resonated gel.

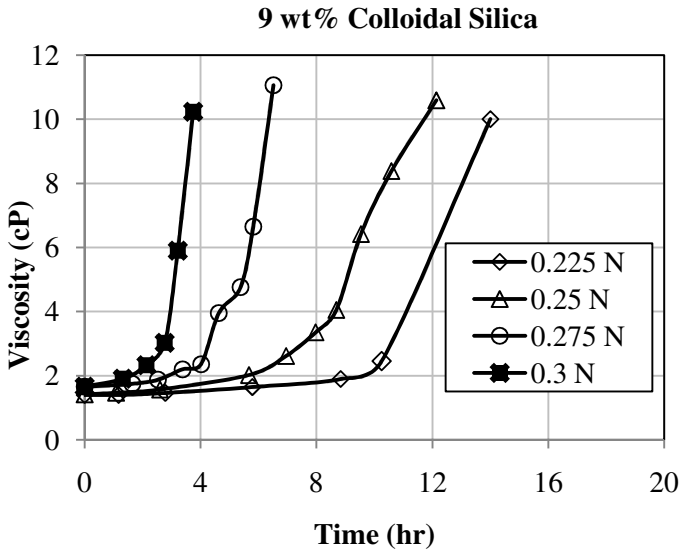

Figure 2.4 Typical gel time curve of colloidal silica at various normalities

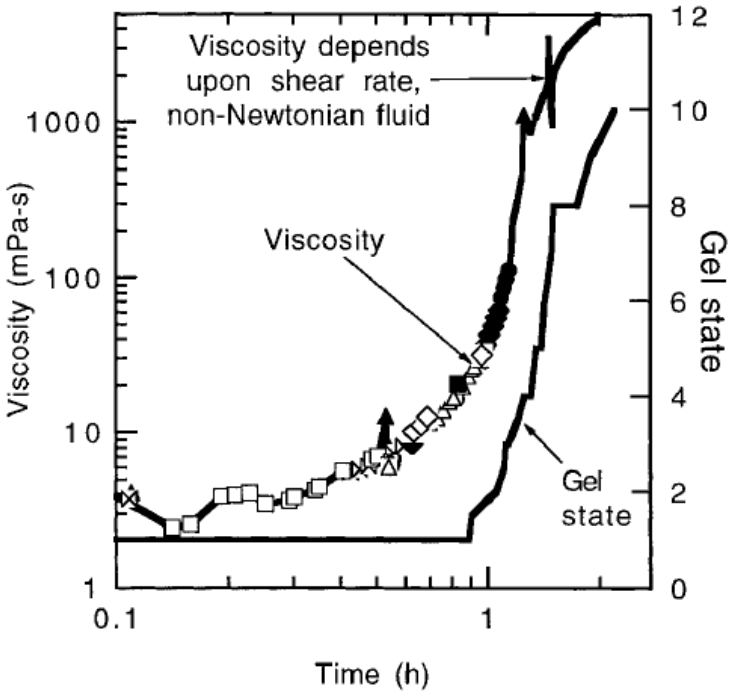

Figure 2.5 Gel Time Curve for Gel States (Persoff, 1999)

Table 2.2 Gel State Descriptions (Persoff, 1999)

Gel State	Description
1	No detectable gel formed; Gel appears to have same viscosity as original solution
2	Highly flowing gel; Gel appears to be only slightly more viscous than initial polymer
3	Flowing gel
4	Moderately flowing gel
5	Barely flowing gel
6	Highly deformable non-flowing gel
7	Moderately deformable non-flowing gel
8	Slightly deformable non-flowing gel
9	Rigid gel
10	Ringing rigid gel; Tuning-fork-like mechanical vibration can be felt

2.2.2. Other Performance Criteria

Colloidal silica has also been found to be permanent, nontoxic, biologically and chemically inert, and has excellent durability characteristics (Iler, 1979 and Whang, 1995). Additionally, CS is cost competitive with other potential stabilizing materials. Table 2.3 shows cost comparisons of CS with other materials.

Table 2.3 Cost comparisons of colloidal silica and other stabilizing materials

Treatment	Cost per m^3 soil
CS (5%)	$60
CS (15%)	$180
Microfine cement	$100-$200
Sodium Silicate	$180
Acrylamide	$500

The strength of soils treated with colloidal silica grout depends primarily on the concentration of colloidal silica. Persoff et al. (1999) found that unconfined compressive strengths of Monterey No. 0/30 sands saturated with colloidal silica ranged from 70 kPa (10 psi) to 345 kPa (50 psi), respectively. Gallagher and Mitchell (2002) found similar trends and reported that the unconfined compressive strength of loose Monterey No. 0/30 sand treated with 5% (by weight) colloidal silica ranged from about 20 kPa (3 psi) to 55 kPa (8psi), while the same sand treated with 20% (by weight) ranged from 200 kPa (29 psi) to 250 kPa (36 psi). Based on these results, it was concluded that liquefiable sands treated with a minimum of 5% (by weight) colloidal silica should provide adequate liquefaction resistance. A secondary factor in the strength gain is the length of time the sample cures prior to testing. The major advantages of colloidal silica over other materials, such as sodium silica grouts, are its permanence and its ability to increase the strength of soils over time. Persoff et al. (1999) found that strength

continued to increase for up to one year after treatment with colloidal silica grout. Studies show the majority of strength gain will occur during a curing time of about 4 times the resonating gel (Gallagher and Lin, 2007). Based on gel time characteristics presented in Table 2.2 and Figure 2.5, this equates to the time to reach Gel State 10.

2.3. Colloidal Silica Applications

Colloidal silica has been primarily used for environmental remediation in the subsurface through permeation grouting. Studies from Persoff (1999) found that sands grouted with colloidal silica produced hydraulic conductivities less than $1*10^{-7}$ cm/s for concentrations greater than 7.4% (by weight). The unique characteristics of colloidal silica gel including gel time behavior, permanence, and reduction in hydraulic conductivity make it a suitable barrier material for containment applications.

Applications of colloidal silica originated as a way for blocking oil flow through porous media (Bennett et al., 1988; Jurinak et al., 1989). Applications evolved into barrier containment, sealing of fractures, and ground stabilization. Noll et al. (1993) performed field tests and confirmed the feasibility of colloidal silica to be used for (1) constructing a hot spot stabilization area and (2) constructing a horizontal containment barrier. Colloidal silica was also shown to be a suitable material for forming horizontal and vertical barriers for waste isolation (Persoff, 1995). Field studies conducted by Moridis et al. (1996) successfully used 30% (by weight) colloidal silica to create a subsurface barrier in unsaturated, heterogeneous deposits of silts, sands, and gravels. Due to its small nano-sized particles, field tests have shown that silica solutions can penetrate apertures smaller than 50μm. Based on this characteristic, a more recent application of colloidal silica was used as a way to seal narrow fractures in tunnels where hydraulic tests revealed a sealing efficiency of about 70% (Funeha and Fransson , 2005)

2.4. Colloidal Silica for Liquefaction Mitigation

Another area in which colloidal silica can be applied is through permeation grouting in which groundwater is replaced within the subsurface, binds to soil particles, and stabilizes the soil. Due to its relevance in passive site stabilization methods, this can be extremely useful when infrastructure rests on liquefiable soil deposits such as loose, saturated sands and artificial fills.

Laboratory, pilot-scale, centrifuge modeling, and full-scale field tests have demonstrated colloidal silica to be an adequate material to mitigate the effects of liquefaction-induced damage. Laboratory tests show that loose sands treated with a minimum of 5-10% (by weight) colloidal silica provide adequate liquefaction resistance and dramatically increases deformation resistance of loose sand under cyclic loading (Gallagher and Mitchell, 2000). In this study, sands treated with 5-10% (by weight) colloidal silica sustained up to 100 loading cycles at cyclic stress ratios ranging from approximately 0.2 to 0.4 while untreated samples failed at an average of 3 cycles. The improvement during cyclic load tests is illustrated in Figure 2.6 for untreated soil versus 10% (by weight) colloidal silica specimens. Additionally, Kodaka (2005) shows improvememt of colloidal silica treated specimens under cyclic and monotonic loading using torsional shear tests. Under 100 kPa (14.5 psi) confinment, shear strains from treated specimens were reduced from 10% to about 3% under similar shear stresses. The study presented by Kodaka et al. (2005) is further discussed in chapter 5, where dynamic behavior of colloidal silica soils are explained in greater detail.

Centrifuge model tests were also performed on colloidal silica soils to study the feasibility of liquefaction mitigation. Gallagher et al. (2007) used centrifuge modeling to examine the effect of colloidal silica treatment (6% by weight) on the liquefaction and deformation resistance of loose, liquefiable sands during centrifuge in-flight shaking. For peak accelerations of 0.2g and 0.25g liquefaction did not occur and strains were reduced from 3-6%

(untreated) to 1-2% (treated). It should be noted that the strains reported from the untreated soil were taken from centrifuge test results with similar soil properties and similar applied shaking motions by Taboada (1995).

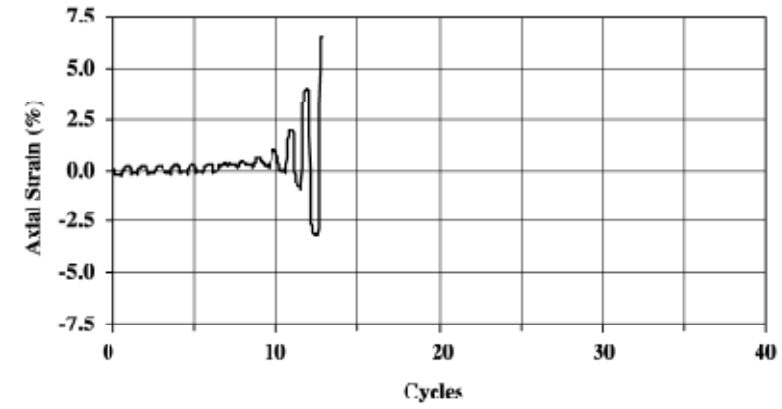

(a)

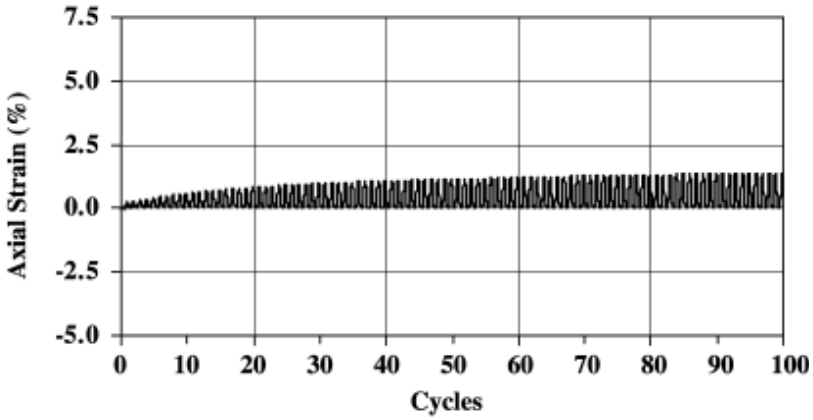

(b)

Figure 2.6 Shear Strain from Cyclic Triaxial Testing for (a) Untreated and (b) 10% colloidal silica treated sands (CSR=0.27)

Additionally, Pamuk et al. (2003) performed centrifuge tests and showed colloidal silica significantly reduces liquefaction resistance surrounding pile foundations. In the model, a three-layer soil profile was used in which a loose sand layer was sandwiched between two lightly cemented layers. End-bearing piles penetrated all three layers. The model was inclined 2º to permit lateral spreading as the loose sand liquefied. In an untreated model, the piles failed due to the effects of lateral spreading. The model treated with 6% (by weight) colloidal silica provided significant liquefaction resistance, greatly reduced the free field lateral deformation, and reduced the imposed moments on the piles from 190–300 kN·m (70 - 110.5 ton·ft) to 94-260 kN·m (35-96 ton·ft). The measured maximum permanent ground deformation was also found to be reduced by 90% in the treated soil zone versus the untreated soil zone.

Finally, a full scale field test was performed to study the performance of soil stabilization using colloidal silica (Gallagher et al., 2006). In this field test, the upper one third of an approximately 10 m (33 ft) thick liquefiable layer was saturated with an 8% (by weight) colloidal silica solution. The colloidal silica was injected under low pressures using permeation grouting techniques. The grouting was performed in a 2-stage, bottom-up process where each stage was isolated using a double packer. Blast-induced liquefaction resulted in a 30% reduction in settlement compared to that of an adjacent untreated test area. While treatment resulted in a significant reduction in surface settlement, CPT and shear wave velocity profiles were unable to detect improvement. This may be attributed to the uncertainty of colloidal silica migration in the subsurface or the lack of correlation between CPT and/or shear wave velocity data to the treatment mechanism.

2.5. Gaps in Knowledge for Colloidal Silica Treated Soils

The attributes of earthquake-induced liquefaction damage is strongly influenced by the response of soils to cyclic loading. This response is controlled by the mechanical properties of the soil. For geologic materials, such as sands and clays, the dynamic soil properties are well

established. Soils treated with colloidal silica, on the other hand, represent a composite material that has its own unique mechanical properties. Research has shown colloidal silica treated soils significantly reduce shear strains and settlements produced under cyclic loading. However, there is a need to look at the mechanical properties of colloidal silica soils in a way that can allow them to be incorporated into soil models that characterize cyclic soil behavior. Soil models fall under three general classes: (1) equivalent linear models (2) cyclic nonlinear models and (3) advanced constitutive models.

Equivalent linear models and equivalent nonlinear models are the most popular soil models used to represent dynamic behavior of soils. Equivalent linear models are the simplest soil models. Cyclic nonlinear models, on the other hand are more complex, but more accurate since they follow the actual stress-strain path. For both of these model types, one of the fundamental requirements is the use of the modulus reduction curve. Recently, resonant column tests were performed for colloidal silica soils and the shear modulus reduction curve was established under low strains (Spencer, 2007). In this way, the shear modulus reduction curve is developed for small strains only and shear modulus must still be determined at high strains to complete the reduction curve. This research aims to define shear modulus at high strain levels so that the shear modulus reduction curve can be established.

Additionally, cyclic nonlinear models also require a series of "rules" that govern unloading-reloading behavior and stiffness degradation. For example, an accurate pore pressure generation model can capture changes in effective stress and capture transmission of stresses between the soil and the colloidal silica during undrained, cyclic loading. Another example is treatment with higher colloidal silica concentration because higher concentrations yield greater unconfined compressive strengths in sands. In order to define the "rules" that govern unloading-reloading behavior and stiffness degradation, factors such as pore pressure response and colloidal silica concentration must first be studied under a wide range of dynamic loading levels.

Liquefaction induced damage includes settlements and lateral spreading that can ultimately lead to tilting, floating, and even total collapse of the existing infrastructure. Testing has shown increases in cyclic strength for colloidal silica soils and decreases in imposed bending moments along pile foundations (Gallagher et al., 2000; Kodaka et al. 2005; Pamuk et al., 2003). There is a further need to study how liquefaction-induced damage will be affected for different site geometry. For example, port facilities often rest on loose artificial fill susceptible to liquefaction, such as that shown in Figure 2.7. The figure shown below represents a liquefiable soil layer overlain by a thin clay layer sloped towards a central water channel. The wharf is embedded within the liquefiable soil layer which in turn supports the crane. Some uncertainties concerning liquefaction mitigation include the required lateral extent necessary to prevent structural damage. One example would be the minimum lateral distance of colloidal silica treatment necessary to prevent structural damage of the wharf and crane. Another example might include the effects treatment would have on non-liquefiable soils that exist above liquefiable soils.

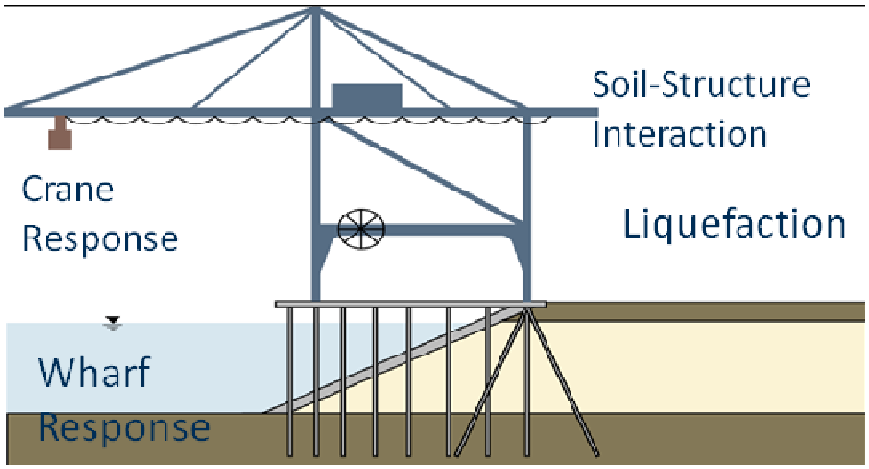

Figure 2.7 Port geometry representation

An additional "gap in knowledge" of colloidal silica soils is a means to identify these soil types under static conditions. For example, when injecting colloidal silica soils into the subsurface, there is a need to identify treatment levels and ensure proper in-situ coverage. Development of such quality control measures would make colloidal silica a more attractive treatment option. Pilot scale and full scale field tests have utilized conductivity probes to measure changes in electrical conductivity of pore fluid as a way to monitor grout advancement (Gallagher et al., 2006; Hamderi, 2010). Although this has shown to be a reliable method to track migration, it does not necessarily reflect the level of improvement once the grout has gelled. Geophysical methods, such as cone penetration testing and shear wave velocities are commonly used in practice to characterize subsurface conditions and soil stiffness. These methods, among others, may also serve as potentially viable means to determine treatment levels.

There are numerous issues remaining for treating with colloidal silica at the full-scale field level as well. Some of the issues include optimal techniques for horizontal delivery. This is a complex issue because grout migration is affected by numerous parameters. Factors such as permeability, soil variability, and subsurface chemistry play a direct role in grout migration along with variable density and viscosity of the gel itself. Hamderi (2010) utilized a 3D flood simulator (UTCHEM) to predict colloidal silica migration measured in a pilot-scale test model. The study concluded UTCHEM was a feasible program to configure optimal well configurations as long as subsurface conditions were well characterized. However, numerical models are limited and do not incorporate important parameters that affect migration. Examples include subsurface irregularities (preferential flow paths) and reaction of CS with chemistry of the subsurface.

2.6. Summary

Based on the unique characteristics of colloidal silica, it has been selected as an ideal material for passive site stabilization. Passive site stabilization allows for soil improvement in developed areas where access is limited and can improve the soil underneath existing structures. Applications of colloidal silica are continuing to evolve as more research is conducted. Based on previous testing, ground improvement for purposes of liquefaction mitigation is one application in which colloidal silica shows promise.

There are still many unresolved issues that remain for liquefaction mitigation using colloidal silica. For predicting dynamic response, soil models are well established for geologic materials such as sands and clays. There is a further motivation to develop similar models for colloidal silica soils (i.e. equivalent linear and cyclic nonlinear). If such models can be developed, they can be eventually incorporated into numerical models for purposes of ground motion response analysis. Therefore, this study aims to experimentally determine some of the basic requirements necessary for developing soil models. This includes modulus reduction curves, pore pressure response characteristics, and colloidal silica concentration effects.

There is also an uncertainty on the effect that treatment will have for different site geometry. Liquefaction has been shown to result in excessive settlements, lateral spreading and ultimately severe structural damage. One example of site geometry is the effect that treatment will have when a sloped embankments exists on the shoreline and rests above a liquefiable soil layer. This geometry type is commonly found at port facilities. This study also aims to model the geometry commonly found at port facilities and compare the overall level of improvement.

Characterizing colloidal silica soil under static conditions also poses a challenge for monitoring treatment coverage in the subsurface. If there is a way to distinguish colloidal silica soils from other geologic materials under static conditions, colloidal silica would be an attractive mitigation method for field applications because treatment coverage could be directly measured.

This study was also motivated to research parameters that could potentially distinguish colloidal silica soils under static conditions and include cone tip resistance and shear wave velocity.

Finally, with only one documented field test using colloidal silica for liquefaction mitigation, there is a greater need to begin to develop field procedures including QA/QC measures. The field test presented in this study aims to address field procedures and offer recommendations to improve future field tests.

CHAPTER 3: CENTRIFUGE TESTS - DETAILS

Two centrifuge tests were conducted at the Center for Geotechnical modeling at the University of California, Davis. The facility is equipped with a 9 m (30 ft) centrifuge arm illustrated in Figure 3.1. This chapter discusses the details of two centrifuge tests that were conducted to evaluate the effectiveness of soils grouted with colloidal silica soils. The model represents a 4.8m (16 ft) thick liquefiable layer overlain by a 1 m (3 ft) thick silty clay layer sloping towards a central channel to study effects of lateral spreading. The centrifuge test evaluates and compares the response of a 9% (by weight) 5.25% (by weight), and 4% (by weight) colloidal silica treated sand and an untreated sand during and after shaking. A sequence of shaking events was applied to the models with a testing centrifugal acceleration of 15g. For each shaking event, 20 cycles of a sinusoidal wave at a frequency of 2 Hz were applied.

Figure 3.1 Centrifuge from University of California, Davis

3.1. Centrifuge Modeling

Centrifuge testing has been used extensively in earthquake modeling because earthquakes are infrequent and unrepeatable. This makes it difficult to obtain the required data to study their effects through actual post-earthquake field investigations. The shaking applied to a centrifuge model can range from a simple, repeating sine wave motion to a recorded acceleration time history from a real earthquake event. The centrifuge applies an increased gravitational acceleration to physical models in order to produce identical self-weight stresses in the prototype through stress similitude. Scaling laws, based upon centrifuge test accelerations, are applied in order to convert the model scale data to the prototype data. The scaling laws for several common parameters are given in Table 3.1.

Centrifuge modeling has been commonly used to model liquefaction and determine the mechanisms that influence it. Similarly, centrifuge model tests can serve as a valuable tool for closely examining methods to mitigate liquefaction.

Table 3.1 Centrifuge scaling factors for common parameters (Kutter, 1995)

Parameter	Ratio of model to prototype
Length	1/n
Area	$1/n^2$
Volume	$1/n^3$
Stress	1
Strain	1
Force	$1/n^2$
Velocity	1
Frequency	n
Time (dynamic)	1/n
Time (consolidation)	$1/n^2$

(1) n = centrifuge test acceleration

3.2. Purpose and Configuration of Test

The overall objective of the tests was to compare the response of liquefaction and lateral spreading in similar slopes both during and after shaking. Various concentrations of colloidal silica were used to treat the liquefiable soils in order to compare the effects of different concentrations of treatment versus no treatment. Both model tests were performed at a centrifugal acceleration of 15 g and the results are presented in prototype units hereafter, unless otherwise noted.

Each test was constructed with similar geometry and soil properties. The two sides were symmetrically sloped 3° towards a 3m wide central channel and comprised of three distinct layers: (1) a bottom layer of dense Monterey 0/30 sand with prototype thickness of 0.75 m (2.5 ft), overlain by (2) a 4.8 m (16ft) thick liquefiable layer of loose Nevada sand, which was overlain by (3) a 1.0 m (3.3 ft) thick layer of compacted Yolo loam (Figure 3.2).

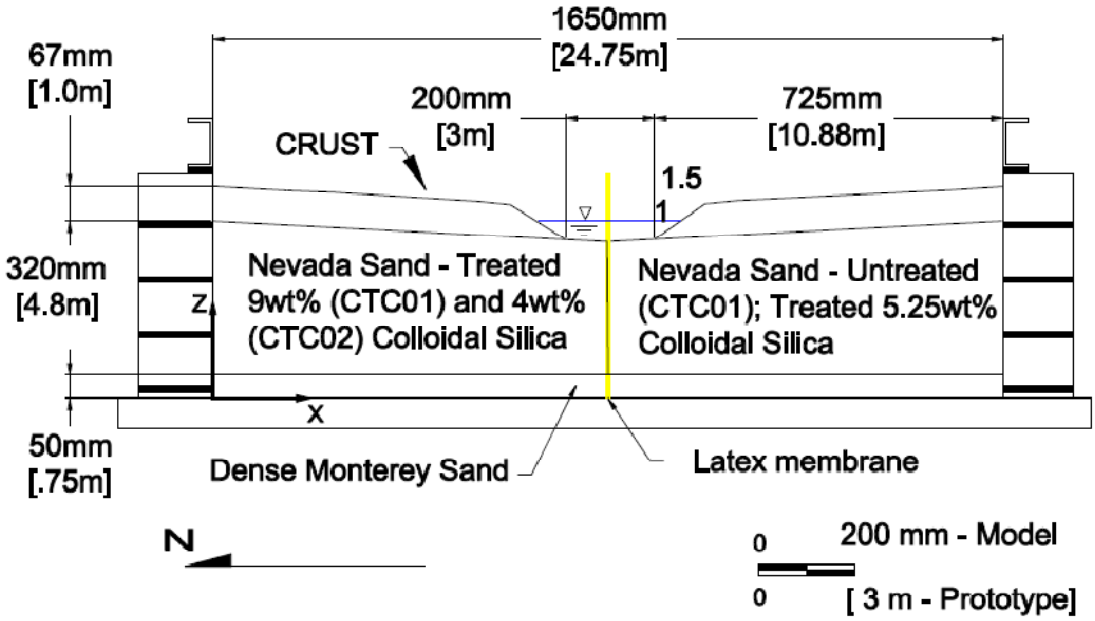

Figure 3.2 Model Geometry

There were two basic objectives of the centrifuge tests: (1) to compare the response of liquefaction and lateral spreading using 4%, 5.25% , and 9% colloidal silica treatment and no treatment in the liquefiable layer and (2) to characterize the effects of various levels of improvement in terms of accelerations, displacements, and pore pressures.

For the first test, the soil upslope of a central channel on one side of the specimen box was treated with 9% colloidal silica stabilizer. The other side of the model was left untreated and the liquefiable layer was saturated with water only. The first test will be denoted as *CTC01*. In the second centrifuge test, the soil upslope of the central channel on one side of the box was saturated with 4% colloidal silica while the other side was saturated with 5.25% colloidal silica stabilizer (Figure 3.2). The second test will be denoted as *CTC02*.

Laboratory triaxial tests performed by Gallagher and Mitchell (2002) show that a minimum grout concentration of 5% was found to provide adequate liquefaction resistace while cyclic torsional shear tests performed by Kodaka (2005) shows that 4% treatment concentration was adequate to provide liquefaction resistance. The purpose of using lower grout concentrations in CTC02 was to establish a limiting grout concentration effective for treatment. It should be noted that gel time tests were performed in the lab prior to the centrifuge tests. The experiments showed that although a 4% CS solution can gel,it did not reach a fully resonated gel state. Therfore, the 4% colloidal silica solution on the “untreated” side was a way to compare the response of a weak, non-resonated gel versus a strong, resonated gel. The 4% colloidal silica solution reached gel state 3 in approximately 84 hours and reached gel state 7 at the time of testing. Gel state 7 is characterized as a moderately deformable non-flowing gel (Table 2.2).

The model was built inside a flexible shear beam model container, denoted FSB3 (Table 3.2). A total of nine shaking events were applied to the models at a centrifugal acceleration of approximately 15 g. All but one motion consisted of 20 cycles of a sinusoidal wave at a frequency of 2 Hz (prototype scale). One motion in CTC02 was a scaled version of a ground motion recorded at San Fernando in 1971 (referred to as the PSL motion).

All shaking events were applied transverse to the river channel in the north-south (longitudinal) direction, and consisted of 20 cycles of a sinusoidal wave, at a frequency of 2 Hz (prototype scale). The testing and shaking sequence is summarized in Table 3.3.

Table 3.2 Model Container Properties (FSB)

Container type	shear beam
Container mass (kg)	920
Volume (L)	770
Max. capacity (kg)	1530
Length (mm)	1650
Width (mm)	790
Height (mm)	586

Table 3.3 Test Shake Sequence

CTC01		**CTC02**	
Event ID	**PBA [(1)]**	**Event ID**	**PBA [(1)]**
CTC01_01	0.007	CTC02_01	0.007
CTC01_02	0.03	CTC02_02	0.03
CTC01_03	0.10	CTC02_03	0.15
CTC01_04	0.19	CTC02_04	0.25
CTC01_05	0.56	CTC02_05	0.69
CTC01_06	0.03	CTC02_06	0.03
CTC01_07	0.18	CTC02_07	0.24
CTC01_08	1.28	CTC02_08 [(3)]	0.89
CTC01_09	0.03	CTC02_09	1.37

(1) Peak Base Acceleration determined by average recordings at north and south base of container

3.3. Model Preparation

3.3.1. Soil and Sensor Placement

The dense and loose sand layers were placed using a dry pluviation technique. A large box pluviator was calibrated and used to achieve an average relative density of approximately 95% in the dense Monterey sand. A barrel pluviator, shown in Figure 3.3, was calibrated and used to achieve an average relative density of approximately 35% (CTC01) and 45% (CTC02) in the loose Nevada sand layer. Prior to pluviating the sand layers, a latex membrane was placed in the center of the container in order to prevent the two different pore fluids from mixing during saturation. In addition to the latex membrane, open steel tubes were placed vertically on the untreated side and treated side (Figure 3.4). The vertical sand tubes were to be filled up with colored sand after placing the sand and crust layers in order to create vertical sand lines throughout the profile. The purpose of the vertical sand lines was to observe the movement of the liquefied soil layer, including the relative movements at the interface between the crust and the loose sand.

Accelerometers, pore pressure transducers, linear potentiometers, and linear variable differential transformers (LPs and LVDTs, respectively) were placed in the model in order to measure accelerations, pore pressures, and horizontal and vertical displacements during and after each shaking event. The various sensors were placed at their prescribed levels during the placement of the soil layers (Figure 3.4). After pluviation of a given sand lift, excess sand was vacuumed to achieve the desired elevation for each sensor. Once the sand surface was vacuumed and sensors were placed, elevations and sensor locations were measured and recorded. The sensor layouts of the models are illustrated in Figure 3.5.

Figure 3.3 Barrel pluviator for sand placement during model preparation

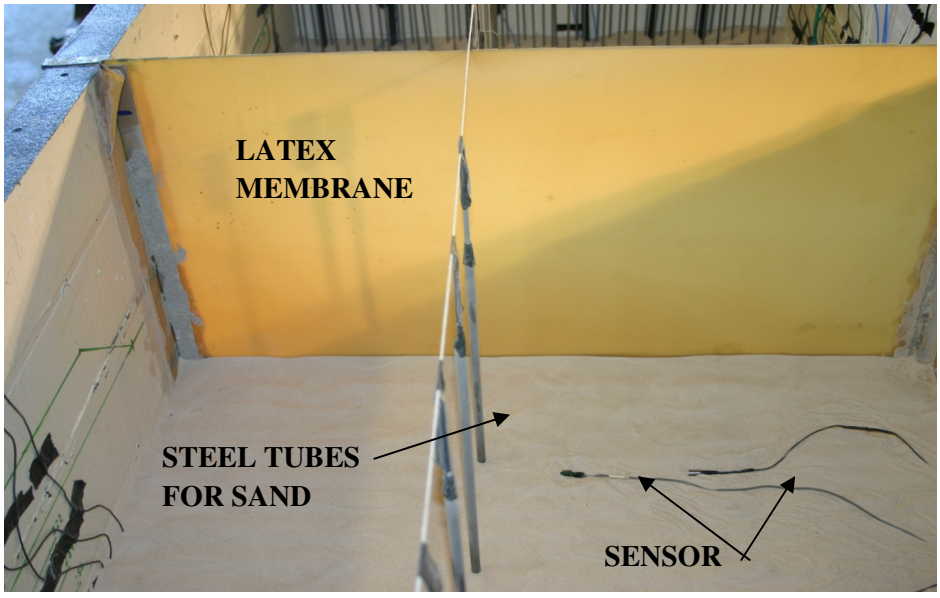

Figure 3.4 Sensor placement during model preparation

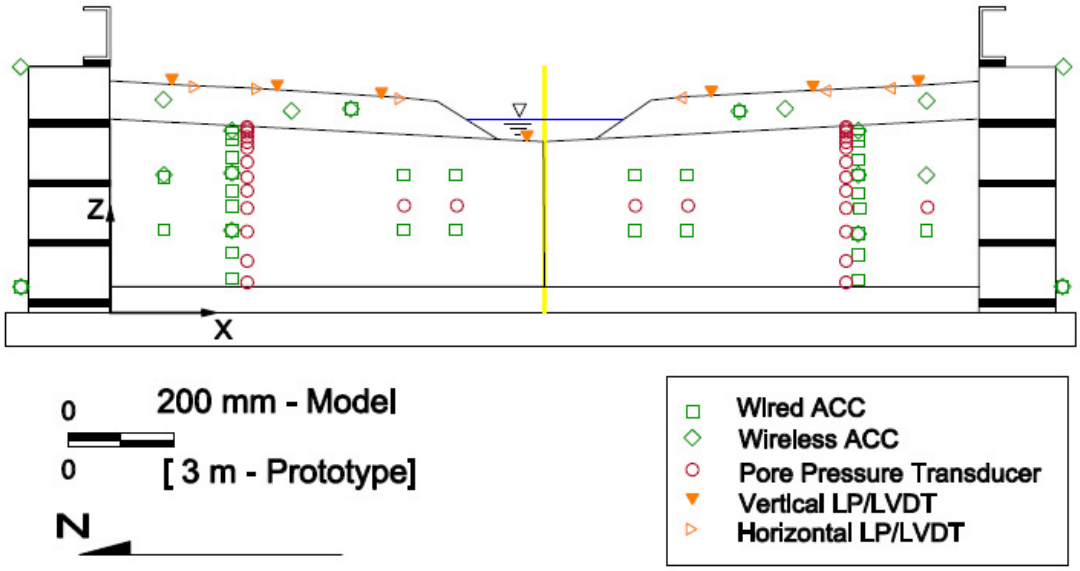

Figure 3.5 Overall Sensor Layout

3.3.2. Colloidal Silica Preparation and Saturation

A minimum target time to reach gel state 3 of the colloidal silica was chosen to be approximately 12 hours based upon (1) the amount of time to saturate the treated zone of the model and (2) to allow the solution enough time to reach its maximum strength gain of at least 4 times the resonating gel time prior to shaking. Once the viscosity of the colloidal silica solution reaches gel state 3, there is a rapid increase in viscosity and at this stage, it becomes nearly impossible for the solution to flow through the liquefiable sand zone. Gel times of the solution for the test were controlled by altering the ionic strength of the solution through the addition of sodium chloride.

Prior to model preparation, laboratory tests were conducted on the colloidal silica solutions at various normalities to establish the normality that yielded the desired time to achieve gel state 3. The time to reach gel state 10 was determined through inspection of laboratory tests when the solution became a ringing ("tuning-fork like), resonated gel. At the time of shaking, the

9% and 5.25% stabilizer solutions had surpassed its maximum strength gain of 4 times that of gel state 10. The properties of the various concentrations of colloidal silica used in the experiments are summarized in Table 3.4.

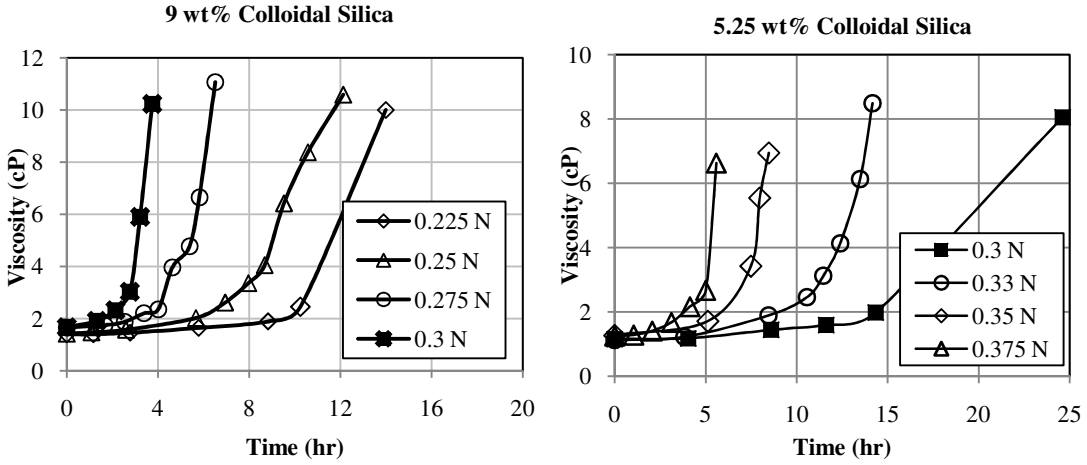

Figure 3.6 Gel Time Lab Tests for (a) 9% and (b) 5.25% colloidal silica

Table 3.4 Colloidal Silica Properties

Colloidal Silica Concentration	9%	5.25%	4%
Normality (N)	0.24	0.33	0.27
Time at Gel State 3 (hr)[1]	13	15	84
Resonating time (hr) [2]	16	26	120
N* gel time at Maximum strength	4	4	N/A
N* gel time at time of shaking	10	12	N/A
Density (g/cc)	1.06	1.05	1.04
Initial Viscosity (cP)	1.3	1.15	1.1

[1] Viscosity of solution measured by a Cannon Ubbelohde Viscometer

[2] Refers to Gel State 10 (Persoff, 1999)

[3] Defined as 4* resonating time or 4* Gel State 10 (Gallagher and Mitchell, 2002)

In CTC01, a total of 176 L (46.5 gal) of 9% CS solution was prepared in a saturation tank by first mixing approximately 130 L (34 gal) of deionized water, and 2.5 kg (5.5 lb) of sodium

chloride, yielding a normality of 0.24. Red food dye was also added to the solution in order to distinguish between the treated and untreated zones and visually inspect treatment coverage during model dissection. The salt/water/dye solution was thoroughly mixed using an air circulation pump. Approximately 46 L (12 gal) of Ludox SM 30 CS was later added to the salt/water/dye solution, yielding a CS concentration of 9%.

The general procedure for saturation of centrifuge models is depicted in Figure 3.7. Prior to saturation, a vacuum lid was placed on the model container and a vacuum pressure of approximately 90 kPa (26 psi) was applied inside the model in order to remove any air within the voids of the soil. As the vacuum pressure was relieved from the model container, it was flooded with carbon dioxide (CO_2) gas in order to ensure that any remaining, less soluble air trapped within the voids of the soil was displaced. Vacuum pressure was then reapplied to prevent any additional air from entering the model during saturation. Once vacuum pressure was reapplied, the solution was introduced into the model from a de-aired water chamber. Figure 3.8 shows the vacuum lid on the container while the model was being saturated under vacuum pressure.

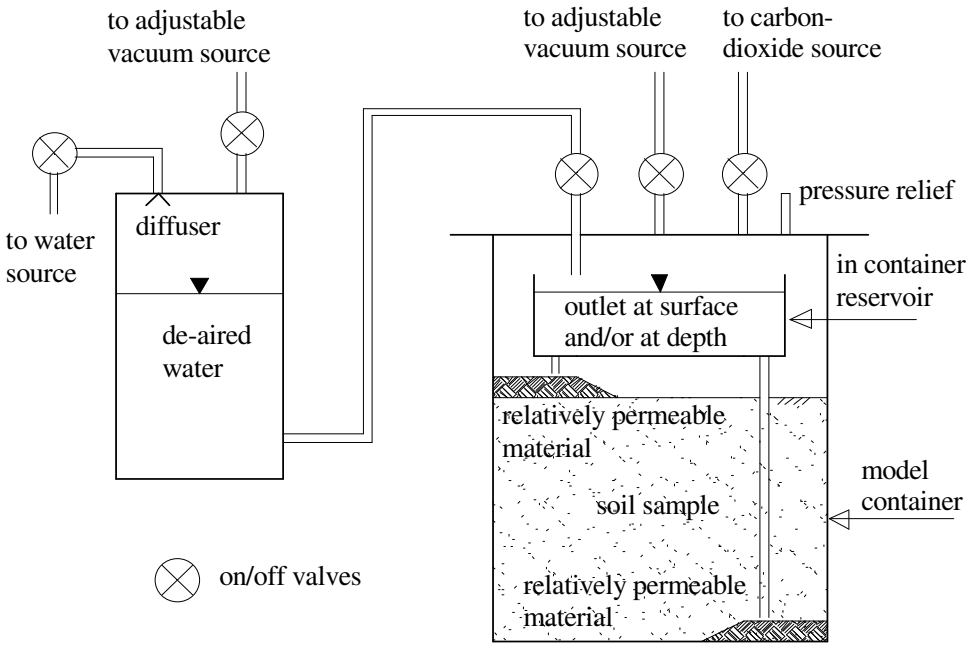

Figure 3.7 Saturation layout for centrifuge tests

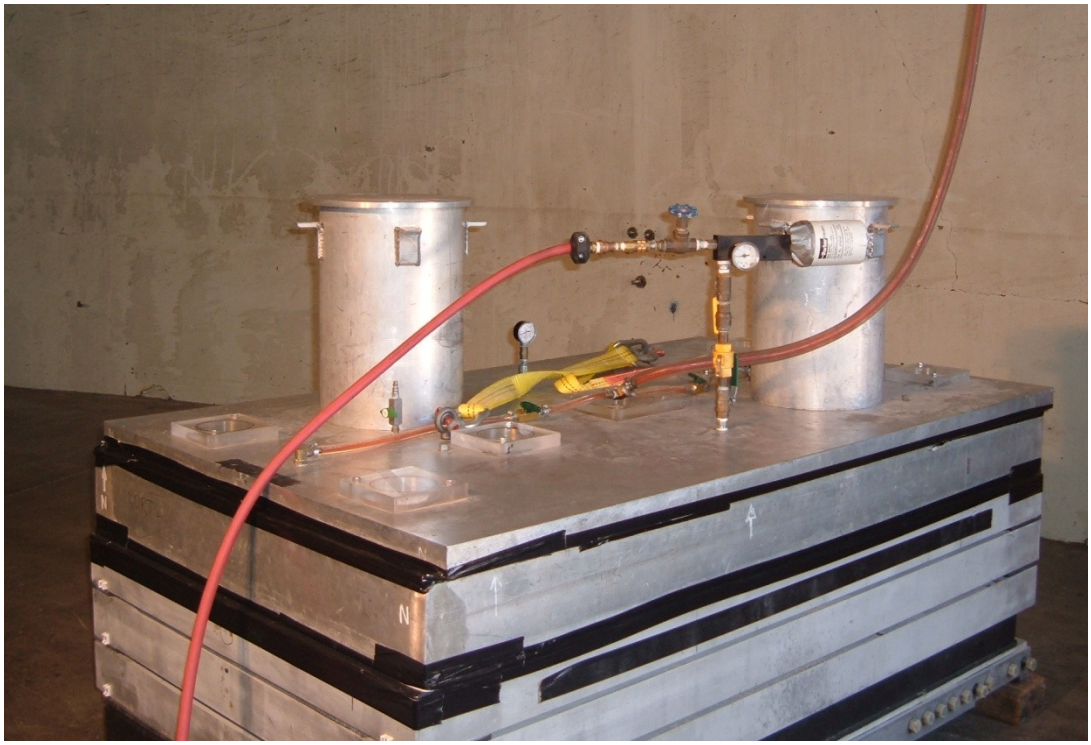

Figure 3.8 Model saturation under vacuum pressure

As the solution was introduced into the model container, it would slowly drip into troughs mounted on the north and south ends of the container. The troughs were connected to saturation tubes which extended to the bottom of the model container. For CTC01, the colloidal silica solution would slowly drip into the north trough such that saturation took place from the bottom up. When saturation was near completion, the injection rate dramatically decreased and it was necessary to modify the saturation procedure such that the solution would slowly overflow the troph and have enough time to fully saturate the model. In this way, the remainder of the saturation process took place from the top, down. In CTC01, the liquefiable layer appeared to be saturated in approximately 5 hours and a total of 115 L (30 gal) of solution was injected into the model.

Once saturation was complete, the vacuum pressure was slowly released from the model and the height of fluid was carefully monitored. While the vacuum pressure was released, the solution elevation decreased below the surface of the liquefiable sand layer, indicating that the solution was continuing to fill in dry pockets within the liquefiable layer. At this point, vacuum release was stopped and more colloidal silica solution was added to the model. This process was repeated until there was no further drop in the level of the solution, indicating that the liquefiable layer was fully saturated. The model surface after colloidal silica saturation is shown in Figure 3.9. After gelation, the excess gel was trimmed to be flush to the surface of the loose sand layer.

Preparation and saturation for CTC02 was similar to CTC01. In CTC02, a total of 195 L (52 gal) of 4% colloidal silica solution was prepared. Red food dye was added to the solution in order to distinguish between the 4% and 5.25% solutions and visually inspect treatment coverage during model dissection. The preparation and saturation of the 5.25% solution was then conducted on the second half of the model. When saturation was complete, a total of 90 L (24 gal) of solution was injected into the model.

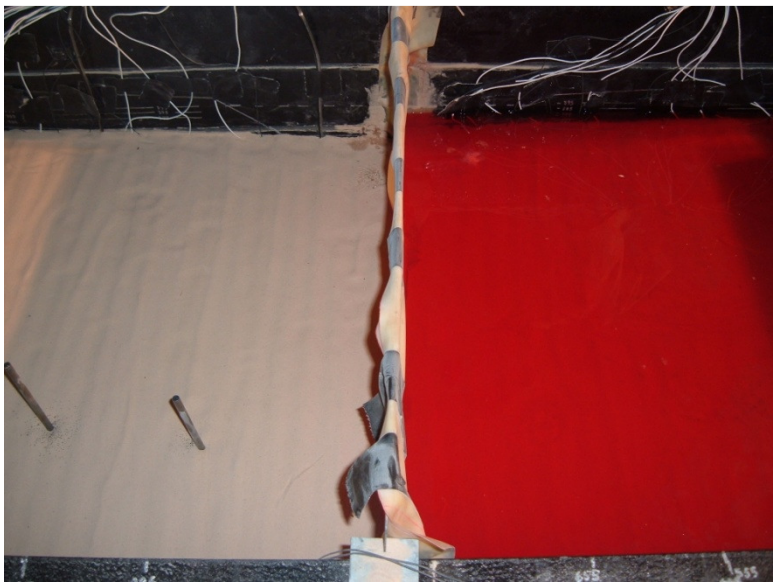

Figure 3.9 Model surface after colloidal silica saturation

During saturation, it should be noted that leaking occurred in CTC01 around the latex membrane and a portion of the colloidal silica flowed into the untreated zone. It was estimated that approximately 20L (5 gal) of solution flowed into the untreated zone. During model dissection, it was observed that the silica solution was only found around the edges of the model in the untreated zone and was not located around any sensors. The leaking did not appear to have significant impact on the sensor readings recorded in the untreated area.

3.3.3. Crust Placement and Saturation of Untreated Side

The crust layer was placed after the liquefiable layer was saturated with colloidal silica. Colloidal silica saturation of the liquefiable layer was performed without the crust layer for several reasons: (i) prevent saturation of the crust layer with colloidal silica (ii) observe the saturation front and (iii) prevent a preferential flow path of the colloidal silica that would potentially create weaker zones that were not fully saturated in the liquefiable layer.

The crust layer was constructed using a natural Yolo Loam, which was sun-dried and sieved to pass a #10 sieve. Water was added to reach a water content of approximately 15%, which was estimated to be the optimum water content for the soil. The crust was placed in several lifts and each lift was compacted with a model-sized sheeps foot roller illustrated in Figure 3.10. The sheeps foot roller created a normal stress on the surface of approximately 9 kPa (1.3 psi). The weight was chosen such that the compaction pressure would not exceed the prototype pressure on the top of the sand layer, estimated to be 10 kPa (1.5 psi). Finally, the crust layer was trimmed to the appropriate sloped geometry.

Once the crust layer was complete, the container was placed on the arm of the centrifuge. In CTC01, the untreated side of the model was saturated with deionized water. Similarly, the model was flooded with carbon dioxide (CO_2) gas and placed under a vacuum. As a result of leaking of colloidal silica solution around the membrane, the saturation tubes on the untreated side became clogged and saturation procedures had to be modified. A total of 90 L (24 gal) of

water was slowly dripped into 6 reservoir troughs on the south end of the model that directed flow towards the surface of the model. In this way, saturation took place from the top, down. During saturation, a latex membrane was placed on the surface in order to prevent erosion of the crust. The modified saturation procedure is illustrated in Figure 3.11.

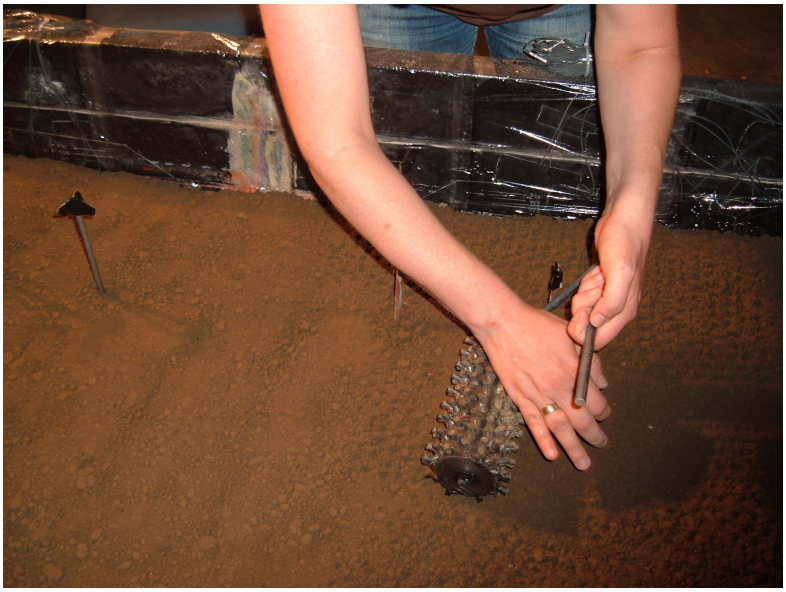

Figure 3.10 Crust compaction using sheeps foot roller

Lastly, deionized water was used to fill the central channel of both models. It should be noted that upon spin-up of the model, the soil consolidated and the water table decreased slightly. In order to maintain the desired elevation in the central water channel, water was slowly added in-flight. The surface of the completed model is later illustrated in Figure 4.1a.

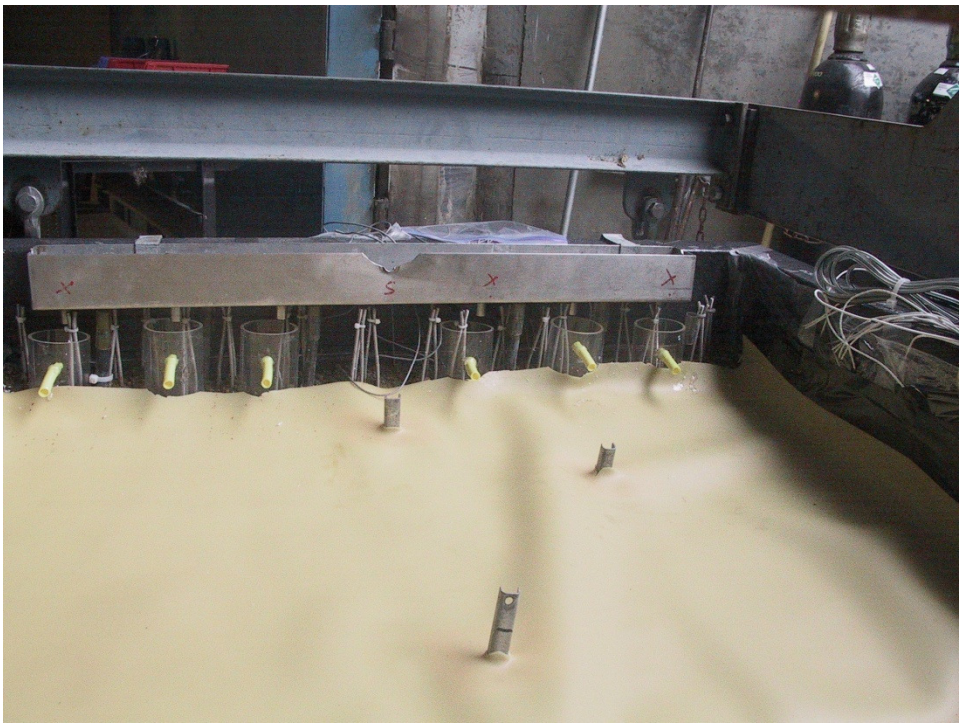

Figure 3.11 Modified saturation procedure for untreated soil (CTC01)

3.4. Soil Properties

3.4.1. Overview

Soil properties for the sand layers and crust are summarized in Table 3.5 and Table 3.6, respectively. The values of minimum and maximum relative density for determining unit weights of the Nevada sand were determined using the Japanese standard method number JIS A1244. The cyclic stress ratio required to cause an excess pore pressure ratio of 100% in 15 uniform loading cycles for the saturated loose sand layer is estimated to be between 0.09 and 0.13. The results were based on torsional hollow cylinder tests reported by Kano (2010, personal communication) and direct simple shear tests by Doygun (2010). Wet unit weight of the yolo loam crust before and after shaking was defined as the average unit weight of yolo loam samples

collected. The water content after shaking was determined by averaging wet and dry weights of samples collected.

Table 3.5 Sand Layer Properties

Parameter	Dense Sand	Loose Sand
Soil type	Monterey 0/30	Nevada sand
Specific gravity	2.64	2.644[(1)]
Mean grain size, D_{50} (mm)	.4[(2)]	0.17
Coefficient of uniformity, c_u	-	1.64
Maximum dry unit weight, γ_{max}	16.81[(2)]	17.5
Minimum dry unit weight, γ_{min}	13.96 (CTC01) 13.74 (CTC02) [(2)]	14.5
Relative density (%)	95 (CTC01) 98 (CTC02)	35 (CTC01) 45
Saturated unit weight (kN/m^3)	23.4 (CTC01) 19.9 (CTC02) [(3)]	19
Permeability (cm/s)	-	2 x 10^{-3}

[(1)] Chen (1995) and Cruz (1995)

[(2)] Kammerer (2004)

[(3)] Crude estimation based on container weight before and after placement of dense layer; assumes SG=2.65

Table 3.6 Crust Layer Properties

Parameter	Crust
Soil type	Yolo Loam
Specific gravity	--
Mean grain size, D_{50}	0.32mm
Coefficient of uniformity	10
water content before compaction[(1)]	15% (CTC01) 12% (CTC02)
water content after shaking [(2)]	15.9% (CTC01) 16% (CTC02)
PL	20
LL[(3)]	33
OCR	1
Estimated unit weight at placement[(4)]	21.8 kN/m^3 (CTC01) 21.5 kN/m^3
Estimated unit weight after end of test [(5)]	25.3 kN/m^3 (CTC01) 27.2 kN/m^3

[(1)] Average of 2 samples collected during placement

[(2)] Average of 4 samples from treated side, bottom and top. Range was 13.3-19.6%; Crust on untreated side completely submerged in water after testing; samples could not be collected

[(3)] Based on 7 measurements

[(4)] Estimation based on average of 2 samples collected during placement

[(5)] Calculated based on 4 samples collected after test: Gs: 2.65

3.4.2. Cone Penetration Test

For each model, two cone penetration tests were performed prior to shaking in order to acquire additional information about the soil properties and compare the different sides of the liquefiable soil. Cone penetration tests were all performed at 15g. During the CPT test, a hydraulic actuator was used to push the cone into the sand at a constant rate. In CTC01, the CPT had a shorter rod length of only 16 cm (6 in) model scale and only had one working load cell at the top. In CTC02, the CPT had a longer rod length of 32 cm (13 in) model scale and it had two load cells. One load cell was used to measure the force at the tip and a second load cell at the top of the shaft was used to measure the combined force of the tip resistance and sleeve friction.

Data from both tests are plotted in

Figure 3.12 as cone tip resistance, q_c. The cone tip resistance was determined as the penetration force divided by the tip cross-sectional area. The plotted value of q_c from CTC01 will be greater than the true value because it includes the shaft friction force. However, the error is estimated to be less than about 1% based on the ratio of shaft friction to tip force in CTC02. The data shows that the sand in CTC01 was initially very loose, with q_c being about 2.5 MPa (363 psi) in the untreated side and having increased to about 5.0 MPa (725 psi) on the 9% side. The increase in q_c due to treatment was a factor of about 2, but still represents a relatively low penetration resistance for sands. The CPT data from CTC02 shows that q_c increased from about 10 MPa (1450 psi) on the 4% treatment side to about 23 MPa (3336 psi) on the 5% side. The difference in q_c between these two sides was again a factor of about 2, which is attributed to the fact that the 4% gel only reached about gel state 7 whereas the 5% soil fully gelled. In addition, data is consistent with a denser sand placed in CTC02 as previously shown in Table 3.5.

.

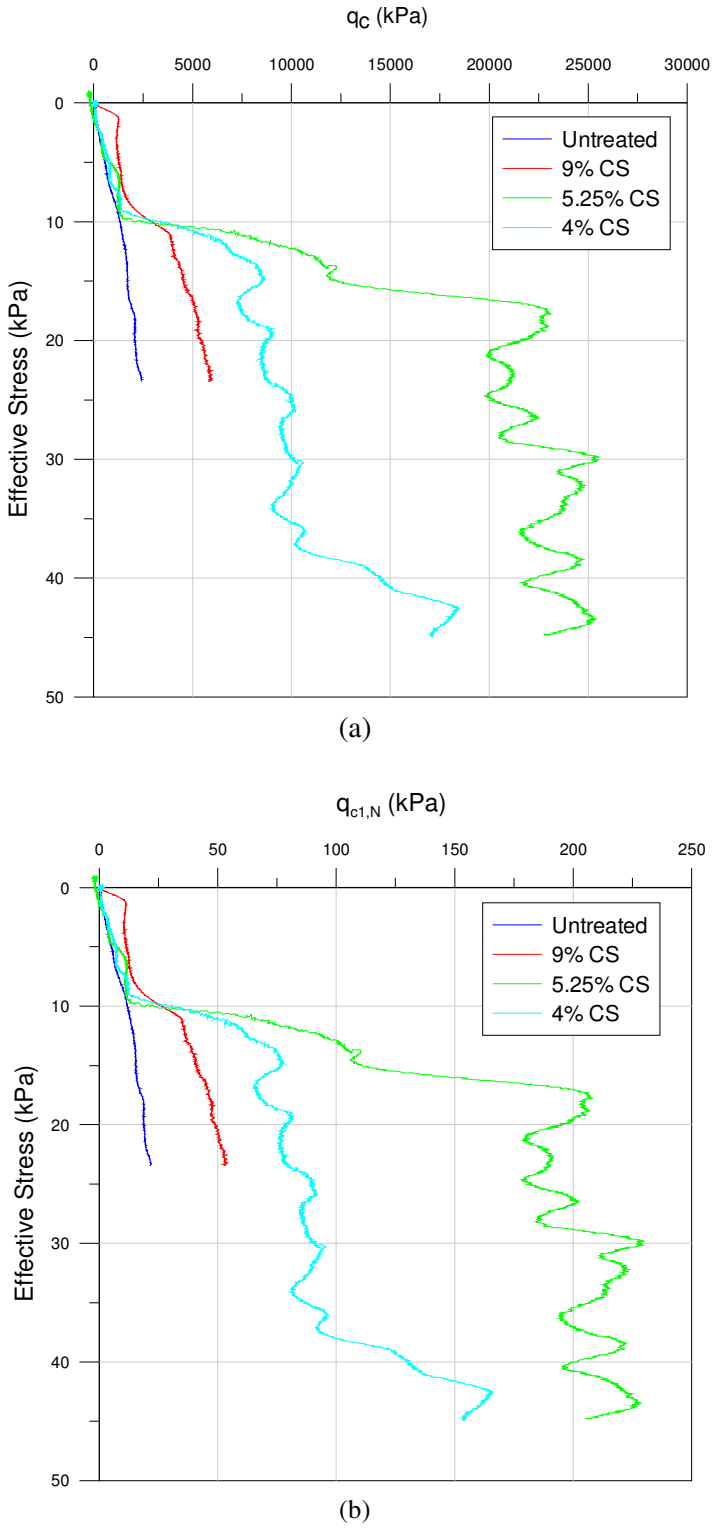

Figure 3.12 (a) Measured and (b) Normalized Cone Tip Stresses

CHAPTER 4: CENTRIFUGE TESTS - RESULTS AND DISCUSSION

4.1. Lateral Spreading and Settlement Response

Immediately after testing, the surface of the crust on the untreated side was completely submerged in water due to the large settlements that occurred when the underlying sand layer liquefied. The sloped crust was almost horizontal, and experienced significant lateral spreading and settlement. Sand boils were also observed on the surface of the crust on the untreated side. The crust layer on the treated side remained virtually intact and experienced minimal settlement. Significant cracking in the direction perpendicular to the direction of shaking was measured up to 1.5 cm (0.6 in) on the treated side. Figure 4.1 compares the model surface of the untreated and 9% CS soils before and after testing.

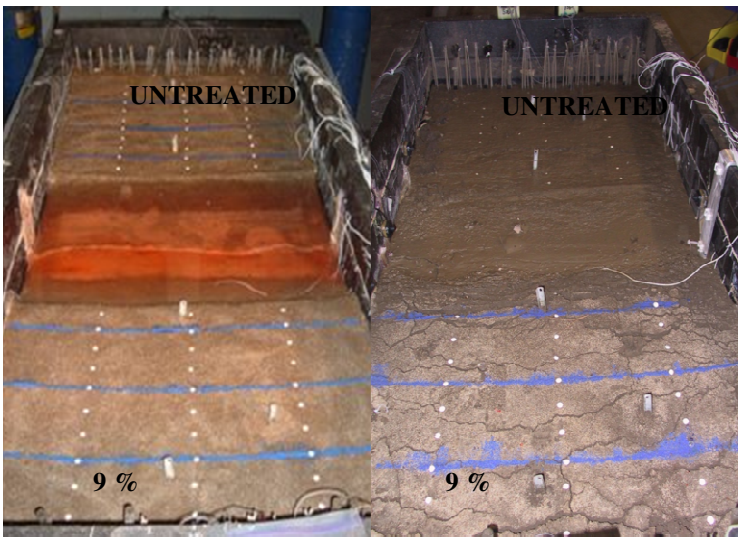

(a) (b)

Figure 4.1 Model Surface (a)Before and (b)After Testing

During model preparation, the crust surface was marked with two types of markers in order to measure and visually capture the dynamic behavior of lateral spreading during and after shaking. The first marker type used was colored sand lines (running east/west) across the surface. This marker type was used to evaluate (1) uniformity of lateral deformations throughout the treated and untreated sides, (2) boundary effects on the container, and (3) observe spatial variability. The second type of marker used was thumbtacks. The thumbtacks were pushed into the crust at fixed distances along the x-axis in order to observe the extent of lateral spreading at various distances from the slope. The locations of the surface lines and thumbtacks were measured before and after testing and are shown in Figure 4.2a and Figure 4.2b for CTC01 and CTC02, respectively.

The surface lines and the thumbtacks moved laterally in a uniform manner suggesting that the crust surface moved as a continuous block with minimal boundary effects. Based on measurements of the surface lines, up to 1 m (3.3 ft) of horizontal movement occurred on the crust surface on the untreated side while the 9% CS soil experienced about 0.7 m (2.3 ft). The 5.25% CS and 4% CS in CTC02 experienced less horizontal movement up to 0.23 m (.75 ft) and 0.38 m (1.3 ft), respectively. This is most likely attributed to the fact that for CTC02, both sides of the liquefiable sand layers were treated with CS and therefore, there was minimal movement throughout the entire model. In CTC01, the untreated side moved significantly which may have subsequently triggered movement on the treated side as well.

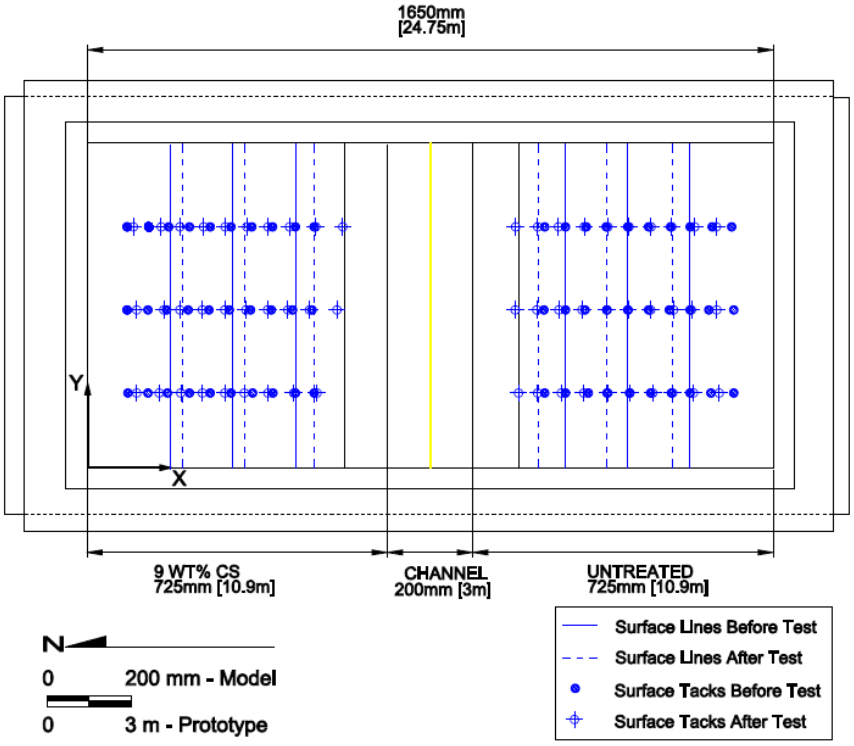

(a)

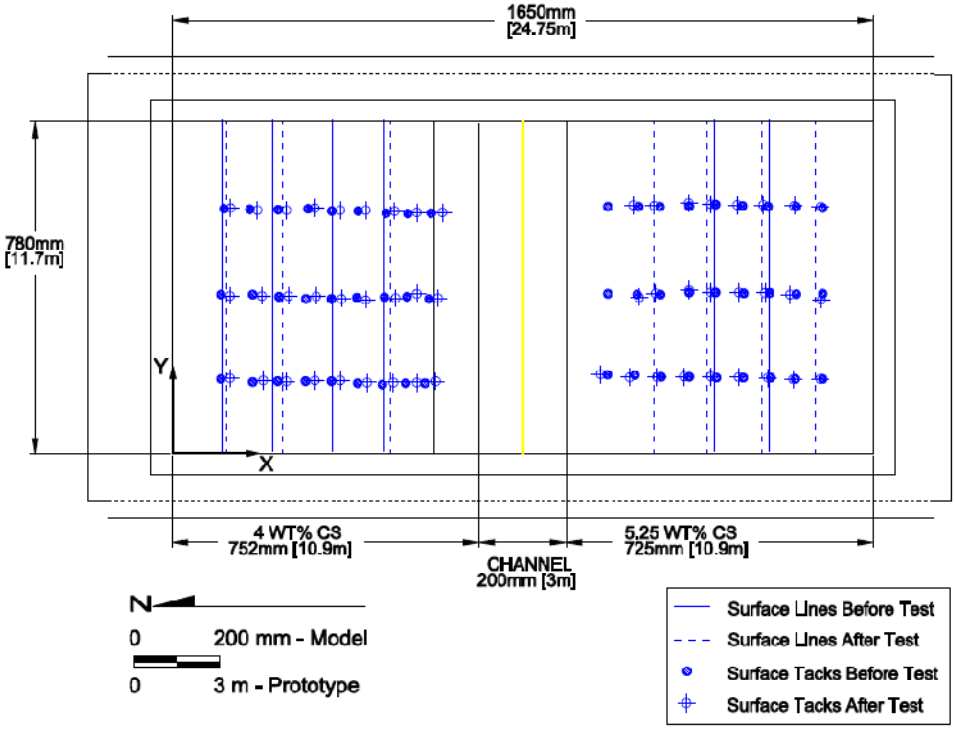

(b)

Figure 4.2 Surface Markers Before and After Test for (a)CTC01 and (b)CTC02

As previously mentioned, open steel tubes were used to place vertical colored sand columns in the model during its construction in order to observe the amount of lateral spreading and displacement along the profile of the liquefiable soil layer. Figure 4.3a and Figure 4.3b show the vertical sand columns measured before and after testing from CTC01 and CTC02, respectively. Lateral spreading within the liquefiable zone was measured as the difference of position before testing and after testing. As can be seen from Figure 4.3, maximum movements within the liquefiable layer took place near the interface of the liquefiable layer and the crust. As can be seen from the deformation pattern, lateral movement was minimal in the treated liquefiable sand. Maximum lateral spreading in the liquefiable layer occurred closest to the open channel and was determined to be 1.35 m (4.4 ft), .03 m (.1 ft), .08 m (.26 ft), and .21 m (.7 ft) in the untreated, 9%, 5.25%, and 4% CS soils, respectively. The measured locations of maximum lateral spreading are marked with an "X" in Figure 4.3. In CTC01, lateral spreading displacements in the liquefiable sand layer decreased with distance from the channel; at a distance of 3 m (9.8 ft) from the channel, the lateral displacements had been reduced to 0.89 m (2.9 ft) and 0.02 m (.06 ft) for the untreated and 9%CS soil, respectively. The lateral displacements in CTC02 (with the exception of the channel locations) were negligible for both 5.25% and 4% CS soils.

Additionally, Figure 4.4 shows the sand column located closest to the crust toe for the 5.25% and 9% CS soils and the untreated side. The sand columns in this figure remain relatively straight in the treated liquefiable sand zones while deformations occur primarily on the crust as it laterally moves towards the central water channel.

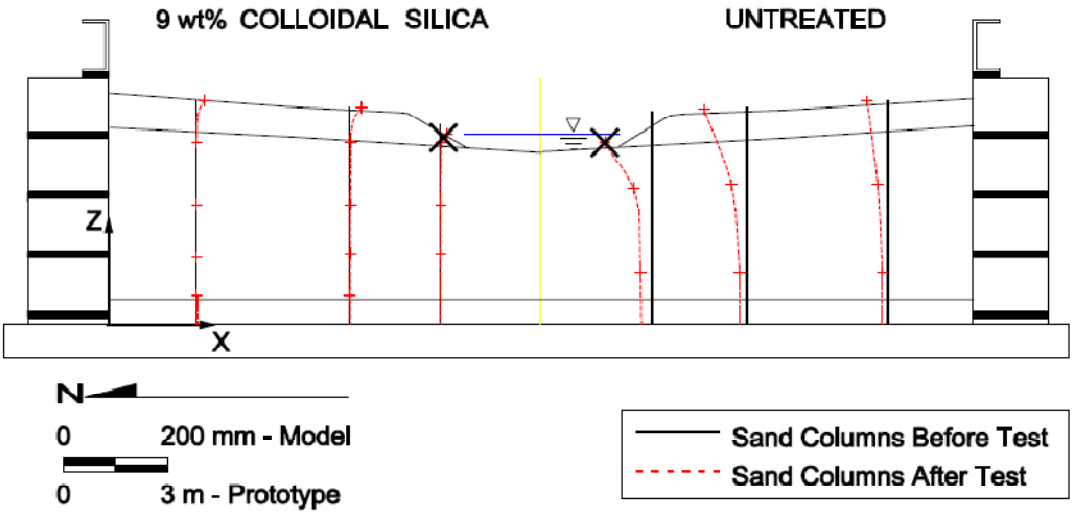

(a)

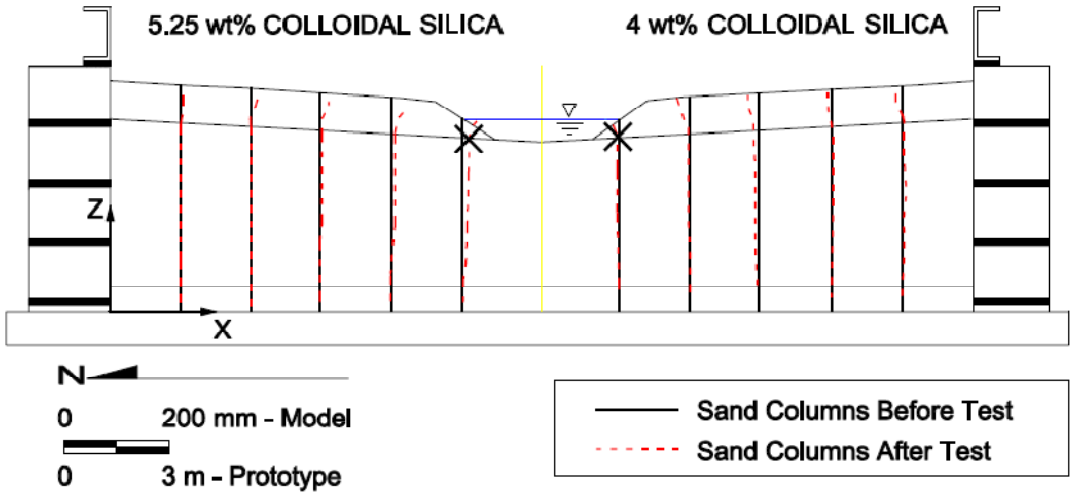

(b)

Figure 4.3 Sand Columns before and after test for (a) CTC01 and (b) CTC02

(a) **(b)** **(c)**

Figure 4.4 Sand columns closest to crust toe after test (a) 5.25% (b) 9% (c) Untreated

In addition to lateral spreading, settlements were measured by recording elevations for each of the 3 soil layers before and after testing. Figure 4.5 illustrates the measured elevations for each of the soil layers before and after testing for CTC01 and CTC02. In the treated sand zone, settlements were minimal on the surface of the liquefiable sand layer compared to that of the untreated surface of the liquefiable layer. Surface settlements for the untreated side ranged from 0.35 m (1.1 ft) to 0.5 m (1.6 ft), with the smallest settlements occurring closest to the container wall. Surface settlements for the 9%, 5.25%, and 4% were found to average about 0.06 m (0.2 ft), 0.17 m (0.6 ft), and 0.15 m (0.5 ft), respectively. Settlements were determined by measuring elevations at several fixed locations of each soil layer before and after testing

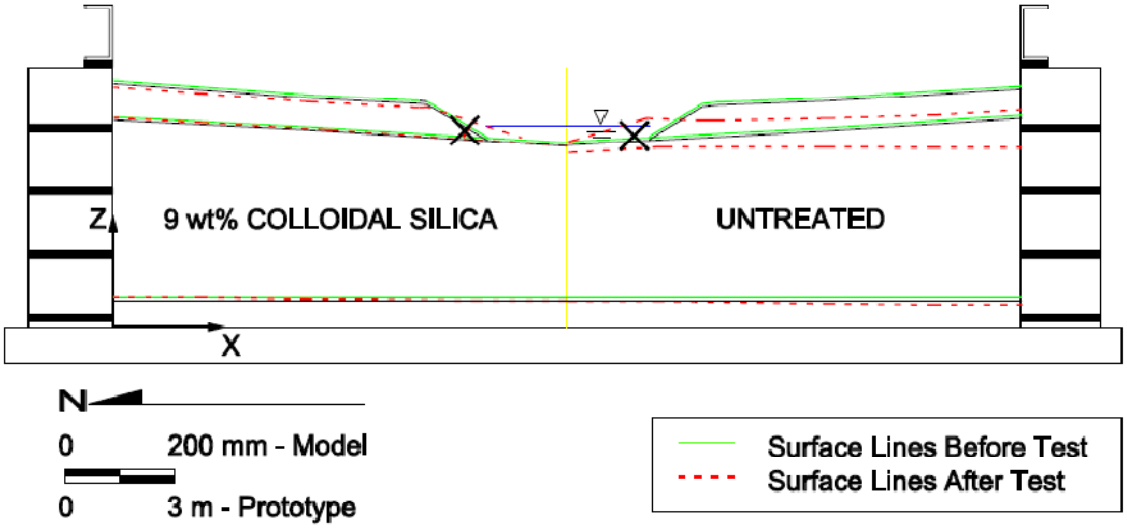

(a)

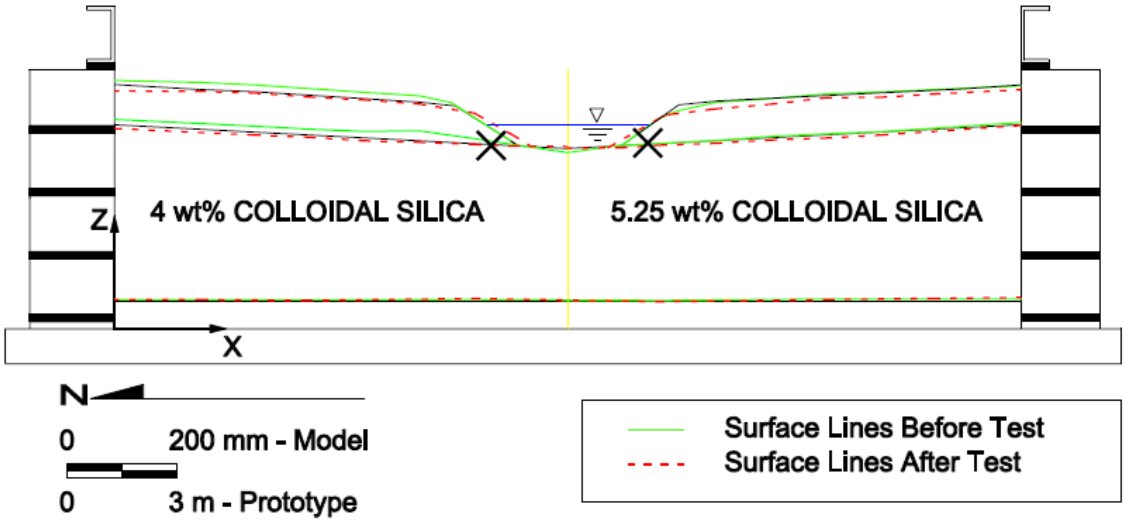

(b)

Figure 4.5 Surface elevations before and after test (a) CTC01 and (b) CTC02

Sensors were also placed on the crust surface to measure lateral spreading and settlement during each shaking event. Linear potentiometers (LPs) and linear variable differential transformers (LVDTs) were placed on the crust surface and mounted to an instrument rack on top of the model container. Teflon plates were placed under the vertical displacement transducers and horizontal transducers were attached to an LP flag and tied with a rubber band to minimize sliding and/or detachment during shaking. Sensor placement for LP/LVDT is illustrated in Figure 4.6.

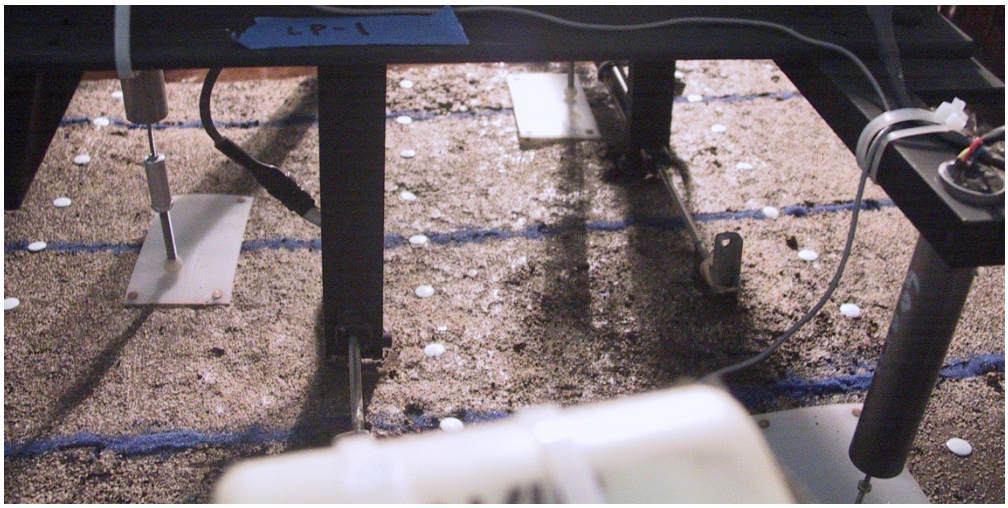

Figure 4.6 Sensor placement of LP/LVDT on crust surface

Figure 4.7 and Figure 4.8 compare settlement and lateral spreading response, respectively, for the treated and untreated zones measured by the LPs and LVDTs on the surface of the model at three locations: (1) near channel (2) mid-way on crust surface, and (3) near the boundary of the container. Refer to Figure 3.5 for locations of the LPs and LVDTs. The cumulative displacements on the surface of the crust at the end of testing are plotted against the peak base acceleration (PBA) for shaking events 1 thru 5. Each shaking event represents 120

seconds. It should be noted that for the stronger shaking events, several of the LPs and LVDTs detached from the Teflon plates and were not capable of measurements. The larger shaking events are therefore excluded from the analysis.

The treated zones show a significant reduction in model surface settlement (negative values indicate surface settlement). For example, at the end of shake 5, the total amount of settlement on the model surface on the 9% CS soil was reduced from nearly 1m (3.3 ft) to 0.08 m (0.26 ft) near the boundary of the container. Similarly, Figure 4.8 shows that the 9% CS soil reduced lateral spreading on the model surface from 0.9 m (3 ft) to 0.15 m (0.5 ft) near the channel. Positive values for lateral spreading indicate movement towards the central water channel. It should be noted that the surface settlement and lateral spreading for the 9% was greater than the 5.25% and 4% CS soils. Although movement within the liquefiable layer was less for the 9% versus the 5.25% and 4%, movement of the overlying crust layer was greater on the 9% CS soil. This is primarily due to the fact that in the first test, an untreated side existed and caused significant movement of the crust layer. Movement of the crust on the untreated side subsequently caused movement of the crust on the 9% side of the model.

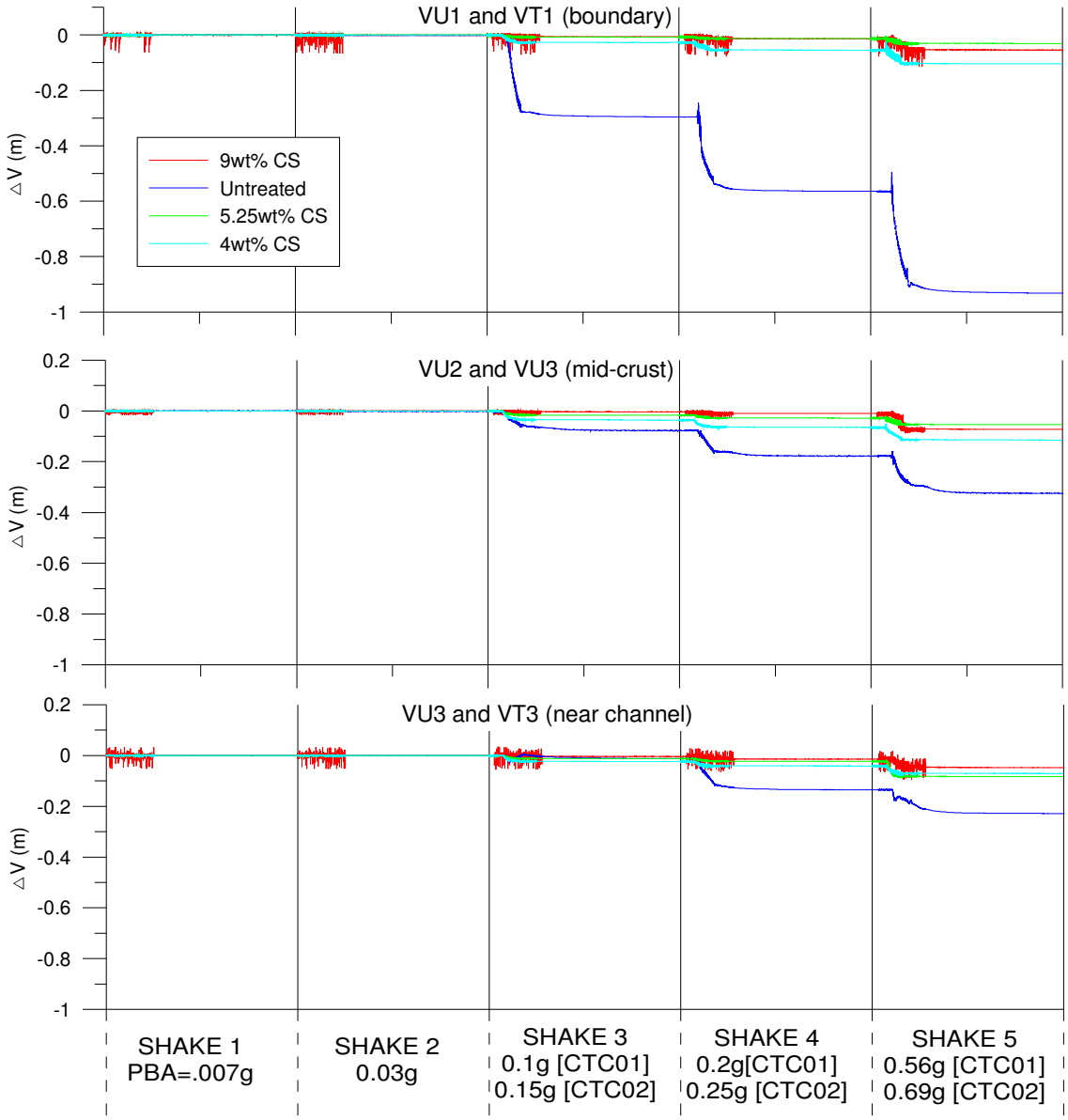

Figure 4.7 Cumulative surface settlement

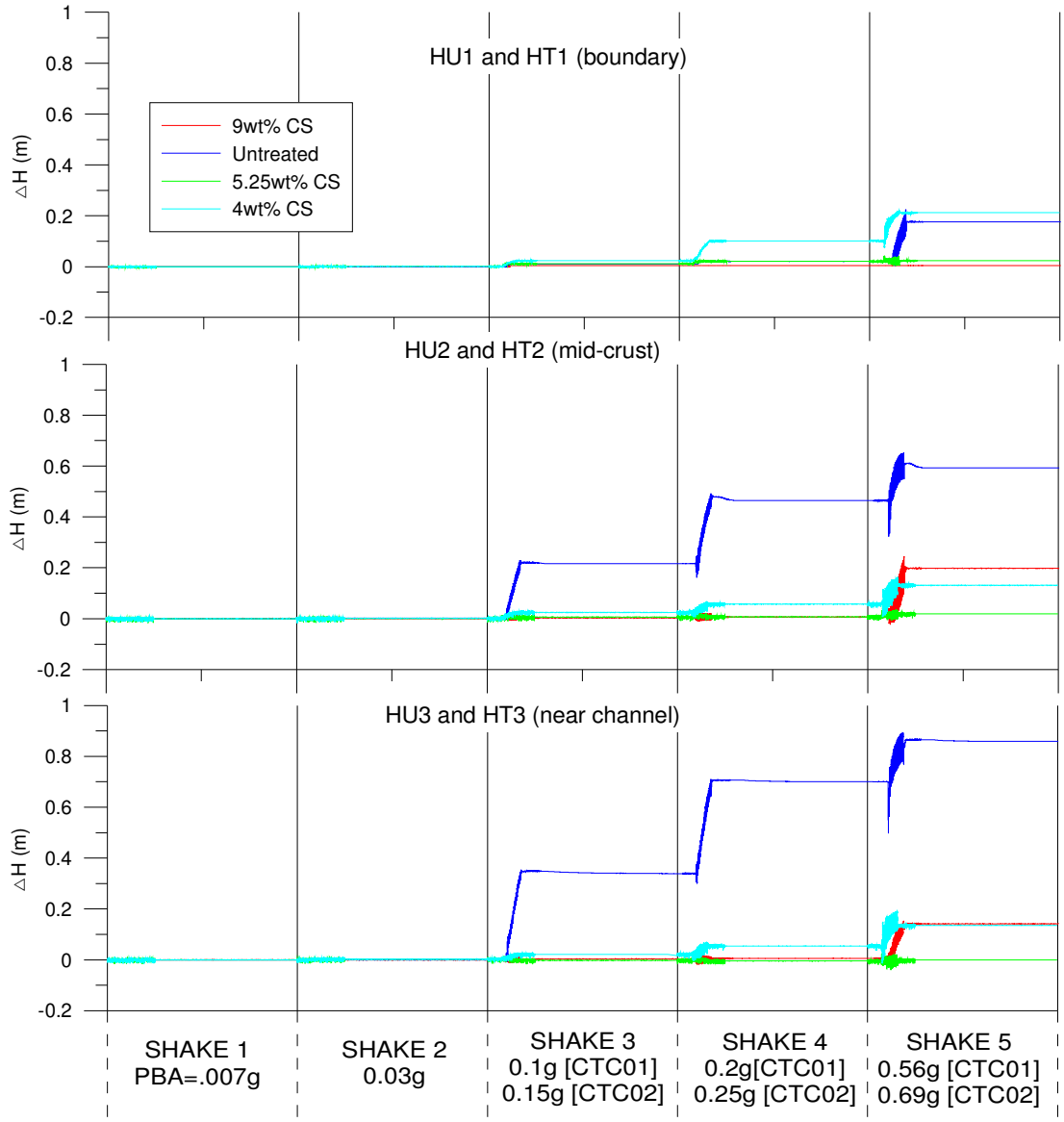

Figure 4.8 Cumulative lateral spreading vs. peak base acceleration

4.2. Pore Pressure Response

Although liquefaction is conventionally defined as the time when excess pore pressure ratio of 1.0 occurs, the significance of excess pore pressure ratios for colloidal silica soils do not represent the same physical meaning. The pore space, in this case, is a gel and even if r_U=1.0 occurs, the soil technically does not "liquefy." However, it is still reasonable to study pore

pressure response to capture the mechanical behavior between the two materials (i.e. sand and gel) at a macro-scale level. For these gelled soils, the change in pressure measured by a pore pressure transducer is believed to correspond to the change in normal stress that develops on the gel within the sand pores. In this way, pore pressure response of colloidal silica soils can offer insight as to the way in which stresses are being transferred between the soil and the gel matrix.

Pore pressure transducers were placed in a vertical array within the treated and untreated liquefiable layers (Figure 3.5). The pore pressure ratio, r_u, was computed for both the untreated and treated sides as the ratio of excess pore pressure (whether on pore water or pore gel) to the initial vertical effective stress. Liquefaction of the sand corresponds to the occurrence of zero effective stress in the sand, which will approximately correspond to r_u being equal to 1.0.

Figure 4.9 through Figure 4.12 plot the excess pore pressure ratios that occurred at various depth for shakes 2 through 5. Figure 4.9 shows the excess pore pressure response that occurred for Shake 2 along the soil profile. During this event, there is very little development of excess pore pressures for all soil types. This is expected for a low shaking amplitude of 0.03g. The pore pressure response for higher shaking amplitude of 0.1g (CTC01) and 0.15g (CTC02) is shown in Figure 4.10. As can be seen from Figure 4.10, liquefaction is initiated in the untreated soil. The excess pore pressure ratios for the 9% CS soil range from approximately 0.25 to 0.75. The excess pore pressure ratios for the 5.25% CS soil range from approximately 0.6 to 0.8. Similar to the untreated soil, the grouted soils develop the majority of pore pressures within the first several cycles of loading. However, the values of these pore pressures are reduced for the grouted soils. The 4% CS soil exhibits varying behavior. For example, the 4% CS soil shows that a pore pressure ratio of 1.0 was achieved at a depth of 3.3 m (10.8 ft) and reaches 0.9 m (3 ft) for a depth of 2.4 m (7.9 ft). On the other hand, pore pressure ratios at depths above and below this zone are reduced and exhibit similar behavior as that of the 5.25% soil.

Figure 4.11 shows the response for shaking amplitudes for shake 4 that were slightly greater than shake 3. In shake 4, amplitudes of 0.2g and 0.25g were applied to CTC01 and

CTC02, respectively. Again, liquefaction is observed in the untreated soil. The grouted soils exhibit a tendency to develop significant negative pore pressures during the stronger event. These negative pore pressures are indicative of dilatancy effects. Based on the pore pressure response in Figure 4.11, the 9% and 5.25% CS soils exhibit the ability to dilate while resisting liquefaction (i.e. r_U does not reach 1.0). The 4wt % CS soil shows similar dilatancy trends; however, pore pressure ratios of 1.0 are achieved for the lower concentration.

Figure 4.12 shows the response for a larger shaking amplitude of 0.56g and 0.69g for CTC01 and CTC02, respectively. During this event, excess pore pressure ratios of 1.0 are clearly achieved in the untreated soil, 5.25% CS soil, and 4% CS soil types. For the 9%, a pore pressure ratio of 1.0 is observed at a depth of 1.7 m (5.6 ft) but remains at or below 0.8 at all other locations. For the grouted soils, negative pore pressures are further enhanced and the majority of increases in pore pressure occur in the early stages of the loading sequence. It is interesting to note the distinct difference in transient pore pressure response between the untreated and grouted soil types. For this shaking event, there are dramatic changes in transient pore pressure response for the grouted soils compared to the ungrouted soils. For each loading cycle, these dramatic increases and subsequent decreases in pore pressure response suggest a greater ability to oscillate between dilatent and contractive behavior compared to untreated soils. The behavior may suggest a unique characteristic response for a gelled filled pore space versus a liquid.

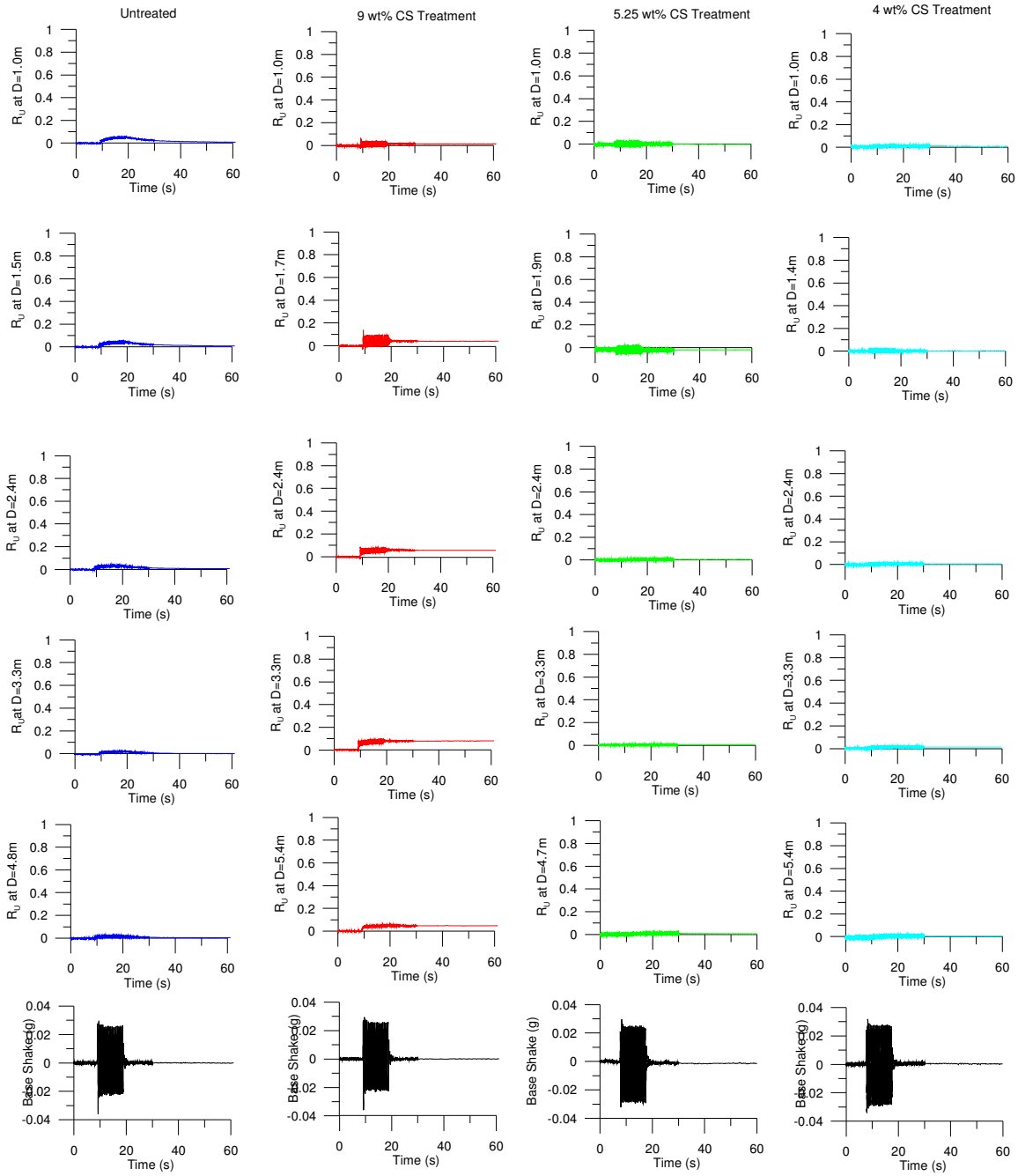

Figure 4.9 Ru Response at Various Depths from PBA = 0.03g (Shake 2)

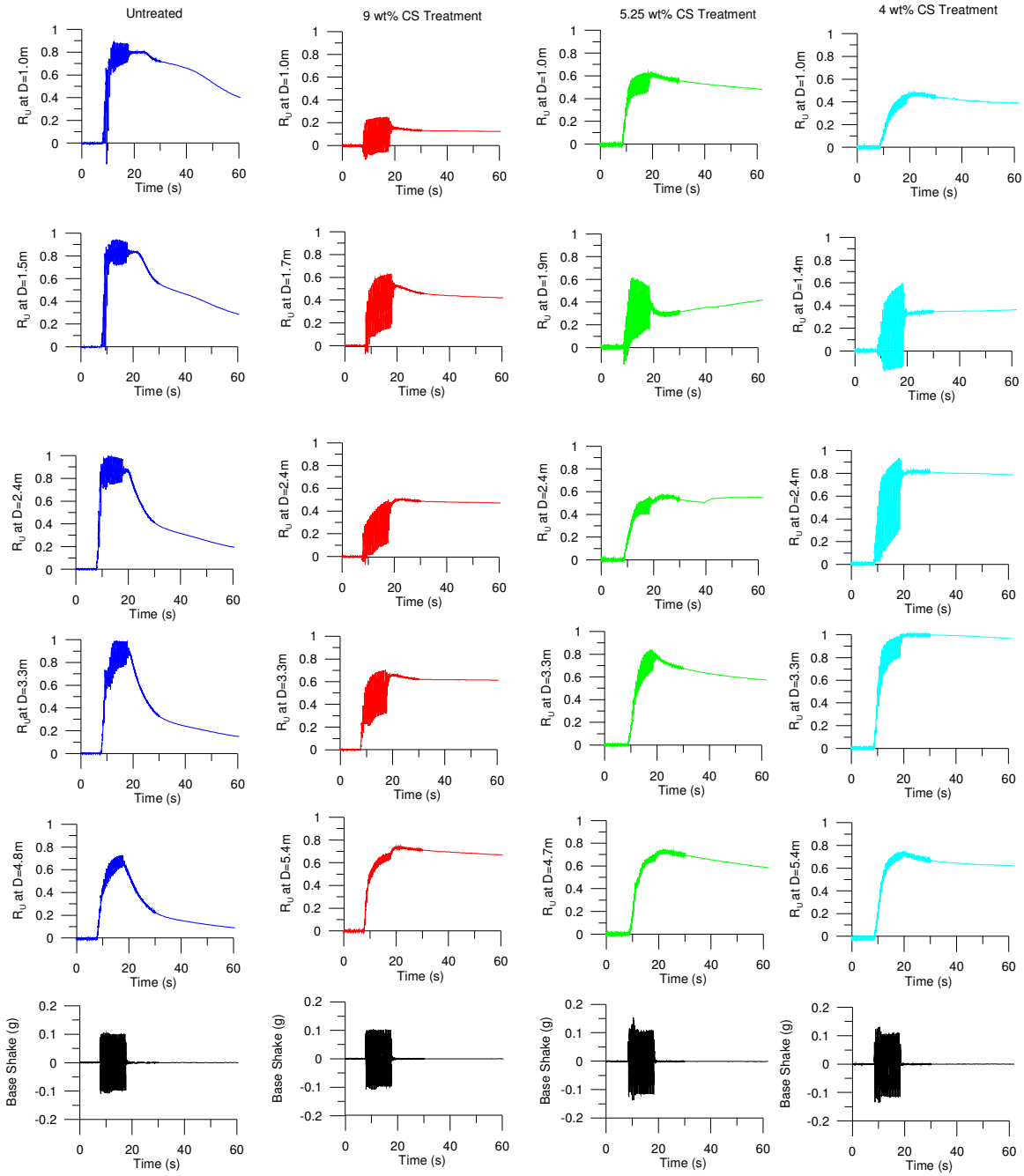

Figure 4.10 Ru Response at Various Depths from PBA = 0.1g for CTC01 and 0.15g for CTC02 (Shake 3)

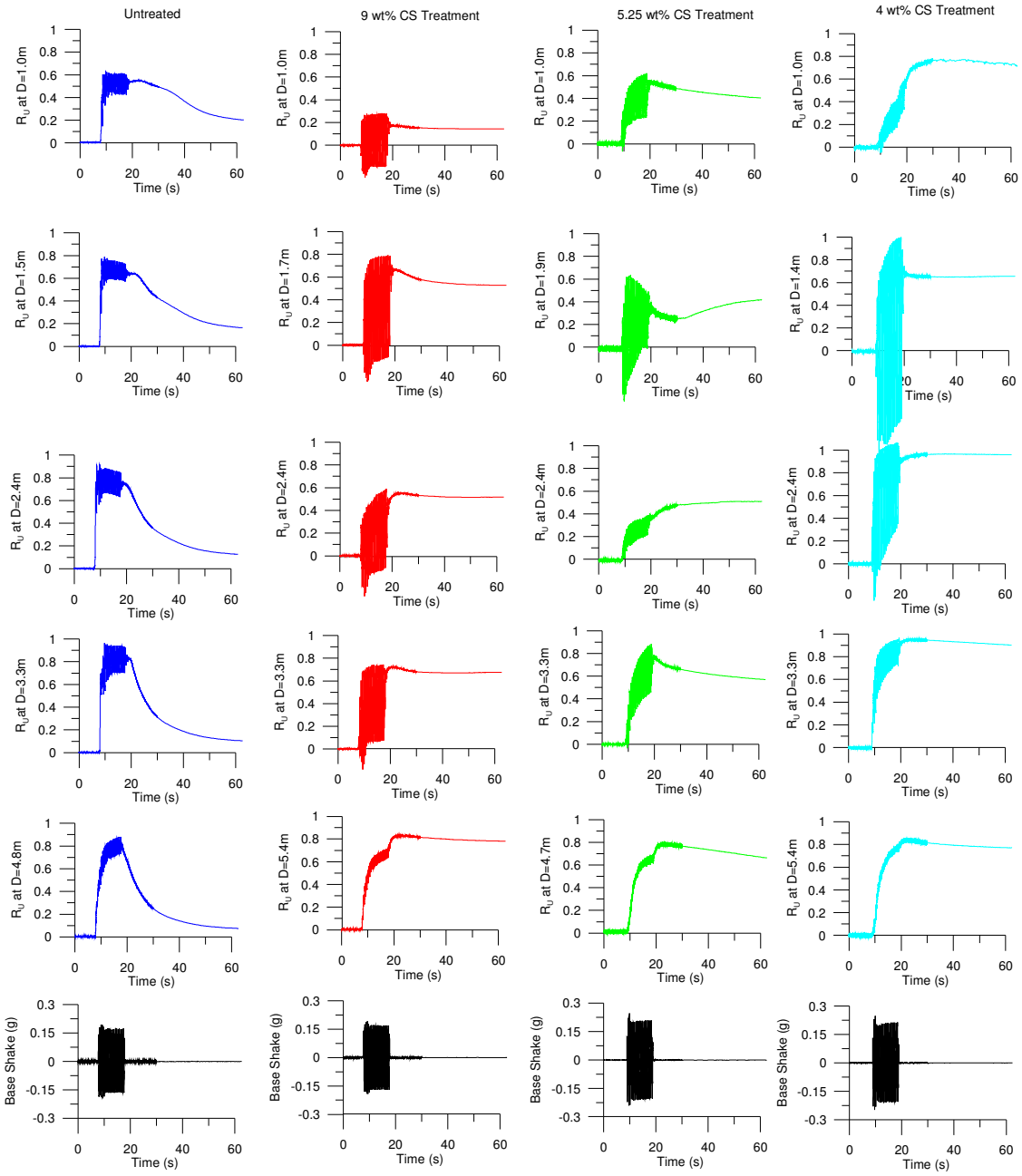

Figure 4.11 Ru Response at Various Depths from PBA = 0.2g for CTC01 and 0.25g for CTC02 (Shake 4)

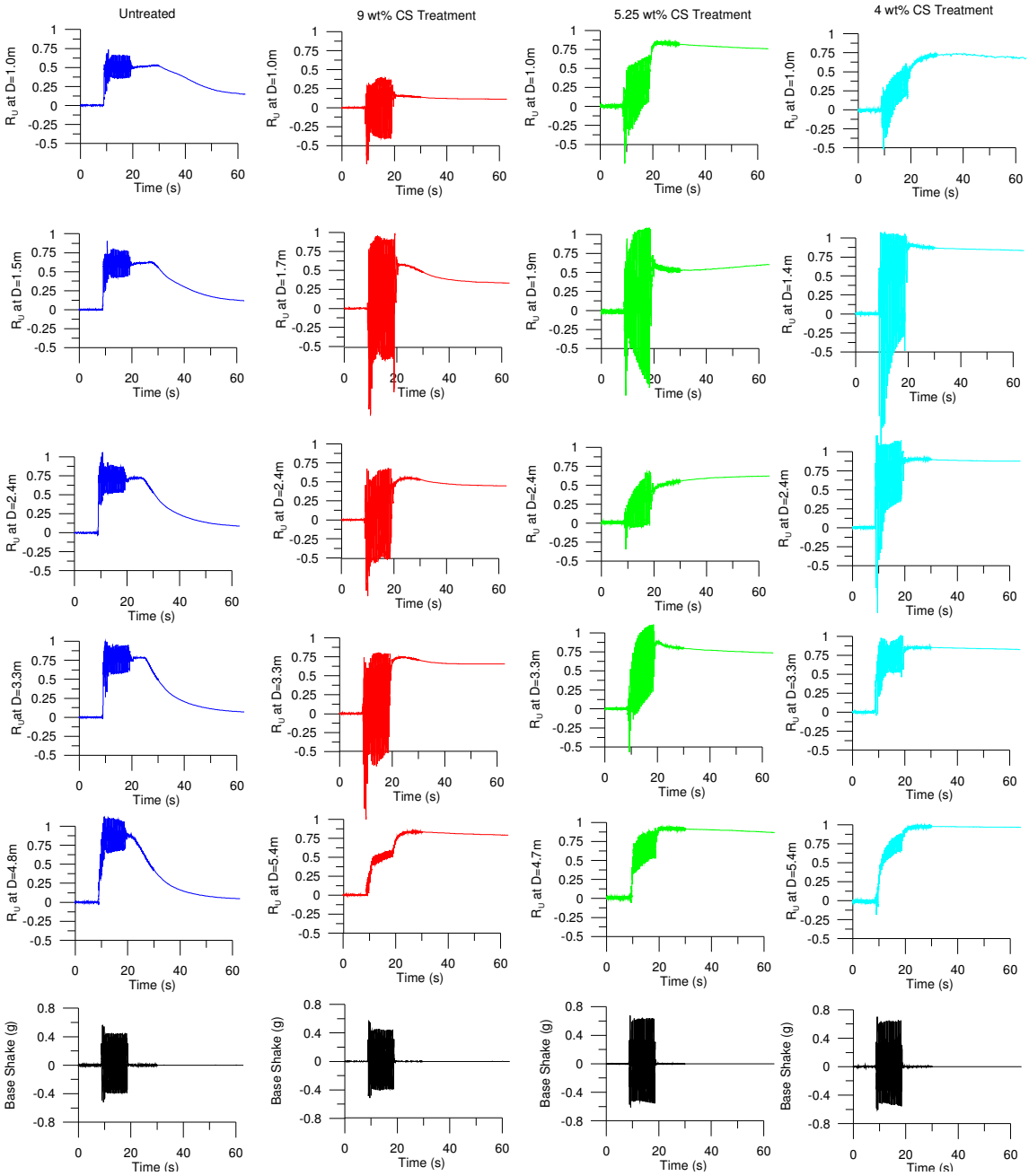

Figure 4.12 Ru Response at Various Depths from PBA = 0.56g for CTC01 and 0.69g for CTC02 (Shake 5)

The general behavior of pore pressure response observed from the model tests are in agreement with studies performed by Diaz-Rodriguez and Antonio-Izarraras (2004). In this study, cyclic simple shear tests were performed on colloidal silica treated specimens and included monitoring of pore pressures. Results for increasing number of loading cycles show that even

though pore pressure ratios of 1.0 could be achieved for grouted soils, the pore pressures developed more slowly compared to that of the untreated specimens and the reductions in pore pressures were directly related to CS concentrations. In the case of the centrifuge model tests, excess pore pressure ratios of 1.0 were developed for the grouted soils, but required significantly stronger shaking amplitudes compared to the untreated soil. This concept is more clearly explained when pore pressure ratio is plotted against peak base acceleration shown in Figure 4.13. Figure 4.13 shows the pore pressure ratio that occurred at about the midpoint of the liquefiable soil layer (D=3.3m [10.8 ft]). As can be seen, pore pressure ratios of 1.0 were achieved in each case, but increasing grout concentration resulted in increasing amplitudes required to achieve r_u=1.0.

The mechanisms for generating pressure on the colloidal silica gel in the sand pores is not yet well understood, but it is believed that the pressure recordings indicate that the effective normal stresses carried by the sand matrix are being transferred to the pore gel as a result of the dynamic loading. The reduction of effective stress in treated sand would have less effect than the same reduction in effective stress on untreated sand because the pore gel does have some shear resistance of its own. CS gels alone has been reported to have an average maximum shear modulus of 15 kPa (2.2 psi) (Forero-Duenas, 1998).

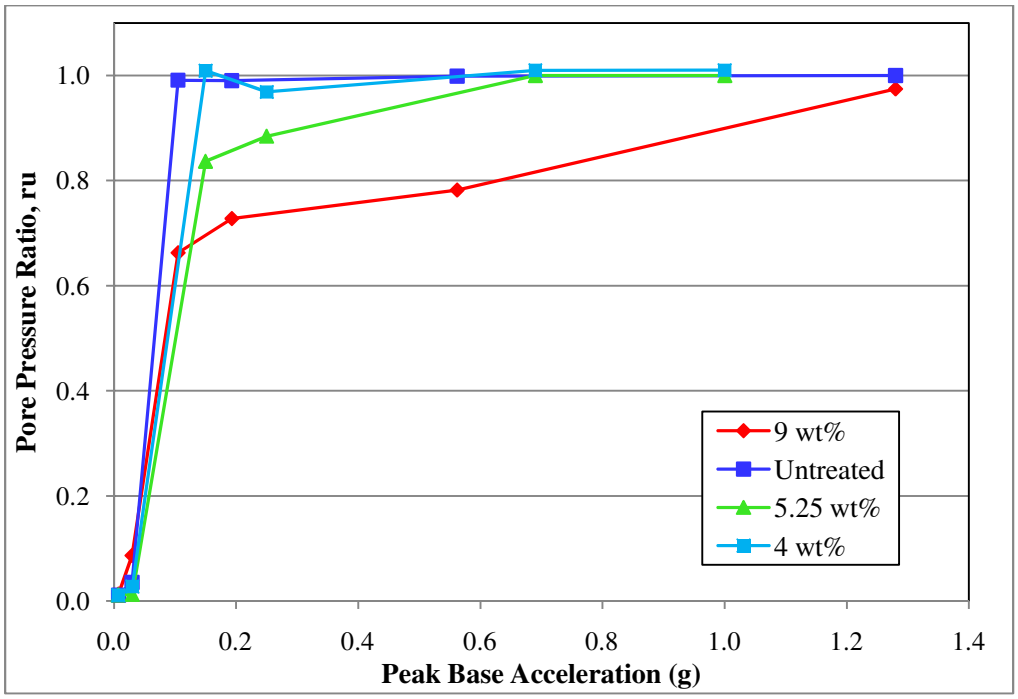

Figure 4.13 Excess pore pressure ratio vs. peak base acceleration at D=3.3m

Limited studies have been conducted to characterize pore pressure response in chemically grouted soils, including colloidal silica. To date, the effects of pore pressure dissipation following dynamic loading is one aspect that remains unexplored. Each event in the centrifuge tests consisted of a 10 second shaking event. Data recordings continued after shaking for an average of 100 seconds in order to observe dissipation of pore pressures. If the pore pressure dissipation effects were restricted to each recorded event, it would appear as if dissipation does not occur in the grouted soils. This concept is illustrated in Figure 4.14 that shows pore pressure response for each soil long after shaking has ended. From Figure 4.14 it is suggested that pore pressure dissipation is significantly less for the grouted soils.

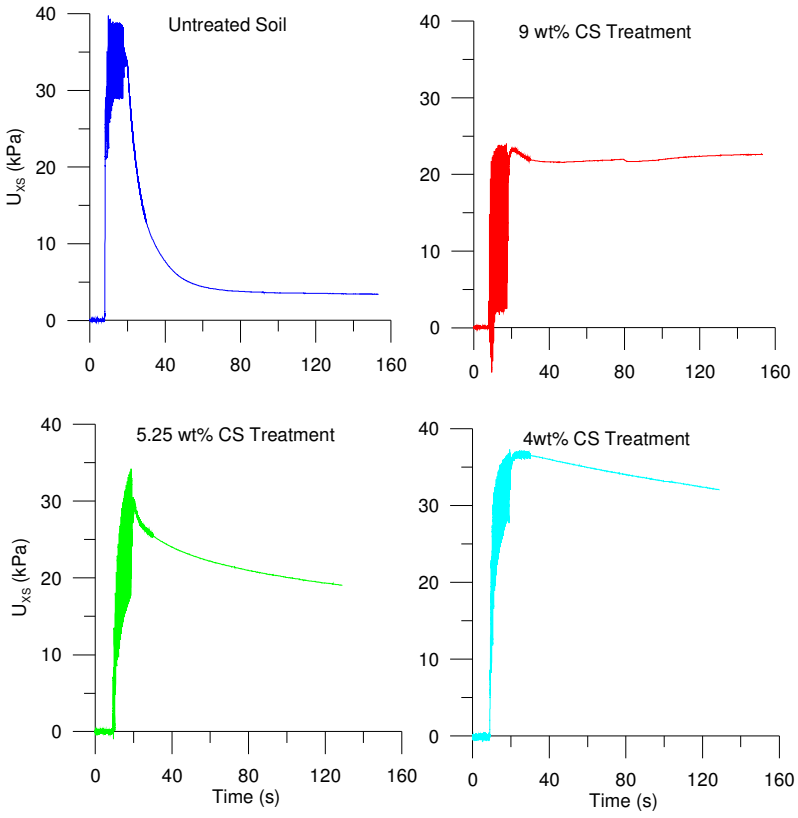

Figure 4.14 Pore Pressure Recordings for Shake 3

Interestingly, the static pore pressures measured at the beginning of subsequent shakes indicate that the majority of excess pore pressures were dissipated, but the dissipation effects occurred over a much longer period of time compared to the untreated soils. Figure 4.15 and Figure 4.16 plots the pore pressure response as a continuation of each shaking event for CTC01 and CTC02, respectively. It should be noted that a rest time of approximately 15 minutes would pass between shaking events as the recorded data was being checked and saved. Due to scaling laws, this would equate to almost 4 hours. For shakes 1 through 3, nearly all the pore pressures generated from the previous shaking event had dissipated. As can be seen from Figure 4.15 and Figure 4.16 , there is slightly less dissipation for shakes 4 and 5. It is worth noting that Figure 4.16 shows less dissipation for the 5.25% CS versus the 4% CS.

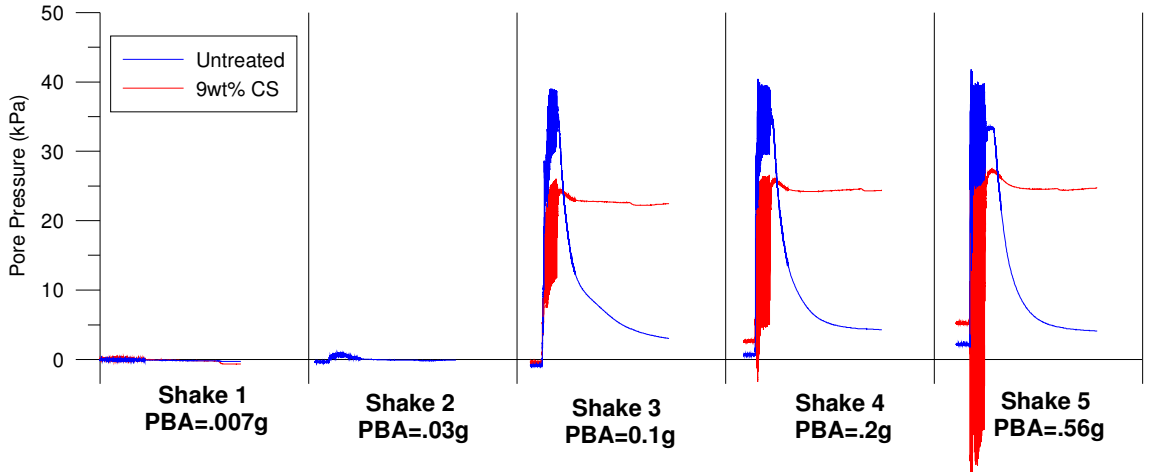

Figure 4.15 Behavior of Pore Pressure Dissipation for CTC01

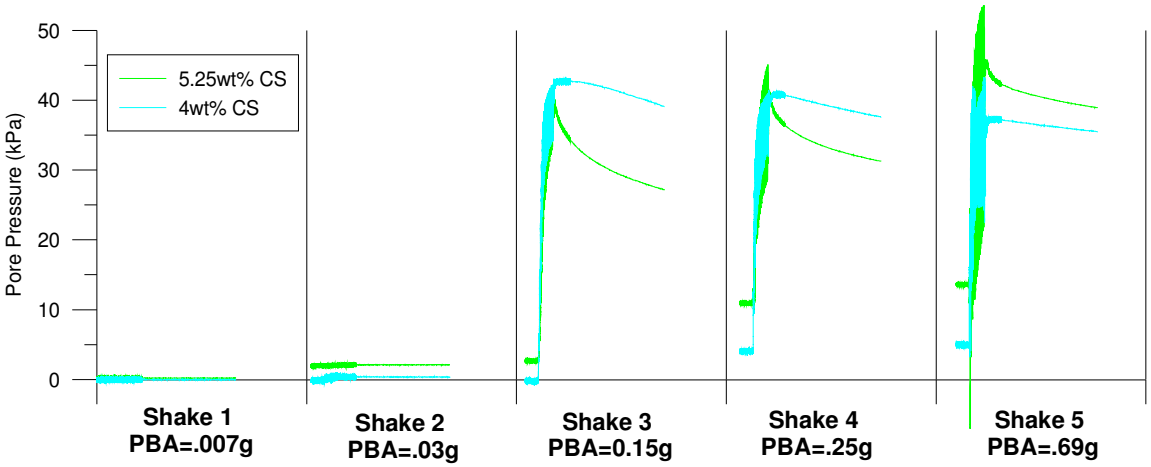

Figure 4.16 Behavior of Pore Pressure Dissipation for CTC02

4.3. Acceleration Response

A total of 10 accelerometers were placed in a vertical array within the liquefiable soil layer. Figure 4.17 through Figure 4.20 shows acceleration time histories for shakes 2 through 4 at various locations in the soil profile. For a small shaking acceleration of .03g (shake 2), Figure 4.17 shows a uniform response throughout the profile for each soil type. When liquefaction is

initiated in the untreated soil during shake 3, Figure 4.18 illustrates the effects of amplification moving up along the profile. The response for the grouted soils, on the other hand, remains relatively uniform. When the applied shaking is increased to 0.2g (CTC01) and 0.25g (CTC02) in shake 3, the untreated soils show dramatic amplification in the first several cycles of shaking followed by a dramatic deamplification (Figure 4.19). Again, the response for each of the grouted soils remains relatively uniform along the profile.

The amplification/deamplification of the acceleration response observed in the untreated soil is directly related to changes in the ratio between input frequency (which was a constant 2 Hz) and the soil profile's natural frequency (which progressively decreases as pore pressures increases). Trends in the acceleration response indicate that the stiffness in the untreated soil has been compromised whereas stiffness in the treated soils is relatively constant.

For the strongest shaking event of 0.56g (CTC01) and 0.69g (CTC02), Figure 4.20 shows a similar, yet more pronounced response in the untreated soil. Dramatic amplification occurs in the first several cycles followed by deamplification. The 9% CS remains relatively uniform. For the 9% CS, the magnitude of the accelerations slightly increase from the base toward the ground surface (i.e., site amplification), with all time histories having relatively uniform amplitudes throughout shaking. It should be noted that during this event, r_U of 1.0 were clearly observed in the 5.25% and 4% CS soils. The acceleration response for both of these soil types reveals strong high-frequency spikes in acceleration at the ground surface. These high-frequency acceleration spikes may be the result of dilation of the sand matrix with associated transient drops in pore gel pressures during cyclic loading. The dynamic response is similar to the cyclic mobility observed in saturated untreated dense sands (e.g., Kutter and Wilson 1999). The fact that these high-frequency acceleration spikes did not develop in the 9% CS soil suggests that higher concentrations provide greater resistance to transient changes in applied stress.

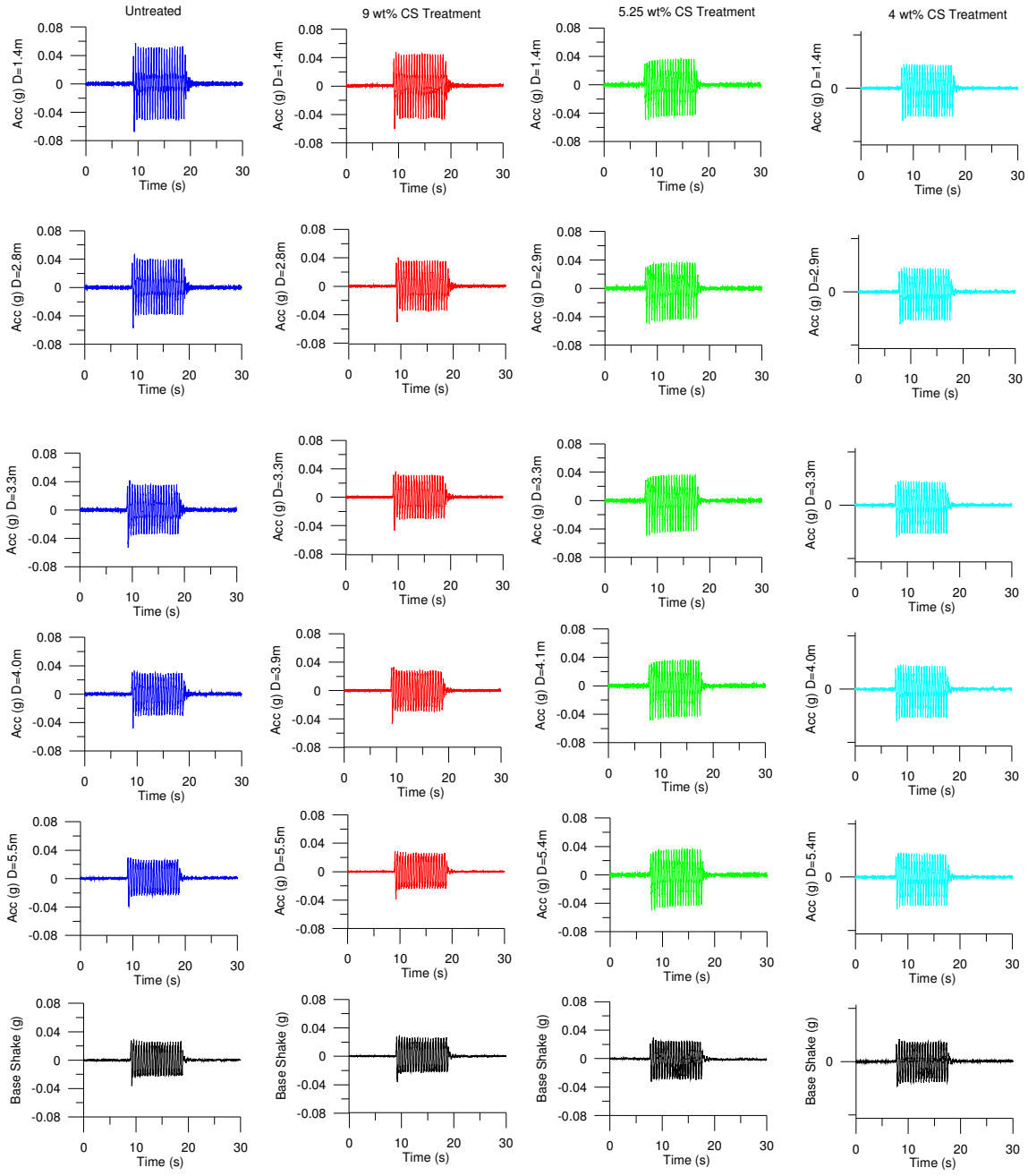

Figure 4.17 Acceleration Response for PBA = 0.03g (Shake 2)

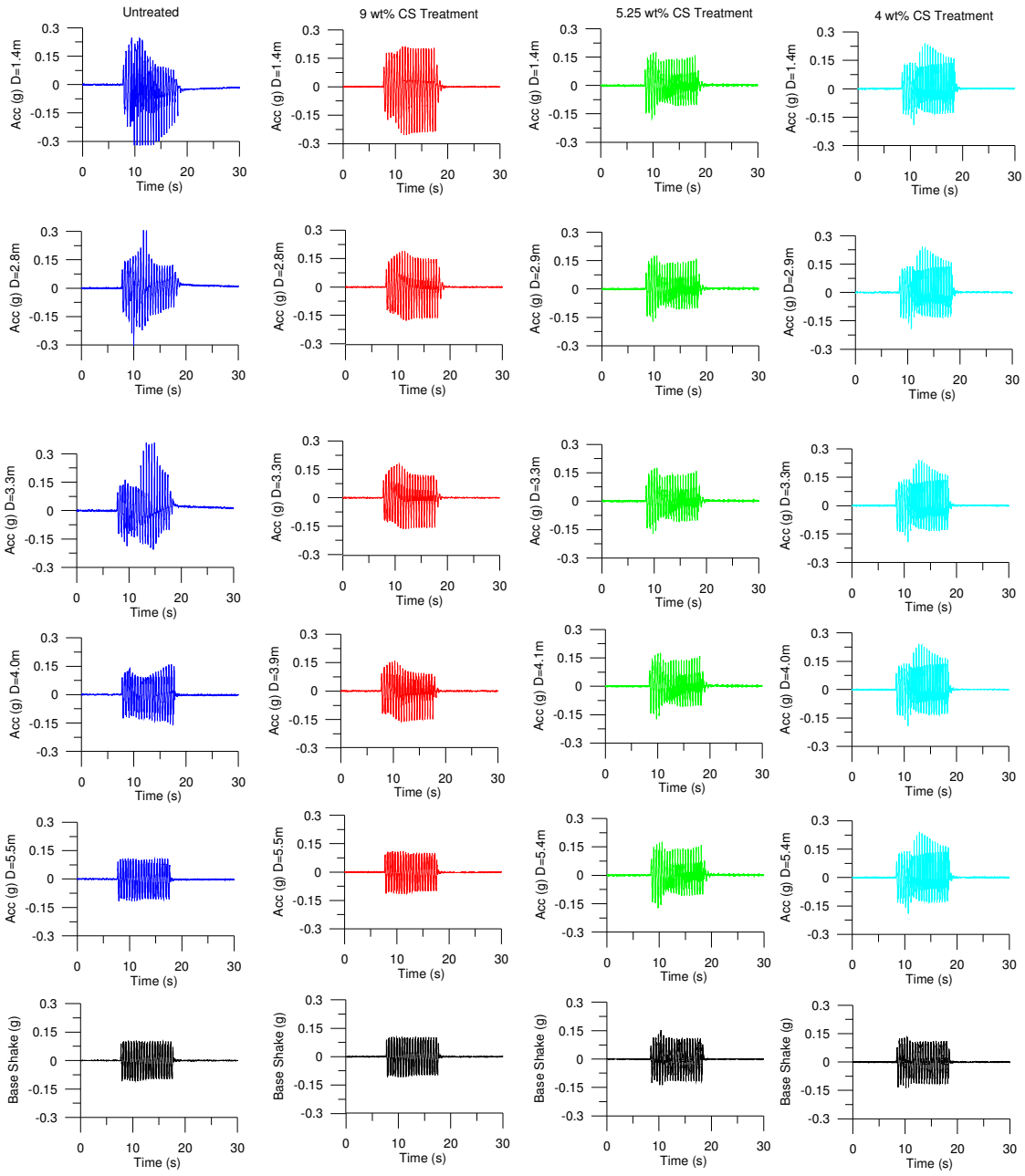

Figure 4.18 Acceleration Response for PBA = 0.1g for CTC01 and 0.15g for CTC02 (Shake 3)

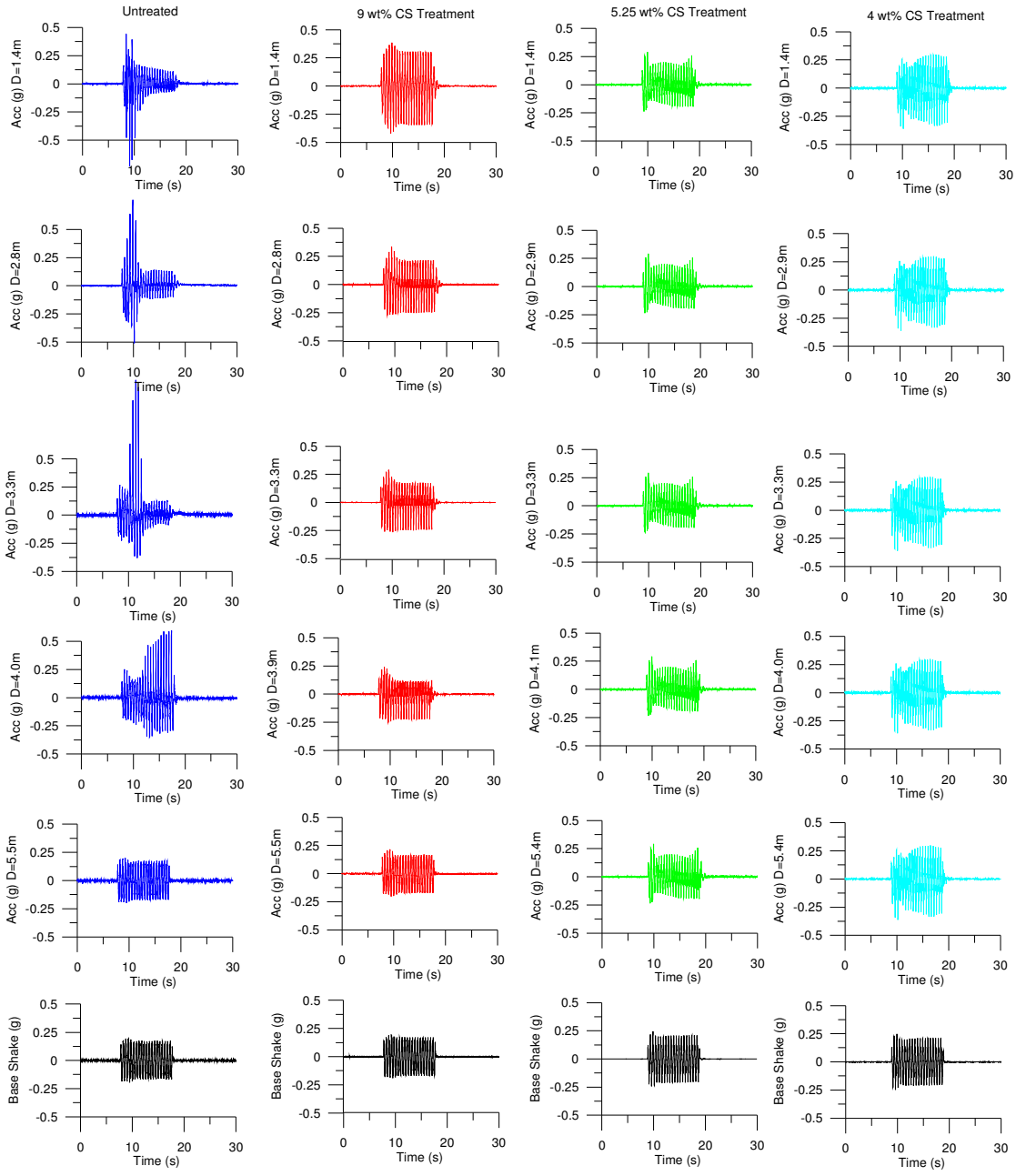

Figure 4.19 Acceleration Response for PBA = 0.19g for CTC01 and 0.25g for CTC02 (Shake 4)

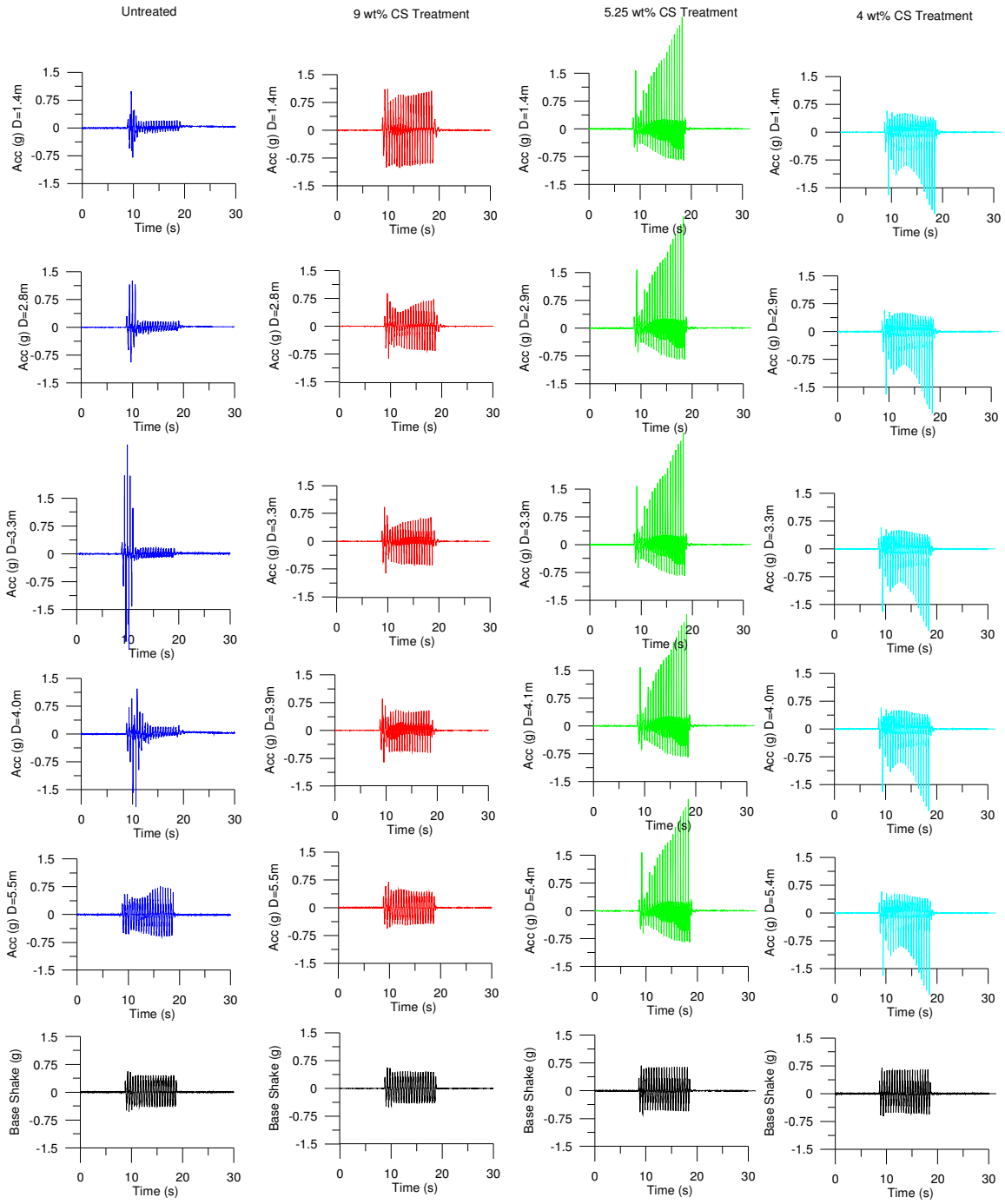

Figure 4.20 Acceleration Response for PBA = 0.56g for CTC01 and 0.69g for CTC02 (Shake 5)

4.4. Relationship between Acceleration and Pore Pressure Response

The time histories of selected accelerations and pore pressures at similar depths are illustrated in Figure 4.21 through Figure 4.24 during shake 5 (PBA=0.56g and PBA=0.69g for CTC01 and CTC02, respectively). The untreated soil in Figure 4.21 shows amplification of acceleration response in the first several cycles followed by deamplification. From Figure 4.21 amplification in the acceleration occurs as pore pressures are increasing. During this time, the untreated soil undergoes cyclic mobility and the acceleration spikes are a result of incremental dilative and contractive behavior. Once pore pressures of 1.0 are developed, there is limited response in the acceleration. The deamplification in the acceleration records occur as a result of liquefaction when the soil has lost all effective stress.

The acceleration response in the 9% CS soil remains relatively constant during this event. It is interesting to note from Figure 4.22 that at the midpoint of the soil layer, there are dramatic changes in transient pore pressures occurring. These changes are conventionally associated with cyclic mobility. This response indicates changes in effective stress of the grouted soil. However, as can be seen from the acceleration response, residual effects of soil strength are negligible.

The dynamic response of acceleration for the 5.25% CS and 4% CS soils show high-frequency spikes in acceleration (Figure 4.23 and Figure 4.24). These high-frequency spikes are consistent with pore pressure response when r_U=1.0 is achieved. Again, the transient changes in pore pressure are dramatic for both soils. The amplification in acceleration coupled with dramatic changes in transient pore pressure clearly indicates changes in behavior of the grouted medium. It is believed that stresses are being transmitted from the soil to the CS as the composite material is cyclically loaded. Unlike the untreated soils, there is no deamplification in acceleration response throughout shaking despite dramatic transient effects. This may be attributed to the result of CS carrying its own shear strength capable of holding soil particles

together. In this way, the composite material maintains a certain amount of effective stress during strong cyclic loading despite the large transient changes in pore pressures.

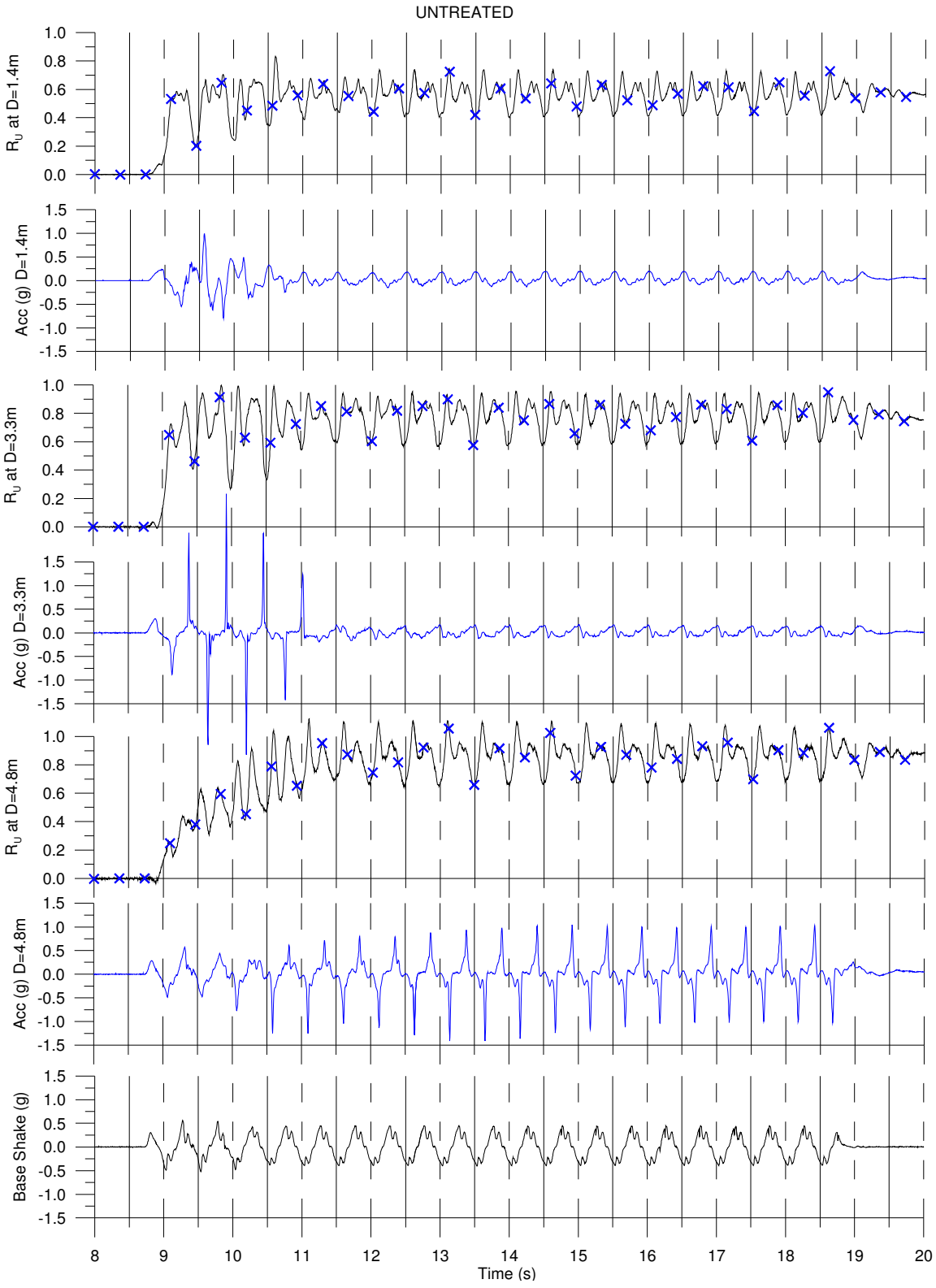

Figure 4.21. Time histories of acceleration and pore pressure response for untreated soil (shake 5)

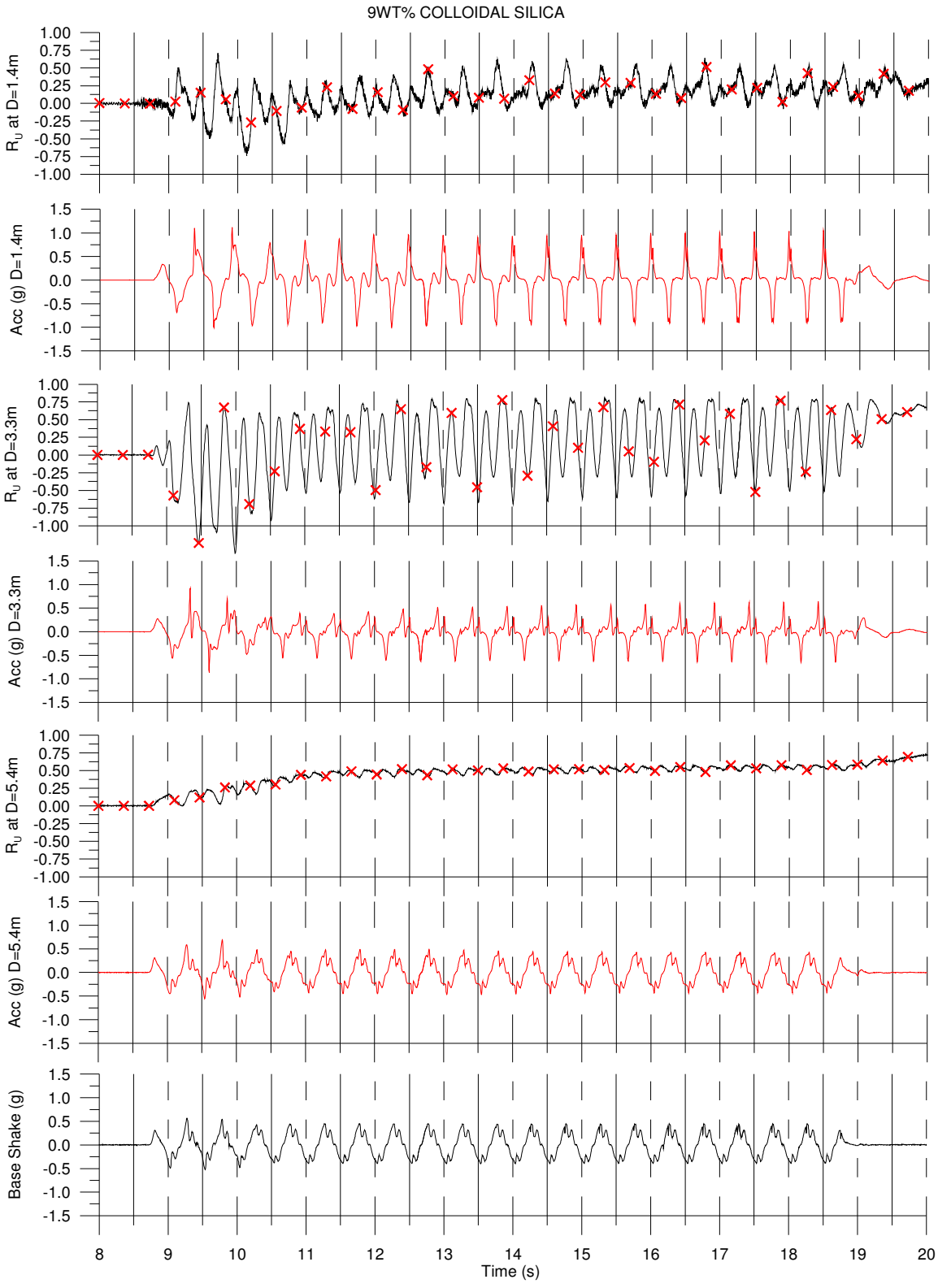

Figure 4.22 Time histories of acceleration and pore pressure response for 9% CS soil (shake 5)

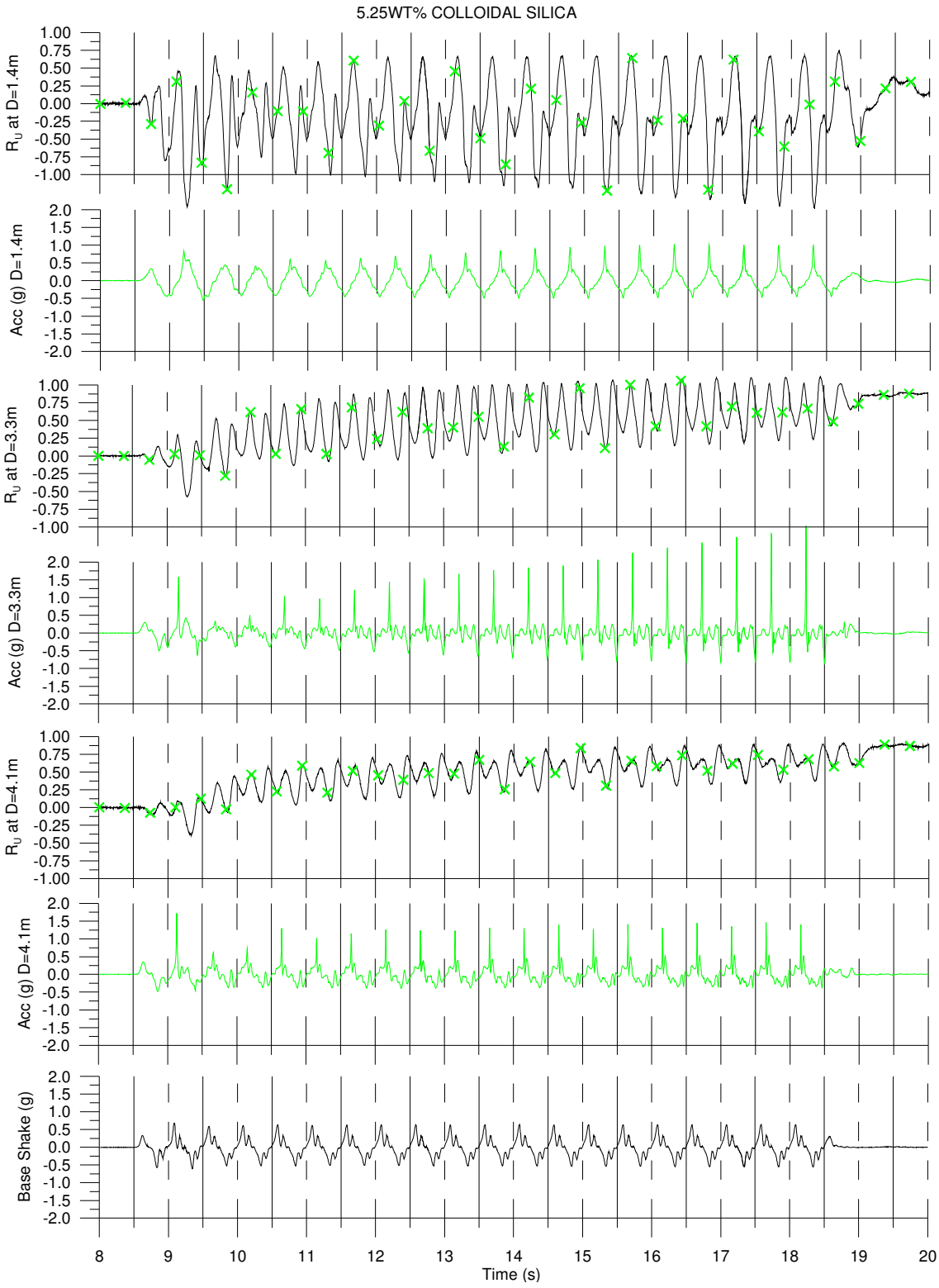

Figure 4.23 Time histories of acceleration and pore pressure response for 5.25% CS soil (shake5)

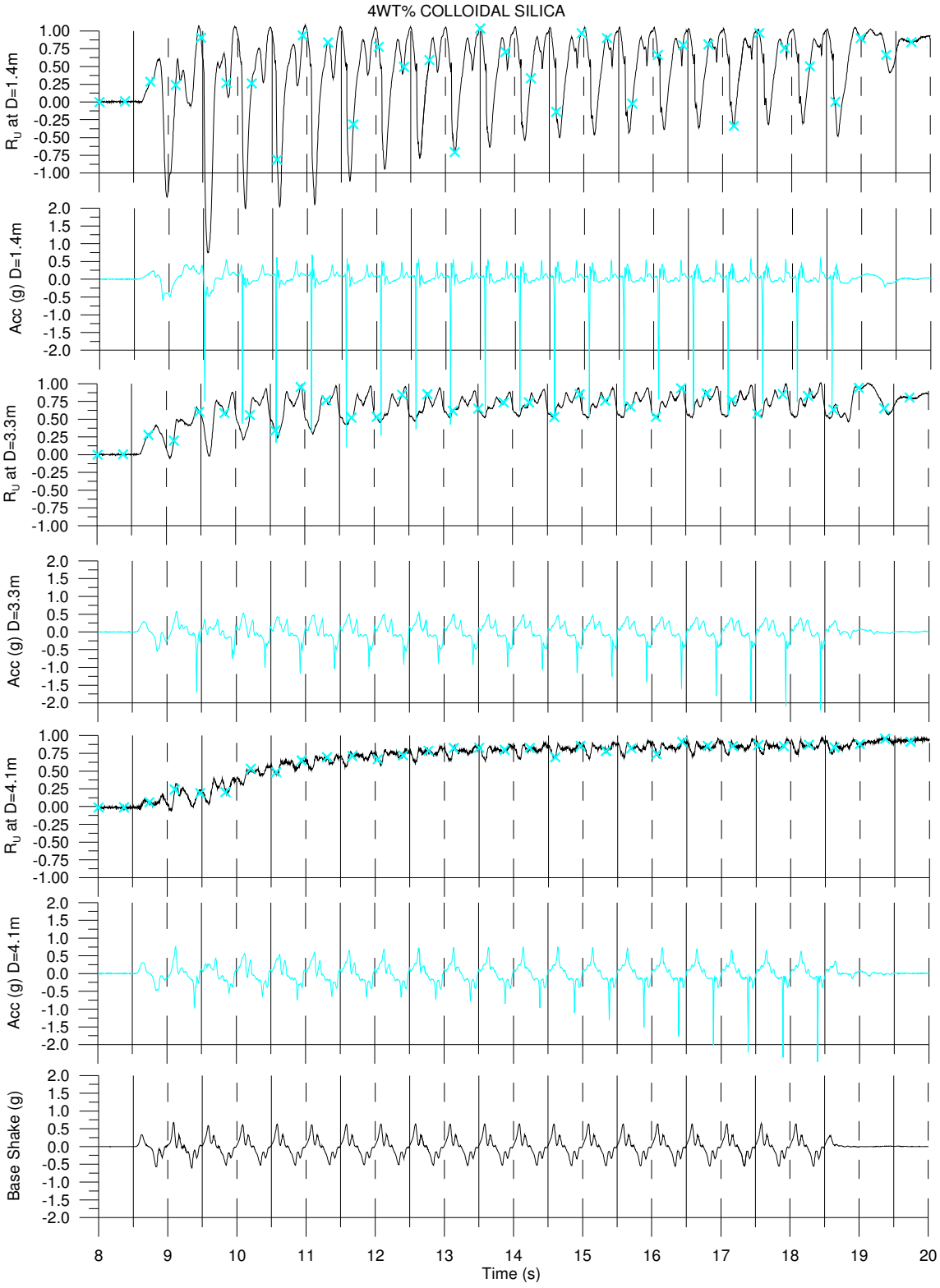

Figure 4.24 Time histories of acceleration and pore pressure response for 4% CS soil (shake 5)

4.5. Summary of Results

Results show a reduction in both lateral spreading and settlement in colloidal silica treated sands versus untreated sands. The pore pressure response indicates CS improvement levels based upon excess pore pressure ratios of 1.0 developing. Additionally, the transient changes in pore pressure response provide insight into the characteristic behavior of stress transmission between the soil and the gel itself. Based on pore pressure data, the soil on the untreated side liquefied at approximately 0.1 g. Excess pore pressure ratios of 1.0 were directly related to grout concentrations where $r_u = 1.0$ was first developed in the 4% CS soil and later in the 5.25 % CS soil which required stronger shaking acceleration. With the exception of a couple of discreet locations, the 9% CS soil did not achieve excess pore pressure ratios of 1.0. The acceleration profiles indicate no significant degradation in stiffness in the liquefiable soil layer treated with 9% CS. In addition, acceleration time histories indicate a direct relationship between concentration of colloidal silica and the strength of treated sand. Despite the incrementally dilative and contractive behavior experienced in the grouted soils (indicated by the pore pressure records), characteristics of the acceleration records show the grouted soils maintained strength and stiffness at higher concentrations.

A summarization of the overall response is presented in Figure 4.25 thru Figure 4.28 for shakes 2 through 5. Each figure depicts time histories of the acceleration, settlement, lateral spreading, and excess pore pressure ratio response. The acceleration response and excess pore pressure ratio response in the figures represent the response at the midpoint of the liquefiable soil layer for a depth of 3.3 m (10.8 ft). The settlement (ΔH) and lateral spreading (ΔV) were measurements taken from the surface of the crust. The settlements plotted were obtained from sensors HT2 and HU2 (Figure 3.5). Similarly, the lateral spreading measurements were obtained from VT2 and VU2 (Figure 3.5).

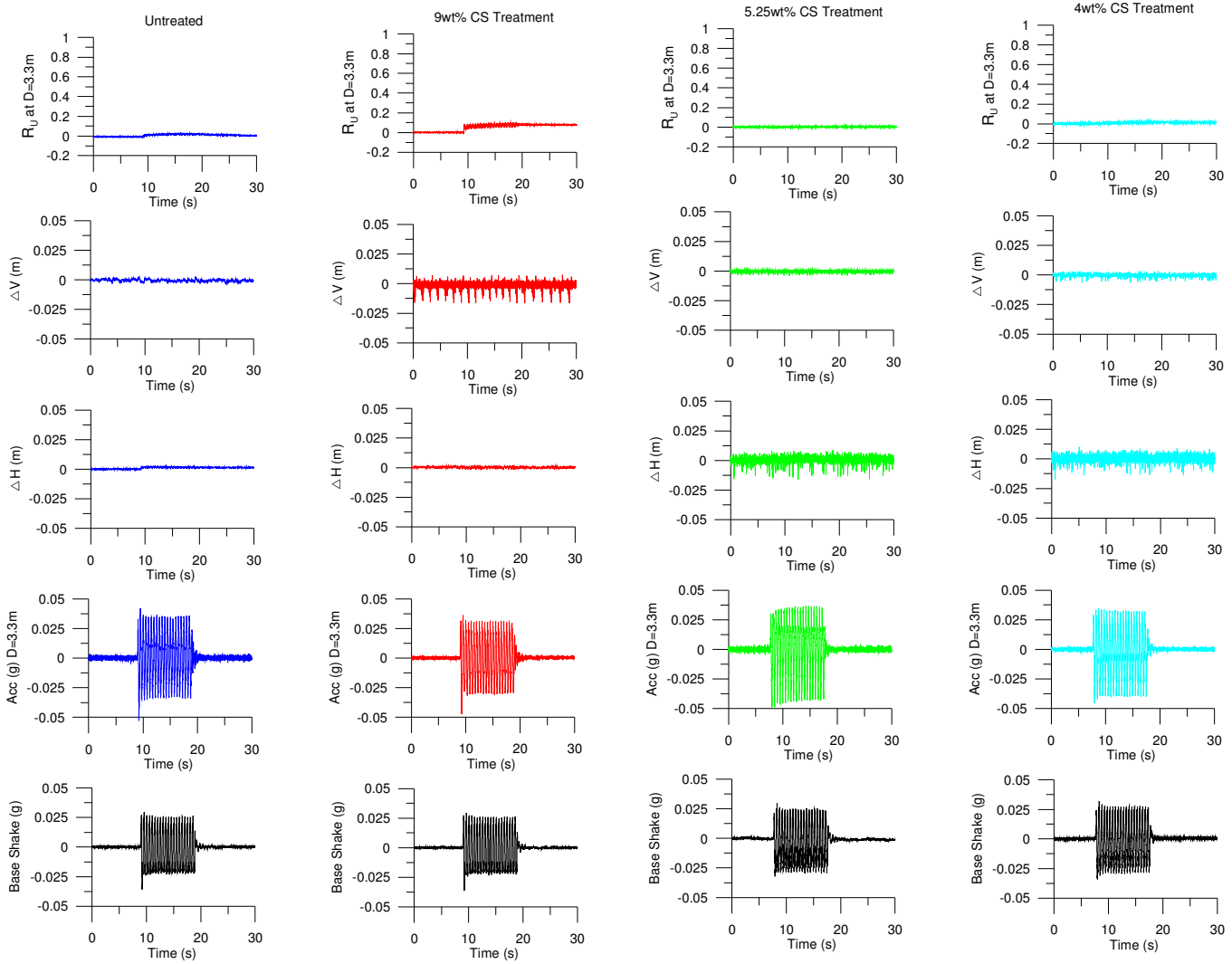

Figure 4.25 Summarization of Response for PBA = .03g (Shake 2

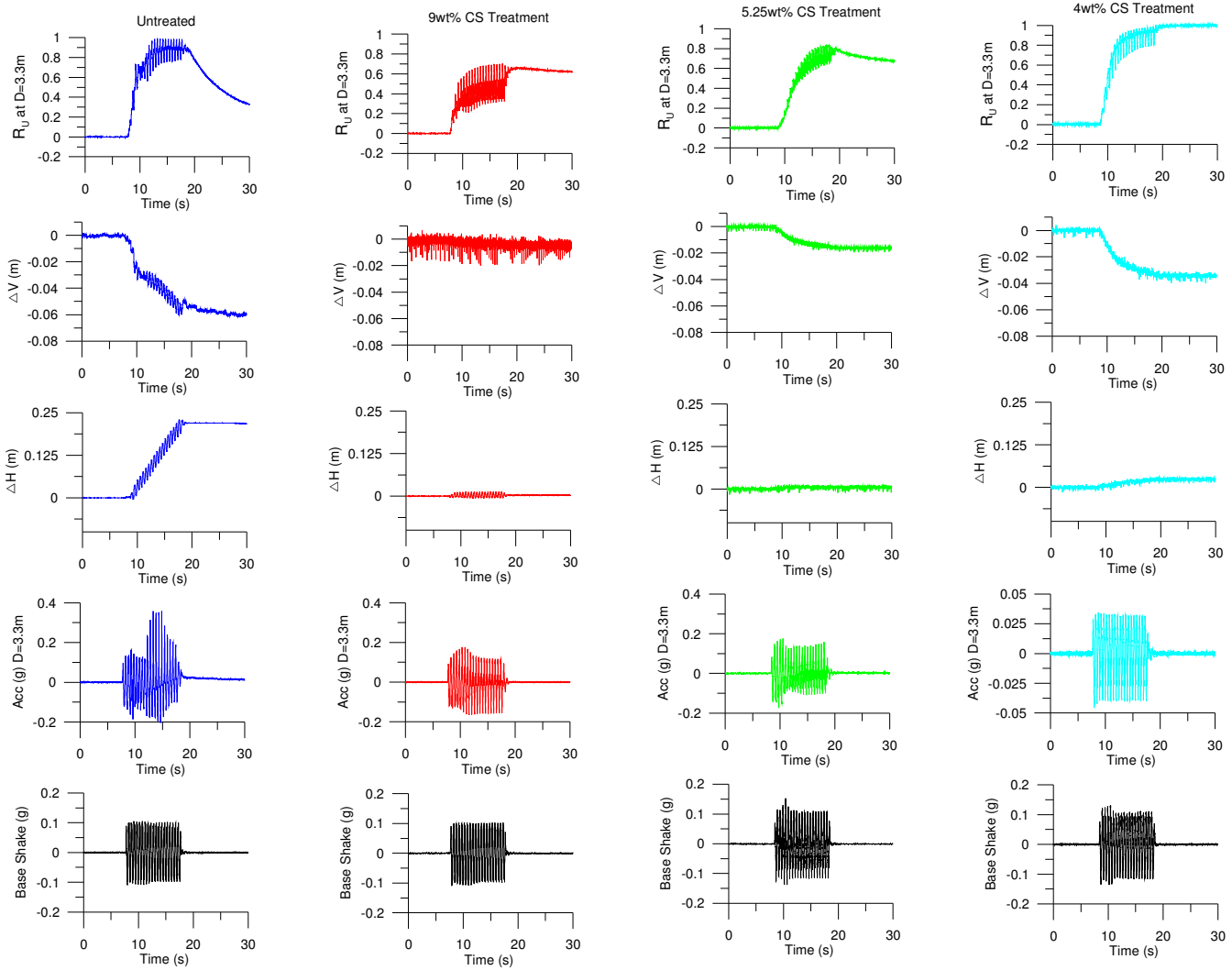

Figure 4.26 Summarization of Response for PBA = 0.1g for CTC01 and 0.15g for CTC02 (Shake 3)

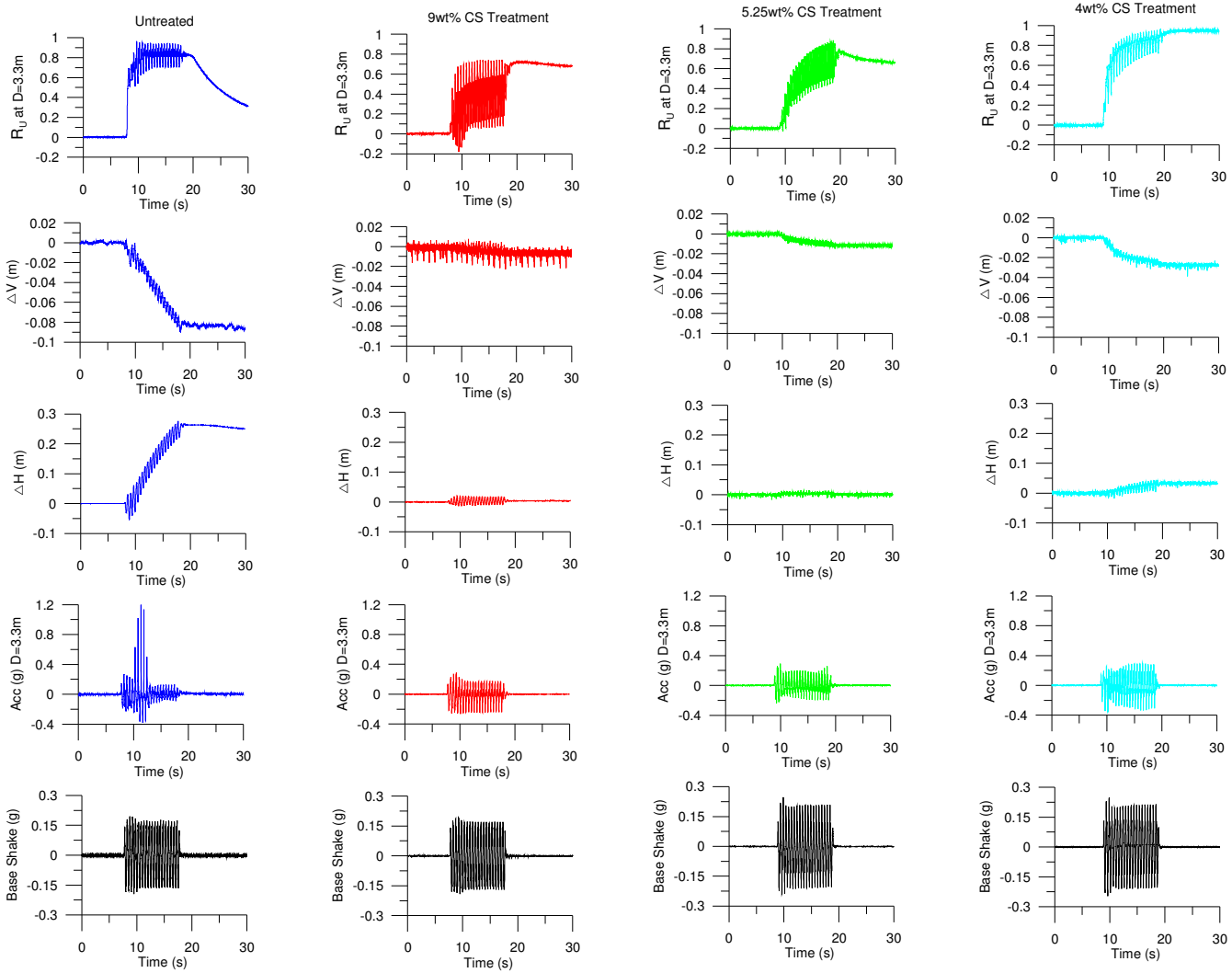

Figure 4.27 Summarization of Response for PBA = 0.2g for CTC01 and 0.25g for CTC02 (Shake 4)

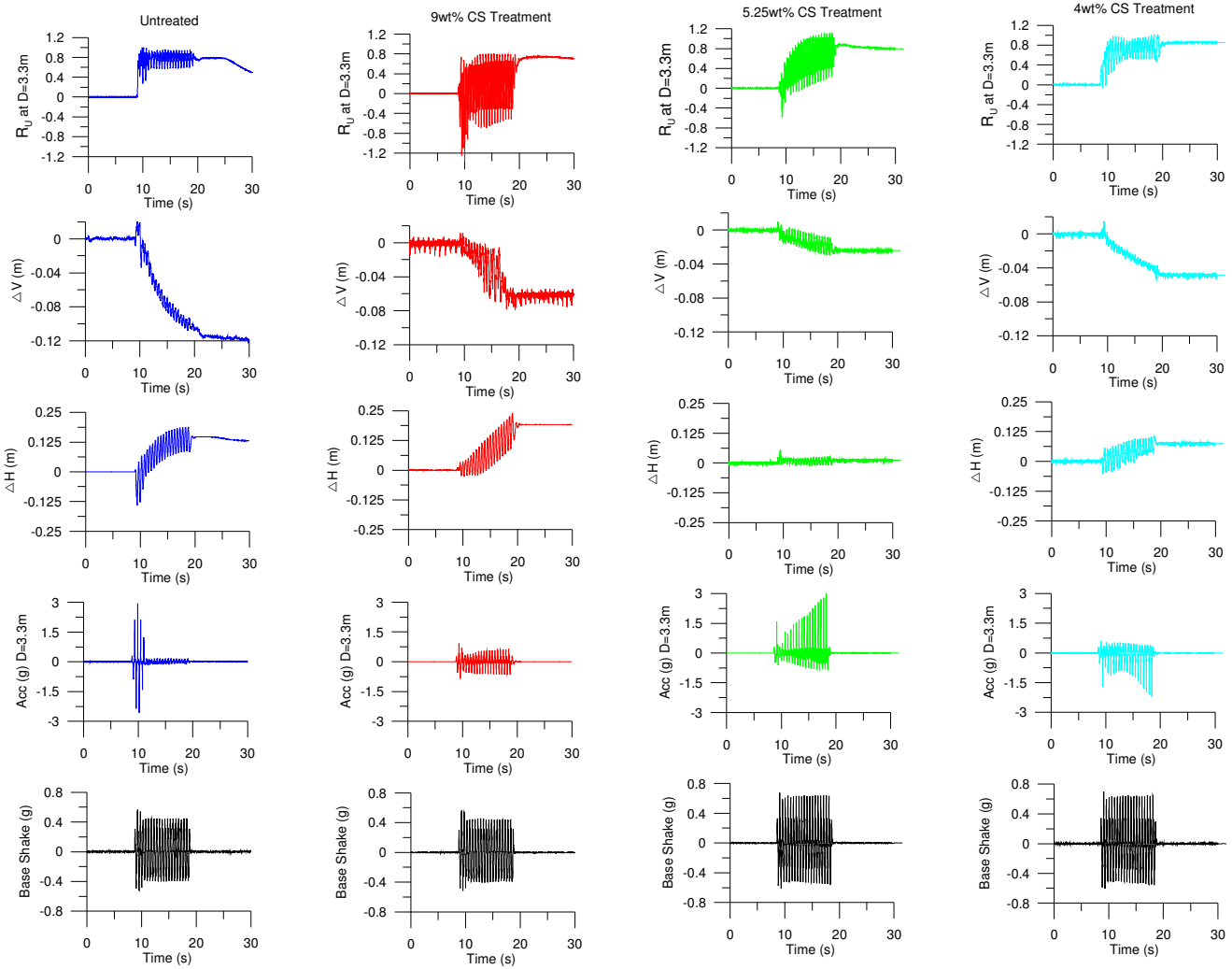

Figure 4.28 Summarization of Response for PBA = 0.56g for CTC01 and 0.69g for CTC02 (Shake 5)

CHAPTER 5: SHEAR MODULUS AND STRESS STRAN RESPONSE FROM CENTRIFUGE MODEL TESTS - DETAILS AND TEST METHODS

5.1. Dynamic Response of Soils

5.1.1. Overview

If the shear stress and shear strain behavior of a soil is tracked during dynamic loading, it will exhibit hysteretic behavior. The behavior can either be described by (1) the actual path of the loop itself from cyclic nonlinear or advanced constitutive models or (2) equivalent linear models based on stiffness and energy parameters. For equivalent linear models, shear modulus, G (or G_{sec}) and damping ratios are used as a way to describe the hysteretic behavior during cyclic loading. The shear modulus, G, is determined as the average inclination of the hysteresis loop and describes the soil stiffness. The damping ratio is determined as the area of the hysteresis loop and is used to describe the amount of energy dissipation that occurs in the soil.

For certain types of ground response analyses, the equivalent linear model approach is used. However, other types of analyses require that the actual path of the hysteresis loop be characterized. In addition, equivalent linear models are limited because they assume that the strain will always return to zero after cyclic loading. For example, the equivalent linear model cannot be used for problems involving permanent deformations because linear models assume zero strain at the end of cyclic loading and therefore, assumes no limiting soil strength. When permanent strains are needed to be incorporated into the analysis, nonlinear or advanced constitutive models are used to describe the behavior. Additionally, nonlinear models can also be used to predict the generation, redistribution, and dissipation of pore pressures, which make nonlinear approaches desirable to study phenomena associated with liquefaction.

The variation of shear modulus and strain is described as a modulus reduction curve. Mitchell and Soga (2005), characterize soil behavior by dividing the shear modulus reduction curve into 4 zones. Figure 5.1 illustrates that at low strain amplitudes, soil behavior is linear elastic and the soil stiffness is at a maximum ($G = G_{max}$). As shear strain amplitudes increase, the

behavior shifts from linear elastic to nonlinear elastic. The threshold shear strain for nonlinear elastic is generally one order of magnitude higher than the linear elastic threshold. Permanent strains in the soil do not occur until larger shear strains cause the soil to enter the pre-yield elastic zone. Finally, further increasing strains will cause the soil to approach its yield envelope where fully plastic behavior occurs.

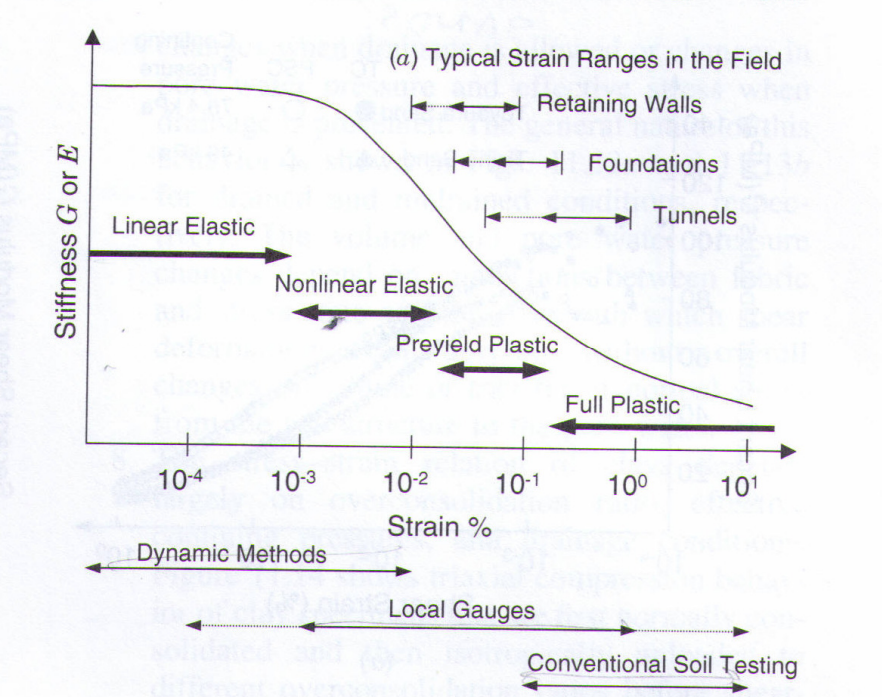

Figure 5.1 Stiffness degradation behavior at various strain levels (Mitchell and Soga, 2005)

5.1.2. Shear Wave Velocity

In dynamic response analyses, characterizing the soil stiffness requires consideration of both the maximum shear modulus, G_{max}, and how the modulus ratio, G/G_{max}, varies with cyclic strain amplitude. This allows for permanent changes in soil stiffness to be quantified for a wide range of cyclic strain amplitudes.

The maximum shear modulus of a soil can be obtained through commonly used geophysical tests that measure shear wave velocity at low strain amplitudes. These methods

include bender element tests, resonant column tests, and torsional shear tests, which can produce shear strains lower than $3*10^{-4}\%$. The maximum shear modulus can then be obtained through the following relationship:

Equation 5-1 $$G_{max} = \rho \cdot V_S^2$$

where shear wave velocity (Vs) is defined as:

Equation 5-2 $$V_S = {}^{L}/_{t}$$

From Equation 5-1, L is the effective distance between two signal measurement points, and t is the travel time for the shear wave to travel through the medium. Other low-strain tests can be used to measure V_s in situ and include SASW (spectral analysis of surface wave) tests, cross hole tests, and seismic down-hole tests. Shear wave velocity is gaining popularity in engineering practice as a way for obtaining the maximum shear modulus and is generally the most reliable way of obtaining the in situ G_{max}. When V_s cannot be obtained, empirical correlations either from lab test parameters (Seed et al., 1984; Zhou and Chen, 2005) or in situ parameters from CPT or SPT are used.

Shear wave velocity has been incorporated into the commonly used simplified procedure (Andrus and Stokoe, 1997; 2000) and is gaining popularity as a means to evaluate liquefaction resistance in soils. Shear wave velocity has also been shown to serve as a valuable tool for quality control techniques in ground improvement. Andrus et al. (1998) compared shear wave velocities between untreated soils and soils improved using a vibrating probe technique. Shear wave velocities were measured by Spectral-Analysis-of Surface-Waves (SASW) testing. In this test, average shear wave velocities determined for the improved and unimproved sand were found to be 192 m/s (630 ft/s) and 167 m/s (548 ft/s), respectively. Two liquefaction assessment procedures related to shear wave velocities from (1) a penetration-based approach (after Andrus and Stokoe, 1999) and (2) a strain based approach (after Dobry et. al. 1982 and Stokoe et al., 1989) correctly predicted no liquefaction for the densified sand and marginal liquefaction for the

undensified sand. Zhou et al (2009) has recently developed an approach to evaluate the improvement level in liquefiable soils treated by stone columns by incorporating differences in void ratio into the V_s relationships of the simplified procedure from Andrus and Stokoe (2000).

5.1.3. Hysteretic Behavior of Soils

Cyclic shear stress-strain behavior is key to understanding how sites will respond under high strain, low frequency dynamic loads such as those created by an earthquake. When a soil liquefies under such loading conditions, its residual strength becomes lower that the shear resistance required to maintain static equilibrium. State-of-the-Art approaches to model the development of liquefiable soils account for a number of important characteristics including the nonlinear elastic, shear stress-strain response that occurs.

As previously mentioned characterizing the soil stiffness also requires consideration of how the shear modulus (or modulus ratio) will vary with cyclic strain amplitude. Boulanger and Idriss (2006) summarize the undrained behavior of sands and clays under monotonic and cyclic loading. For sands undergoing cyclic loading, the typical effective stress path and stress-strain response is presented and illustrated in Figure 5.2a and Figure 5.2b , respectively. Early in the loading sequence, Figure 5.2a shows that the effective stress decreases for each loading cycle as a result of increasing pore water pressures. There is initially very little increases in shear strains as illustrated in Figure 5.2b and the behavior more or less exhibits elastic behavior. Additional loading cycles will result in continuing decreases of effective stress until it evenutally becomes zero. When the effective stress become zero “initial liquefaction” occurs and is defined here as the time when the excess pore pressure ratio temporarily becomes 100%. Once liquefaction is intiated, shear strains progressively increase (Figure 5.2b). At this point, additional applied streses will cause the sands to temporarily shift back and forth from dilative to contractive behavior (i.e. cyclic mobility) where the sand undergoes phase transformation. For loose sands, only a few

additional loading cycles are typically required after phase transformation to cause the sand to develop dramatic increases in permanent strains and ultimate collapse of the specimen.

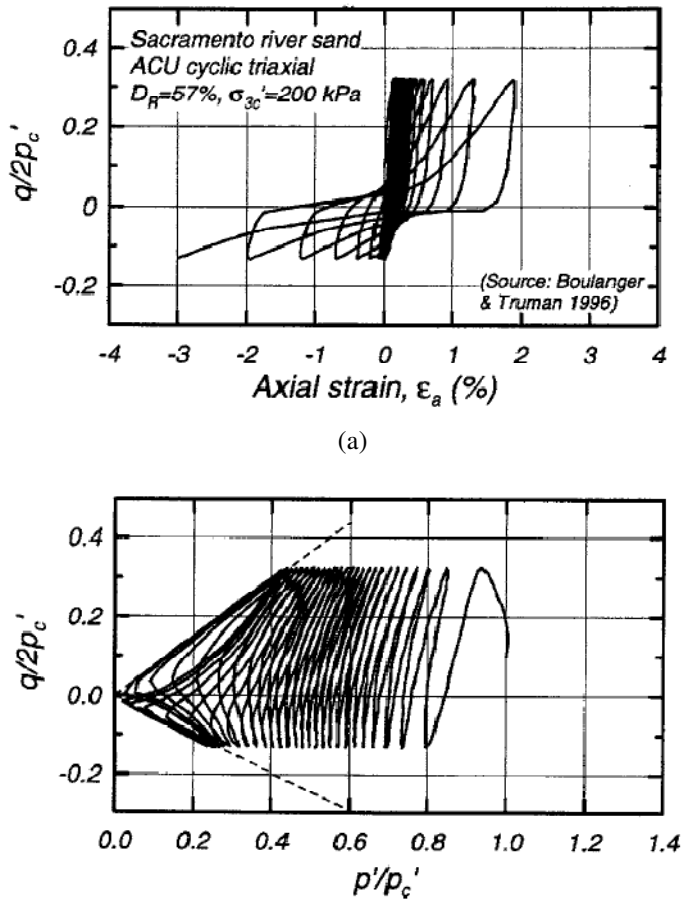

Figure 5.2 (a) Stress-strain response and (b) effective stress path for saturated sand (Boulanger and Idriss, 2006)

In general, clays under monotonic loading exhibit a relatively plastic stress-strain response. Contrary to sands, there is no phase transformation prior to yield. Additionally, the shear strength for sands is highly dependent on relative density whereas the shear strength for clays is highly dependent on the consolidation stress history.

A typical stress-strain response and effective stress path for a normally consolidated saturated clay is illustrated in Figure 5.3. Figure 5.3a shows decreases in effective stresses as pore pressures increase. Unlike sands , a rapid increase in strains occur at an earier point in the loading sequence before the effective stress reaches a value of zero and a significant amount of damping occurs. The increasing development of shear strains appears to occur when the excess pore pressure is about 80% (versus 100% for sands). Additionally, the area of the hysterisis loops are much larger compared with the area of the hysteresis loop for sands. This indicates that the dampening effects (or energy dissipation) is greater for clays than sands. Finally, the stress-strain paths developed in Figure 5.3b indicate that cyclic mobility is not a phenomenon associated with clays.

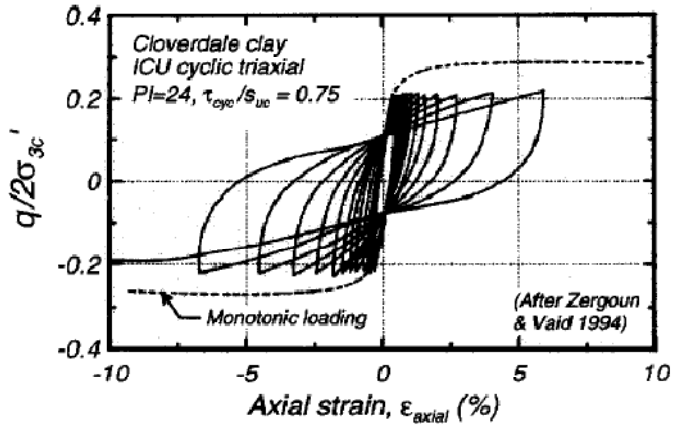

(a)

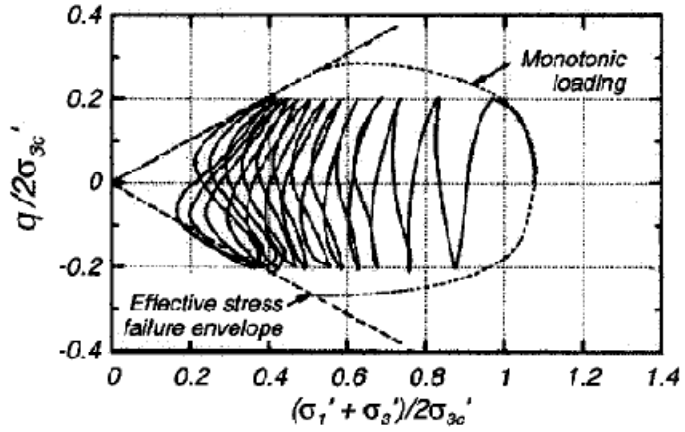

(b)

Figure 5.3 (a) Stress-strain response and (b) effective stress path for clay (Boulanger and Idriss, 2006)

5.2. Dynamic Response of Chemically Grouted Soils

The dynamic behavior of chemically grouted soils, including silicate-based grouts, have been investigated extensively through laboratory testing. Maher et al. (1993) studied the effects of shear modulus under both low strain and high strain dynamic loads for sodium silicate grouts. Resonant column tests were used to study small strain behavior (10^{-4}% to 10^{-2}%) while cyclic triaxial tests were used to study large strain behavior (10^{-2}% to 1%). In general, results showed

higher shear moduli for grouted soils compared to ungrouted soils. Similar to ungrouted sands, shear modulus would increase with increasing confining stress and decrease with increasing shear strain. At higher shear strain amplitudes, the difference in shear modulus between grouted sands and ungrouted sands became less pronounced. Results also showed that the number of cycles have minimal influence on grouted sands. At lower strain amplitudes up to about .015%, little cyclic stiffening occurred after 30 cycles. For cyclic strains tested at higher strain amplitudes of up to about 1%, shear modulus readings were nearly constant after 30 cycles. The reduced influence of cyclic prestraining and number of cycles on shear modulus can be attributed to the fact that the grout restricts particle movement and reorientation. Finally, tests were conducted to observe the effects of sodium silicate grout concentration and curing time. While results showed increasing shear modulus with increasing grout concentration, there was negligable influence on curing time after 60 days. It should be noted that monotonic loading tests indicate the majority of strength gain of sodium silicate grout occurs within 14 days (Maher et al., 1994).

Li and Woods (1987) investigated low strain dynamic properties of soils treated with chemical grouts including sodium silicate grout in resonant column tests. Results showed increases in G_{max} for chemically grouted soils, increasing grout concentration, and increasing curing time. Additionally G_{max} was found to be unaffected by stress history for confining pressures less than 200 kPa (29 psi) and strain amplitudes less than $8*10^{-5}$%.

Brachman (2004) conducted in situ cross-hole tests to determine shear wave velocities and assess whether this technique could be used to determine the quality of various types of grouted soils including sodium silicate grout. In this field study, shear wave velocities were determined in 0.5 m increments between depths of 10 m (33 ft) and 13 m (43 ft) below the ground surface and compared to an ungrouted soil. Visual observations were made from borehole samples and a large diameter shaft to verify measurements. In general, results indicate that shear wave velocities are slowest for ungrouted sands, fastest for sands that are well grouted, and

highly variable for poorly grouted or uncured grouted zones. It was concluded that shear wave velocity measurements were able to identify well-grouted zones, but unable to detect zones of poor grout quality and/or variable coverage.

5.3. Dynamic Response of Colloidal Silica Soils

Low strain dynamic behavior on colloidal silica treated sands has been studied by Spencer et al. (2008) through resonant column testing. The effects between G_{max} on varying colloidal silica concentrations (5% and 9%) and curing time were investigated and compared to an untreated dry sand specimen. The resonant column tests were performed at shear strains ranging from $1*10^{-4}$% up to .03%. The results are illustrated in Figure 5.4 showing shear modulus versus cyclic shear strain for 5% CS, 9% CS, and untreated sand specimens. In general, test results showed higher G_{max} for treated soils compared to the untreated soil. G_{max} for both concentrations appeared to be unaffected up to strains of about $1*10^{-3}$% and then gradually decreased at higher strain amplitudes from about 65 MPa (9,430 psi) to 45 MPa (6,530 psi). A very minor increase in shear modulus was observed with increasing concentrations; however, this increase was almost negligible. Additionally, effects of curing time for 5% concentration were tested over a constant strain of $2.5*10^{-4}$%. After curing for 28 days, an increase in G_{max} by 6 MPa (870 psi) was observed and was continuing to increase. As a result, G_{max} will continue to increase over some unknown time. It should be noted that Persoff et al (1999) found strength gain in colloidal silica treated sands to occur for up to 1 year. However, long-term testing on colloidal silica treated sands is limited and beyond the scope of this study.

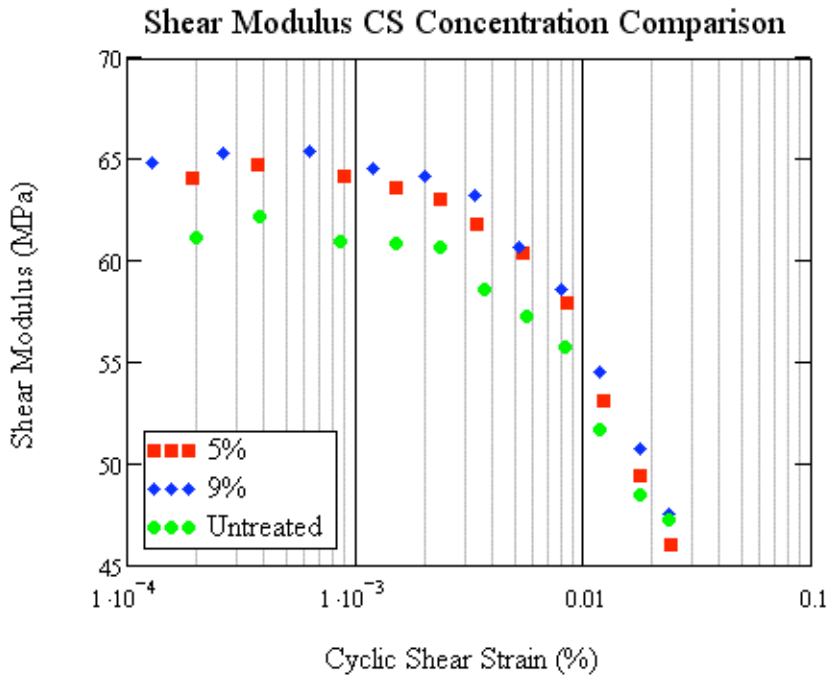

Figure 5.4 Shear modulus comparison of CS mixtures to untreated sand (Spencer, 2008)

The large strain dynamic behavior of soils grouted with colloidal silica have also been investigated through various laboratory testing methods. Monotonic load tests have been conducted by Gallagher and Mitchell (2002) and Kodaka (2005) using triaxial and torsional shear tests, respectively. Gallagher and Mitchell (2002) performed unconfined compression tests to determine the strength of 5% CS and 10% CS specimens that had previously been subjected to cyclic loading and were compared to 5% CS and 10% CS specimens that did not undergo cyclic loading. Overall, results showed that compressive strengths increased with increasing CS concentrations. For specimens that were not previously tested under cyclic loading, UC strengths ranged from 32 kPa (4.6 psi) to 110 kPa (16 psi) for 5% CS and 15% CS, respectively. For samples that were cyclically loaded, the 5% CS and10 % CS decreased in compressive strength by about 15% when previously subjected to 2% and 1% strains, respectively. When the 5% CS

and 10% CS specimens exceeded 2% and 1% strain, strength degradations ranged between 30% and 60%.

Monotonic load tests were also conducted by Kodaka et al. (2005) using torsional shear tests. The purpose of the testing was to compare the strength characteristics between colloidal silica treated sands and untreated sands. Samples were grouted, cured for 4 weeks, and tested at various confining pressures. Results from this study are presented in Figure 5.5 and Figure 5.6 for untreated and treated soils, respectively.

Comparisons of Figure 5.5 and Figure 5.6 indicate a substantial increase in shear strength for the treated soil. In each figure, the failure line (FL) and phase transition line (PTL) are identifiied. While the inclinations of the FL for the treated and untreated soil are nearly identical, a smaller inclicnation of the PTL can be seen for the treated soil. This reduction in inclination produces an increasing area between the PTL and the FL, which represents the dilatency region prior to failure. The ability of a soil to dilate allows the soil to resist increased levels of shear stress. It should be noted that relative to loose sands, this larger dilatency region is also characteristic of dense sands. Based on the results presented from this study, it is expected that shear strains in grouted soils will develop rapidly, but the increasing dilatency region of the grouted soils suggests that the treateds soils can resist larger shear stresses compared with untreated soils.

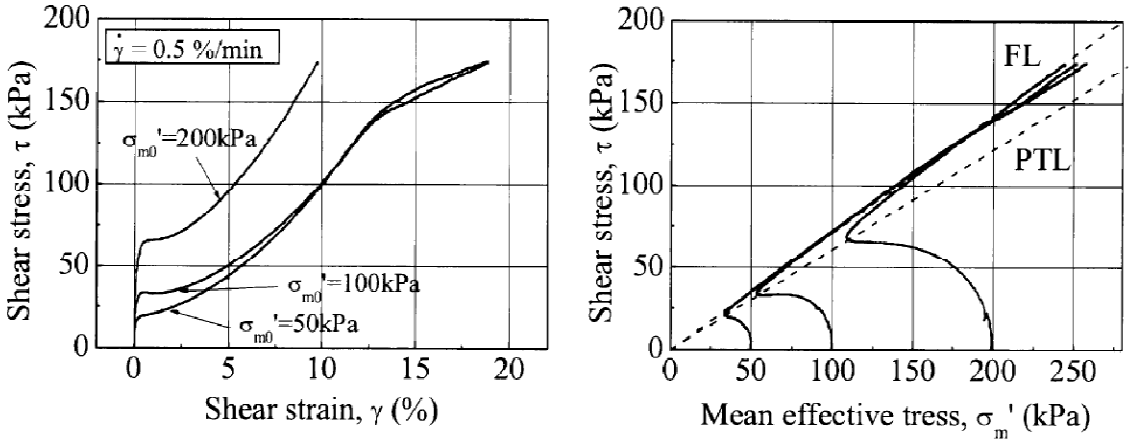

Figure 5.5 Monotonic loading undrained behavior for Untreated sand (Kodaka, 2005)

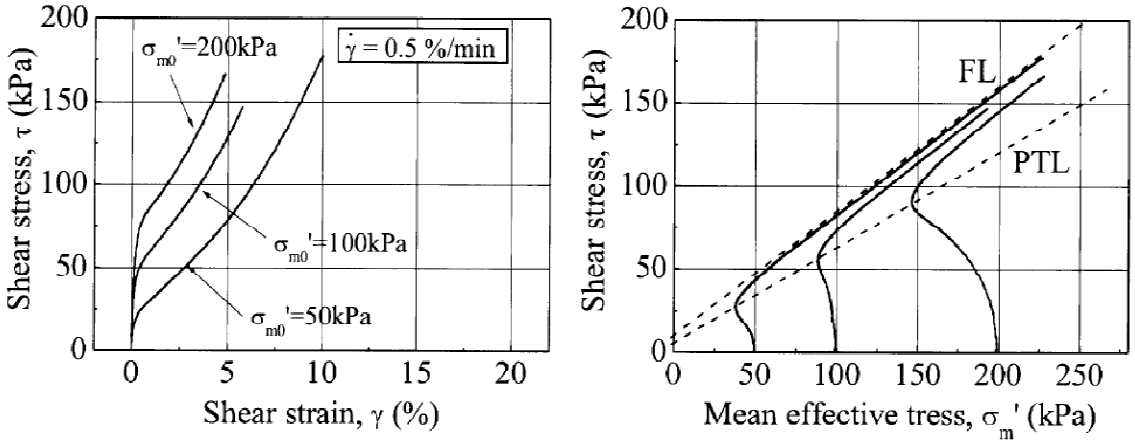

Figure 5.6 Monotonic loading undrained behavior for Treated sand (Kodaka, 2005)

The behavior of CS treated soils under cyclic loading have also been studied in the laboratory using triaxial tests (Gallagher and Mitchell, 2000), torsional shear tests` (Kodaka et al., 2005), and cyclic simple shear tests (Diaz-Rodriguez and Antonio-Izarraras, 2004).

Gallagher and Mitchell (2002) performed cyclic triaxial tests to study strain effects for varying CS concentrations and curing times at various CSR values. The CS concentrations ranged from 5% to 20% and were all tested under 100 kPa confining stress. In general, results

showed decreases in strains for increasing CS concentrations and curing times. It should be noted that for CSR values tested up to 0.4 and 100 applied loading cycles, a maximum of about 5% DA strains were developed; however, there were no cases in which samples collapsed. Kodaka (2005) also studied the behavior of colloidal silica treated soils subjected to cyclic loading from torsional shear tests. Similar to results obtained in Gallagher and Mitchell (2002), studies showed that grouted soils tested at a CSR of about 0.4 experienced about 5% DA strain after 100 loading cycles. For purposes of comparison, collapse of untreated sand specimens may occur in as little as 13 cycles for a CSR of 0.27.

The hysteretic stress-strain behavior for CS treated and untreated soils from cyclic torsional shear tests are presented in Figure 5.7a and Figure 5.7b (Kodaka, 2005). Based on Figure 5.7a and Figure 5.7b, results of CS grouted sands show distinctly different deformation behaivor compared to that of untreated sands. For the untreated soil tested at a CSR of 0.23, Figure 5.7a shows typical dynamic response of loose sands undergoing cyclic loading. Initially, the untreated sand shows little development of shear strains. However, when the effective stress state reaches the PTL, rapid development of shear strains occur and the soil collapses after a few additional cycles. The CS soil, on the other hand, shows several characterisitc differences in loading behavior. Figure 5.7b shows the response of a CS treated speciment for an applied CSR more than tweice that as the untreated specimen from Figure 5.7a. From Figure 5.7b there is a quick development of decreasing effective stress, increasing strains are quickly developed in the beginning stages of loading and a large amount of energy is dissipated in the soil. Figure 5.7b shows that effective stresses are dramatically reduced and strains of about 1% are developed in the first loding cycle. With each additional loading cycle, there are only minor decreases in residual effective stresses and the soil remains within the dilatentcy region (i.e. between the PTL and FL). During this stage of dynamic loding, strains slowly increase from 1% up to 2.5% strain with a significant amount of damping for each loading cycle. Even with additional applied cycles

and a high CSR of 0.6, the shear strains do not go beyond 2.5% and the soil does not collapse (i.e. does not fall on the failure line from Figure 5.6).

Finally, Diaz-Rodriguez and Antonio-Izarraaras (2004) studied dynamic behvior of colloidal silcia sands through cyclic simple shear tests. The distinguishing feature of this test program was that pore pressures were monitored during cyclic loading and used to compare initial liquefaction in both ungrouted and grouted soils. Differences in pore pressure response show that the development of pore presure is greately reduced in the beginning stages of loading. For example, the untreated specimen showed an exess pore pressure ratio of 1.0 occurred after 4 loading cycles while the treated specimen produces only 1/3 of the exess pore pressure ratio at a similar point in the loading sequence. Based on pore pressure response, a CSR of 0.4 showed that liquefaction was induced after 40 cycles of loading versus 4 cycles of loading for treated and untreated soils, respectively. The results showed that an ru=100% in the CS sands correspond to DA strain of 5%.

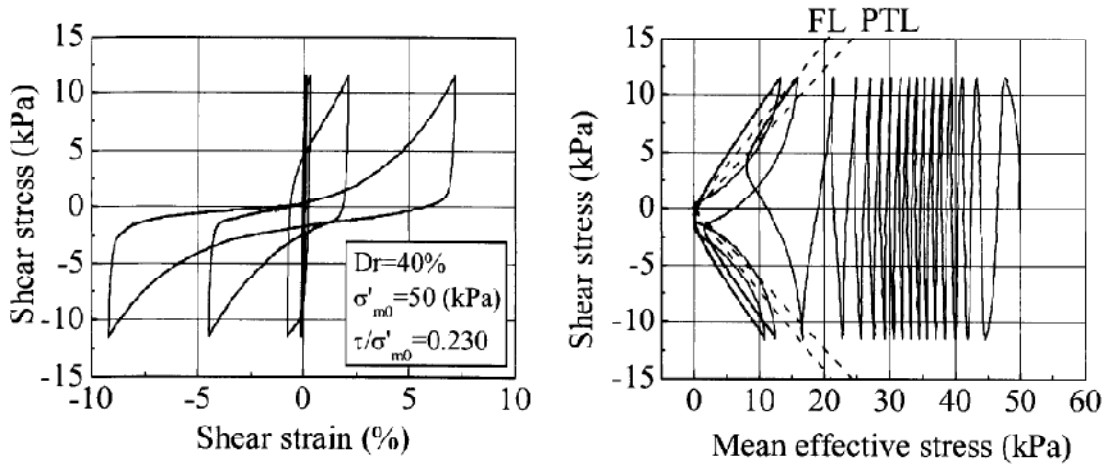

(a) Untreated Sand

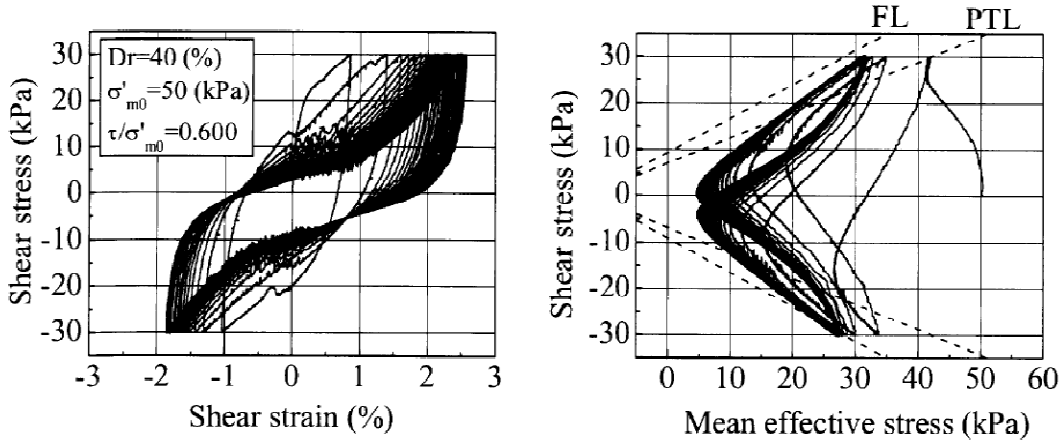

(b) Sand Treated with Colloidal Silica

Figure 5.7 Stress strain behavior and effective stress path for (a) untreated sand and (b)colloidal silica grouted sand (Kodaka, 2005)

5.4. Methods

From the centrifuge model tests that were performed and previously discussed, the dynamic response of colloidal silica treated soils were studied based on: (1) measurements of shear wave velocity and (2) determination of cylic shear stress and cyclic shear strain behavior. Again, concentrations of 9% CS, 5.25% CS, and 4% CS were analyzed and compared with the untreated soil. As previously noted, curing times of approximately 10 to 12 times the initial gel

time was achieved for the 9% CS and 5.25% CS. The 4% CS never reached a resonated gel state and was characteristic of a weak, non-resonated gel with zero curing time.

Two methods for determining shear wave velocities were utilized in the centrifuge model tests. Measurements were taken in between shaking events ranging from .007g up to about 1.3g. In this way, effects of shear wave velocity could be studied over a wide range of induced shear strains. Shear stress and shear strain profiles were determined along the soil profile using inverse analysis methods from a dense array of accelerometers. In this way, hysteretic behavior could be established and the strength and stiffness of the soil could be tracked during each shaking event.

5.5. Shear Wave Velocity Determination

5.5.1. Pulse Wave Analysis for V_S Determination (CTC01)

Shear wave velocity measurements were originally planned to be determined from bender elements installed in the model. However, in CTC01, the bender elements failed as a result of insufficient water-proof polyurethane coating on the bender elements. This resulted in the signals short-circuiting and data could not be recorded. An alternative method for monitoring shear wave velocities was therefore proposed. The method would utilize the centrifuge shaker to simulate a single pulse wave at the base of the model container. The signal through the liquefiable soil profile would be monitored from the vertical accelerometer arrays placed in the model as shown in Figure 5.8. A total of five pulse waves were applied to the model in between varying levels of applied ground motions summarized in Table 5.1.

Table 5.1 Pulse wave testing sequence (CTC01)

Pulse #	After PBA (g)
0	initial
1	0.1
2	0.19
3	0.56
4	1.28

The instrumentation layout for shear wave velocity determination for CTC01 is shown in Figure 5.8. As the shear wave traveled through the liquefiable soil, the vertical array of accelerometers picked up the signal. Unlike bender testing, the data was collected from a discreet signal, with a sampling rate of 20,000 Hz. Each pulse wave was measured to have an average peak base amplitude of .025g. The distance between the two signal measurement points, *L*, was taken as the difference in elevation from one accelerometer to the next in the vertical array. These elevations were measured during model preparation (before testing) and during model excavation (after testing). The travel time, *t*, was taken as the cumulative time shift of the pulse wave from bottom accelerometer to successive sensors in the array (Figure 5.8).

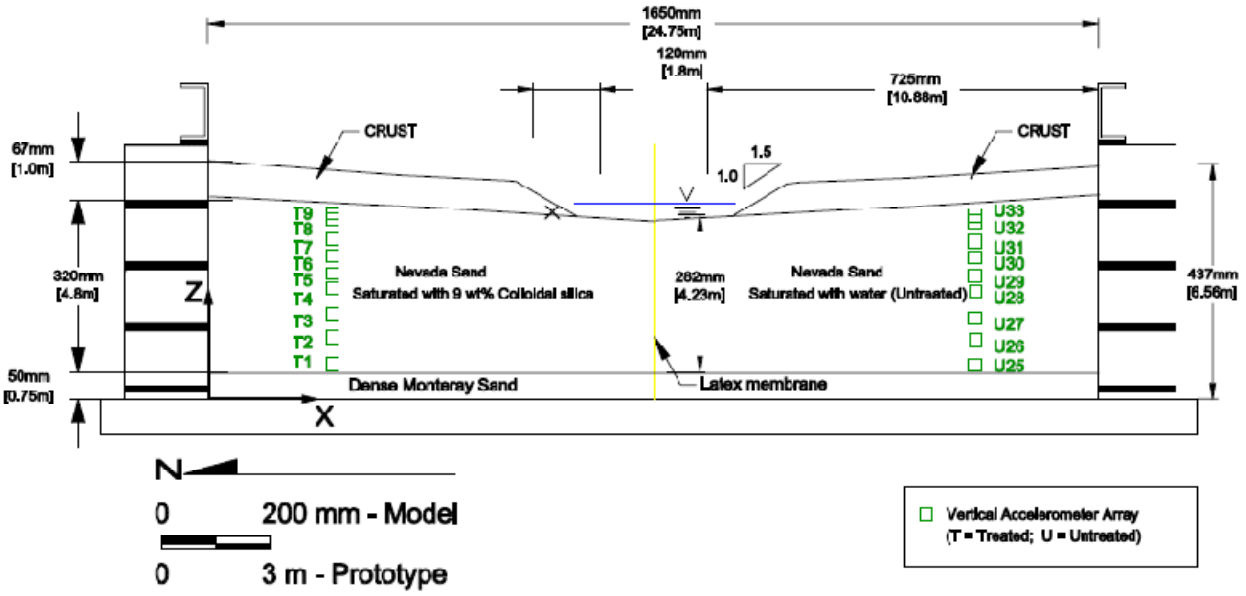

Figure 5.8 Instrumentation Layout for Pulsewave Testing in CTC01

The time shift of the pulse wave between accelerometers was determined using cross correlation methods implemented in MathCad. Prior to applying a cross correlation to the data, the acceleration records needed to be filtered. The purpose of the filter is to cut out undesirable frequencies such as those caused by excessive noise from movement of the spinning centrifuge arm and other uncontrollable factors (predominantly high frequency zones). A filter is essentially a function that has a value close to 1 in the range of freqencies that are desired to be retained for analysis and a value close to zero in the frequencies that are desired to be eliminated. Details of data filtering are further described in Section 5.6. Additionally, baseline shifts of the signal may occur as a result of frequency-dependent time shifts in the signal (predominantly low frequency zones). A 7^{th} order bandpass filter with corner frequencies of 1Hz and 80 Hz was applied to the original pulse wave record for each accelerometer. In order to more adequately capture peaks in the signal, the accelerations were normalized such that the maximum amplitude reading would be 1.0g. Figure 5.9 compares the normalized signal before and after applying the filter. The small

bumps in the overall signal can be seen in Figure 5.9a and illustrates the effects of high frequency noise while the filtered signal results in a smoother response.

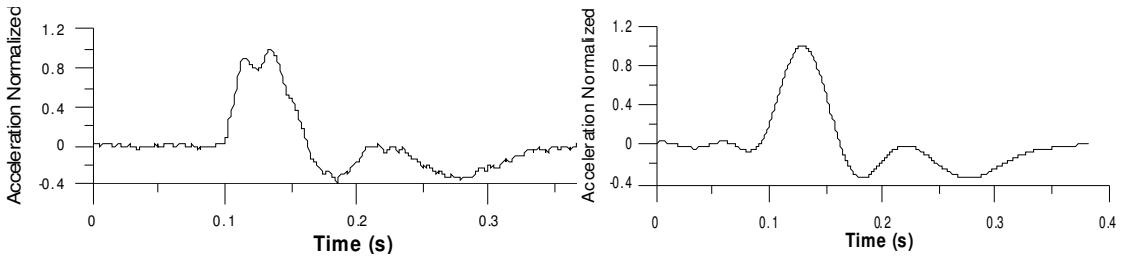

(a) **(b)**

Figure 5.9 Pulse wave signal (a) before and (b) after applied filter

Figure 5.10 illustrates the response of the wave propagation through the soil profile for the 9% treated soil. The figure describes typical behavior of the recorded signals where a wave-like propagation can be seen as the signal passes from one accelerometer to the next in the vertical array.

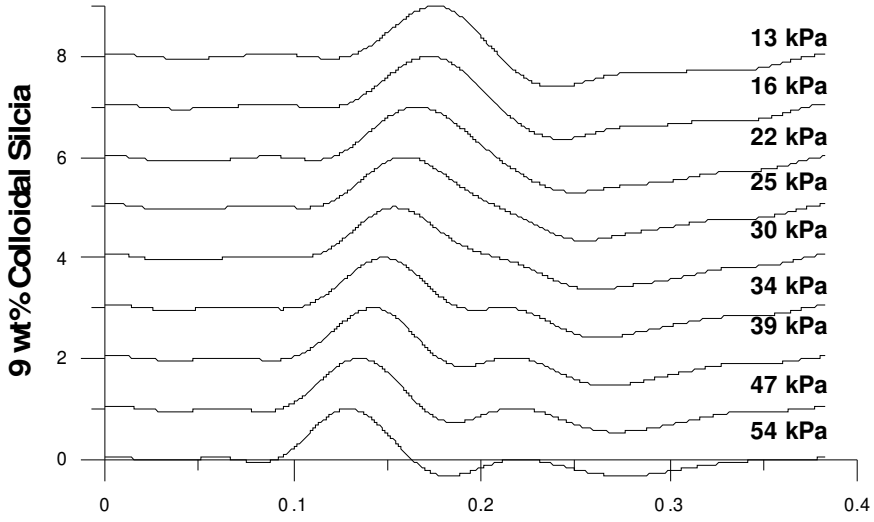

Figure 5.10 Normalized signals of vertical accelerometer array for 9% treated soil

The travel time, *t*, between two recorded signals in space can be determined from a cross correlation function. The cross correlation function will reach a maximum value when the time

shift, Δt, equals the travel time of the impulse between the two points (Arulnathan et al., 1998). The correlation function between 2 signals, *S1(t)* and *S2(t)*, is written as:

Equation 5-3

$$CC_{S1-S2}(\Delta t) = \lim_{T\to\infty} \frac{1}{T} \int_T S1(t+\Delta t) S2(t) dt$$

where T = the total time length of the signals, and τ = the time shift between the two signals. Arulnathan et al. (1998) recommends the correlation of the signal be performed in the frequency domain. To convert to frequency domain, a fast Fourier transform (FFT) was applied to each of the accelerometer signals by:

Equation 5-4

$$L_{S1}(f) = FFT(S1(t))$$
$$L_{S2}(f) = FFT(S2(t))$$

where $L_{S1}(f)$ and $L_{S2}(f)$ are the frequency domain representations of subsequent accelerometer recordings. The cross power spectrum $(G_{S1\text{-}S2}(f))$ of the input and output is then calculated as:

Equation 5-5

$$G_{S1=S2}(f) = L^*_{S1}(f) \cdot L_{S2}(f)$$

where L^*_{S1} is the complex conjugate of L_{S1}. The resulting cross correlation is then expressed as:

Equation 5-6

$$CC_{S1-S2}(\tau) = IFFT(G_{S1-S2}(f))$$

where *IFFT* is the inverse fast Fourier transform.

Cross correlations in the model were taken from signal T1 to T2, T2 to T3, T3 to T4, etc. This process is illustrated in Figure 5.11 . The incremental shear wave velocity at various depths along the profile were determined from Equation 5-2 where *t* represents cumulative travel times determined from the cross correlation (Δt_{cum}) and *L* represents the cumulative sensor elevations (Δz_{cum}) with respect to sensors T1 and U25.

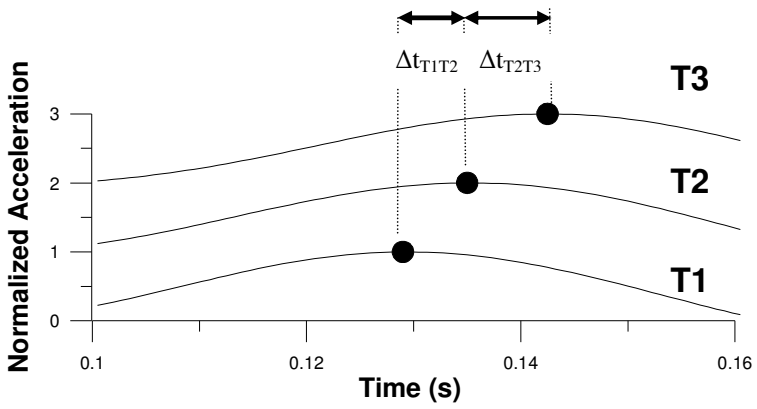

Figure 5.11 Travel time determination by cross correlation

It should be noted that the signals for sensors T9 and U31 were of poor quality and were therefore omitted from the analysis. It should also be noted that when initial liquefaction first occurred in the untreated soil (PBA = 0.1g) , it was assumed that the accelerometers had moved a substantial amount within the liquefiable layer and the elevations for shear wave velocity calculations for pulse waves 1 thru 4 were taken as the elevations of the sensors measured after the test. This is a reasonable assumption because water on the untreated side of the model was observed flowing out on the model surface and a substantial amount of surface settlement (0.075m [0.25ft]) and lateral spreading (0.2 m [0.65 ft]) was measured during this time.

5.5.2. Bender Element Testing for V_S Determination (CTC02)

In CTC02, bender elements were used to estimate the shear wave velocities of the grouted soils at various depths. Figure 5.12 shows that a source bender and receiver bender were placed approximately 100 mm [3.9 in] apart at four elevations for each side of the model. A total of nine bender tests were applied at various stages of the ground motion test sequence and are summarized in Table 5.2.

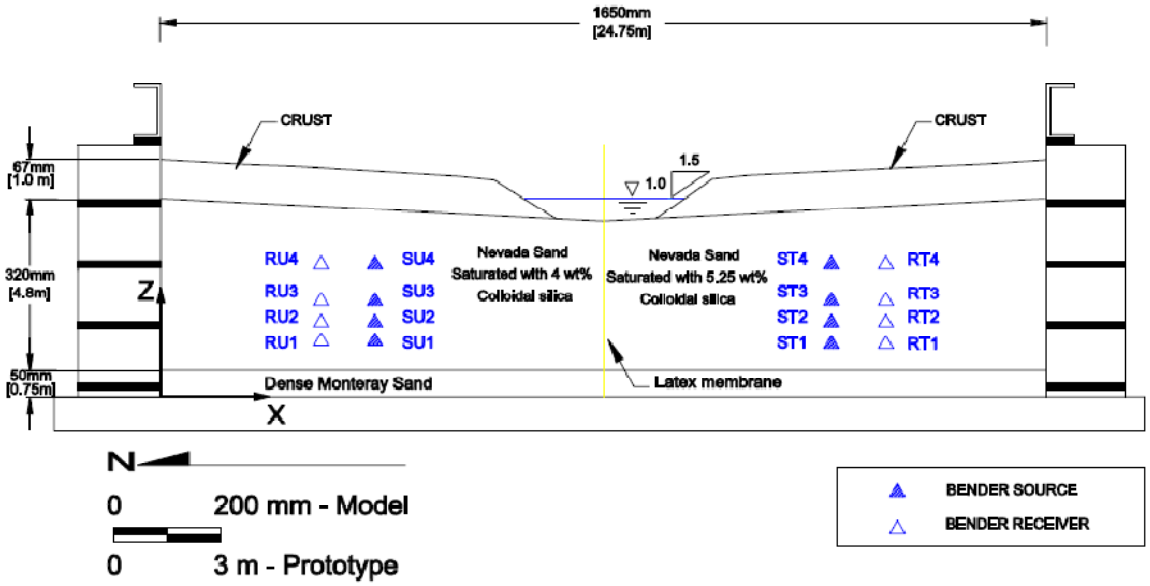

Figure 5.12 Sensor Layout for Bender Element Testing in CTC02

Table 5.2 Bender testing sequence (CTC02)

Bender Test #	After PBA (g)
0	initial
1	0.007
2	0.03
3	0.15
4	0.25
5	0.69
6	.25
8	0.89
9	1.3

Bender elements were first introduced into soil laboratory testing by Shirley and Hampton (1978) and were later verified for determination of shear modulus by Dyvik and Madshus (1985). Bender elements are piezoelectric transducers that transform electrical energy into mechanical energy and vice versa. By applying an electric potential to a source bender, the element will distort and induce a voltage potential across the receiving bender element to produce

a signal (Arulnathan et al., 1998). Bender elements have been extensively used in resonant column tests, triaxial tests, and odometer tests to measure shear wave velocity in laboratory specimens. On the other hand, bender element testing in centrifuge models poses unique challenges mainly due to the high-g environment, larger model size, and associated data handling during acquisition.

Most recently, Brandenberg et al. (2008) developed a test system to address some of the issues associated with centrifuge model tests. The system involves an innovative signal stacking technique to improve signal to noise ratio and incorporates signal processing software to handle high sampling frequencies required in high g environments. The signal stacking technique is based on 10 pulses sent out in quick succession which are then stacked from the receiving signals accordingly to improve signal-to-noise ratio (SNR). After these 10 pulses, it checks whether the SNR is satisfactory and if not, it sends another 10 pulses. When the SNR is satisfactory, the successive waves are stacked into a single signal. The data is transmitted and received using a data acquisition system. LabView (National Instruments, Austin, TX) is used to control the data acquisition system and process the acquired signals. Further details regarding the bender element software and hardware systems are discussed in Brandenberg et al. (2008).

The centrifuge test consisted of several bender element tests conducted at various stages of the shaking test sequence. Each bender test sent a square source wave set at an amplitude of 9 Volts and a sampling frequency of 90,000Hz. From Equation 5-2 , the distance between the two signals, *L*, was taken as the tip to tip distance from the source bender to the receiving bender and the travel time, *t*, is taken as the time of first arrival of the receiving signal (Brandenberg, 2008). The tip to tip distance between bender signals was carefully measured at the time of sensor placement prior to testing and after testing (Table 5.3).

The output data files generated for each bender test were truncated and normalized in order to adequately capture the signal itself and acquire more accurate travel times. Unlike data

handling for CTC01, it was not necessary to filter the raw data because the signals acquired through the bender software program included a built- in Bandpass Butterworth filter function.

Figure 5.13 shows the normalized wave amplitude versus time from Bender Test #1 (after PBA=.007g). As can be seen from the figure, bumps in the signal before the first arrival may occur as a result of near field effects which can result in an overestimation of shear wave velocities. For more accurate results, Brandenberg et al. (2008), defined travel time as the time corresponding to the zero wave amplitude before the first major peak. Following this definition, travel times were manually determined from the plotted signals by identifying the times associated with the first departure points. The results are summarized in Table 5.4 and Figure 5.13 plots the signals and identifies the first departure points for Bender Test #1.

Table 5.3 Measured tip-to-tip distance from source to receiving bender, L

Bender Depth, D (m)	*L* Before Test (m)		*L* After Test (m)	
	5.25%	4%	5.25%	4%
4.03	0.10	0.10	0.10	0.10
3.4	0.10	0.10	0.10	0.11
2.66	0.11	0.10	0.11	0.11
1.75	0.10	0.10	0.11	0.10

Table 5.4 Travel time determination from Bender element Tests

Bender Test #	After PBA (g)	*t* for 5.25% (msec)				*t* for 4% (msec)			
		D=4.03m	D=3.4m	D=2.66m	D=1.75m	D=4.03m	D=3.4m	D=2.66m	D=1.75m
0	N/A	0.52	0.53	0.59	0.62	0.62	0.64	0.70	0.77
1	0.007	0.54	0.55	0.62	0.66	0.60	0.64	0.69	0.77
2	0.03	0.55	0.56	0.64	0.68	0.55	0.65	0.70	0.77
3	0.145	0.59	0.64	0.74	0.81	0.64	0.70	0.80	0.88
4	0.25	0.60	0.68	0.78	0.85	0.62	0.68	0.80	0.90
5	0.69	0.72	0.81	0.92	1.04	0.75	0.77	0.87	0.99
6	0.25	0.62	0.71	0.81	0.92	0.61	0.66	0.75	0.84
7	0.89	0.61	0.67	0.75	0.87	0.61	0.65	0.69	0.78
8	1.36	0.77	0.86	0.98	1.20	0.77	0.82	0.90	0.98

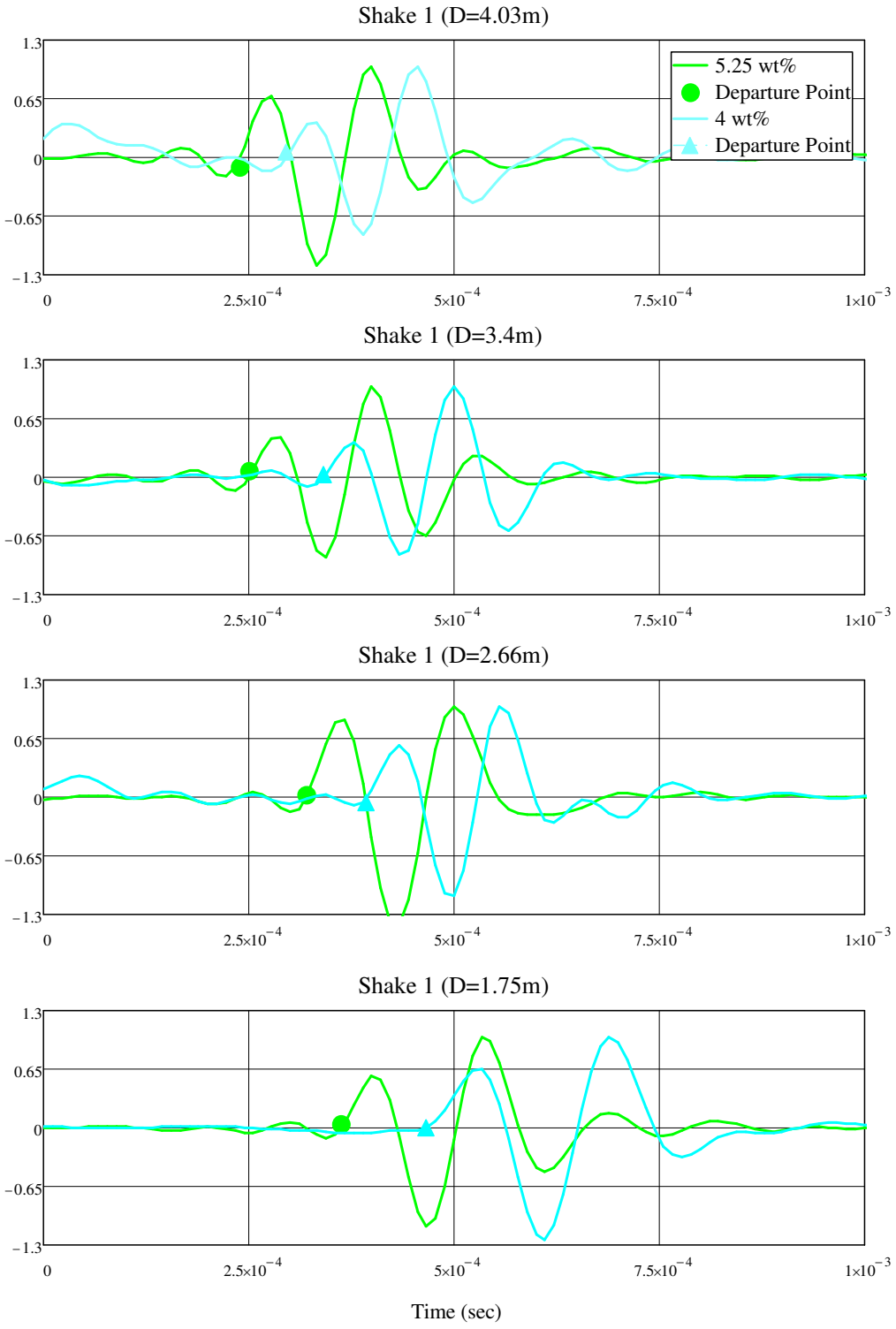

Figure 5.13 Travel time identification from receiving bender signals

5.5.3. Normalization of V_S

For liquefaction prediction methods (e.g. simplified procedure), correlations require the shear wave velocity to be normalized to a reference overburden stress, P_a,=100 kPa (14.5 psi). As described in Robertson (1997) the stress corrected shear wave velocities, V_{s1} was determined using the following equation

Equation 5-7
$$V_{S1} = V_s \frac{P_a^{0.25}}{\sigma_v'}$$

where P_a represents atmospheric pressure taken to be 100 kPa (14.5 psi) and σ_v' is the initial effective overburden stress. In each test, the effective stresses were calculated based on known soil properties, soil layer thicknesses, and pore pressure readings measured at similar depths. The static pore pressures were determined from the initial readings of pore pressure data recorded for the corresponding shakes. It should be noted that new values of initial effective stresses were calculated for each pulse test and bender test to account for changes in cyclic loading history.

5.6. Determination of Stress-Strain Profiles

Inverse analysis techniques are currently being used to define the dynamic stress-strain response of soils in the field and in physical models. Similarly, these methods can also be applied to centrifuge model tests using acceleraton records taken from various locations throughout the model. Following this technique, shear strains are determined by double integrating acceleration series data to obtain transient displacments and then differentiating those displacements in space. The stress-strain profiles were obtained from data recordings of vertical accelerometer arrays placed within the liquefiable soil layer (Figure 5.8).

The methods used for CTC01 and CTC02 were followed from a recent study by Kamai and Boulanger (2010) where the model geometry and sensor configuration was nearly identical. In this study, several inverse analysis techniques for defining the dynamic stress-strain response in liquefiable soils for centrifuge model tests were analyzed and compared. The methods for

computing the shear strains utilized a dense vertical array of acceleromaters placed within the soil profile. The analysis assumed 1D shear-beam response with upward propogation of shear waves. It should be noted that surface waves and reflected P-waves from the container boundaries were assumed to be negligable.

5.6.1. Instrument Spacing

As decribed by Kamai and Boulanger (2010), inverse analysis techniques perform accurately when the instrument spacing is less than about one eighth of the shortest wave length expressed in Equation 5-8.

Equation 5-8

$$\Delta Z_{max} = \frac{\lambda_{max}}{8} = \frac{V_S}{8 \cdot f_{max}}$$

Stress corrected shear wave velocities in both CTC01 and CTC02 ranged from about 180 m/s to 230 m/s for the smaller shaking events. As shaking amplitudes incresed, shear wave velocities decreased for both treated and untreated soil. At the time of shaking, the minimum stress corrected shear wave velocity for these larger shaking events was estimated to be 20 m/s (66 ft/s), which occurred during shake 5 of the shaking sequence. The dominant shaking frequency, f_{max} in bothe tests was 2 Hz. Following Equation 5-8, the maximum wavelength ranges from about 10 m (33 ft) to 115 m (377 ft). This is equated to a maximum sensor spacing of 14 m (46 ft) for the smaller shakes and 1.25 m (4.1 ft) for the larger shakes. The maximum senor spacing was measured at 1.2 m (3.9 ft) with an average sensor spacing of about 0.65 m (2.1 ft) prototype. Therefore, the vertical array of accelerometers was dtermined to be sufficiently dense enough to capture wave transmission accurately.

It should be noted that the sensors were measured during model preparation before shaking and during model excavation after shaking. After liquefaction occurred in the untreated soil in CTC01 (Shake 3) the sensors were assumed to have moved a significant amount. As a result, the sensor locaitons measured after shaking were used to define sensor depths for Shakes 4

thru 9. In CTC02, both sides of the model were grouted and there was minimal movement throghout the tests. For CTC02, only the senosr locations measured before testsing were used to define sensor depths.

5.6.2. Calculation of Shear Stress

Shear stresses were determined at the midpoints between accelerometers in the vertical arrays as illustrated in Figure 5.14. MathCad was used to process the data and compute the shear stresses from the acceleration records. The original shear beam equation below shows that the shear stress at any depth, *z*, is obtained by integration of the density, ρ, times the acceleration.

Equation 5-9 $$\tau(z) = \int_0^z \rho \cdot a \cdot dz$$

Unlike field data, surface accelerations cannot be directly measured in centrifuge models because the instruments require sufficient contact with the soil and must be buried within the model. As a result, rigid body motion in the centrifuge was assumed. This is a reasonable assumption because the distance from the surface to the first accelerometer was only about 0.8m. Based on rigid body motion, the acceleration from the surface to node 1 is considered constant and equivalent to the acceleration measured at node 1 (Figure 5.14). The equations used for calculation of shear stress are shown below in Equation 5-10 through Equation 5-12. Equation 5-10 and Equation 5-11 represent the shear stress in elements 1 and 2 (Figure 5.14) and express the rigid body motion assumption from the first element. The shear stresses of the remaining elements are expressed in Equation 5-12.

Equation 5-10 $$\tau_{e,1} = \rho \cdot \frac{z_1}{2} \cdot a_1$$

Equation 5-11 $$\tau_{e,2} = \tau_{e,1} + \rho \cdot \frac{z_1}{2} \cdot a_1 + \rho \cdot \frac{z_2 - z_1}{2} \cdot \left(\frac{3 \cdot a_1 + a_2}{4}\right)$$

Equation 5-12 $$\tau_{e,j} = \tau_{e,j-1} + \rho \cdot \frac{z_{i-1} - z_{i-2}}{2} \cdot \left(\frac{3 \cdot a_{i-1} + a_{i-2}}{4}\right) + \rho \cdot \frac{z_{i-1} - z_{i-1}}{2} \cdot \left(\frac{3 \cdot a_{i-1} + a_i}{4}\right)$$

In the above equations, ρ is the density of the soil, $\tau_{e,j}$ is the shear stress at element *j*, and z_i and a_i are the depth and acceleration at node *i*.

The shear stresses were then normalized by the initial effective overburden pressure at the beginning of each shake to establish the cyclic stress ratio. The CSR was determined as the ratio of shear stress at the midpoints of each element by the initial effective vertical stress at similar depth. The effective vertical stress was calculated based on unit weights of the sand and crust. In both tests, the unit weight of sand was about 19 kN/m^3 (121 pcf). The unit weights of the crust layer varied from 21.8 kN/m^3 (139 pcf) to 19.9 kN/m3 (126 pcf) for CTC01 and CTC02, respectively because of varying water contents. Pore pressures were based on sensor data recorded near the bottom of the container. It should be noted that since a different pore pressure response is observed for grouted and ungrouted soils, a different pore pressure transducer was used for each side of the model.

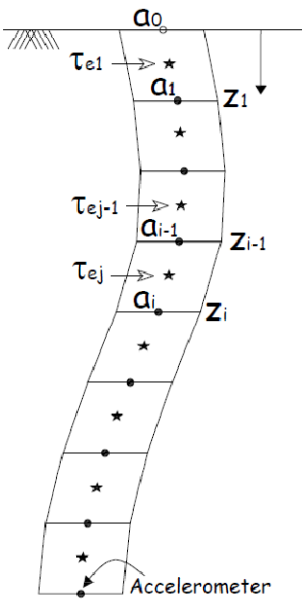

Figure 5.14 Schematic of 1-D shear-beam model for interpreting the vertical array data (Kamai and Boulanger, 2010)

5.6.3. Calculation of Shear Strains

Shear strains are obtained by first calculuating transient displacments through double integration of the acceleration records. Then, the transient diplacmenets are differentiated in space to obtain shear strains. When double integrating acceleration records, errors due to noise and baseline shifts can be extremely senstivie to the transient displacements obtained. Accurate displacments therefore require filtering of the acceleration records. The purpose of filtering is to correct for undesirable frequencies contained in the record such as those caused by external noise and ambient vibrations.

When applying filters to acceleration series data, unwanted errors may occur because of non-zero readings measured outside of the shaking record. Non-zero readings will occur because of factors such as external noise and ambient vibrations created from the spinning centrifuge. To minimize this effect, it is reccommended to leave the extraneous data points present in the record and force them to equal zero while there is no shaking (Brennan, 2005). This method is commonly referred to as zero padding and was applied to each of the acceleration records. A seventh order bandpass Butterworth filter was applied to the data. The function for the bandpass filter applied is expressed as:

Equation 5-13

$$H_u^{Bandpass} = \frac{1}{\sqrt{1+\left(\frac{f_{c1}}{f}\right)^{2\cdot n_1}}} \cdot \left(1 - \frac{1}{\sqrt{1+\left(\frac{f_{c22}}{f}\right)^{2\cdot n_2}}}\right)$$

where
f_{c1} =high pass corner frequency
n_1 = high pass filter order
f_{c2} = low pass corner frequency
n_2 = low pass filter order
f = frequency vector

A Fast Fourier Transform function was applied to the acceleration records in order to convert data from the time domain to the frequency domain. The Fourier amplitude spectrum for

one of the ground motion records is illustrated in Figure 5.15. By plotting the acceleration records in the frequency domain, the natural frequency in Figure 5.15 can be clearly idenfiied as 2 Hz, which was the frequency of the applied shaking motions. The Fourier spectrum was also used to select the cutoff frequency parameters from Equation 5-13. The cutoff frequencies represent the minimum and maximum frequencies in which the data is judged to be reliable in terms of signal-to-noise ratio. From analysis of Figure 5.15, the corner frequencies for the low-pass and high-pass filter were selected to be 1 and 10 Hz respectively for both CTC01 and CTC02.

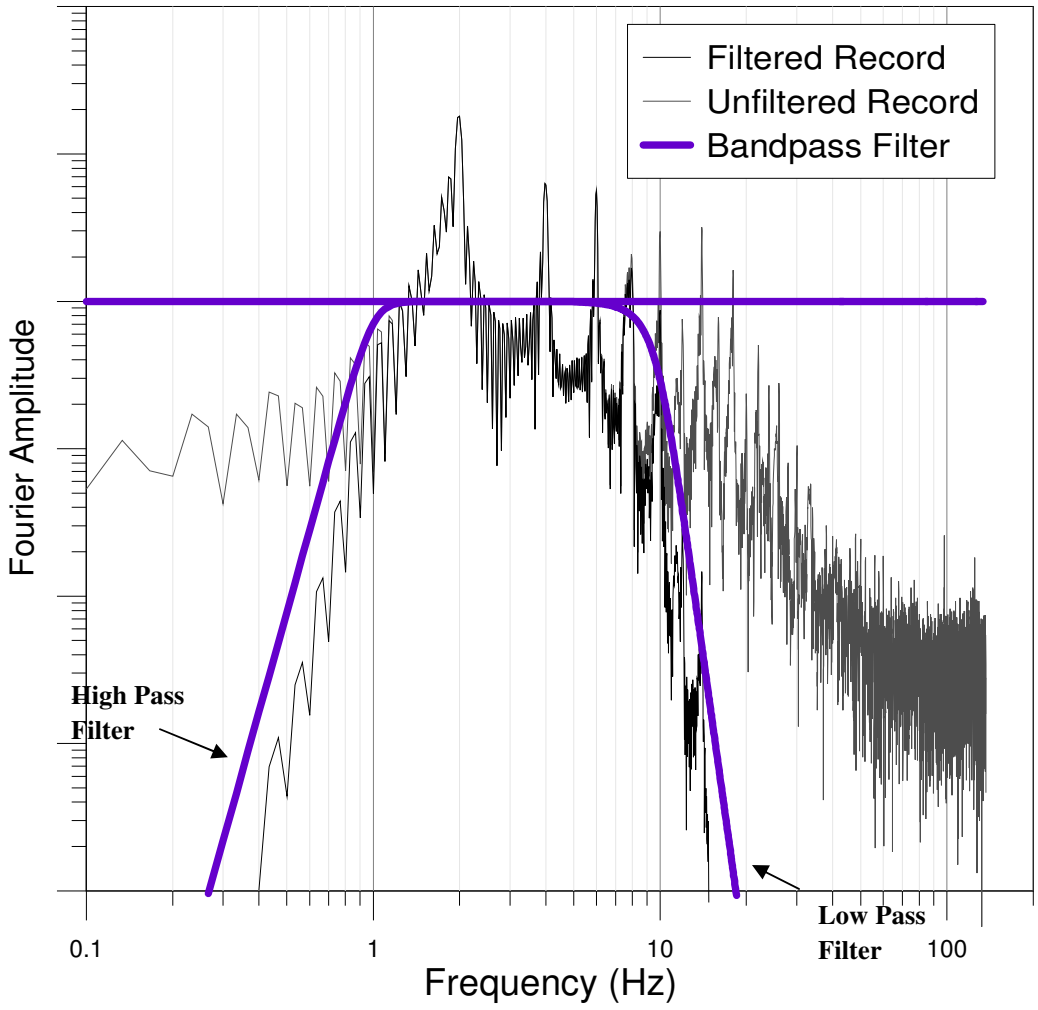

Figure 5.15 Fourier Spectrum of Acceleration Record (CTC01_04 at D=3.3m)

The filtered records were obtained by multiplying the filter function (Equation 5-13) by the Fourier transform of each of the acceleration records. Next, transient displacements were determined by double integration of the filtered acceleration records. It should be noted that at larger shaking amplitudes, the effects of data processing methods such as zero padding and filtering are not always discernable in the acceleration record. However, the errors become increasingly significant when integration methods are used to obtain velocity and displacement records, respectively. This concept is illustrated in Figure 5.16. Figure 5.16a shows the acceleration record for a PBA=0.2g before and after the applied filter. In this case, differences of the two records are almost indistinguishable. However, the effects can easily be seen in the displacement record from Figure 5.16b where erroneous displacements are obtained when filtering and zero pads are not applied.

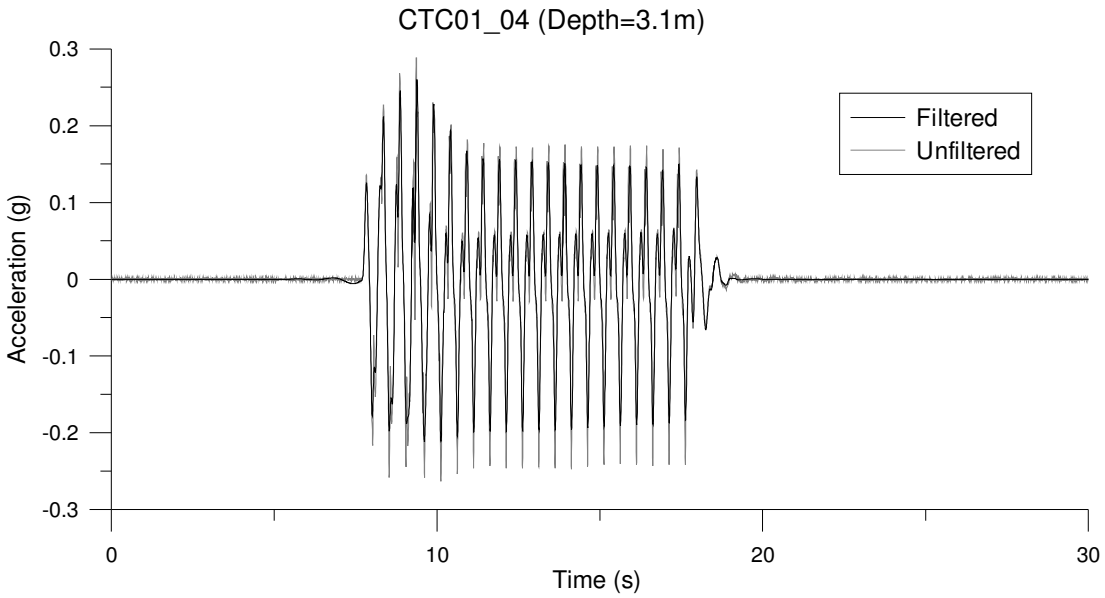

(a)

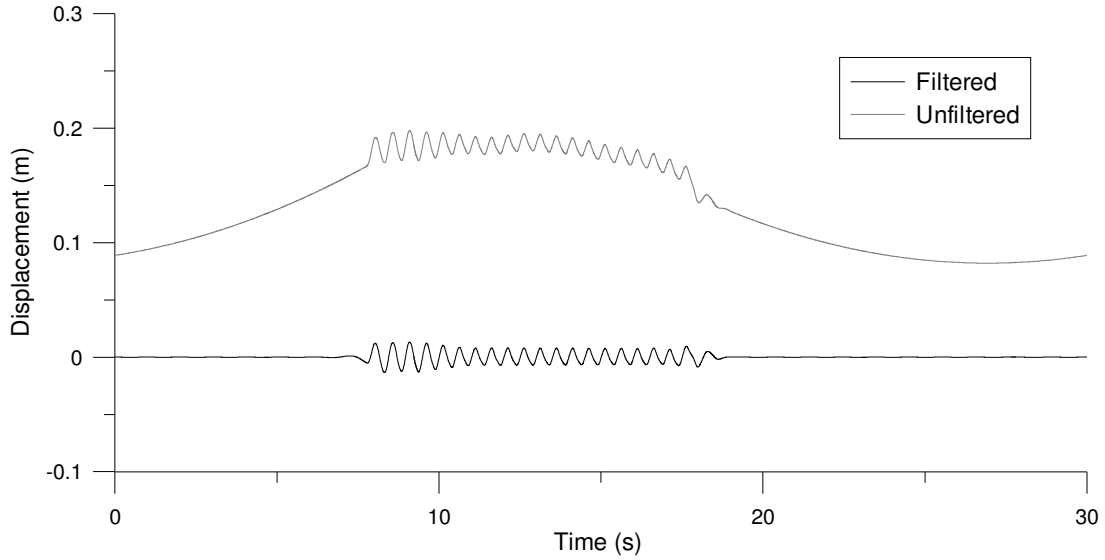

(b)

Figure 5.16 Filtered and Unfiltered (a) Acceleration and (b) Displacement Records

Shear strains were calculated by taking the derivative of the transient soil displacements with depth. As previously mentioned, Kamai and Boulanger (2010) compare and anlayzed several techniques for computing the derivative of transient displacements to obtain strain for a

dense, vertical acceleromater array. The methods analyzed included (1) weighted residual, (2) cubic spline (3) cosine series (4) polynomial, and (5) piece-wise. Results showed that both weighted residual and cubic spline performed equally well and produced consistent shear strain profiles representative of the general behavior of liquefiable soils. The other methods studied did not prove to be as effective and generally produced erratic shear strains throughout the soil profiles. It should be noted that one of the distinguishing feature of the weighted residual method from the other methods mentioned is that it is a direct differentiation approach whereas the other methods utilize an interpolation function to describe the distribution of displacements between 2 discrete points.

Following Kamai and Boulanger (2009), the shear strains at each of the sensor locations were determined through differentiation following the weighted residual method and the shear strains at the midpoints between sensors was determined by linear interpolation.

CHAPTER 6: SHEAR MODULUS AND STRESS-STRAIN RESPONSE - RESULTS AND DISCUSSION

6.1. Considerations

Prior to discussion of results presented in this study, several issues and limitations must first be addressed. It is important to note that due to failure of the bender elements in CTC01, there are drastic differences in the methods used to obtain shear wave velocities. As a result, CTC01 and CTC02 cannot be quantitatively compared. The most significant difference between the two approaches is probably the shear strains that were induced for each test method. For example, bender element tests typically induce strains lower than $3*10^{-4}$% while the shear strains induced for the pulse wave were determined to range between .005% up to .02%. The difference in shear modulus between such strain levels in CS soils can vary by about 30% (Spencer, 2008). As a result, pulse wave testing is not an accurate way to establish the maximum shear modulus.

Additionally, the shear wave velocity determined from the pulsewave is taken from a discreet signal compared to bender elements which are obtained from a continuous signal. The sampling rate to monitor travel times of the pulsewave is therfore significantly less than the bender element tests (90,000 Hz vs. 20,000 Hz). While zero padding and filtering techniques can improve the quality of the data, the weaker resolution can still lead to inaccuracies in travel times.

Pulsewave test data proves to be a sufficient method for obtaining approximations of shear wave velocities for a given shear strain. Bender element tests data, on the other hand, can provide a more reliable measurement of shear wave velocity at small strains and can therefore be used to establish the maximum shear modulus. Although results from CTC01 and CTC02 cannot be quantitatively compared, the overall trends and affects in V_S due to cyclic prestraining can be established.

Another issue to be addressed is the overall quality of data obtained in CTC02 for the 4% CS soil. Initially, the purpose for grouting with a low 4% CS solution in CTC02 was to establish

a limiting concentration that would provide adequate strength and stiffness and the behavior of a lower gel state could also be studied. The 4% CS represented a "weak" gel in which a fully resonated gel state was never attained. Based upon shear wave velocity data and stress-strain profiles, trends in behavior for 4% CS treatment could not be established. The overall dynamic response for this "weak" gel was erratic and became especially apparent in the stress-strain profiles. Based on analysis of shear wave velocity and stress strain data, it was reasonable to conclude that despite good grout coverage, a poorly gelled grout produces poorly defined soil characteristics. The results discussed will therefore focus on behavioral trends observed for the 9% CS, 5.25%CS, and untreated soils.

6.2. Shear Wave Velocity Results

The normalized shear wave velocity and shear modulus for CTC01 and CTC02 are summarized in Table 6.1 and Table 6.2, respectively. Figure 6.1 plots the normalized shear wave velocity at various depths after various shaking amplitudes. With the exception of the 4% CS soil, the initial shear wave velocities prior to shaking were similar for both the CS sands and untreated sand and averaged between 214m/s to 228 m/s (702 ft//s to 748 ft/s). The behavior is consistent with results obtained from Tsukamoto (2006) in which bender element tests were conducted for soils treated with silicate-based grouts and compared to an untreated sand. In this study, V_S values for D_r=40% were shown to produce shear wave velocities of 220 m/s (722 ft/s) and 216 m/s (709 ft/s) for the grouted and ungrouted sand, respectively. The initial shear wave velocity for the 4% CS soil are significantly less than the other soil types. This discrepancy may be attributed to the fact that the 4% concentration represents a "weak" gel that never establishes a resonated state.

Similar to the untreated sands, CS sands lose stiffness as it loses effective stress and thus, the shear modulus of the sand is reduced as pore pressures accumulate. As previously discussed,

pore gel pressures do not dissipated until long after shaking and dissipation is further limited with increases in applied peak horizontal accelerations. Since V_S measurements were taken immediately after each shaking event, pore pressures likely remained elevated at the time of testing, thus contributing to reductions in shear wave velocity. On the other hand, reductions in V_S (and G) would be less in CS soils versus untreated sands for the same reduction in effective stress. This is because the gel alone has its own stiffness which has been reported to have an average maximum shear modulus of 15 kPa (Forero-Duenas, 1998). Although the stiffness of the gel alone is substantially less than the stiffness of sands alone, the post-shaking stiffness is essentially a composite stiffness of the sand (with its reduced effective stress) and the gel. As the applied input motions increase in amplitude, shear wave velocity subsequently decreases for all soil types; however, the reductions in V_S values for grouted soils are less pronounced.

It is interesting to note the increase in V_{S1} during Bender Test #6 when the applied base shake acceleration is reduced back down to 0.25g as in Bender Test #4. The values of V_{S1} for Bender Test #4 and Bender Test #6 are nearly the same ($V_{S1} \simeq 190$ m/s and 191m/s). Additionally, the measured shear strains induced for both shaking events when PBA=0.25g were similar and found to be 0.02% and 0.03%, respectively despite shear strains of of 2.5% developed between Bender test #4 and #6 when the model was subjected to a peak horizontal base acceleration of 0.69g. Results show that the CS soil retained its memory from prior cyclic strain levels in previous shaking events. This was also observed for the 9% CS sand in CTC01 when the peak base horizontal acceleration of 0.2g was applied during shakes 4 and 7 of the testing sequence with a stronger base shaking of 0.56g (shake5) applied between events. The average shear strain developed in the 9% CS was measured to be 0.53% and 0.54% respectively for shake 4 and 7, respectively, despite the fact that the 9% CS had developed larger strains of about 1.2% during shake 5 of the test sequence. The untreated soil in CTC01, on the other hand, did not retain its

memory from prior cyclic strain levels in previous shaking events and developed different shear strains of 1.5% and 1.1% for shakes 4 and 7, respectively.

Table 6.1 Shear Wave Velocity Summary from Pulsewave Tests (CTC01)

PULSEWAVE	After PBA Shake (g)	V_{s1} (m/s)		G (MPa)	
		9%	Untreated	9%	Untreated
#0	initial	220	214	94	89
#1	0.1	217	196	92	74
#2	0.19	178	164	61	52
#3	0.56	170	146	56	41
#4	1.28	133	183	35	65

Table 6.2 Shear Wave Velocity Summary from Bender Element Tests (CTC02)

Bender Test #	After PBA Shake (g)	$V_{S1,avg}$(m/s)		G_{max}(MPa)	
		5.25%	4%	5.25%	4%
0	0	228	188	101	68
1	0.007	220	190	94	70
2	0.03	216	192	90	72
3	0.145	199	175	77	59
4	0.25	190	186	70	67
5	0.69	165	163	53	51
6	0.25	191	194	71	73
8	1.36	153	160	45	50

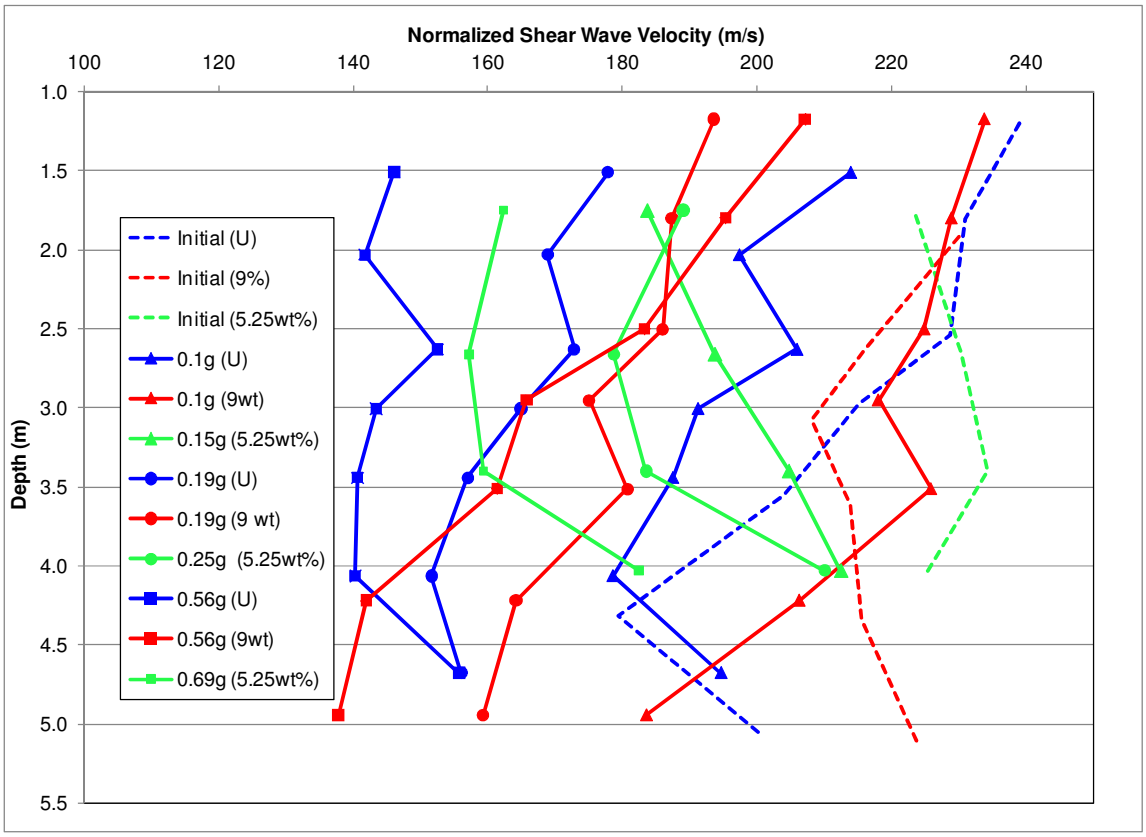

Figure 6.1 Shear Wave Velocity vs. Depth

Additionally, Figure 6.2 presents the variation of shear modulus for various cyclic shear strains developed throughout the test sequence. The cyclic shear strain from Figure 6.2 represents the maximum cyclic shear strain developed during the shaking event prior to V_S measurements. Although the shear strains developed in the grouted soils are reduced at similar PGA events, the trends are the same as untreated soils for shear strains up to 4%.

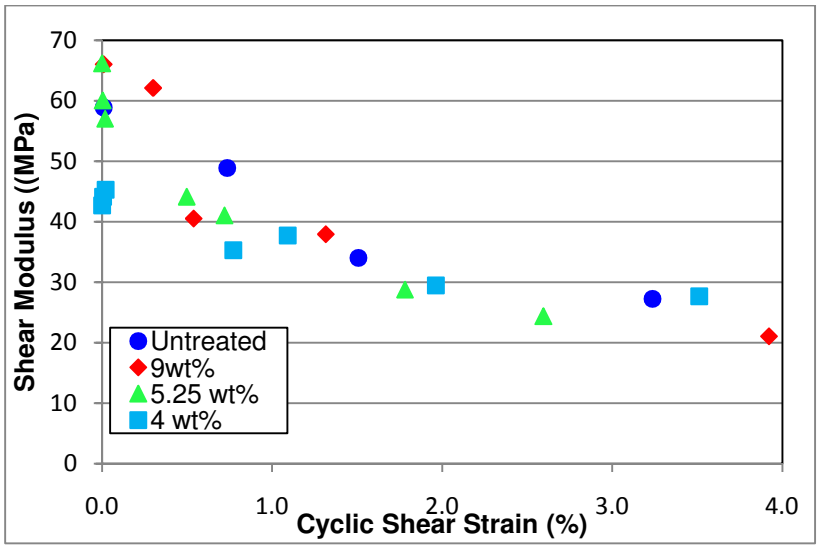

Figure 6.2 Shear Modulus vs. Cyclic Shear Strain

Overall, initial shear wave velocity does not show dramatic increases in colloidal silica soils versus untreated soils. This suggests that shear wave velocity is not an effective parameter to assess ground improvement even though CS treatment results in greater soil strengths. With applied dynamic loading, increases in pore pressures are generated for both untreated and treated soils. As the pore pressures increase, effective stresses are reduced and in untreated soils, this results in reductions in stiffness that is reflected in shear wave velocity measurements. For the colloidal silica soils, increases in pore pressure are believed to indicate that normal stresses are being transferred to the gel. The reduction in stiffness are therefore less pronounced for the colloidal silica soils since the gel provides its own shear resistance and can hold soil particles together. It should be noted that average values of maximum shear modulus for the gels alone have been reported to be about 15 kPa (2.2 psi) (Forero-Duenas, C.A., 1998).

The corrected shear wave velocity was plotted on the curves developed by Andrus and Stokoe (2000) for liquefaction prediction. For each subsequent shaking event, shear wave velocities were measured and the maximum cyclic resistance ratio was determined for the corresponding shake. Results were plotted against curves developed for liquefaction prediction

from the simplified procedure. Figure 6.3 plots the data in which liquefaction occurred (r_u values of 1.0 were achieved) and where liquefaction did not occur. For cyclic resistance ratios of about 0.3, liquefaction was incorrectly predicted in the 9% and 5.25% CS soils. Additionally, for a cyclic resistance ratio of 1.2, liquefaction was incorrectly predicted in the 9% CS soils. Although shear wave velocities decrease in these treated soils at high shaking levels, they maintain high cyclic resistance ratios. Therefore, correlations between the two parameters do not necessarily reflect the mechanical behavior and treatment mechanism inherent of colloidal silica soils.

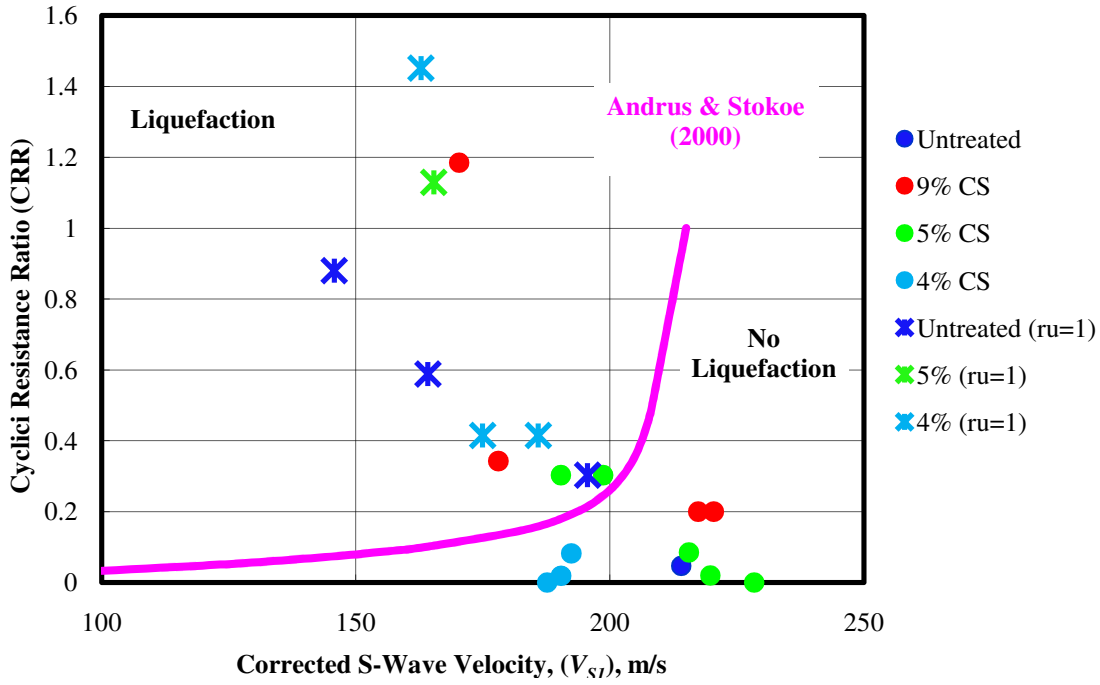

Figure 6.3 Liquefaction Prediction using the simplified procedure

6.3. Stress Strain Results

The stress-strain responses for different depths throughout the soil profile were determined for various shaking events. The results are presented to show the behavior for (1) small base shaking amplitude when excess pore pressure ratios are low (2) medium base shaking

amplitude when r_U=100% occurs in the untreated soil and (3) large base shaking amplitude when r_U=100% occurs in the untreated soil and grouted soil. Again, it should be noted that the sand treated with 4% CS yielded erratic stress strain behavior and is omitted from the analysis. As previously mentioned, the erratic behavior is most likely attributed to poor grout quality due to the fact that the CS did not become a fully resonated gel.

In the beginning of the test sequence, sinusoidal motion with a peak base acceleration of .03g was applied to both models. During this event, the pore pressure response, previously discussed, shows that very small increases in excess pore pressure ratio occurred for the treated and untreated soils (refer to Figure 4.9). The stress-strain response illustrated in Figure 6.4 also revealed similar behavior between grouted and ungrouted soils. For a CSR of approximately 0.1, shear strains of about .025% were achieved for each of the soil profiles. While the cyclic shear stresses are low, the strains that develop are elastic and the soil exhibits no tendency for volume change and therefore, no excess porewater pressures occur under undrained conditions. The shear strain magnitudes presented are consistent with liminting shear strains on the order of .01% that exhists for liquefiabels soils below which no porewater pressures will develop (Drnevich and Richart, 1970; Dobry and Ladd, 1980; Dobry et al. 1982).

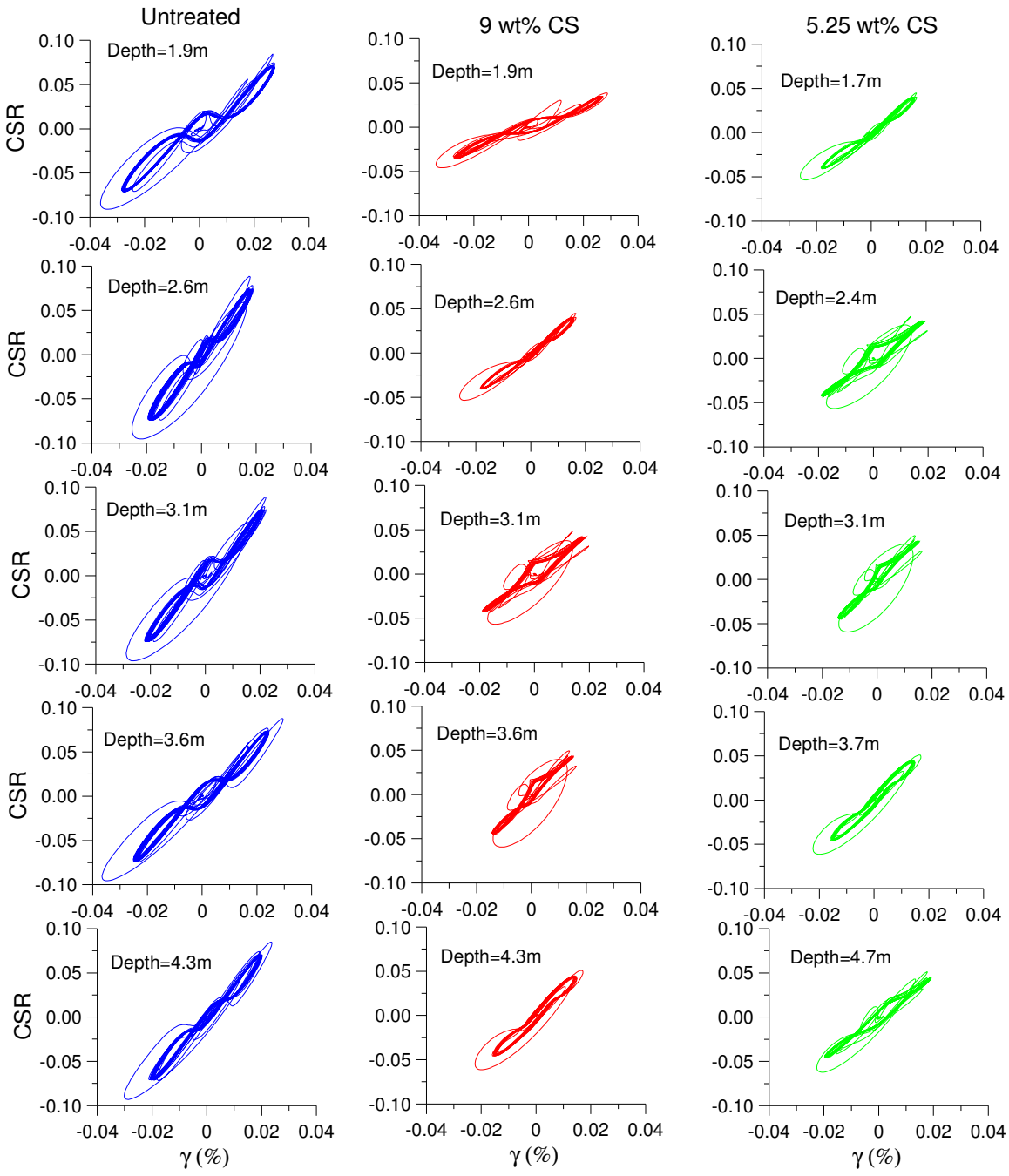

Figure 6.4 CSR vs. Shear Strain for Shake 2 (PBA=.03g)

According to the historical definition of liquefaction when excess pore pressures of 100% develop, initial liquefaction occurred during shake 3 in the untreated soil when a peak base acceleration of 0.1g was applied to the model. Based on the response from Figure 4.10, r_U=1.0

first occurred during the 4th shaking cycle in the untreated soil layer and remained below 0.8 for the 9% CS and 5.25% CS soils. The stress strain response for the untreated soil, 9% CS and 5.25 % CS soils for shake 3 is presented in Figure 6.5. Figure 6.5 also includes stress strain profiles at specific cycles in the shaking sequence to capture the behavior (1) before the onset of liquefaction, (2) shortly after the onset of liquefaction in the untreated sand, and (3) at the end of the shaking event. Prior to the onset of liquefaction in cycle 2, there is generally an elastic response for the untreated soil and strains remain at approximately 0.5%. A similar elastic response is observed for the grouted soils during cycle 2 with reduced shear strains compared with untreated sand ($\gamma \simeq 0.2\%$). As the excess pore pressure approaches 100% in the untreated soil, the shear strain amplitudes develop rapidly up to 1.3% during cycle 5 for a CSR of 0.4. In this case the behavior of the untreated soil is plastic, which is marked by the large shear strains accompanied by decreases in CSR. During this point in the loading sequence, zero effective stress is achived and the soil reaches the failure envelope at which point the sand very briefly undergoes cyclic mobility accompanied by minor transient drops in excess pore pressure ratio. Compared with untreated sands, CS soils at this point in the shaking sequence show reductions in shear strains directly related to CS concentrations. For example, at the midpoint of the liquefiable soil layer (D=3.1m), the shear strain from cycle 2 to cycle 5 increase by 0.1% and 0.3% for the 9% CS and the 5.25% CS soil, respectively.

Towards the end of the shaking event (cycle 19), differences in behavior between the grouted and ungrouted soils are more pronounced. Figure 6.5 shows significant loss in stiffness in the untreated soil indicated by the dramatic difference in the stress-strain path between cycle 2 and cycle 19. The unusual stress strain path during cycle 19 is primarily attributed to further soil softening by additional loading cycles applied to the liquefied soils, thus precluding transmission of motions along the profile. Another contributing factor to the unusual stress-strain path observed from cycles 5 and 19 may be due to movement of the sensors in the loose sand layer as

it liquefies and experiences large deformations. The 9% CS soil, on the other hand, shows that the response during cycle 19 is nearly identical to that from cycle 5 with. The characteristic response for the 9% CS sand shows that for a CSR of about 0.2, a maximum shear strain is reached ($\simeq$0.3%) early in the shaking sequence at which point there is a negligible affect with increasing loading cycles. For a CSR of 0.25, the 5.25% CS soil, on the other hand, experiences continuously incremental increases in shear strain with further loading cycles. For example, at the midpoint of the layer (D=3.1m), shear stains in the 5.25% CS soil increases from about 0.2% to 0.65% from cycles 2 to 19.

Overall, the shaking amplitudes during this event were large enough to cause excess pore pressure ratios to reach 100% in the untreated soils but were prevented for both the 9% and 5.25% CS concentrations. The maximum CSRs and shear strains developed were both reduced for the CS treated sands and reductions correlated well with treatment levels. For example, the average of maximum CSRs determined along the profile was 0.3, 0.25, and 0.2 for the untreated sand, 5.25% CS, and 9% CS sands respectively. Similarly, average values of maximum shear strains developed along the profile were determined to be 0.7%, 0.4%, and 0.3% for the untreated sand, 5.25% CS, and 9% CS sands, respectively. Another characteristic response revealed in Figure # for CS sands is the significan amount of damping despite the limiting development of shear strains for increasing cycles. The overall behavior agrees with observations from Kodaka (2005) previously discussed.

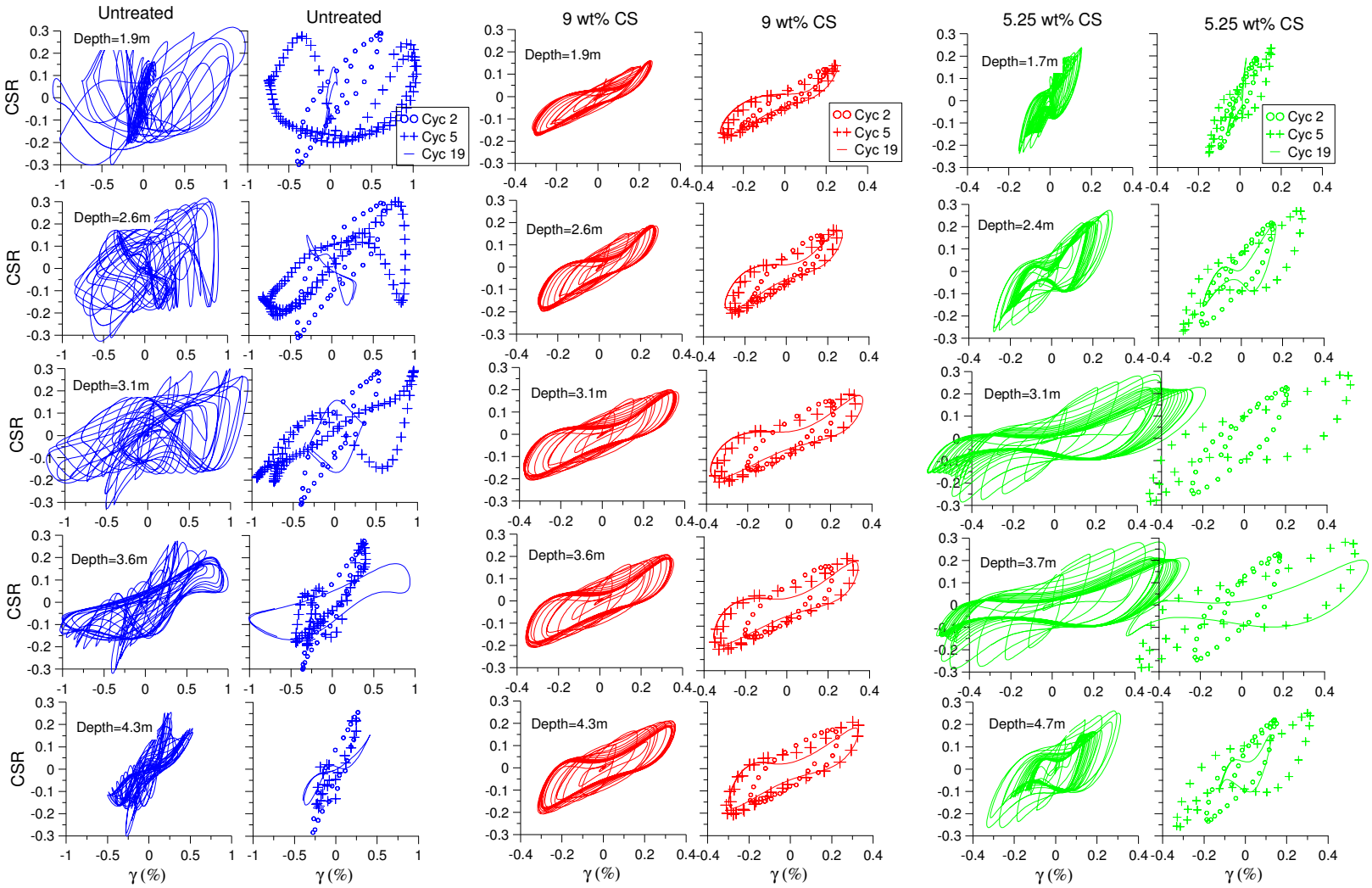

Figure 6.5 CSR vs. Shear Strain for Shake 3 (PBA=0.1g to 0.15g)

The last shaking event to be discussed represents the largest shaking event of 0.56g and 0.69g applied to CTC01 and CTC02, respectively (shake 5). During this event, excess pore pressure ratios of 1.0 are clearly achieved in the untreated soil and 5.25% CS soil (Figure 6.6). Pore pressure ratio of 1.0 in the untreated sand quickly occurred in the first cycle of shaking while the 5.25% CS soils developed r_U=1 as early as cycle 2 of the sequence. In general, the majority of excess pore pressure ratios developed in the 9% CS soil did not exceed 0.8.

The stress strain behavior for the event is presented in Figure 6.7. The single cycles shown in the figure capture the response during liquefaction for the untreated sand and 5.25% CS sand (cycle 2), shortly after liquefaction (cycle 5), and at the end of shaking (cycle 19). As can be seen from Figure 6.7, the untreated soils experience very large strains at the beginning of the shake sequence when liquefaction was initiated. Again, the flattened response is expected for liquefiable soils that essentially have zero stiffness and with increasing loading cycles, there is no response in the stress-strain behavior. The lack of response is primarily due to further soil softening that prevents motion to be transmitted through the profile.

Behavior of the grouted soils shows that shear strains quickly develop in the early stages of cyclic loading and are directly related to CS concentration . For example, during cycle 2 of the sequence at a depth of 3.1m, shear strains of 1.5% and 2.5% are developed for the 9% CS and 5.25% CS concentrations, respectively. Beyond these strain amplitudes, the stress-strain response of CS treatment is unaffected by additional loading cycles. Although r_U values in the grouted soils reach 1.0, the response of the grouted soils show that strength and stiffness have been maintained. The maximum shear strains developed for the 9% CS is clearly identified at about 1.5% while the 5.25% CS soils develop shear strains up to about 2.5%.

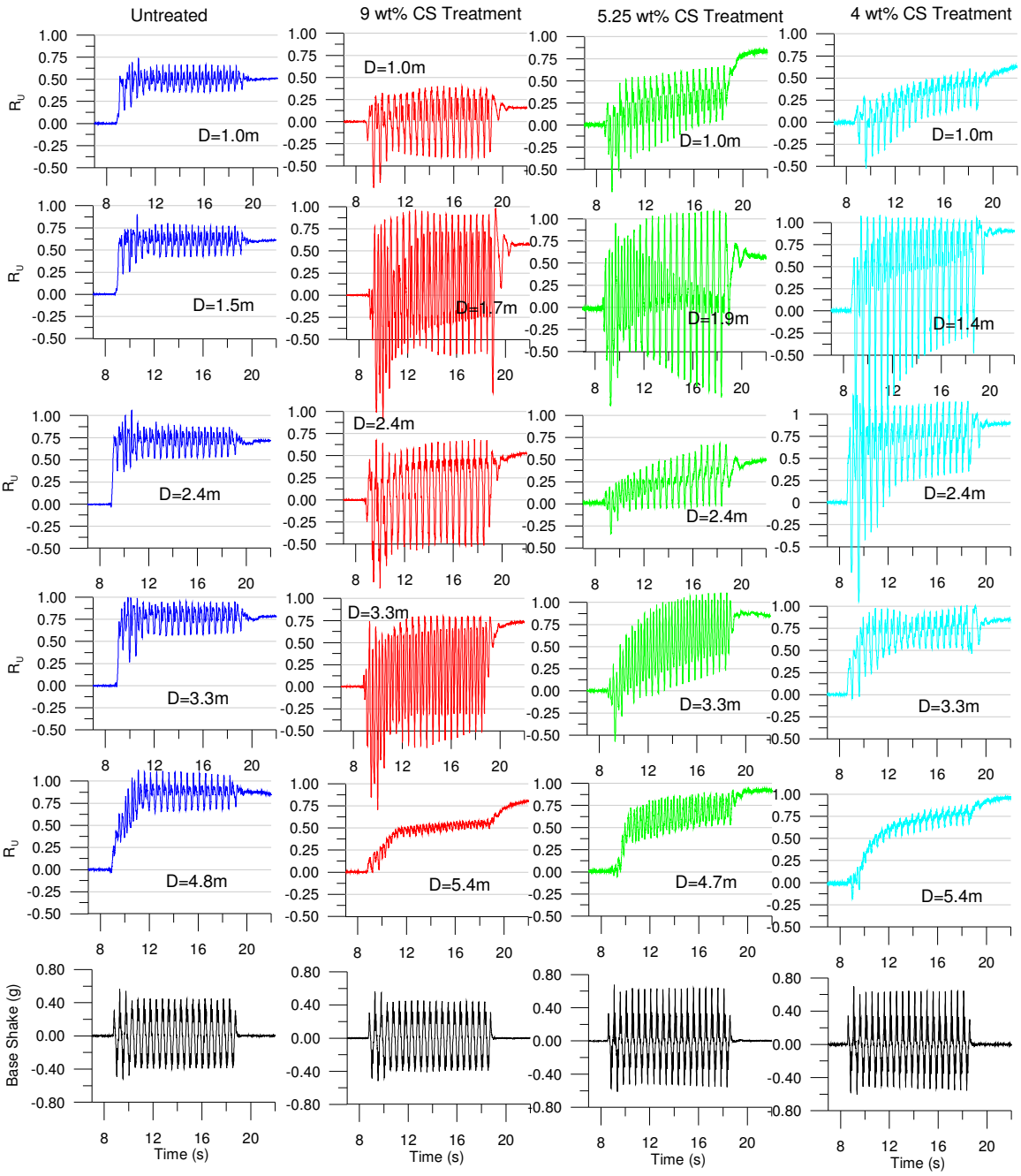

Figure 6.6 Excess Pore Pressure Ratio for Shake 5 (PBA=0.56g to 0.69g)

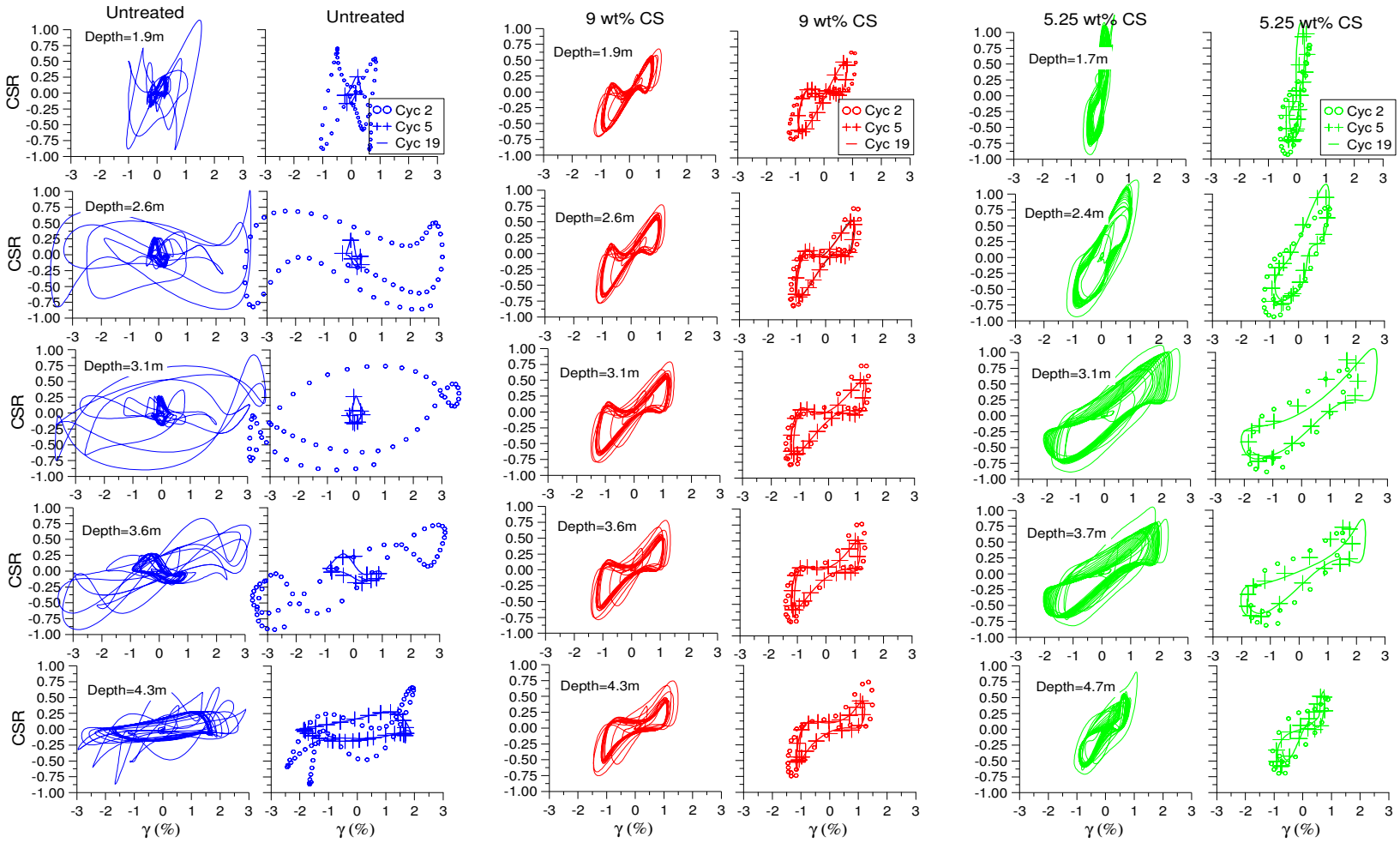

Figure 6.7 CSR vs. Shear Strain for Shake 5 (PBA=0.56g to 0.69g)

127

6.4. Stress History

In CTC01 and CTC02, the models were subjected to a stepdown shaking sequence in which lower shaking amplitudes were applied in between high shaking amplitudes. For example, a PBA=0.19g was applied before and after a larger shaking amplitude of 0.56g. The stepdown shaking sequence for CTC01 and CTC02 is summarized below in Table 6.3. The purpose of the step-down amplitude was to observe permanent changes in stiffness and deformations in the grouted soils versus the ungrouted soil and identify stress history effects. Figure 6.8 shows the average shear strain amplitudes developed for the applied peak base accelerations. As can be seen from the figure, there is clearly an overall reduction in shear strains directly for the CS sands. Differences in shear strains for similar shaking events are reduced from 0.4% in the untreated soil to only 0.01% in the 9% CS soil for the same applied shaking amplitude of 0.19g. Differences in shear strain fort the 5.25% is only about 0.06% for the same applied shaking amplitude of 0.25g. The minimal difference in shear strains induced for similar applied shaking events between larger shaking events suggest that CS soils experience minimal permanent changes in soil stiffness unlike untreated sands . Additionally, CS soils retain their memory from previously applied events.

Table 6.3 Shaking sequence for step-down motions

PBA	
CTC01	**CTC02**
0.19	0.25
0.56	0.69
0.03	0.03
0.19	0.25

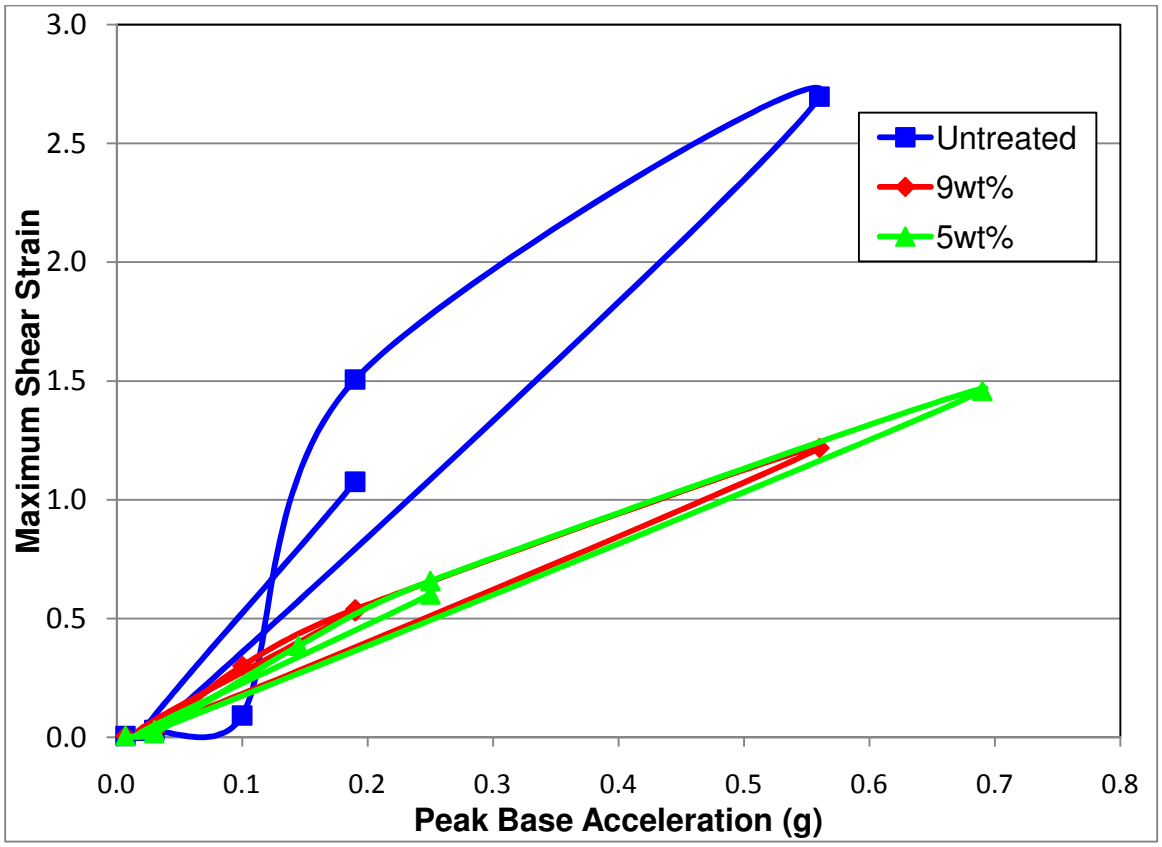

Figure 6.8 Permanent Reductions of Shear Strain from Step-down shaking

6.5. Test Limitations

6.5.1. Shear Wave Velocity

As ground displacements increase, the potential error in V_S becomes fairly large and even larger with shear modulus. Relative to bender element testing, pulse wave testing is a fairly crude technique for measuring shear wave velocity and can therefore only be interpreted as a rough approximation. Unfortunately, there are too many differences in the application of methods between the pulse wave test and the bender element tests for the two techniques to be quantitatively compared. The pulsewave method applied a base acceleration of .025g, which produced initial shear strains that were measured to range between 0.005% up to 0.02%. Bender test, on the other hand induce much lower shear strains of about $3*10^{-4}$%. As shown by Spencer (2008), difference in shear modulus by about 30% can occur at these different strain levels. Another source of error in this method may be attributed to the fact that data is taken from a discreet signal resulting in the sampling rate being reduced from 90,000 Hz (from bender element tests) to only 20,000 Hz. The weaker resolution could have resulted in misreadings of travel times.

From bender element tests, travel time determination has a profound effect on the measured shear wave velocity. Travel times in CTC02 were selected based on definitions proposed by Lee and Santamarina (2005) and Brandenberg (2008). It should be noted, however, that definitions of travel time remains a controversial issue and several definitions have been used. The definitions depend on installation, application , and input signal. Direct methods, such as cross correlation, have also been explored for travel time determination. However, such methods must accommodate for several frequency response functions (e.g. electronic, soil response from bender source, and soil response from bender receiver) which are not always feasible.

Furthermore, bender elements produce waves in both transverse and in-plane directions. Errors in travel times can be caused by the difficulty in identifying departure points. As can be seen from Figure 5.13, bumps in the signal may occur prior to the arriving shear wave as a result of interfering P-waves that reflect from the model container. This potential source of error was minimized by placing the bender elements as far away from the container boundaries as possible.

As mentioned earlier, phase lag also occurs in the bender tests due to dynamic interaction between the soil and benders. Due to the fact that the soil and bender elements themselves have different natural frequencies, phase distortions result as the source bender responds dynamically to the soil to produce an elastic wave and then again as the elastic wave in the soil responds dynamically to the receiving bender to generate an output. The phase distortions result in longer travel times and an underestimation of shear wave velocity. Phase lag was minimized in the centrifuge test by placing the source and receiver benders far enough away from each other. Additional errors may have also occurred as a result of undetectable movements of the benders in the soil during applied shakes. A slight rotation or movement of the bender elements could result in erroneous travel times produced by skewed source waves being sent to the receiving benders and vice versa.

6.5.2. Stress Strain Response

The stress-strain response from the analysis used in this study depends strongly on instrument spacing and the quality of accelerometer data. Regardless of the methods used, poor data quality or data collected at sampling intervals that are too large cannot provide reliable results. In general, the quality of the acceleration data in this study is reduced as the base shaking amplitudes increase during the test sequence. For example, during shake 5, the minimum shear wave velocity in the untreated soil dropped to approximately 20 m/s (66 ft/s). This meant that the minimum wavelength transmitted through the soil was only 10 m (33 ft). Based upon instrument spacing requirements previously described, the required sensor spacing to adequately capture

wave propagation during shake 5 was very close to the maximum sensor spacing measured in the vertical array. Additionally, during the larger shaking motions, there is a greater potential for the sensors to move and rotate as the soil liquefies which can significantly alter the recorded motions throughout the profile. With further soil softening due to liquefaction, the relative influence of the model container also becomes increasingly significant.

Finally, the actual stress-strain response for this model test is three dimensional and nonlinear. On the other hand, the methods used to obtain the stresses and strains utilize inverse analysis techniques which assume one dimensional behavior where shear strains and shear stresses vary linearly between discreet locations.

6.5.3. Effects on Model Preparation

The affects that model preparation methods have on the measured response are an important consideration to make for data analysis. For the case of soil grouting procedures, the liquefiable layer in both centrifuge models was permeated on a dry sand with colloidal silica grout cured under zero confinement. Additionally, CPT tests required the model to be subjected to 2 cycles of spin-up and spin-down prior to shaking. In other words, the model was subjected to cycles of stresses from 15 kPa (2.2psi) to 75 kPa (11 psi). To date, there is limited knowledge on the affects of factors such as surcharge loading, treatment on wet sands versus dry sands, and cyclic prestraining for CS soils. However, Tsukamoto (2006) studied these effects using various model preparation methods for silicate-based grouts. Results showed greater cyclic strengths for soils grouted on dry sands versus soils grouted on water saturated sands. The cyclic strengths were defined as the CSR causing 4% DA strain after 20 loading cycles and were found to be 2.5 and 2 times greater, respectively compared to that of untreated, saturated specimens. The study showed negligible affects in cyclic strengths of samples cured under zero confinement versus 100 kPa (14.5 psi) confinement. Results also demonstrated negligible affects of surcharge loading on

grouted sand specimens. The greatest affect on cyclic strength for grouted soils from the study was found to be the initial relative density (or void ratio) of the soil.

6.6. Summary of Centrifuge Test Results

Both centrifuge model tests show that settlements occur as a result of liquefaction can be significantly reduced by treating liquefiable zones with colloidal silica. Additionally, colloidal silica treatment shows that lateral spreading can be dramatically reduced for sloped embankments resting on liquefiable soils.

The acceleration response reveals a lesser degree of nonlinearity in CS soils versus untreated soils. The acceleration response also reveals affects of grout concentrations where soil dilation is more pronounced for lower concentrations of colloidal silica. For the 5.25% and 4% colloidal silica soils, dramatic amplification in the acceleration response is observed at a peak base acceleration of 0.69g while the amplification in the 9% CS are significantly less. This behavior correlates well with pore pressure response when r_U=1.0 is achieved and there are significant changes in transient pore pressures for each loading cycle.

Pore pressure response can provide information of how stresses are being transferred between the soil and the colloidal silica. The pore pressure transducer recordings in the treated sands indicate that dynamic loading caused an increase in the normal stress on the pore gel and thus a decrease in the effective stress on the sand matrix. Although pore pressure ratios reached 1.0 for the grouted soils, greater shaking accelerations were required to achieve this state. The occurrence of r_U=1.0 appeared to be related to grout concentration. After liquefaction in the untreated soil, r_U = 1.0 was first observed in the 4% and later observed in the 5.25% CS for a stronger shaking event. Excess pore pressure ratio of 1.0 in the 9% CS soil occurred last and was only observed at discreet locations.

Contrary to observed behavior for each individual shake, pore pressure dissipation was found to occur in the treated soils, but occurred at much slower rate. Considering scaling laws,

dissipation took at least 3 hours verses a couple of minutes for water saturated soils.

Colloidal silica sands result in a stronger and stiffer soil formation. Although colloidal silica treated sands yield higher cone tip and sleeve friction resistance than in water saturated sands, the cone tip resistances were still relatively low and would not necessarily be a strong indication of treatment levels. Similarly, the initial shear wave velocities were not sufficiently high relative to untreated sands and are not necessarily a viable method for determining treatment.

The stress-strain response was caluclated using the dense vertical accelerometer array in order to plot hysteretic behavior and track soil strength and stiffness during cyclic loading. Overall, the stress-strain loops determined from the model tests demonstrate cyclic mobility behavior for CS sands commonly associated with dense of critical sands in undrained cyclic loading. Like untreated sands, drops in pore pressure coincide with peak shear stresses and stiffening stress-strain loops. On the other hand, CS soils exhibit behavior unlike dense of critical sands in that there is a significant amount of damping observed with increasing loading cycles. Additionally, the hysteretic response determined for increasing applied horizontal base accelerations in subsequent shakes confirms the ability of CS sands to provide adequate cyclic shear resistance despite the occurance of increasing shear strains, increasing excess pore gel pressures, and limited pore gel pressure dissipations that were observed. As the applied peak horizontal accelerations in the centrifuge model tests were increased for subsequent shakes, increases in shear strains and excess pore pressures were observed. However, the larger shaking amplitudes were also accompanied by larger cyclic fluctuations in pore pressures and the ability of the gel pressures to produce incremental dilation as incremental decreases in pore gel pressures occurred. In this way, the gelled sand matrix continued to provide significant shear resistance which also translates well with the expanded dilation region observed for CS soils during phase transformation under monotonic loading (Kodaka, 2005).

Shear wave velocities were also measured in between each shaking events to monitor changes in shear modulus. The post-shaking shear wave velocities of colloidal silica soils progressively decreased as the peak base accelerations increased. The response can be attributed to two factors: (1) residual pore pressures induced on the gel from previous shaking events and (2) permanent damage to the gel and disruption of the sand matrix. Finally, the overall degradation in shear modulus with increasing shear strains for CS soils follow the same trends as that of untreated sands.

CHAPTER 7: FIELD TESTING OF COLLOIDAL SILICA STABILIZER

7.1. Purpose and Configuration of Test

As part of the NEESR Grand Challenge Project, a field test was conducted from July to August, 2008 in Myrtle Beach, South Carolina as a collaborative project with the University of Texas at Austin to study the effectiveness of two ground improvement techniques: (1) prefabricated vertical earthquake drains and (2) colloidal silica (CS) stabilizer.

This chapter focuses on field test procedures used when grouting with colloidal silica for purposes of ground stabilization and liquefaction mitigation. Field test procedures discussed will include site characterization for determining groutability, grouting design, instrumentation, batching, injection methods, and QA/QC techniques. Additionally, the methods for data processing of ground motions are discussed in detail. There were two primary objectives of the field test. The first objective was to compare and examine the behavior of a 1.5 m (5 ft) thick liquefiable soil layer versus a similar liquefiable soil layer saturated with CS stabilizer. The effectiveness of the improvement mechanism for CS stabilizer was analyzed in terms of accelerations, pore pressure response, strains, and cone penetration testing. The second objective of the field test was to investigate proper field procedures, such as optimal injection methods of CS in terms of efficacy, cost, and suitability for variable soil conditions.

In this field test, permeation grouting methods were carried out under low pressures to saturate a 1.5 m (5 ft) thick layer of liquefiable soil between depths of 2.1 m (7 ft) and 3.7m (12 ft). A total of 15 injection sites spaced at 1.5 m (5 ft) were used to compare two different injection methods. The treatment test area was approximately 9.3 m^2 (100 ft^2). Post-grouting cone penetration test (CPT) was conducted at the center of the test area prior to shaking.

Additionally, two sensor arrays were placed between depths of 2.4 m (8 ft) and 2.7m (9 ft) along the centerline of the test area. Each sensor array consisted of three sensors placed in a

triangular pattern. Each sensor measured the three-dimensional acceleration response and pore pressure response. Liquefaction was induced using a vibratory mandrel for both the CS grouted area and an adjacent untreated area.

7.2. Site Characterization

7.2.1. Test Site

The field test was conducted at a construction site adjacent to Highway 501 about 9 miles west of Myrtle Beach, South Carolina. The site was chosen because extensive testing was previously performed at the site by the project geotechnical engineer (S&ME, 2006) and the soil conditions were well characterized. Additionally, the surficial soil layers were loose and liquefiable according to the original geotechnical report. The grout area was chosen based on accessibility and uniformity of test borings in the area. Figure 7.1 shows the layout of the test site along with locations of Standard Penetration and Cone Penetration Testing (S&ME,2006). As can be seen from the figure, the grouted test location is approximately 46 m (150 ft) from US Highway 501 and lies within borings C-8, B-8, A-12, and C-13. The untreated test location is adjacent to the treated test area and is located within borings B-7,C-7,A-12, and C-8 (Figure 7.1).

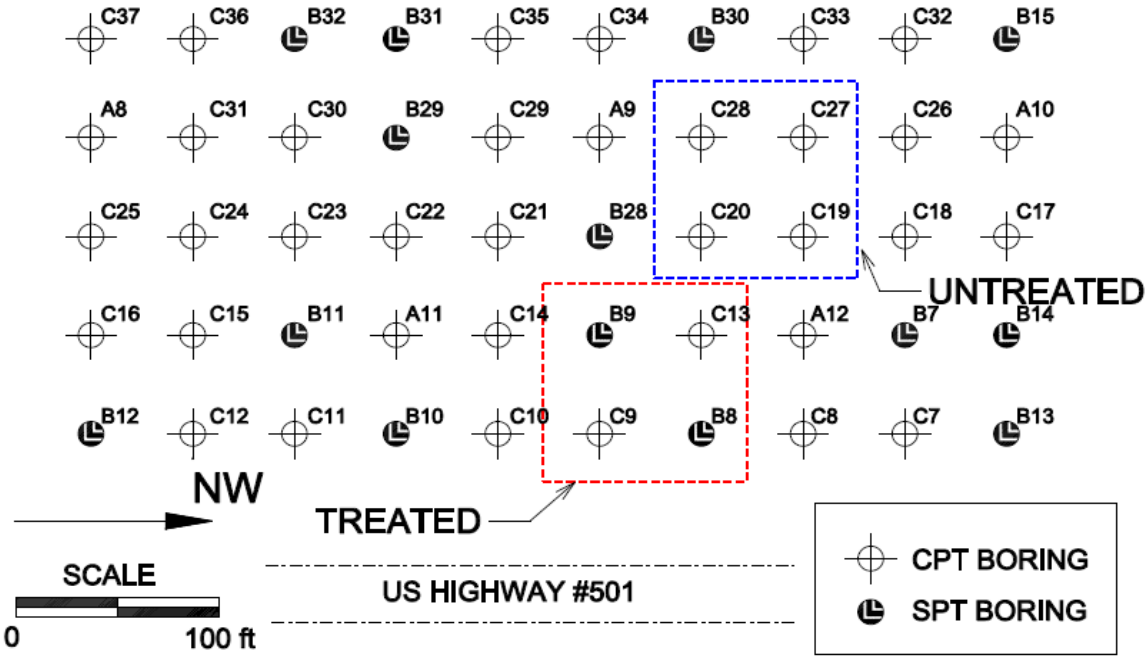

Figure 7.1 Test Site Area with Boring Locations

7.2.2. Standard Penetration Test Data

Based on available soil descriptions and blowcounts from standard penetration test data, there appears to be a potentially liquefiable soil layer at depths of about 1.7 m (5.5 ft) to 3.7 m (12 ft). Three standard penetration tests were previously conducted in the vicinity of the test area and provided by the contractor. The boring locations for the test area are from borings B-7 B-8, and B-9 (Figure 7.1). The SPT data is summarized in Table 7.1 (S&ME, 2006). SPT profiles from borings B7 and B8 are similar and indicate about a 0.8 m (2.5 ft) thick layer of poorly graded sand with clay (SP-SC) underlain by a 0.6-0.8m (2- 2.5 ft) thick layer of poorly graded sand with silt (SP-SM). Below this layer exists a 3.7m (12 ft) thick layer of poorly graded sand (SP) up to a depth of about 5.5 m (18 ft). SPT from B9 differ in that a thicker, 2.7 m (9 ft) layer of poorly graded sand with silt (SP-`SM) exist from depths of 0.9-3.7 m (3-12 ft) overlain by a thinner, 1.4 m (4.5 ft) thick layer of poorly graded sand (SP) from depths of 3.7 m to 5 m (12ft to

16.5 ft). In each case, a final layer of sandy fat clay extends to the maximum boring depth of 6.1 m (20 ft).

Table 7.1 Summary of Standard Penetration Test Data

Depth (m)	N (blows/m)		
	B-7	B-8	B-9
0.6	39.4	16.4	19.7
1.4	16.4	72.2	29.5
2.1	14.7	49.2	32.8
2.7	13.1	23	13
4.4	151	164	157.5
5.9	3.3	6.6	--

Cubrinovski and Ishihara (2001) present empirical correlations between N and D_r that incorporate the effects of grain-size and fines content on relative density. Based on blow count data, relative density was determined to be approximately 36%. The relative density based on the correlations is expressed as

Equation 7-1

$$D_r = \left\{ \left[\frac{N \cdot \left(.23 + .06 / D_{50} \right)^{1.7}}{9} \right] \left[\frac{98}{\sigma_v'} \right] \right\}^{.5}$$

where
N = SPT number (blow/ft)
D_{50} = median grain diameter (mm)
σ_v' = effective overburden stress (kPa)

Relative density was estimated in the middle of the potentially liquefiable layer at a depth of about 2.7 m (9 ft). An average SPT N-value of 16.4 blows/m (5 blows/ft) was established at 2.7 m (9ft) for borings B7,B8, and B9. The effective overburden stress was determined based on the depth of the water table measured at 0.45m (1.5) at the time of drilling and the moist and saturated unit weight of the soil was reported to be 18.8 kN/m^3 (120 pcf) and 19.6 kN/m^3 (125 pcf), respectively (S&ME, 2006). It should be noted that upon arrival at the site, the depth of the

groundwater table was later measured to be 0.6m (2ft) at the time of testing and will be incorporated later into the data analysis. Median grain diameter was also obtained from sieve analysis conducted by S&ME (2006) for soil samples at a depth of 2.6-3.0 m (8.5-10 ft). The grain size data is discussed in a later section.

7.2.3. Cone Penetration Test Data

Soil stratigraphy and soil type were based on several cone penetrometer test results located within the test area that were provided by the contractor(S&ME, 2006). Cone penetration test data within the treated area are illustrated in Figure 7.2 for borings C9 and C13. The data indicates that cone tip resistance varies significantly within the treatment zone at a depth of 2.1-3.7 m (7-12 ft). Tip stresses in the top half of the liquefiable zone 2.1- 2.7 m (7 - 9 ft) range from about 2.7 - 10.7 MPa (25 - 100 tsf) while tip stresses in the bottom half at a depth of 2.7- 3.7m (9 - 12 ft) range from about 4.3 - 15MPa (40 - 140 tsf).

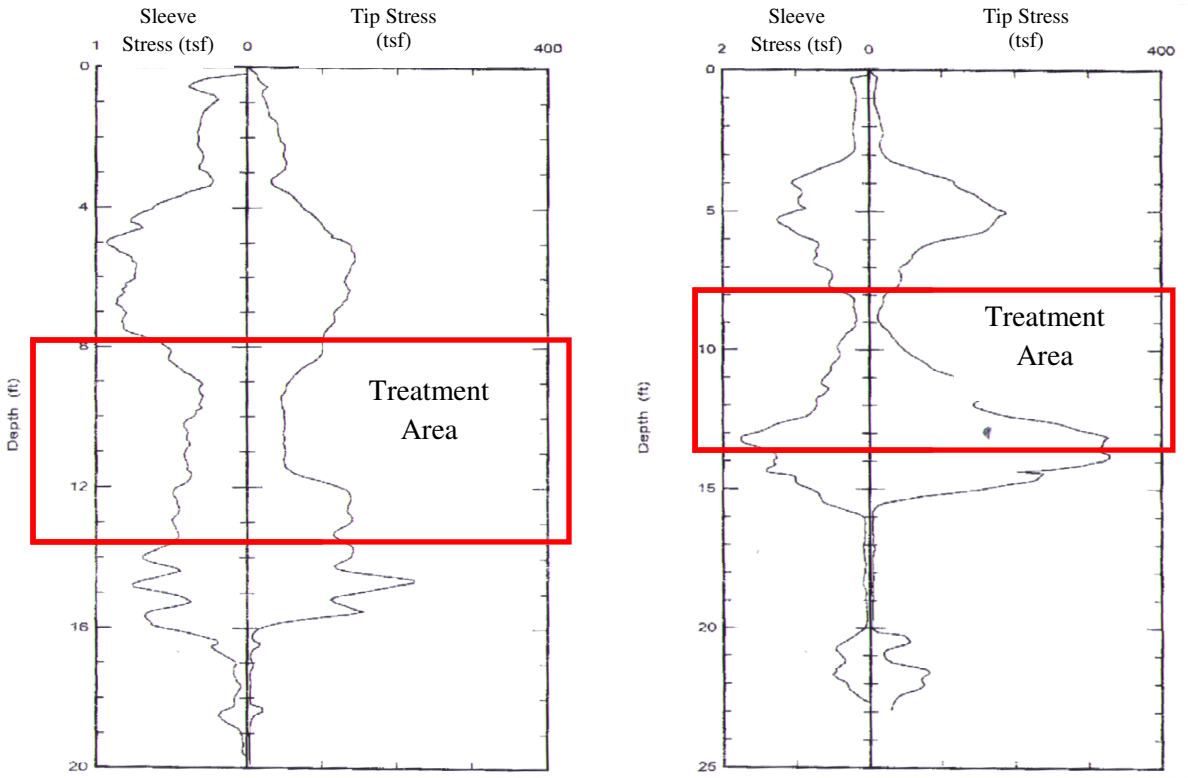

(a) **(b)**

Figure 7.2 Cone penetration data within treated test area from borings (a)C9 and (b)C13 (S&ME, 2006)

The soil behavior type (SBT) was also identified. SBT has been developed as a classification method obtained from CPT data based on (a) cone resistance and pore pressure parameter or (b) cone resistance and friction ratio (Robertson , 1990) . Figure 7.3 shows twelve different soil types that have been identified (1=Sensitive fine grained; 2=Organic material; 3=Clay; 4=Silty clay to clay; 5=Clayey silt to silty clay; 6=Sandy silt to clayey silt; 7=Silty sand to sandy silt; 8=Sand to silty sand; 9= Sand; 10=Gravelly sand to sand, 11= Very stiff fine grained; 12=Sand to clayey sand).

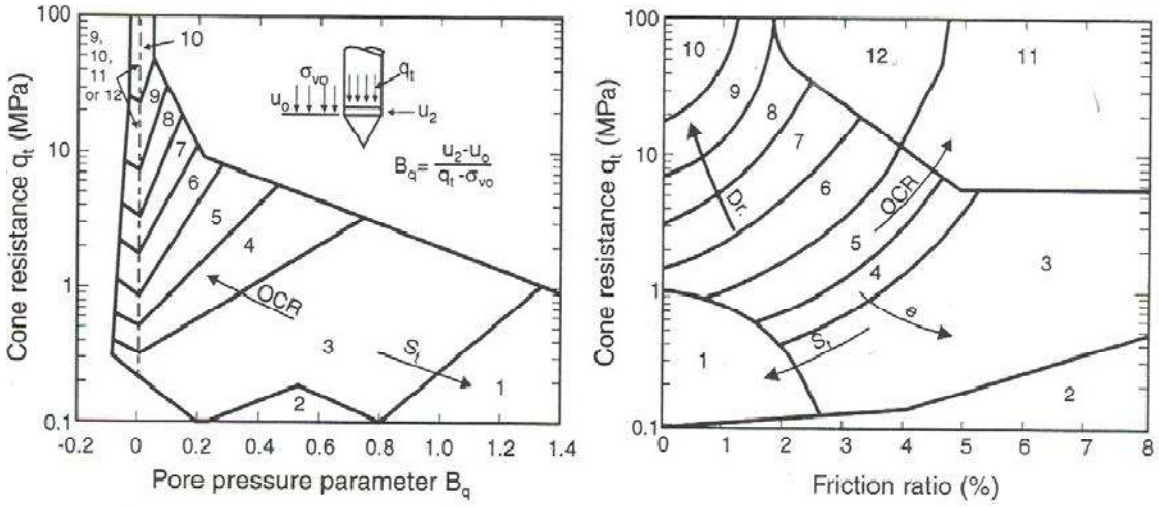

(a) (b)

Figure 7.3 Soil behavior type charts based on (a) Pore Pressure and (b) Friction Ratio (Robertson, 1990)

From the recommended charts developed by Robertson (1990), SBT indices were obtained from average cone resistance and friction values within the liquefiable layer. The soil classifications all fell within SPT-7 (silty sand to sandy silt), 8 (sand to silty sand), and 9 (clean sand). It should be noted that two additional CPTs were later performed using equipment provided by nees@UTexas. One CPT was conducted in the untreated area and one CPT was conducted in the treated area prior to shaking. Results from these tests are compared and discussed in a later section of the chapter.

7.3. Grouting Design and Considerations

7.3.1. Overview

Permeation grouting was selected as the appropriate method for injecting the colloidal silica stabilizer at the test site. Permeation grouting can be defined as a method of replacing the water in voids between the grain particles with a low viscosity gelling solution at low injection pressures (Karol, 1990). Theoretically, there is no change in the volume or structure of the

original ground with permeation grouting. Additionally, permeation grouting is the only kind of grouting for which design equations and relationships exist (Berry, 2006).

The grouting process in the field can be divided into five stages, each of which will be addressed in this chapter:

(1) Research of soil conditions
(2) Design of grouting procedure and equipment
(3) Grout mixing and injection
(4) Monitoring tests during injection
(5) Post-job evaluation

Colloidal silica through permeation grouting serves as an alternative method when cement grouts are no longer feasible. This will occur in geologic formations with low permeabilities such as fine sands, silts, and crystalline rocks where voids to be treated run below 0.1 mm (.004 in) in size. Compared with cement grouting, colloidal silica grouting is conducted at low pressure, but may still migrate far from the injection point if not monitored properly (Lindblom and Jansson, 2004). .

7.3.2. Groutability of Test Site

First and foremost, as with any grouting project, it was necessary to determine groutability or whether the formation at the test site was able to receive grout. Groutability depends on the properties of the soil and the properties of the grout being injected. The properties considered are addressed in this section and include (1) general classification of the soil (2) porosity (3) permeability or hydraulic conductivity (4) viscosity (5) pumping rate/pumping pressure and (6) gel time.

7.3.2.1. Soil Classification

The general classification of soils can serve as an index of groutability. For example, medium to coarse sands can usually be readily grouted, medium to fine sands and loose silts may

be difficult to grout while silty clays and silts cannot be grouted at all. Baker (1982) presents a chart of groutable soils in terms of particles size shown in Figure 7.4. The chart indicates that the finest soil that is groutable has grain sizes of approximately .04 mm (.0016 in).

Grain size distribution curves were created from sieve analyses taken from several SPT boring locations at the test site (S&ME, 2006). The sieve test data is summarized in Table 7.2 and consisted of two depth ranges that were within the proposed treatment layer. Grain size data for depths of 1.8 – 2.3m (6 - 7.5 ft) were taken from borings B-1, B-5, and B-10. Grain sized data for depths of 2.6 – 3 m (8.5 -10 ft) were taken from borings B-2 and B-6. Figure 7.5a and b show the plotted distribution curves for the respective sample depths. Based on grout distribution curves, the soil was considered to be groutable.

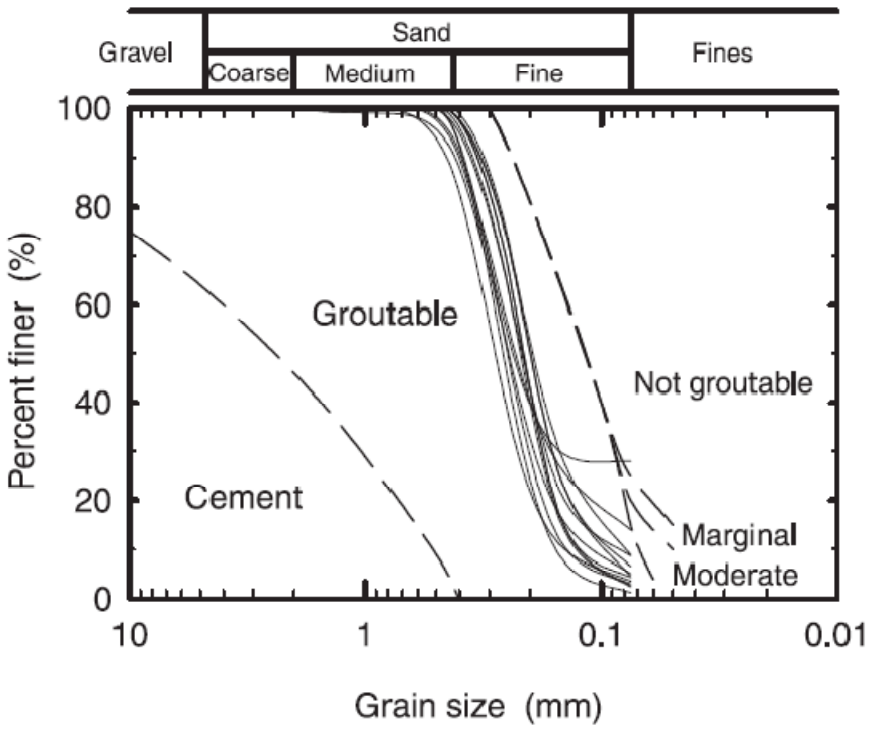

Figure 7.4 Grain size ranges for chemically groutable soils (Baker, 1982)

Table 7.2 Summary of Sieve Test Data

Sieve #	Opening Size (mm)	%Finer (Depth = 1.8-2.3 m)			%Finer (Depth = 2.6 to 3 m)	
		B-1	B-5	B-10	B-2	B-6
10	2	100	100	100	100	92
30	0.595	84	69	92	85	70
40	0.42	54	44	69	47	56
60	0.25	15	11	27	13	26
100	0.149	2	2	6	3	3
200	0.074	1	2	4	2	2

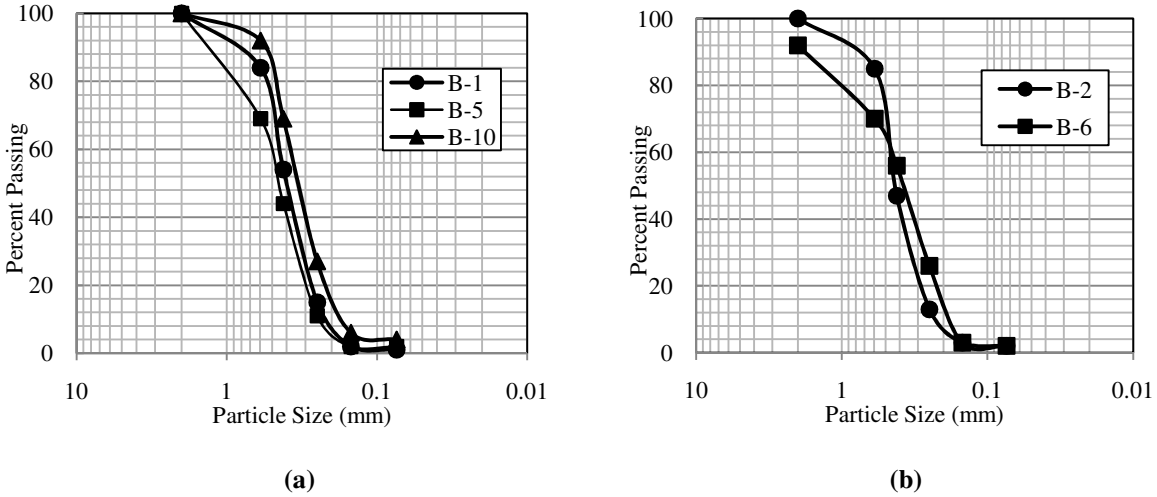

Figure 7.5 Grain Size Distribution Curves for (a) Depth = 1.8 – 2.3 m and (b) 2.6 – 3m

7.3.2.2. Porosity

Porosity is a parameter closely related to grain size distribution and describes the void space in the soil. The porosity of the soil is used for determination of grout volume necessary for treatment of the formation. It will also be later used to estimate the permeability of the soil.

The Army Corps of Engineers (1997) presented a methodology for estimating porosity from grain size distribution. The porosity is a function of (1) the median grain diameter at the 50% point from the grain size distribution curve (d_{50}) and (2) the sorting ratio, S_0, defined as

Equation 7-2

$$S_0 = \sqrt{\frac{d_{75}}{d_{25}}}$$

where d_{75} and d_{25} are the grain size diameters at the 75% and 25% passing point, respectively.

Relationships between porosity and grain size distribution curves are illustrated in Table 7.3. From these relationships, the porosity of the test area was estimated to be about 34- 35% at depths ranging from 1.8-2.3 m (6 - 7.5 ft) and 2.6-3 m (8.5 - 10 ft), respectively. Table 7.4 lists the various parameters used to obtain porosity.

Table 7.3 Porosity relationships from grain size distribution (USA Corps of Engineers, 1997)

S_0	Size → / Sorting ↓		Coarse Upper	Coarse Lower	Medium Upper	Medium Lower	Fine Upper	Fine Lower	Very Fine Upper	Very Fine Lower
			(Porosity,%)							
1.0	extremely well sorted	L	44.7	44.7	46.6	45.6	45.7	48.7	49.8	51.4
		P	43.1	42.8	41.7	41.3	41.3	43.5	42.3	43.0
1.1	very well sorted	L	42.7	44.1	44.3	43.9	44.8	47.5	49.6	51.8
		P	40.8	41.5	40.2	40.2	39.8	40.8	41.2	41.8
1.2	well sorted	L	41.2	43.7	42.5	43.9	44.7	46.0	49.5	51.9
		P	38.0	38.4	38.1	38.8	39.1	39.7	40.2	39.8
1.4	moderately sorted	L	37.4	37.6	39.4	41.0	41.9	44.1	48.1	52.6
		P	32.4	33.3	34.2	34.9	33.9	34.3	35.6	33.1
2.0	poorly sorted	L	33.5	34.9	36.4	38.0	41.8	47.3	52.7	57.0
		P	27.1	29.8	31.5	31.3	30.4	31.0	30.5	34.2
2.7	very poorly sorted	L	33.3	30.2	37.2	38.8	48.3	55.0	57.8	63.2
		P	28.6	25.2	25.8	23.4	23.5	29.0	30.1	32.6

1.000 0.710 0.500 0.350 0.250 0.177 0.125 0.088 0.044
grain diameter in mm

Table 7.4 Porosity Determination

Parameter	Depth = 1.8 - 2.3 m				Depth = 2.6 – 3 m		
	B-1	B-5	B-10	Average	B-2	B-6	Average
d_{10} (mm)	0.22	0.25	0.17	0.21	0.23	0.18	0.21
d_{25} (mm)	0.29	0.32	0.24	0.28	0.31	0.25	0.28
d_{75} (mm)	0.50	0.72	0.45	0.56	0.75	0.50	0.63
d_{50} (mm)	0.40	0.45	0.34	0.40	0.44	0.38	0.41
d_{60} (mm)	0.45	0.50	0.38	0.44	0.45	0.45	0.45
S_o	1.31	1.50	1.37	1.39	1.56	1.41	1.48
n [(1)]	0.38	0.34	0.34	0.35	0.34	0.34	0.34

[(1)] After US Corps of Engineers (1997)

7.3.2.3. Permeability

Permeability is the property of a soil which permits water to flow through its pores. It is the soil property most closely related to groutability and the general relationships is shown in Table 7.5 (Karol, 1990). According to Table 7.5 grouts with viscosities less than 2 cP can typically be pumped without any trouble into soils with permeabilities as low as 10^{-4} cm/s ($4*10^{-5}$ in/s). At 5 cP, grouts may be limited to soils with permeabilities higher than 10^{-3} cm/s ($3*10^{-4}$ in/s). At 10 cP, grouts may not penetrate soils below 10^{-2} cm/s ($3*10^{-3}$ in/s).

Table 7.5 Relationships between porosity and groutability

k (cm/s)	Groutability
10^{-6} or less	Ungroutable
10^{-5} to 10^{-6}	Groutable with difficulty by grouts with under 5cP viscosity and ungroutable at higher viscosities
10^{-3} to 10^{-5}	groutable by low-viscosity grouts but with difficult when μ>10cP
10^{-1} to 10^{-3}	groutable with all commonly used chemical grouts
10^{-1} or more	Use suspended solids grout or chemical grout with filler

Permeability values at the test site were estimated (1) prior to arrival at the site and (2) via in-situ pumping tests. Prior to arrival at the site, permeability was estimated to be about .02 cm/s (.008 in/s) for water and .016 cm/s (.006 in/s) for colloidal silica. These values are characteristic of a soil with medium permeability found in sandy soils. The widely used Kozeny-Carman relationship was used to estimate the permeability, which is defined as

Equation 7-3 $$\boldsymbol{k = \left(\frac{\gamma}{\mu}\right) \cdot \left(\frac{1}{C_{K-C}}\right) \cdot \left(\frac{1}{S_0^2}\right) \cdot \left(\frac{e^3}{1+e}\right)}$$

where

γ = density of permeant (kg/m^3)
μ = viscosity of permeant
$C_{K\text{-}C}$ = Kozeny-Carman empirical coefficient
e = *void ratio*
S_0 = *Specific surface area per unit volume of particles*

Following Carrier (2003), $\gamma/\mu = 9.93*10^4$ (cm·s)$^{-1}$ is used when the permeant is water at 20°C (68°F). The Kozeny-Carman empirical coefficient is usually taken to be equal to 5. The void ratio was determined as

Equation 7-4 $$\boldsymbol{e = \frac{n}{1-n}}$$

where n is the porosity and was determined from relationships based on grain size distribution curves previously described.

For most projects, permeability can be determined in situ by conducting pumping tests. Upon arrival to the site, several pumping tests were conducted to confirm permeability estimates and determine groutability of the area. Data from the pumping tests were used to determine permeability by (1) graphical approach (Neuman, 1975 and Walton, 1979) and (2) Bouwer-Rice method. The pumping tests were performed within 15 m (50 ft) of the test area. Two wells were drilled to a depth of about 3.7 m (12 ft) and spaced 1.5 m (5 ft) apart. The wells were made of 10 cm (4in) corrugated PVC pipes that were covered with a polypropylene geotextile fabric. During the test, water was pumped out at a constant rate from one well while the other well served as an observation well. For extracting water, a 1.3 cm (½ in) air operated double diaphragm (AODD)

pump was used while changes in groundwater level were monitored in the observation well. As extraction of water took place, the flow rate was monitored by measuring the volume of water out of the well every few minutes. The water level in the observation well was measured using a cable marked off in 2.5 cm (1in) intervals that was attached to a conductivity probe.

The graphical approach used was based on non-equilibrium radial flow in an unconfined aquifer described after Neuman , 1975 and Walton, 1979 (Applied Hydrogeology , 2001). This method is based on data recorded from measured drawdown during pump tests. The solution is presented as

Equation 7-5 $$h_0 - h = \frac{Q}{4\pi T} W(u_A, u_B, \Gamma)$$

where
Q = pumping rate
h_0-h = drawdown
$W(u_A, u_B, \Gamma)$ = Well Function for the water table aquifer

Permeability was estimated to be about $1.6*10^{-3}$ cm/s ($6*10^{-4}$ in/s) up to a depth of about 3.7 m (12 ft) in the treatment area. This value falls somewhere between low to medium permeability and can be characterized for soil types ranging from silty sands to clean sands. It should be noted that effects due to varying soil types at different depths were not investigated because a packer system was not yet available until later in the field test. Although results showed lower permeability than that determined from the grain size analysis, it confirmed groutability of the test site.

For confirmation of the measured permeability, a second approach was used. This was based on the Bouwer-Rice (1976) solution for an unconfined aquifer in a slug test. A slug test is based on the rate of recovery of the groundwater after a small volume has been displaced. During the pumping tests, recovery data was recorded by monitoring the time and water level in the wells after pumping stopped. Data was recorded until the water level returned to the original depth. Based on Bouwer-Rice (1976) permeability can be directly estimated by :

Equation 7-6 $$k = \frac{r_c \ln\left(R_e / r_w\right)}{2L_e} \cdot \frac{1}{t} \cdot \ln\left(\frac{h_0}{h}\right)$$

where
r_c = radius of well casing
r_w = radius of well
R_e = distance over which head is dissipated
L_e = length of well screen
t = time since $h=h_0$
h_0 = drawdown @ t=0
h = drawdown @ t=t

The average estimated permeability was determined to be $4.9*10^{-3}$ cm/s (.002 in/s). This value still falls within the low to medium permeability range and is characteristic of soil types ranging from silty sands to clean sands. Again, permeability values based on in-situ pumping tests confirmed groutability of the test site.

7.3.2.4. Viscosity

Viscosity is a key parameter for maintaining injection and controlling migration into a porous formation. Viscosity can be described as a measure of the internal friction mobilized against shearing forces (Karol, 1990). The initial viscosity of colloidal silica grout is close to the viscosity of water where the viscosity of water is 1 cP and the initial viscosity of 9% colloidal silica is about 1.2 cP. However, the viscosity of CS grout increases over time at an exponential rate. As previously mentioned, grouts with viscosities less than 2 cP can be pumped without any trouble into soils with permeabilities as low as 10^{-4} cm/s ($4*10^{-5}$ in/s). The permeability at the test site was estimated to be as low as $1.6*10^{-3}$ cm/s ($6*10^{-4}$ in/s). Based on this data, the grout may be unable to penetrate the soil when the viscosity of the colloidal silica approaches 10cP. This aspect is considered in the selection of gel time which is described in a later section of the chapter.

7.3.2.5. Pumping Rate and Pumping Pressure

Due to its low initial viscosity, colloidal silica will flow through the ground like water and it is important to maintain close control of the injection pressure and volumes. Additionally, colloidal silica is slightly denser than water and has a tendency to sink if it remains in the subsurface too long before gelling. If the downward movement is slower than the expansion of the grout-groundwater interface during pumping, the sinking has little effect on the shape and location of the grouted mass. However, if pumping stops, and grout remains in place as a liquid, it will continue to migrate downward until it sets.

In the field, it is required that chemical grouts, such as CS, be injected at pressures and flow rates consistent with good engineering practice and at injection rates that make use of the grout economically desirable. A "Golden Rule" of permeation grouting is "don't disturb the soil." If it is pumped too fast, the small particles can pack up in the soil forming a filter cake which blocks flow through the formation. In this case, pressure will increase and if pumping is continued, the grout will burst through the soil in a lens, where a new bubble of grout will form. Once this happens, the grout migration is unpredictable and it is likely that the formation has been damaged (Berry, 2006). On the other hand, if pumping is too slow ($\simeq$ 3.8L/min [1gpm]), grouting tends to become an uneconomical method for solving a field problem.

The major limiting factor in pumping rate is pumping pressure. For a given permeability and grout viscosity, pumping rates are dependent on the pumping pressure (Karol, 1990). Ozugalrel and Vipulananen (2005) conducted column test to investigate the relationship between sand gradation and injection pressures for an acrylamide grout. Their tests show that injection pressures vary exponentially with increasing fines content of the soil expressed as

Equation 7-7 $$I = I_0 e^{0.25F}$$

where

I = injection pressure (psi)
I_0 = minimum injection pressure (psi) [= 0.75 psi for acrylamide]
F=fines content (%)

The relationship from Equation 7-7 is illustrated in Figure 7.6 for both acrylamide grout and water. The relationships for water and acrylamide from Figure 7.6 can be easily be compared to colloidal silica grout because colloidal has similar initial viscosities and densities. The fines content at the test site was determined as the average percent passing the #200 sieve from the grain size distribution curves previously described. Based on low fines content of 2%, Figure 7.6 shows that the treatment area would easily be grouted as long as injection pressures remained above 10.3 kPa (1.5 psi).

If injection pressures during grouting are too high, damage of the formation due to fractures or uplift may occur. Uplift will occur when pumping pressures exceed overburden stress of the soil. Fracturing is most likely to occur in uniform soils where permeability and strength parameters are nearly isotropic. Pressures that cause fracturing may be as low as 1/3 to 1/2 the pressures that cause uplift.

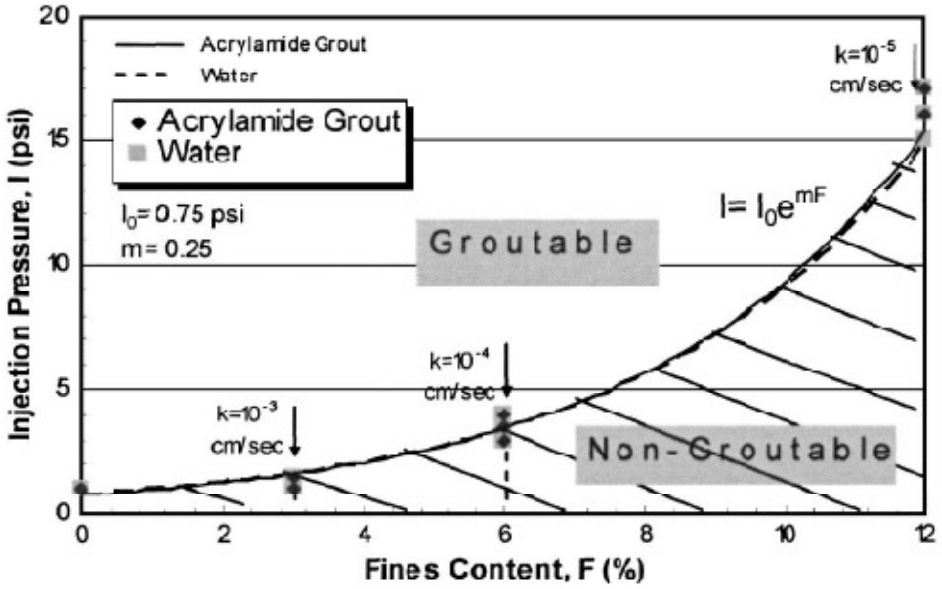

Figure 7.6 Effect of fines content and injection pressure on groutability of soils (Ozugalrel and Vipulananen, 2005)

When fracture occurs, cracks form and injection rates increase dramatically as the cracks fill with grout. This concept has sometimes been considered as a treatment practice, called fracture grouting. The method is desirable for the contractor because grout can be injected much more quickly into the ground. Whether or not to allow fracture to occur depends on (1) the strength increase required at the site and (2) the ability of the grout itself to meet that strength criterion (Karol, 1990). If the strength properties of the grout alone are less than the grouted soil, the grout-filled fractures will serve as planes of weakness and decrease the overall shear strength of the formation. There is currently little data available regarding the effectiveness of controlled fracture grouting or even the pressures that cause fractures in the formation to occur. Until more is known about this phenomena, Karol (1990) recommends three general guidelines regarding grouting pressures.

(1) To prevent uplift, grouting pressures should be maintained below 6.9 kPa (1 psi) per 0.3m (1 ft) of depth
(2) Grouting pressures should be kept below 13.8 kPa (2 psi) when working at shorter gel times.
(3) It should be permitted to exceed the fracturing pressure by a small amount when grout takes are less than 7.6 L/min (2 gpm) and the danger of structural damage due to fracturing is negligible.

7.3.2.6. Gel Time

Selection of gel time for colloidal silica grout is a crucial factor for successful treatment coverage. If the selection of gel time is too short, the CS solution could gel prematurely before it has a chance to be pumped into the ground. Additionally, high grout viscosities will cause grout pressures to rise and can create fractures or uplift in the formation. If the selection of gel time is too long, the grout solution could have ample time to flow into less desirable locations in the subsurface. For this reason, it is advantageous to use short gel times in higher permeability soils so that it remains in the desired formation. Longer gel times are generally better in low permeability soils so it will have time to permeate the desired area prior to setting.

In the field, the most practical and cost-effective method for controlling gel time is increasing the ionic strength of the solution through the addition of sodium chloride. Minimum gel times were selected based on batch size and injection rates. It was planned to mix the grout in 379 L (100 gal) batches and, as mentioned previously, injection rates should be no less than 3.8 L/min (1gpm) (Karol, 1990). Based on these criteria, minimum gel times would have to be about two hours. From Figure 3.6, a 9% solution with a 0.3 N salt concentration would be sufficient yielding a gel time of approximately 2.5 to 3 hours.

It is important to mention that environmental factors, including (1) chemistry of the soil (2) chemistry of the groundwater and (3) temperature can affect gel times in the field and should be considered for proper grouting procedures. Persoff et al. (1995) finds that the sodium ions from the added salt can exchange with calcium ions on clay particles in the soil, causing uncontrolled gelation of the grout. Similarly, exchangeable ions in the groundwater can increase ionic strength and cause unexpected gel times. If this is the case, preflushing with a NaCl saltwater solution may become necessary to eliminate exchangeable cations in the soil.

For the field test, a conductivity probe was used to measure salinity of the groundwater at the site. Testing showed very high concentrations of dissolved salts at about 0.3N. The high salt concentrations in the groundwater could result in premature gel times if (1) there is sufficient mixing between the groundwater and grout during injection and (2) it is used to make the grout solution. As a result, preflushing at the test site was considered and it was decided not to use groundwater for batching the grout solution.

It should be noted that although pre-flushing was considered, but was decided agains it for two compelling reasons. Firstly, permeation grouting under the low pressures used in this test would not cause significant dispersion or mixing between the injected fluid and displaced fluid. Therefore, it was not a concern that the grout solution would mix with the groundwater. Secondly, there was a very narrow time window between the time to grout and the time in which shaking would occur at the site and pre-flushing was avoided to expedite the grouting process.

The effect of temperature on the viscosity of CS is illustrated in Figure 7.7 (DuPont®). This figure shows that a temperature increase from 70°F to 90°F for a 10% solution can decrease the gel time by a factor of almost 3. Although it is evident that temperature can change gel time, the temperature at the site was nearly the same temperature that the gel time tests were performed (75°F) and therefore, did not affect expected gel times.

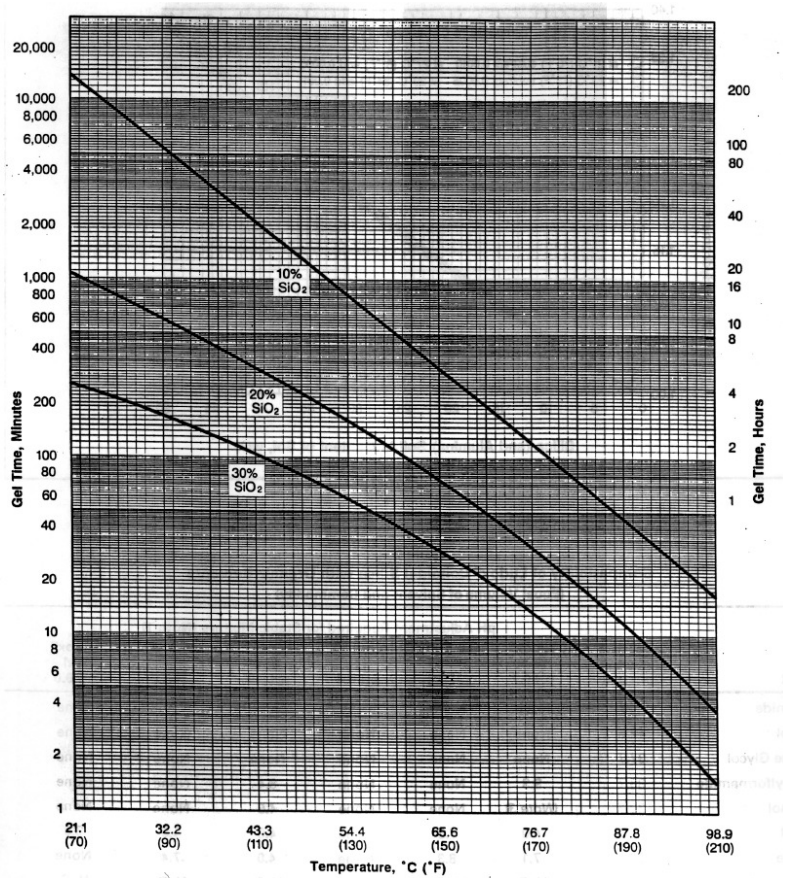

Figure 7.7 Effect of Temperature on Gel Time

7.4. Preliminary Test Plan

The preliminary test plan called for colloidal silica stabilizer to be injected into the upper 5 ft of a liquefiable soil layer at depth of 2.1 - 3.7m (7 - 12 ft). Two grouting systems would be used to grout the desired treatment thickness and be compared side by side. Each grouting method would consist of a total of seven injection points laid out in a hexagonally shaped area. The preliminary test layout is illustrated in plan view in Figure 7.8. The first grouting system utilized a mandrel injection technique while the second grouting system utilized a well/packer system. After colloidal silica injection was complete, cone penetrometer and cross-hole tests were conducted to compare soil properties before and after grouting. A large mobile shaker was used to mimic earthquake motions and induce liquefaction. The treatment area would be laid out in a hexagonal pattern to match the shaker pad from the TRex, which was also hexagonally shaped and measures 2.3 m (7.5 ft) in width and 2.3 m (7.5 ft) in height. The TRex shaker is shown in Figure 7.9.

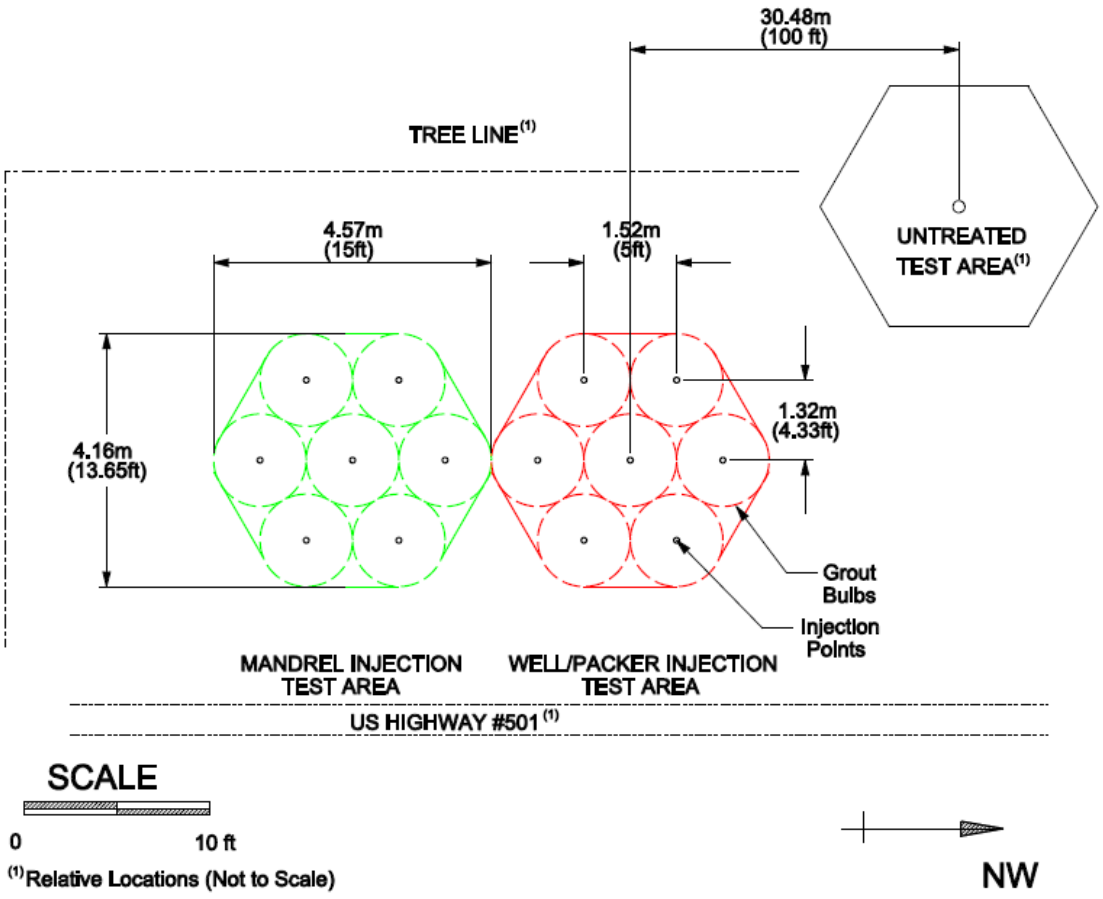

Figure 7.8 Preliminary Test Layout

Figure 7.9 TREX mobile Shaker

Sensor arrays containing 3D accelerometers and pore pressure transducers were to be placed within the treated soil zone to measure dynamic behavior of CS treated sands. Post shaking analysis would consist of cross-hole tests and collecting Shelby tube samples (or split spoon samples). The cross-hole tests would be conducted to measure shear wave velocity in the grouted test area. The Shelby tube samples would be later used to test unconfined compressive strengths and verify treatment. Numerous modifications, however, were made to the original test plan while the field test was on-going. This is discussed in the *Grouting Procedure* section.

Finally, results from the test were compared to an adjacent untreated test area located approximately 30.5 m (100 ft) away from the treated test area (Figure 7.8). Comparisons between the treatment test area and untreated test area included cone penetrometer data, cross-hole test data, and shake data (i.e. pore pressures and accelerations from sensor arrays).

7.5. Test Layout

The test pattern for the injection points was chosen in order to form a zone of contiguous areal coverage. Upon arrival to the site, it was first necessary to mark off the desired injection locations. A grid was formed by marking off five rows of potential injection points spaced 1.5 m (5 ft) on-center in a staggered pattern. The original plan called for a total of 7 injection points for each grouting method. The injection points were given designations corresponding to row

number and hole number. The final test layout, illustrated in Figure 7.10, shows the possible injection points that were marked off in the field along with their designations. It is important to note that more injection points than needed were marked off at the site in order to provide ample area and flexibility in choosing injection locations. This would also allow room for secondary and tertiary holes to be drilled as grouting progressed. The injection points in Figure 7.10 do not necessarily reflect the injection locations that were actually grouted as further explained in the *Grouting Procedure* section. Figure 7.10 also shows the test area where SPT, cross-hole, and shake data were monitored. Comparing Figure 7.8 and Figure 7.10, the final test layout is drastically different than the preliminary test layout. The contrast is mainly because (1) grouting with the mandrel proved to be unsuccessful and (2) the mandrel replaced the TRex mobile shaker for inducing liquefaction.

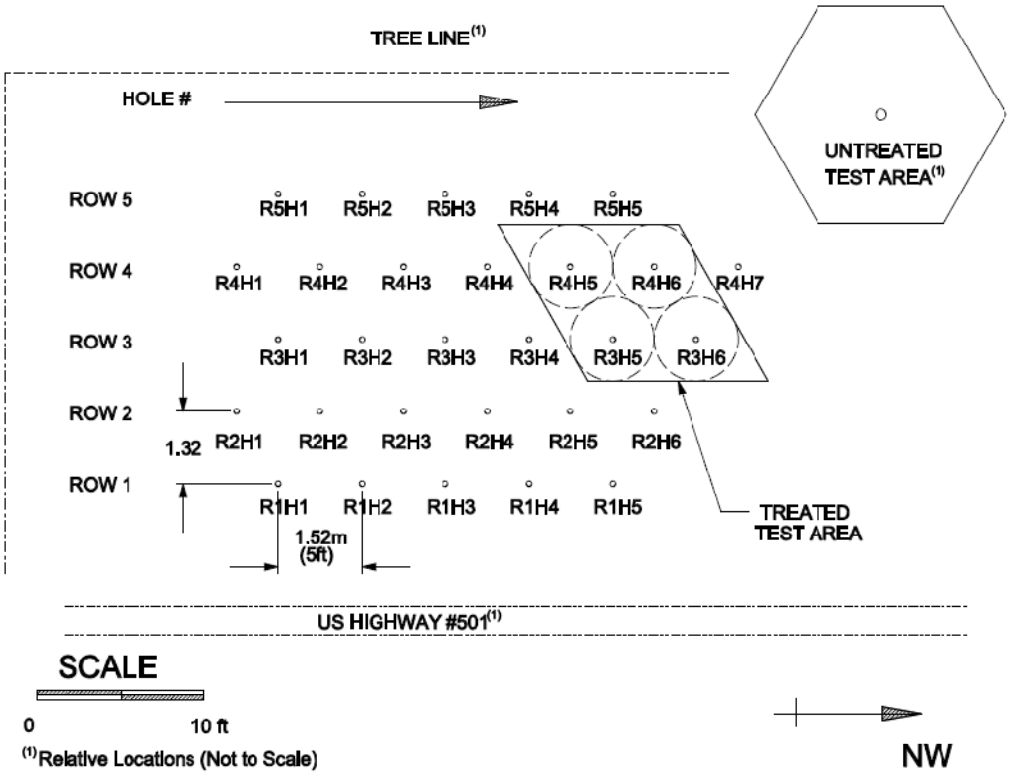

Figure 7.10 Final Test Layout

7.6. Grouting Procedure

7.6.1. Colloidal Silica Batching

The grout used in the test consisted of a mixture of water, Ludox SM-30 colloidal silica (30%) shipped in1,040 L (275 gal) totes , and sodium chloride. Batches were mixed in two 379 L (100 gal) polypropylene tanks which were calibrated and volumetrically labeled in 19 L (5 gal) increments. Each batch was made with 280 L (74 gal) of water, 98 L (26 gal) of Ludox SM 30, and 7 kg (15 lb) of NaCl. The proportions of water, colloidal silica and NaCl were purposely selected to achieve a colloidal silica solution of 9% by weight that had a gel time of approximately 2.5 hours.

The selection of weight percentage was conservatively chosen with consideration of the field test conducted by Gallagher et al. (2007). When mixing large volumes of grout with limited monitoring equipment, there is greater room for error in the volumes used. A minimum concentration of about 5% by weight is necessary for soil improvement using colloidal silica solutions under highly controlled conditions, such as laboratory testing. Below this concentration, the grout may not gel at all. In Gallagher et al. (2007) concentrations of about 8% by weight successfully gelled. Furthermore, Gallagher and Mitchell (2002) showed from cyclic triaxial tests that greater concentrations of CS yield greater cyclic strengths. As a result, a concentration of 9% would ensure complete gelation and, assuming adequate migration, discernable soil improvement.

For practicality purposes, it was initially planned to use the groundwater at the site to mix the solution. However, due to the high salinity of 0.3 N measured in the groundwater, it was decided to acquire water from a municipal supply for mixing the grout solution instead. A water trailer with a volume capacity of 1893 L (500 gal) was filled from a nearby fire hydrant and taken to the test site to be used for batching.

During batching, a 5 cm (2 in) hose was used to feed water directly into the batch tanks. Water was filled to the desired volume into the batch tanks, which were marked off in 19 L (5

gal) increments. Next, the salt was weighed using a digital floor scale accurate to ± 0.1kg (± 2.2lb) and added to the tank. The water and salt were initially mixed with a sump pump. However, the sump pump quickly clogged and the batches were manually mixed thereafter until visual inspection revealed the salt was dissolved in the water. For better volume control, 19 L (5 gal) graduated buckets were used to monitor the volume of CS added to each batch. An AODD pump was used to transport the CS from the tote to the 19 L (5gal) buckets. This particular model pump was an ARO ½" high performance diaphragm pump manufactured by *Ingersoll Rand*. Lastly, about a 1L (¼ gal) of red color food grade dye was added to improve observations of in-situ migration. Again, the mixture was thoroughly mixed prior to injection.

7.6.2. Grouting with the Mandrel

The test plan for grouting with the mandrel would utilize a drill rig to drive the mandrel to the desired grouting depth . The mandrel consists of a 15 cm (6 in) Schedule 80 pipe with an outside diameter of 16.5cm (6.5 in) equipped with a vibratory hammer. Attached are three 20cm x 1.3cm (8 in x1/2 in) fins that span the full length of the pipe.

An air operated double diaphragm (AODD) pump was used to pump the grout from the batch mix to the top inlet of the mandrel. Then the grout filled the mandrel pipe and flowed out of the bottom orifice. Once a pre-determined volume of grout was injected, the mandrel was pulled up to the next prescribed elevation and grouting continued in this manner in a bottom-up staging process. The objective for treatment was to achieve horizontal grout migration of 0.8m (2.5 ft) in all directions from the initial injection point. This would ultimately create circular grout bulbs for a lateral diameter of 1.5 m (5 ft). For optimal coverage, it was decided to grout in multiple stages for small incremental thicknesses of 15 cm (6 in). For a soil porosity of about 0.4, the required grout take was estimated to be approximately 110 L (29.4 gal) per stage.

Figure 7.11 Grouting with the Mandrel

Grout was pumped using the AODD from a single batch tank through a 2.5 cm (1 in) rubber hose. The pump was a SandPIPER air powered double diaphragm plastic pump model PB 1/2 manufactured by Warren Rupp. The AODD was chosen because it provided the most reliable control over maximum total hydraulic head. Advantages of the AODD pumps are that they prime easily (can pump air bubbles at startup) and have little potential for corrosion damage and electrical failure. Additionally, AODD pumps can handle a wide range of viscosities.

During injection, pressures were to be monitored using a manometer and water pressure gauge while volumetric flow rates were to be measured with a flow totalizer. Unfortunately, this equipment failed due to fluctuating stresses induced by the pump along with the corrosivity of the grout. As a result, the air pressure gauge from the AODD pump was used as an alternative method to monitor grout injection pressures. This was an adequate way to estimate injection

pressures because AODD pumps operate on a 1:1 air to liquid pressure ratio. Therefore the grout pressures would be approximately equal to the air-side pressure inlet on the opposing side of the diaphragm. Pressures were monitored and recorded in approximately 5 minute intervals.

In order to monitor flowrates, volume levels marked on the batch tanks were recorded with time. Additionally, the needle on the air pressure regulator gauge would pulsate at a consistent rate as grout takes were successfully being achieved. Listening to the rhythmic sounds of the pump cycling served as an easy, yet reliable indication of successful grout take. When the rhythmic cycling sounds from the pump slowed significantly or stopped completely, this was an indication that injection pressure was increasing and careful attention would be needed to prevent pressures from rising above the threshold that could cause fracture in the soil. As previously mentioned, a common rule of thumb for the prevention of fractures in the soil is to maintain static pressure less than 6.9kPa (1 psi) per 0.3m (ft) of injection depth.

Eventually, injection using the mandrel was abandoned and deemed an impractical method of grouting in the field. As the vibratory mandrel was driven into the ground, there was a large amount of disturbance of the surrounding soil. The fins around the mandrel were the main source for disturbance, creating fractures and a preferential flow path around the annular space of the mandrel. During injection, the grout would continue to short-circuit up around the annular space of the mandrel and spill out onto the ground surface. Using similar methods as in Gallagher et al. (2007), attempts were made to seal the annular space of the mandrel by filling the interface with bentonite for a depth of about 0.6 -0.9m (2-3ft). Attempts were unsuccessful as grout return would continue to occur during injection. An additional reason for abandoning this particular grouting procedure was that it required constant monitoring and use of the drill rig and mandrel by the operator, which could become impractical and expensive for potentially future projects.

7.6.3. Grouting with the Packer

Another injection method consisted of a perforated grout pipe and packer system. This method would take advantage of the quick installation system for the earthquake drains, which would be used as injection wells, while the packer would be used to isolate the treatment layer. Quick well installation was achieved because the earthquake drains served as the injection wells. The earthquake drains were installed using patented, proprietary installation methods performed by *Ellington Cross*. The earthquake drains, illustrated in Figure 7.12, are made of perforated pipes that consist of a slotted PVC pipe wrapped with polypropylene geotextile filter fabric. The nominal diameter of the drains used for the injection wells was 10 cm (4 in) and were 4.9 m (16 ft) long. The drains were inserted into the mandrel pipe and then inserted into the ground at the desired depth using the drill auger. Attached to the bottom of the drains were 20 cm (8 in) V-shaped steel plates . The purpose of the steel plates was to prevent soil from entering the drains as they were being drilled into the ground and also to serve as an anchor as the mandrel was being extracted. Once the drains (or wells) were driven to the appropriate depth, the mandrel was pumped with water as the mandrel was extracted. The purpose of pumping with water was to prevent collapse of the surrounding soil into the void space of the drain.

Figure 7.12 Prefabricated Earthquake Drains for Injection Wells

Following well installation, the grout pipe packer was lowered into the injection wells and held at the desired depth to be inflated with nitrogen. The packer system, manufactured by RST Instruments Ltd, is shown in Figure 7.13. The packer consisted of two, 1m long stainless steel shafts that had an inner diameter of 3.5 cm (1.38 in). The packer was equipped with two perforation options for treatment isolation of either 0.8m (2.5 ft) or 1.5 m (5 ft) sections. The deflated diameter and maximum inflated diameter of the packer was 7 cm (2.83 in) and 14.8 cm (5.82 in) respectively.

Grout injection was achieved through an air operated double diaphragm pump that ran on a 1HP air compressor. The AODD pump is illustrated in Figure 7.14. A 1 cm (3/8 in) Kobalt air pressure regulator was connected in-line between the pump and air compressor and was used to estimate injection pressures. As previously mentioned, the air pressure regulator was a viable method for determining injection pressures because the AODD pump operates on a 1:1 ratio of

air pressure to liquid pressure. Grout from the batches was pumped through a 2.5cm (1in) diameter PVC pipe which was connected to the inlet valve of the AODD pump (Figure 7.14). Grout was then delivered to the pipe-packer system through a 2.5cm (1in) rubber hose attached to the outlet valve of the pump.

Figure 7.13 Packer

As previously mentioned, the packer had two perforation options for isolation of the treatment depth. One option was a 0.8 m (2.5 ft) section and the other was a 1.5 m (5 ft) section. Thus, the packer system allowed grouting to be done in one stage or two stages. It was initially decided to grout in a single stage to save time. A single stage treatment method would avoid the need to deflate, raise the packer to the next depth interval, and then re-inflate the packer.

Figure 7.14 Air operated double diaphragm pump for grout injection

The first three injection wells were grouted in a single stage, 1.5 m (5 ft) section placed from 2.1-3.7 m (7-12 ft). The depth was selected for spanning the permeable layer that would potentially take the most grout. Each of the wells successfully took at least 1136 L (300 gal) of grout, which is the theoretical volume needed to saturate a 1.5 m (5 ft) diameter, 1.5 m (5ft) thick section with a soil porosity of about 0.4.

In general, the packer grouting system has the advantage of being able to isolate a given thickness of soil that may be otherwise difficult to grout. However, there were several failed attempts to grout following the first three holes. In this case, only about half of the estimated required volume of grout was injected successfully before the grout short-circuited and was observed flowing out on the surface at a relatively high rate. At this point, it was possible that grout injected from the previous wells had gelled and was preventing additional grout to flow through the formation. Another possibility was that soil variability existed within the shallower portion of the targeted soil layer and was not accepting the grout. CPT tests in the untreated area

(located about 30.5 m (100 ft) away from the grout area) showed that stiffer sands were located at shallower depths while a relatively loose layer of soil existed below at a depth of 2.7-3 m (9-10 ft).

In order to prevent potential grout return and break-through to the surface, a top down grouting approach was used to create a seal above grout stages at greater depths. The modifications were relatively successful for several holes spanning grout depths from 2.1-3.7 m (7-12 ft). When grouting was complete, a test area was selected based on injection wells that accepted sufficient volumes of grout. A summary of the grout injection locations using both the mandrel and the packer system are shown in Figure 7.15. Also shown in the figure are the proportions of grout volumes that were injected at each location.

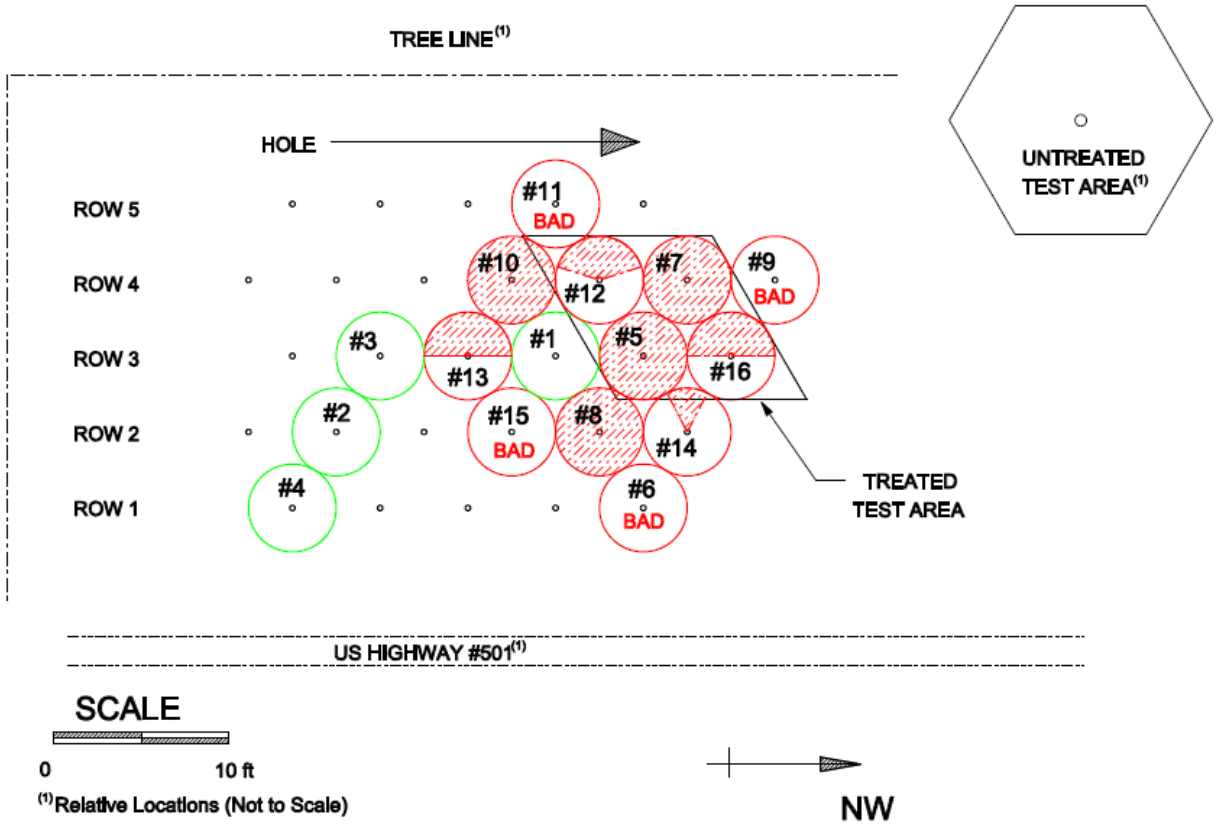

Figure 7.15 Grout Injection Summary

7.7. Field Modifications During Grouting

Several modifications were made to the original test plan as a result of some preliminary assessments upon arrival at the site. On the first day of arrival, the TRex shaker was operating in a nearby, untreated area to induce liquefaction, which would later be used to compare the grouted test area. The large mobile shaker was deemed inadequate for inducing liquefaction at greater depths from the surface. As a result, it was decided to use a combination of the vibratory hammer and mandrel as the source of motion during testing. This was chosen primarily due to the availability and convenience. Considerations, however, would be needed during data analysis because the induced shaking sequence would no longer be the same controlled motions as with the TRex.

The decision to use the mandrel instead of the TRex also influenced the required size of the treatment area. As previously mentioned, the horizontal extent of treatment could be reduced from a 7 point injection, hexagonal configuration to a 4 point injection quadrilateral configuration.

Originally, the test plan called for a comparison of two grouting injection methods: one with the mandrel and another with the earthquake drain/packer system. However, after several failed attempts in grouting with the mandrel, this method proved to be an unsuccessful way of injecting the grout through the formation and the two methods could no longer be compared.

Finally, several modifications were made to the packer grouting system, namely, one stage versus two stage processes. While some injection wells failed to take sufficient volumes of grout and some wells did not, the test area was selected based on the most adequate volume intakes that formed a quadrilateral pattern. The wells chosen for the test area include wells #5,#7,#12, and #16 (Figure 7.15).

7.8. Field Instrumentation

The T-Rex mobile shaker was provided by nees@UTexas (Figure 7.9). Although the T-Rex mobile shaker was not used to induce liquefaction at the test site, it was used for (1) installation of the cone assembly for the CPT, (2) installation of source pipe for pre and post-shaking cross hole tests, and (3) installation of the liquefaction sensor arrays. Figure 7.16 and Figure 7.17 show the respective plan and profile views for the locations of field instrumentation utilized at the treated test site before and after shaking. Similarly, Figure 7.18 and Figure 7.19 show plan and profile views for the locations of field instrumentation utilized at the untreated test site.

Prior to shaking, cone penetration tests were performed in the grouted test area and untreated test area and their test locations are shown in Figure 7.16 and Figure 7.18, respectively. The CPT assembly was provided by nees@UTexas. This moveable assembly consists of a hydraulic cylinder mounted on the rear of the T-Rex which allows for on-site insertion of the CPT cones. The CPT cones are capable of measuring tip resistance, sleeve friction, and friction ratio and can reach depths of up to 30.5 m (100 ft). The hydraulic cylinder is shown in Figure 7.21 while liquefaction sensors were being installed . Further details and specifications can be found at the official website (nees@UTexas).

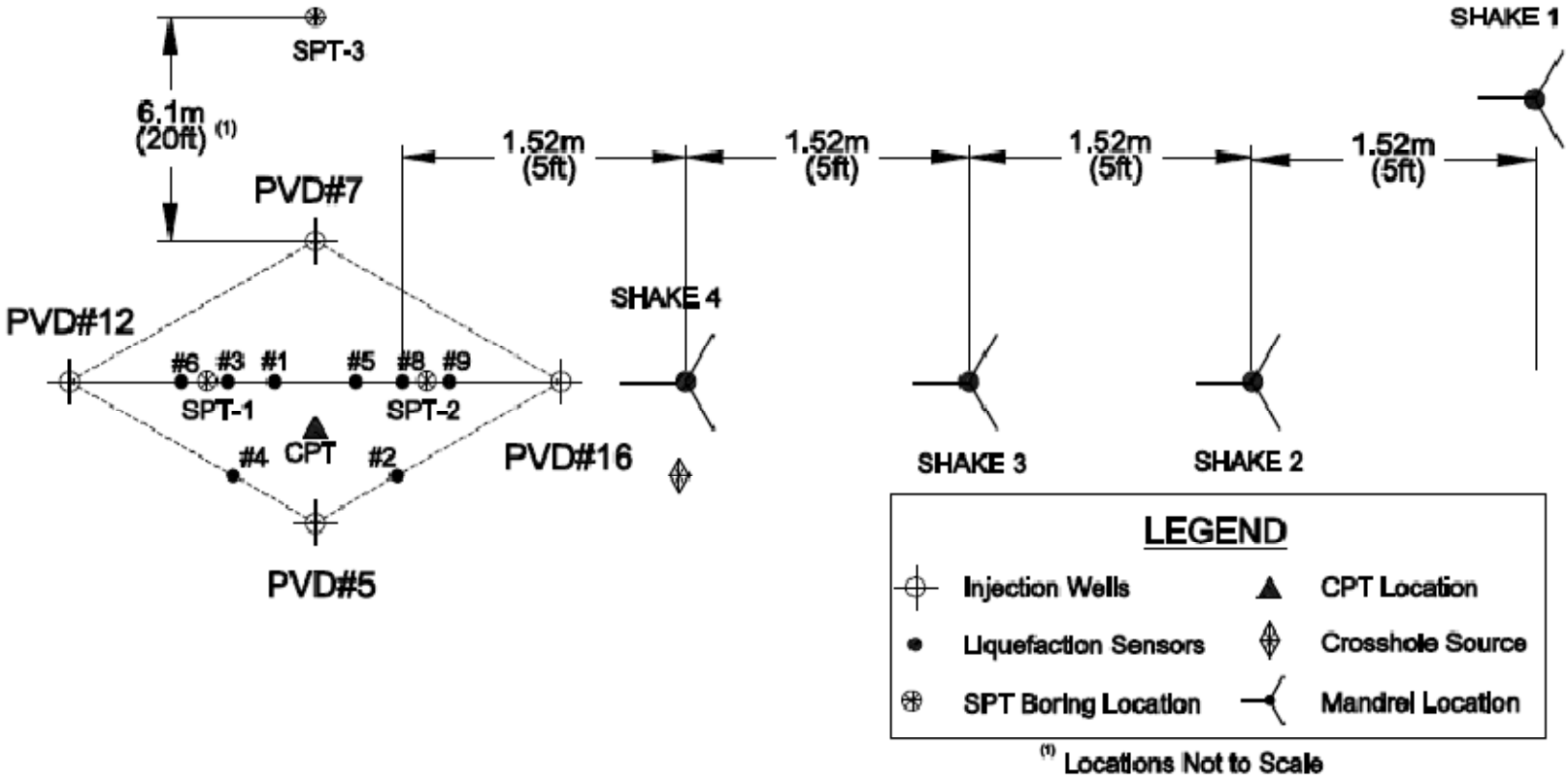

Figure 7.16 Treated Test Layout (Plan)

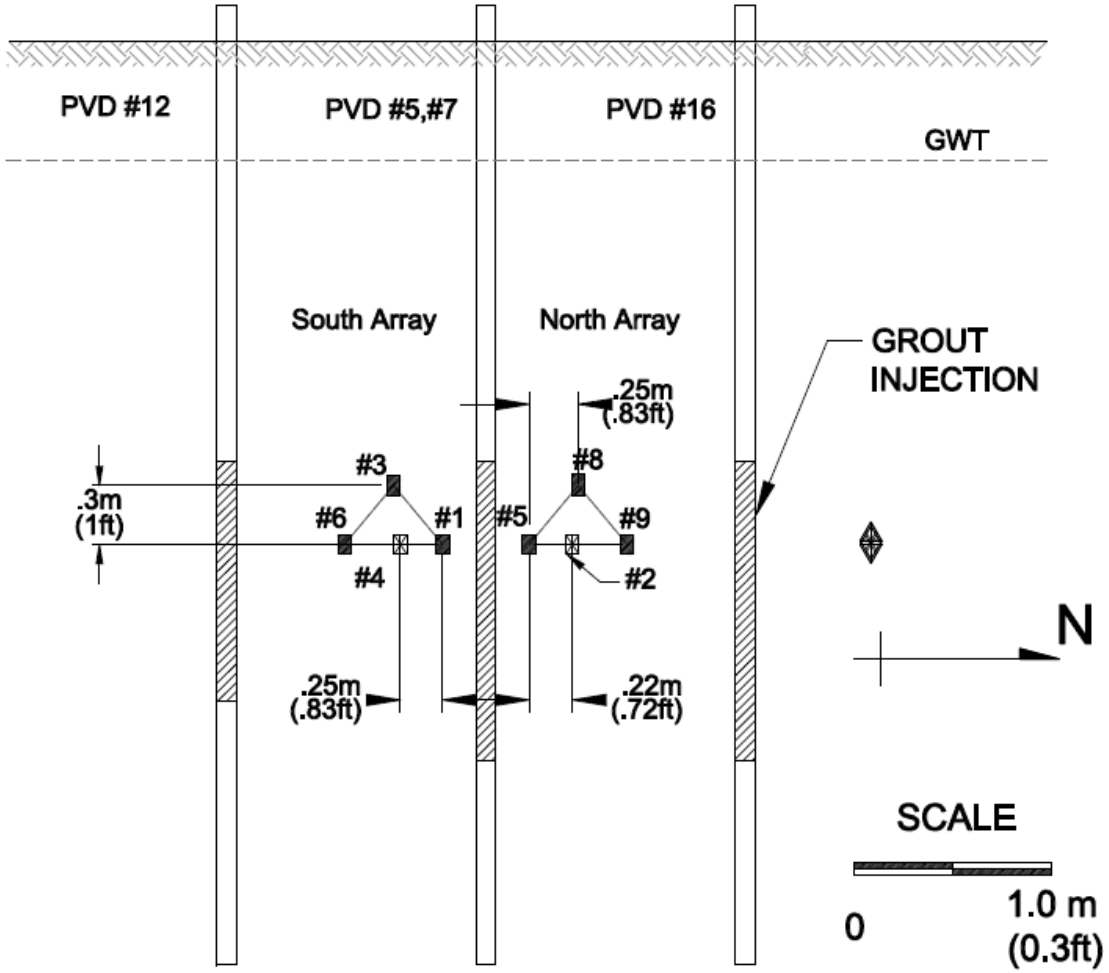

Figure 7.17 Treated Test Layout (Profile)

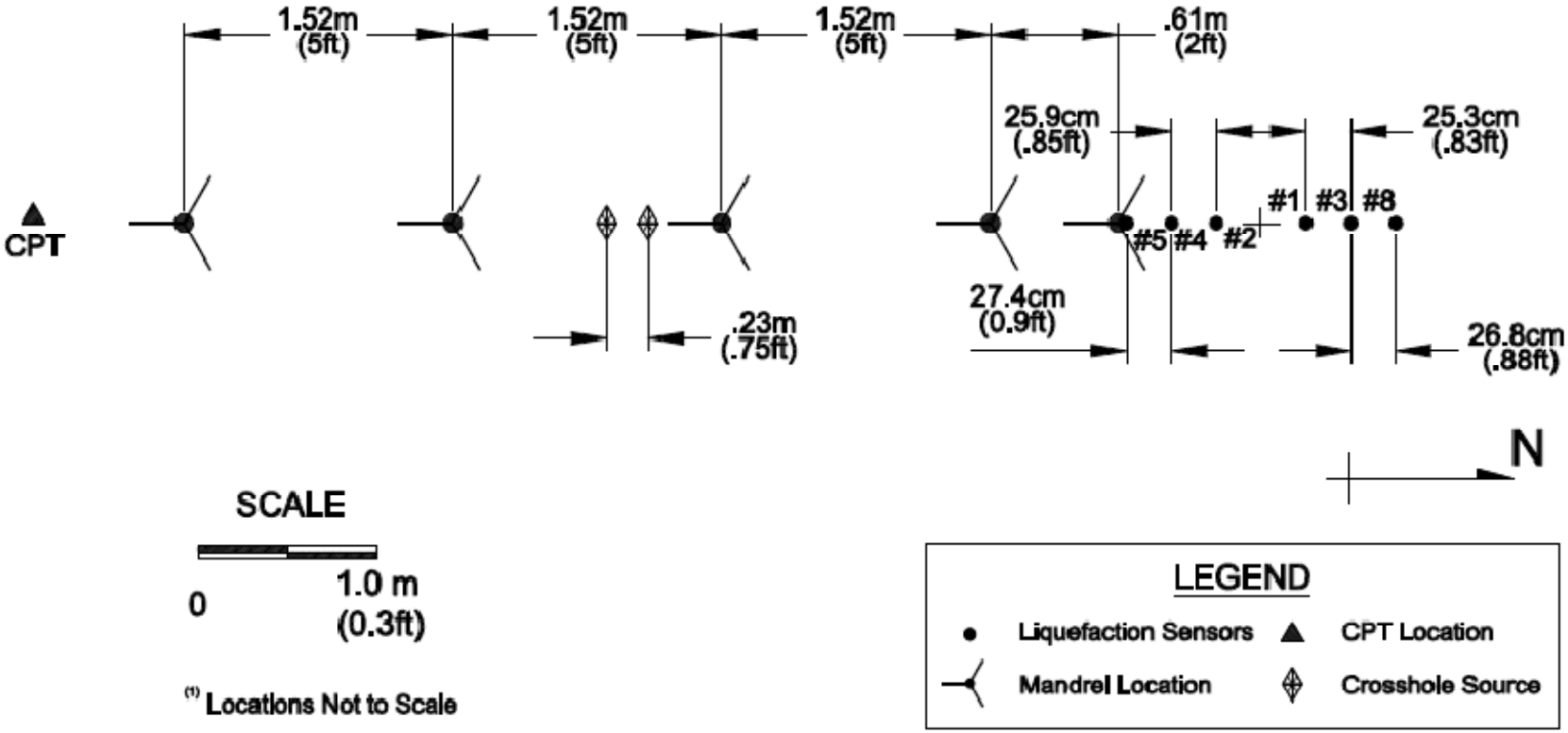

Figure 7.18 Untreated Test Layout (Plan)

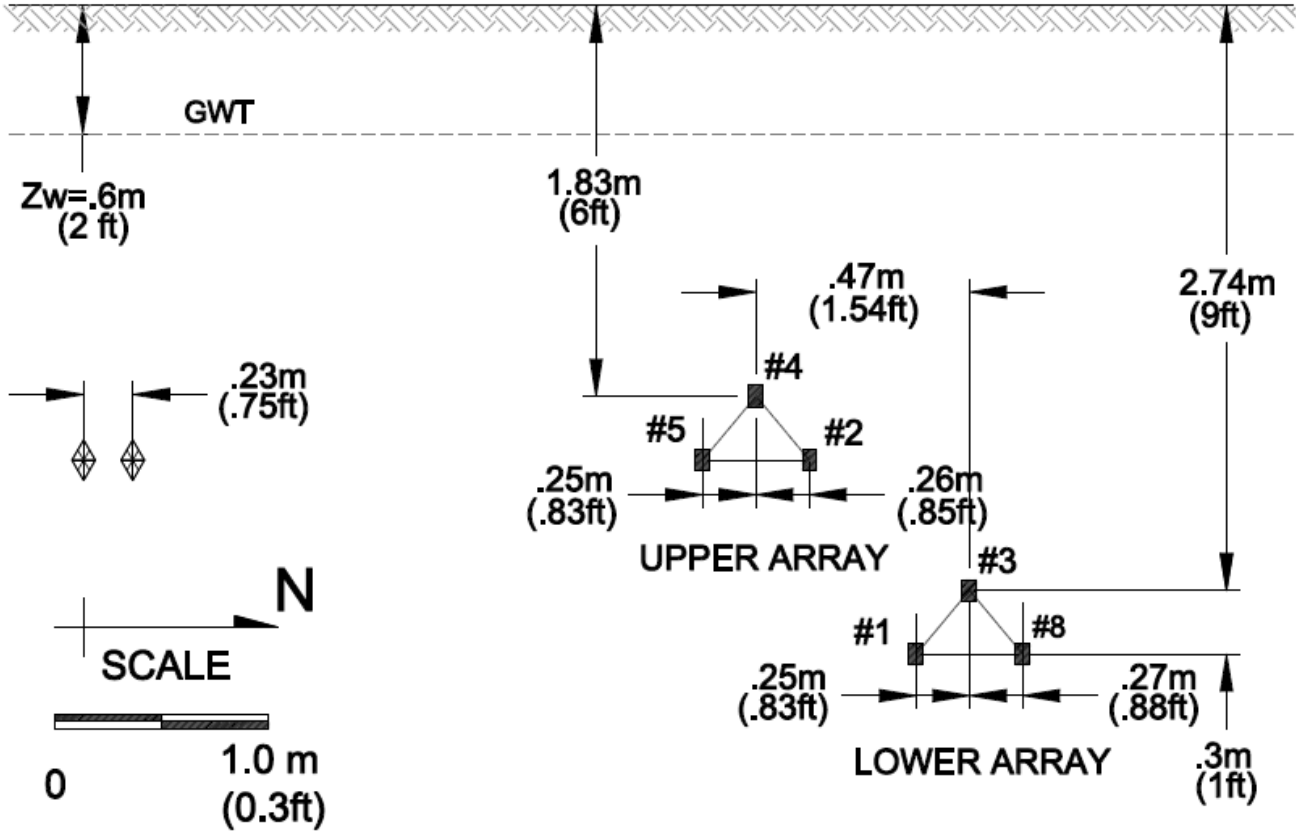

Figure 7.19 Untreated Test Layout (Profile)

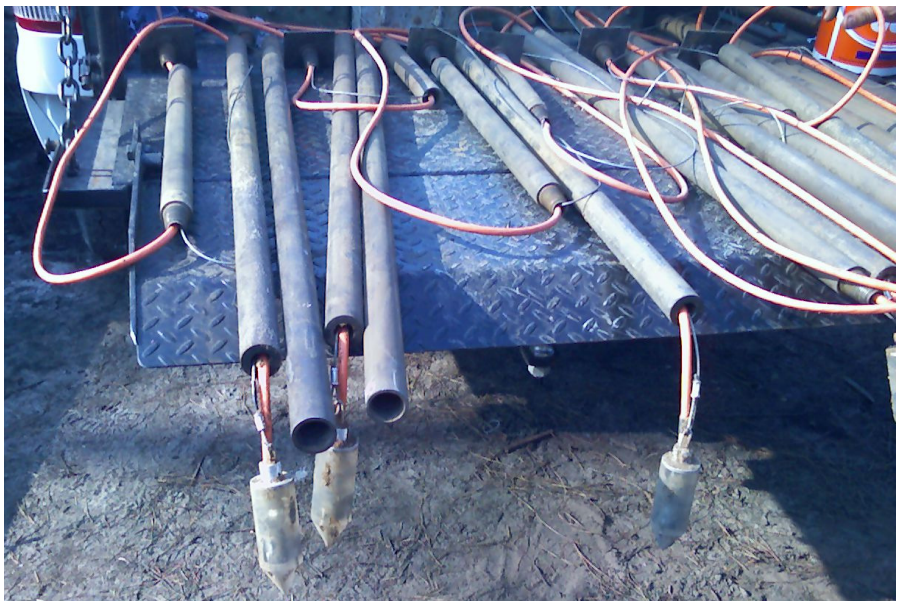

Figure 7.20 Liquefaction Sensors

Liquefaction sensors were installed to monitor accelerations and pore pressures during shaking. The liquefaction sensors were designed and built by Brady Cox at the University of Austin Texas. As can be seen from Figure 7.20, the main body of the sensor is a cylindrical, acrylic case with a conical tip. The sensor measures 12.7 cm (5 in) from tip-to-tip and 9.7cm (3.8 in) diameter. Figure 7.21 shows the liquefactions being installed using the hydraulic cylinder mounted on the back of the TRex. Each sensor consists of (1) a 3-component, 3D Micro-Electrical Mechanical Systems (MEMS) accelerometer and (2) a miniature pore water pressure transducer (PPT) protected by a porous bronze filter. More detailed information and specifications for the sensors can be found on the nees@UTexas site.

Figure 7.21 Installation of Liquefaction Sensors

The locations of the liquefaction sensor arrays for the treated and untreated test areas are shown in Figure 7.17 thru Figure 7.19, respectively. For the treated test area, two triangular liquefaction sensor arrays, denoted as north array and south array, were placed along the centerline of the test area. The bases of the triangular arrays were two sensors at a depth of 2.7 m (9 ft) and spaced at approximately 25 cm (10 in) apart. These are labeled as #6/#1 and #5/#9 for the south and north array, respectively. The top of the triangular arrays were at a depth of 2.4 m (8 ft) labeled as #3 and #8 for south and north arrays, respectively. In addition, two standalone sensors (#4 and #2) were both placed 51 cm (20 in) away from well #5 toward each of the neighboring holes bounding the test area. Sensor #4 was placed towards well #12 and sensor #2 was placed towards well #16. In the untreated test area, two triangular liquefaction arrays were also used and are denoted as upper array and lower array (Figure 7.18). For both triangular arrays, the sensors at the bases were placed approximately 25 cm (10 in) apart. The base of the

upper triangle array was located at a depth of 2 m (7 ft) (sensors #2 and #5) while the base of the lower triangle array was at a depth of 3 m(10 ft) (sensors #1 and #8). The tops of the triangular arrays were at depths of 1.8 m (6 ft) (sensor #4) and 2.7 m (9 ft) (sensor #3) for the upper and lower array, respectively.

Cross hole tests were also performed in the treated and untreated test area before and after shaking to determine shear wave velocities. For the treated area, the cross hole test were conducted using two standalone sensors (#2 and #4) and a source pipe placed 1.5m (5 ft) away from standalone sensor #2 (Figure 7.16). For the untreated area, cross-hole tests utilized the bases of each of the liquefaction sensor arrays. The source pipe for the lower array was placed closest to sensor #1 at a lateral distance of 3.9m (12.8 ft). The source pipe for the upper array was placed closest to sensor #5 at a lateral distance of 2.7 m (8.75 ft) (Figure 7.18). After shaking, three SPT borings were drilled and split spoon samples were extracted in the test area. Samples were taken at depths of 2.1-2.7 m (7-9 ft) and 3.4-4 m (11-13ft). Two of the SPT borings were taken midway between Wells #3 and #6 and Wells #1 and #4, respectively. The third SPT boring was taken approximately 6 m (20 ft) northwest of the grouted area (Figure 7.17). The samples were later taken back to Drexel University to conduct unconfined compression strength tests. Results are discussed in a later section.

All data, including CPT, cross-hole, accelerations, and pore pressures, were recorded using a VXI Analyzer Data Acquisition (DAQ) System manufactured by Agilent. This particular DAQ is primarily used for liquefaction and surface wave studies. The VXI is equipped with 72 channels and can reach sampling rates up to 50 samples/s. The ActiveX open platform enables the system to be utilized by software such as LabVIEW® and Matlab®. Further specifications of the DAQ can be found at the **nees@UTexas** official website.

7.9. Dynamic Loading and Induced Liquefaction

The original test plan called for liquefaction initiation through vibro-seismic shaking using the TRex mobile shaker. Liquefaction sensors were installed in a trial test area and the TRex was used to apply dynamic loading at various shaking levels (UTAustin). Acceleration recordings ranged between 0.05g and 0.4g. The measured pore pressure response, however, indicated no significant increases in pore water pressure (Δu < 0.5 kPa [.07 psi]). Figure 7.22 shows a photograph taken of the ground surface after dynamic loading was applied with the TRex. The figure shows how the pressures exerted by the base plate of the T-Rex created significant depression on the soil surface and indicates that a very soft loose sand existed within the top 1m of the profile. Through field observations and pore pressure measurements made during the trial test, it was uncertain as to whether the TRex could produce significant strains and initiate liquefaction at greater depths.

Figure 7.22 Localized depression on ground surface from T-Rex base plate (Marinucci, 2010)

An alternative approach for dynamic loading of the test sites was to use the vibratory steel mandrel as the source of excitation. The mandrel has an operating frequency between 1400 rpm and 1600 rpm (approximately 25Hz) and is equipped with a vibratory hammer to supply the excitation (Figure 7.23a). For each ground motion, the vibratory hammer was employed as the steel mandrel was driven into the ground to a maximum depth of 6 m (20 ft). From this method, complex shearing of the soil deposit is initiated through a combination of compression waves and shear waves as the mandrel is driven to depth. In this way, significant strains could occur and liquefaction could be achieved at greater depths. A schematic of the body and surface waves generated by the excitation source is illustrated in Figure 7.23b.

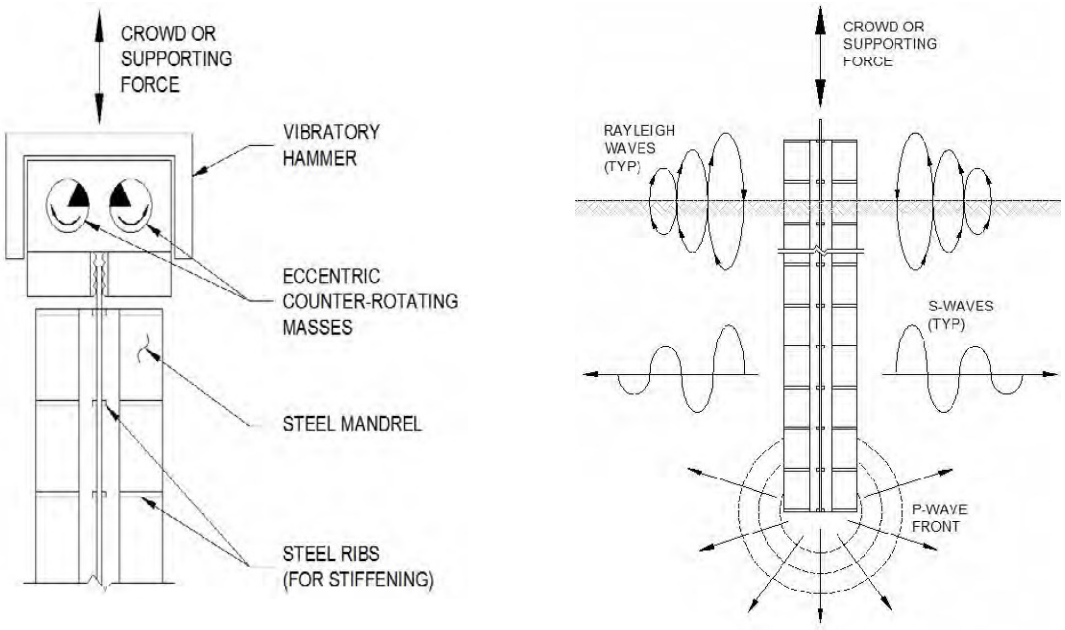

Figure 7.23 Schematic of (a) vibratory excitation source and (b) Rayleigh waves generated by excitation source (Marinucci, 2010).

The locations of the source shaking for the untreated area are illustrated in Figure 7.18. The figure shows that for the untreated area, the mandrel was driven at lateral distances of about 1.5 m (5ft), 3 m(10ft), 4.6 m(15ft), and 6 m (20ft) away from the liquefaction sensor locations. For each shaking location, the applied ground motions consisted of four source excitations in the following sequence:

(1) Driving the mandrel to maximum depth with vibratory hammer operating at maximum frequency (about 25Hz)

(2) Vibration of the mandrel at a frequency of about 12 Hz at maximum depth for 20-30 seconds

(3) Vibration of the mandrel at maximum frequency (25Hz) and at maximum depth for 20-30 seconds.

(4) Extracting the mandrel at maxim mum frequency

The source excitation locations for the treated area are shown in Figure 7.16. Similar to the untreated area, the motions were applied at various lateral distances of 1.5 m (5ft), 3 m(10ft), 4.6 m(15ft), and 6 m (20ft) away from the liquefaction sensors. An onsite review of the data recorded from the untreated test area revealed that the greatest response occurred when the mandrel was operating at maximum frequency and was being driven into the ground at maximum depth. It was therefore decided that the ground motion sequence for the treated area would consist of a single recording while the mandrel continuously operated at its maximum frequency of 25Hz. Therefore, the recorded motions for the grouted area represent the response as the mandrel was being driven into the ground at maximum depth and extracted back up to the surface.

7.10. Quality Assurance and Quality Control

Since permeation grouting with colloidal silica for liquefaction is a relatively new technique, quality assurance and quality control (QA/QC) measures are still evolving. Several QA/QC measures were taken before, during, and after the field test. In addition to improving the quality of the test, these QA/QC measures would allow for lessons to be learned regarding future field test procedures.

Prior to arrival on the site, gel time tests were conducted in the laboratory in order to develop gel time curves for varying salt concentrations of colloidal silica solutions. Due to the fact that last minute changes may arise in the field which may call for different target gel times, the gel time curves serve as a valuable tool for formulating colloidal silica grout recipes quickly and efficiently.

When preparing the grout batches in the field, chloride concentration was recorded for each batch using a conductivity meter. Knowing the chloride concentration for each batch is verification that the proper proportions of water, sodium chloride, and colloidal silica were added

to the mix. Values for chloride concentration ranged from about 18.5 - 19.75 g/L (2.5-2.6 oz/gal). Additionally, as each batch was mixed, smaller samples were collected and labeled with a batch number and mixing time. The purpose of collecting samples was to visually inspect whether the solution had gelled within the desired time frame. Average gel times occurred between 1.5 to 2.5 hrs. This was a desirable gel time because injection of each batch would typically take 70-100 min. It should be noted that premature gelation was a concern as complications during injection arose in the field. If complications did occur during the field test, smaller quantities of water were added to the batches in order to increase the gel time. However, it is recommended that sodium hydroxide be used as an alternative in future field tests for two main reasons. Firstly, it is less labor intensive to add several drops of sodium hydroxide versus several gallons of water. Secondly, sodium hydroxide delays gelation by a different mechanism than adding water does. Adding water to the solution dilutes the concentration of colloidal silica whereas the sodium hydroxide alters the pH of the solution, forcing particles to repel one another. Ultimately, this would result in a stronger solution versus the diluted solution.

During the grouting sequence, injection pressures, injection rates, and total volumes injected were monitored. As previously explained, monitoring grouting pressures ensures that uplift and fracturing do not occur. Injection rates were monitored mainly to ensure that injection was not occurring slow enough to cause premature gelation of the grout batches. Monitoring the total volume injected in each well was a way to estimate whether or not a sufficient amount of grout was injected to fully saturate the desired treatment zone.

Pumping pressures were monitored and recorded using an air pressure regulator. The grouting pressures during pumping typically ranged from about 35-83 kPa (5 - 12 psi). When the grouting pressure increased rapidly, it was most likely due to one of two things: (1) colloidal silica viscosity from the batch was beginning to increase or (2) grout was being pumped into an area that was already gelled. While grouting with the packer, pressure increases were observed up to 183 kPa (20 psi) in Well #12 and Well #16. While injecting into these test wells, grout was

observed oozing out of adjacent wells. This suggested that the grout had migrated laterally for the desired treatment length. Additionally, the "oozing" of the grout was an indication that viscosity of the injected solutions were beginning to increase.

Injection rates were approximated by monitoring volumes of grout injected from the calibrated batch tank every 5 to 10 minutes. The average injection rate recorded was approximately 5.7 L/min (1.5 gpm). Additionally, the total volume of the grout injected at each well were recorded. Prior to grouting, the required volume to grout the desired treatment zone was approximated based on values of porosity at the site and the desired treatment area. It was found that approximately 1,078 L (285 gal) were needed to be injected at each well for a 1.5 m (5 ft) thick treatment layer. These volumes were considered when selecting the final treated test area. A summary of the injection sequence, volumes of grout injected, and average flow rate for each well are summarized in Table 7.6.

Post grouting CPT and cross-hole tests were performed to assess whether these commonly used test methods could be used to characterize the improved soil. Results are discussed in a later section. After shaking, soil borings and split spoon samples were obtained to measure compressive strength and confirm soil improvement.

Table 7.6 Summary of Grout Injection

Date	R/H	Grout Order	Grout Depths (m)	No. Stages	Σ VOL_{in} (L)	% Treated	Q_{avg} (L/min)	Grout Method
7/26/2008	R3H4	1	2.4 - 2.9	2	90.7	8	3.3	Mandrel
7/26/2008	R2H2	2	1.8-2.7	5	185.2	17	7.1	
7/26/2008	R3H2	3	1.7-1.8	2	86.9	8	3.9	
7/27/2008	R1H1	4	2.4-4	8	616.1	57	5.3	
7/27/2008	R3H5	5	2.1-3.7	1	1145.3	106	4.7	Packer
7/28/2008	R1H5	6	1.5-3	1	238.1	22	5.2	
7/28/2008	R4H6	7	2.1-3.7	1	1134.0	105	6.7	
7/28/2008	R2H5	8	2.1-3.7	1	1134.0	105	5.6	
7/29/2008	R4H7	9	2.1-3.7	1	192.8	18	4.4	
7/29/2008	R4H4	10	2.1-3.7	1	1228.5	113	6.4	
7/29/2008	R3H3	N/A	N/A	N/A	N/A	N/A	N/A	
7/29/2008	R5H4	11	1.8-3.4	1	94.5	9	5.0	
7/29/2008	R4H5	12	2.1-2.9	1	434.7	40	4.6	
7/29/08- 7/30/08	R3H3	13	2-2.7	1	563.2	52	3.4	
7/30/2008	R2H6	14	2.1-2.9	1	166.3	15	2.8	
7/30/2008	R2H4	15	2.9-3.7	1	136.1	13	4.5	
7/30/2008	R3H6	16	2.1-2.9	1	774.9	72	5.5	

CHAPTER 8: FULL SCALE FIELD TEST - SIGNAL PROCESSING AND RESULTS

This chapter is a continuation from Chapter 7 and will discuss the signal processing methods used to generate the dynamic response recorded from the liquefaction sensors. Signal processing methods include appropriate filtering and integration techniques of acceleration records in order to obtain shear strains. Results of the dynamic response are presented as time histories of acceleration, pore pressure, and shear strains for a series of dynamic loading events. Additionally, results of various in situ test parameters, such as shear wave velocity, CPT, and unconfined compressive strengths for assessing ground improvement in situ will be summarized.

8.1. Signal Processing of Ground Motion Records

Fifty years after the first anologue accelerographs were developed in the United States, digital accelerographs were developed. The digital accelerographs were capable of producing strong motion data on re-usable media and provided solutions to the limitations of analog recorders. More specifically, digital accelerographs are able to operate continuously and by use of pre-event memory; in this way, they can retain first wave arrivals regardless of low amplitudes. Additionally, their frequency range is wider (50 – 100 Hz for typical transducers) and analog-to-digital conversion is performed within the instrument, eliminating the need to digitize records (Boore and Bommer, 2004).

Although the digital accelerometers used today far surpass the earlier accelerographs, there is still a need to apply data processing techniques to the raw, digitized data. Ground motion records, to some degree, will always be affected by noise and this noise will need to be accounted for in the record. Data processing will typically involve correcting for (1) background noise (2) dynamic response characteristics associated with instrument response, and (3) errors associated with triggering. In an effort to make corrections and improve strong motion records through data

processing, there will always be some portion of the signal (in frequency domain) that is sacrificed. The critical issue is selecting what range of frequencies are representative of the actual motion by considering both signal-to-noise ratios and adjustments applied to the record.

Boore and Bommer (2004) discuss current procedures for removing noise from digital accelerograms, such as baseline correction, low-cut (or "high pass") filtering, and high cut (or "low pass") filtering. Unfortunately, there is no single solution for removing noise of strong motion recordings because a wide range of noise sources exist and there is a lack of accurate noise models. Although the objectives are the same, different authors and agencies will use various steps in data processing. The procedures will depend primarily on the type of instrument, the nature of the ground motion recorded, and the engineering application for which the records are to be used for.

8.2. Signal Processing of Acceleration Records

Signal processing of the acceleration responses from the field test was performed in the following sequence:

1. Truncation and zero correction of data from the MEMS accelerometer series
2. Filtering acceleration series
3. Integration of acceleration series and Decimation of Data (Acceleration, Velocity, and Displacement)

Each processing step was performed using the Mathworks Inc. MATLAB® software program.

8.2.1. Truncating and Zero Correction

The data from the liquefaction sensors were recorded at a relatively high sampling frequency of 8192 Hz and consisted of data for long periods when no excitation was applied. The original records were therefore truncated prior to processing the signals in order to reduce file size and remove unnecessary data. Once the data was truncated, the acceleration series consisted of recordings 1 second prior to shaking and 10 seconds after shaking.

A zero correction factor was introduced in order to remove the at-rest signals that were mainly attributed to noise and ambient vibrations. This zero correction, or offset value, was determined by taking the average value recorded in the first second prior to shaking.

8.2.2. Filtering

8.2.2.1. Filter Application

Applications of filters for digital recordings can easily be applied to remove undesirable high and low frequencies due to noise. This is the most important processing application for ground motion records. Although filters can be applied in either the frequency domain or time domain, their application is best understood in the frequency domain. In the frequency domain, a filter is essentially a function that has a value close to 1 in the range of frequencies that is desired to retain for analysis and has a value of zero in the range of frequencies that is desired to be eliminated. The filter can be applied in the frequency domain by multiplying the filter function with the Fourier amplitude spectrum (FAS) of the time history, which is later converted back to the time domain.

8.2.2.2. Filtering Methods

Although a wide variety of generic filters are available, only minor differences exist between them and the results obtained from the type of filter used is negligible relative to the application. A commonly used bandpass Butterworth filter was applied for analysis. Butterworth filters are characterized as having a relatively flat response in the passband with small, roll-off slopes.

More important than the type of filter selected is whether it is applied causally or acausally. Boore and Bommer (2004) recommend filters be applied acausally because they do not produce phase distortion in the signal. The filters are described as acausal because in order to achieve the zero phase shift, they need to start to act prior to the beginning of the record. This is

done by adding data points before and after the record that include zero amplitudes (also known as *zero pads*). If zero pads are not used prior to using the acausal filter types, incompatibilities between the response spectra and integrated time histories (e.g. velocity and displacements) may result. Zero pads were therefore applied for each record by adding points at the beginning and end of the record. Initial and final points were assigned zero amplitude and the remaining data points were fitted to the original record through linear interpolation.

8.2.2.3. High Pass Filter

A major problem encountered with digital accelerograms is distortions and shifts of the reference baseline, which are generally the result of long-period (low frequency) noise. The shifts of the reference baseline are not always evident in the acceleration series data as shown in

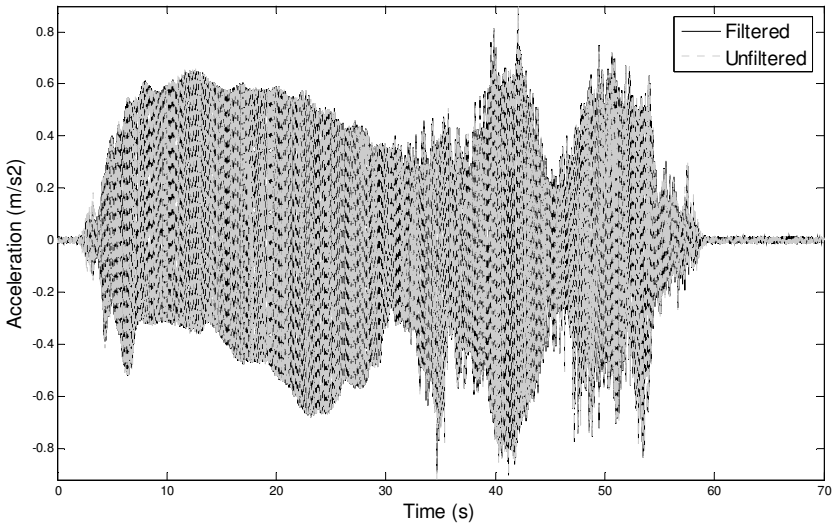

Figure 8.1. However, these effects become more discernable in the velocity and displacement time histories obtained through double integration. This concept is illustrated in Figure 8.1 through Figure 8.3 where signal drifts in the velocity and displacement records become increasingly significant. To remove the low frequency noise, a high pass filter was applied to the field data to correct for baseline shifts.

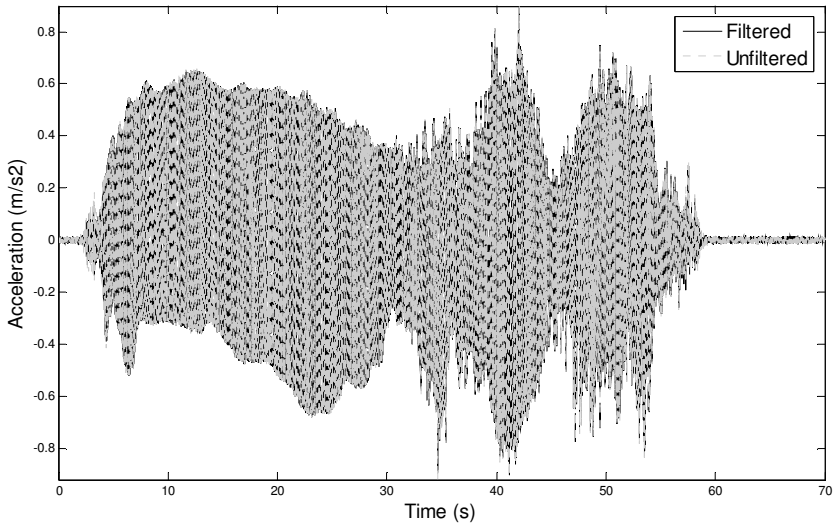

Figure 8.1 Acceleration Record Before and After Filter (15' Untreated)

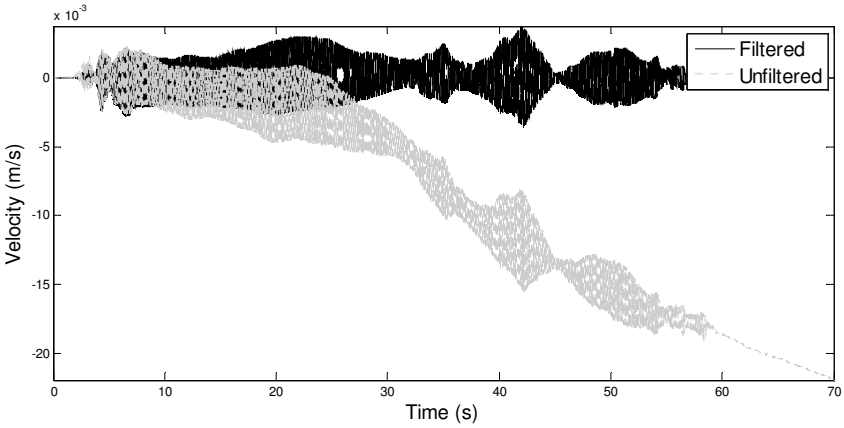

Figure 8.2 Baseline Effects of Velocity Series (15' Untreated)

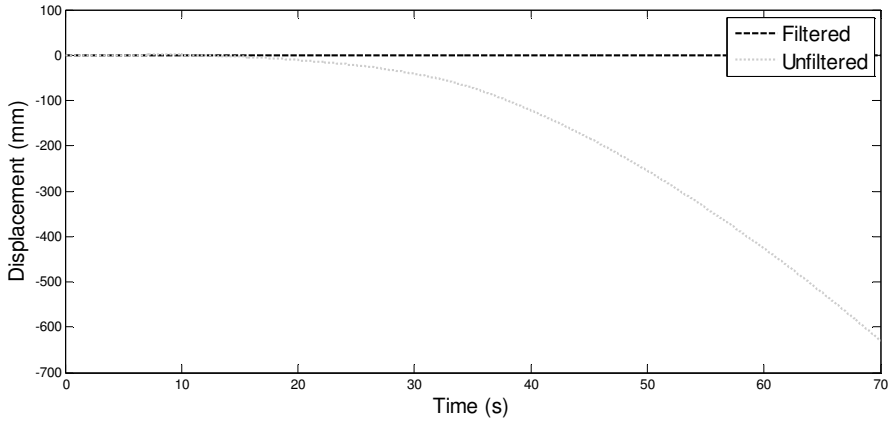

Figure 8.3 Baseline effects of displacement series (15' Untreated)

8.2.2.4. Low Pass Filter

A filter that removes high frequencies is referred to as a low-pass filter. This is the most effective and least subjective method for removing high-frequency noise. An important consideration in selecting low pass filter parameters is the relevance between the Nyquist frequency and the low-pass corner frequency. The Nyquist frequency represents the maximum frequency in which characteristics of the motion can be correctly determined. The Nyquist frequency from the field test is 4096 Hz and was determined as half of the sampling frequency. Frequencies filtered beyond the Nyquist frequency will have no effect on the ground motion record.

8.2.2.5. Filter Parameters

The key parameters to be selected when applying filters are (1) filter order, n and (2) the corner frequency, *fc*. The higher the order of the filter, the more rapid the "roll-off." For example, if the order selected for the filter is too high, the filter could abruptly cut out frequencies associated with real ground motion data and result in severe distortions of the waveform. Mollova (2006) demonstrated the need for filters to be applied at lower orders and found that an 8^{th} order filter produced abnormally different waveforms. Analysis of the field testing data showed that a 6^{th} order filter was appropriate and was therefore applied to each acceleration series.

Another key parameter needed for filter application was selection of corner frequencies. The corner frequencies represent the minimum and maximum frequencies in which the data is judged to be reliable in terms of signal-to-noise ratio. Boore and Bommer (2004) propose various methods for optimal selection of corner frequencies. In reference to the proposed criteria, the corner frequencies were chosen based on (1) comparisons of the Fourier Spectrum with that of the noise and (2) visual inspection of the velocity and displacement time-histories obtained by double integration.

To select the corner frequencies, a fast Fourier transform function was used to convert data to the frequency domain and obtain the Fourier Spectrum. The Fourier Spectrum for a shaking source 4.6 m (15 ft) away from the measured response is illustrated in Figure 8.4 for the treated and untreated test areas. The Fourier spectra show how the amplitude of the ground motion is distributed with respect to frequency and the frequency content of the given acceleration record can be fully determined through the Fourier series plots. For example, a relatively constant amplitude of the Fourier spectrum at frequencies outside of the motion frequency band indicate a large amount of low/high frequency noise. The Fourier spectra are also used to identify the predominant period or fundamental frequency of the motion. From Figure 8.4, the fundamental frequency occurs at approximately 35Hz.

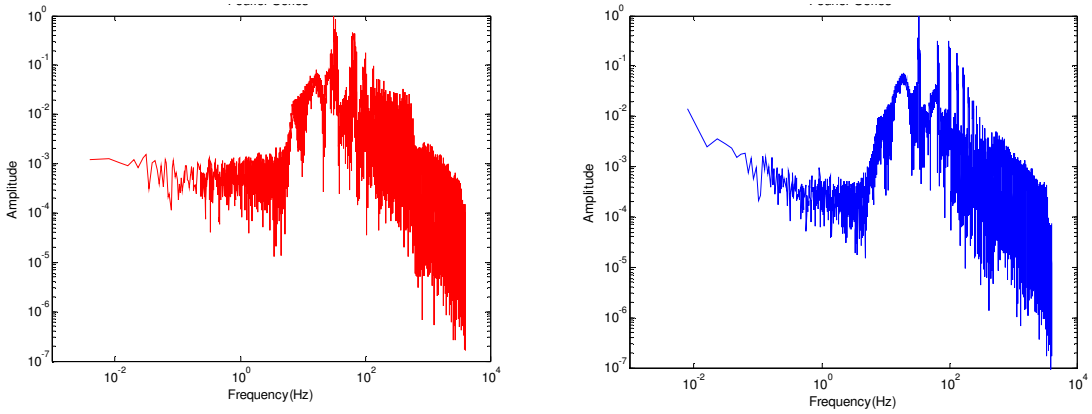

(a) **(b)**

Figure 8.4 Fourier Series of Acceleration Data for (a) 15' Treated and (b) 15' Untreated Test Area

With consideration of the Fourier Spectum, a sixth order filter was selected with cutoff frequencies of 15 Hz and 4000 Hz for all acceleration records. The selected filter parameters were checked by plotting unfiltered vs. filtered displacement records, such as that shown in Figure 8.3.

8.2.3. Integration and Decimation of Data

In order to obtain cyclic strain data from the recorded ground motion, it was necessary to obtain the transient displacements from acceleration recordings by double integrating the acceleration series. Single and double integrations were performed on the filtered acceleration series to obtain velocity and transient displacements, respectively. It should be noted that the original acceleration data was recorded in units of g's. Prior to integration for obtaining velocity and displacement data, the signals were converted to m/s^2.

The acceleration, velocity, and displacement series were decimated to every 10^{th} point to further reduce file size. Decimation was performed after integration because decimation prior to integration was observed to influence the velocity and displacement response (Figure 8.5).

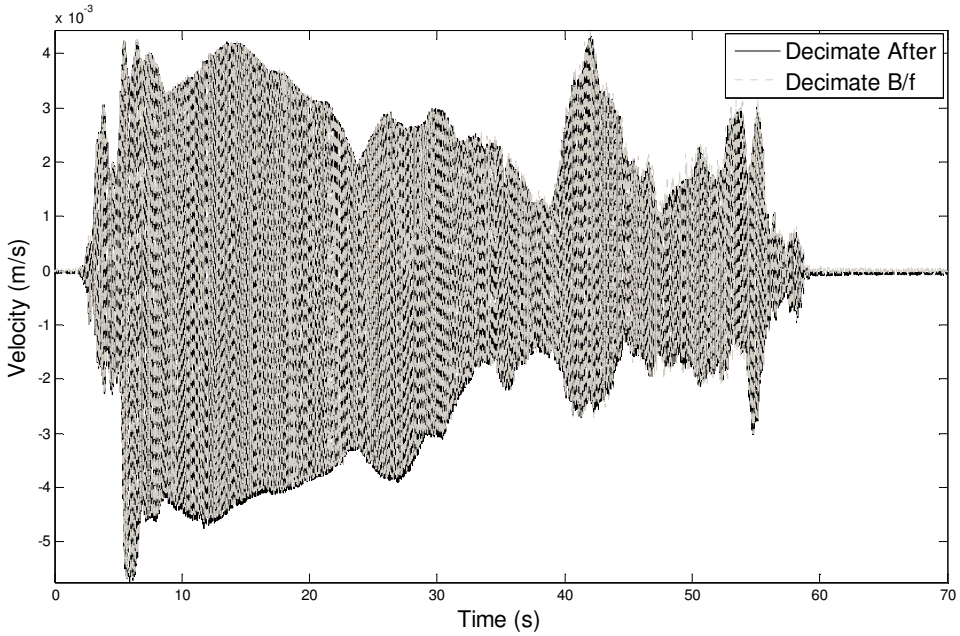

(a)

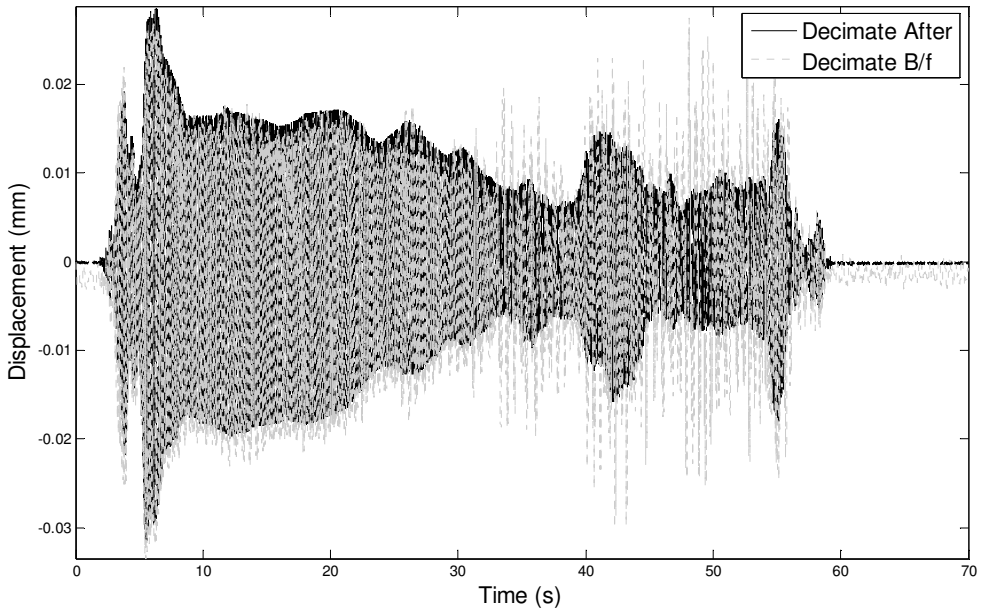

(b)

Figure 8.5 Effects of Decimating Before and After Integration for (a) Velocity and (b) Displacement Series

8.3. Cyclic Shear Strains and Finite Element Analysis

From the transient displacement records obtained, shear strains were calculated based on finite element analysis techniques. As previously discussed, each liquefaction sensor consisted of 3 accelerometers that formed a triangular array in 2-D space. For each accelerometer, motions were recorded in the *x*, *y*, and *z* directions. In this way shear strains were obtained in both in-plane and cross-plane directions. The methods for obtaining shear strain will be discussed in this section and were performed in the following sequence:

1. Define Nodal Geometry
2. Compute shape function
3. Compute shear strains

8.3.1. Nodal Geometry

Each sensor array was oriented such that it formed a triangular element consisting of 3 nodes in 2-dimensional space as shown in Figure 8.6. In terms of finite element analysis, this configuration represents a constant strain triangle defined as a plane triangle whose displacements vary linearly with Cartesian coordinates to produce a constant strain field. In other words, the displacements are assumed to vary linearly between nodes.

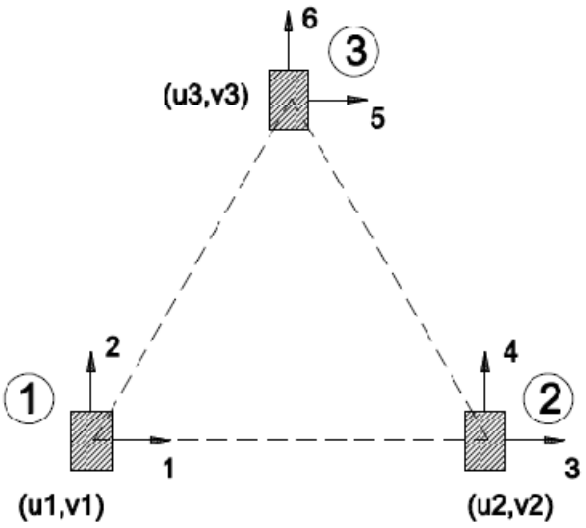

Figure 8.6 Nodal Geometry for Constant Strain Triangle

8.3.2. Shape Function

The strain approximation in terms of the strain-displacement matrix can be expressed as

Equation 8-1 $$\{\boldsymbol{\varepsilon}\} = [\boldsymbol{B}] \cdot \{\boldsymbol{d}\}$$

where *{ε}* and *{d}* are the strain and stress fields, respectively, and *[B]* is referred to as the strain displacement matrix. Definition of normal strain, ε, can be described as the change in length divided by the original length. The shear strain, γ, is the amount of change in a right angle. The strains can be computed from the displacement field such that the *x*-direction displacement, *u*, and *y*-direction displacement, *v*, are functions of the coordinates: *u=u(x,y)* and *v=v(x,y)*. By applying

a partial derivative and letting Δx and Δy approach zero, the 2D strain components in a Cartesian coordinate system are defined as

Equation 8-2
$$\varepsilon_x = \frac{\partial u}{\partial x}\ , \quad \varepsilon_y = \frac{\partial v}{\partial y}\ , \quad \gamma_{xy} = \frac{\partial u}{\partial x} + \frac{\partial v}{\partial x}$$

For a two dimensional element, Equation 8-2 can be rewritten in matrix form as

Equation 8-3
$$\begin{Bmatrix} \varepsilon_x \\ \varepsilon_y \\ \gamma_{xy} \end{Bmatrix} = \begin{bmatrix} \frac{\partial}{\partial x} & 0 \\ 0 & \frac{\partial}{\partial y} \\ \frac{\partial}{\partial y} & \frac{\partial}{\partial x} \end{bmatrix} \begin{Bmatrix} u \\ v \end{Bmatrix}$$

By expanding Equation 8-3 we obtain matrix expressions for defining horizontal, vertical and shear strains in two dimensions. The strain displacement matrix, *[B]*, from Equation 8-1 represents the linear interpolation of strain as a function of displacement between nodes defined as

Equation 8-4
$$[B] = [\partial][N],$$

where *N* is referred to as the shape function for a 2 dimensional CST. The shape function represents the interpolated displacement at any point within the element in terms of the displacements occurring at the nodes of the CST. In this way, the resulting shape function N_i will yield a value of 1 at node *i* and a value of 0 at all other nodes. For a 2 dimensional constant strain triangle, the shape functions for nodes 1,2 and 3 from Figure 8.6 are as follows:

Equation 8-5
$$N_1 = \frac{a_1 + b_1 x + c_1 y}{2A}\ , \quad N_2 = \frac{a_2 + b_2 x + c_2 y}{2A}\ , \text{ and } \quad N_3 = \frac{a_3 + b_3 x + c_3 y}{2A}$$

where *A* represents the area of the CST element and *a,b*,and *c* are functions of the locations at each node in global coordinates. Further details on the physical meaning and derivations of the shape function can be found in any finite element analysis text, including Cook et al. (2002).

As can be seen from Equation 8-5 above, it is necessary to define the locations of the nodes in global coordinates (*x* and *y*) in order to compute the shape function. Figure 8.7a and Figure 8.7b show the upper and lower sensor array layout for the untreated area. From Figure

8.7a, Sensor #5, Sensor #2, and Sensor #4 represent CST nodes 1,2, and 3 respectively. From Figure 8.7b, Sensor #1, Sensor #8, and Sensor #3 represent nodes 1, 2, and 3 respectively. Figure 8.8a and Figure 8.8b shows the north and south sensor arrays from the treated test area. Similarly, sensors #5,#9,#8 (north array) and Sensors #6,#1,#3 represent nodes 1,2,and 3.

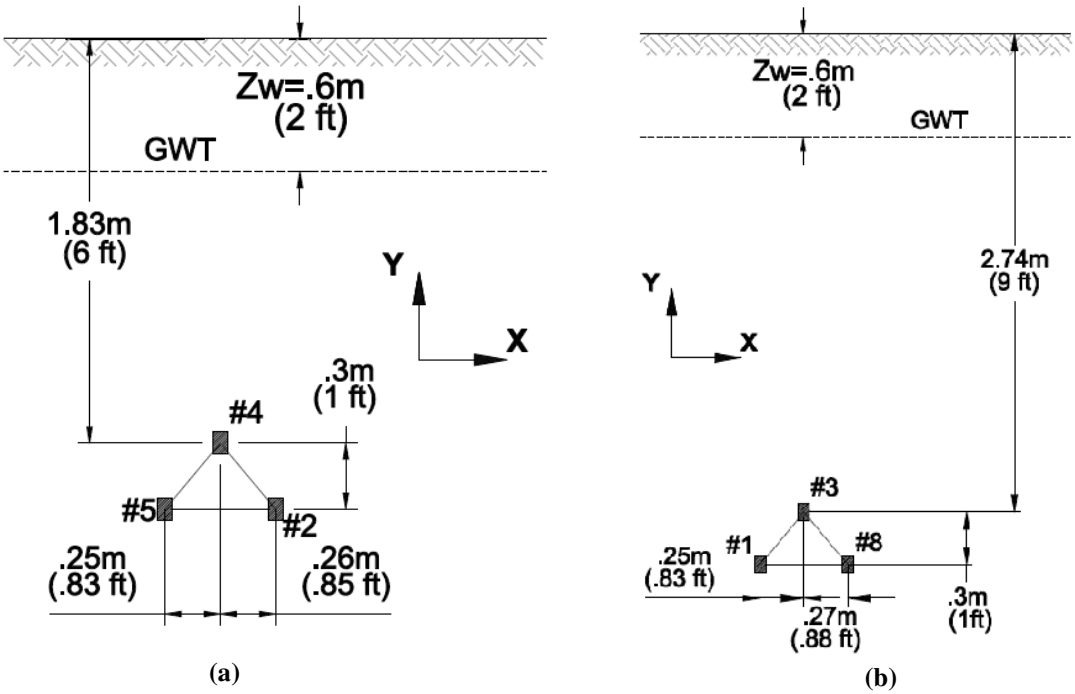

Figure 8.7 Untreated Sensor Layout for (a) Upper and (b) Lower Triangular Arrays

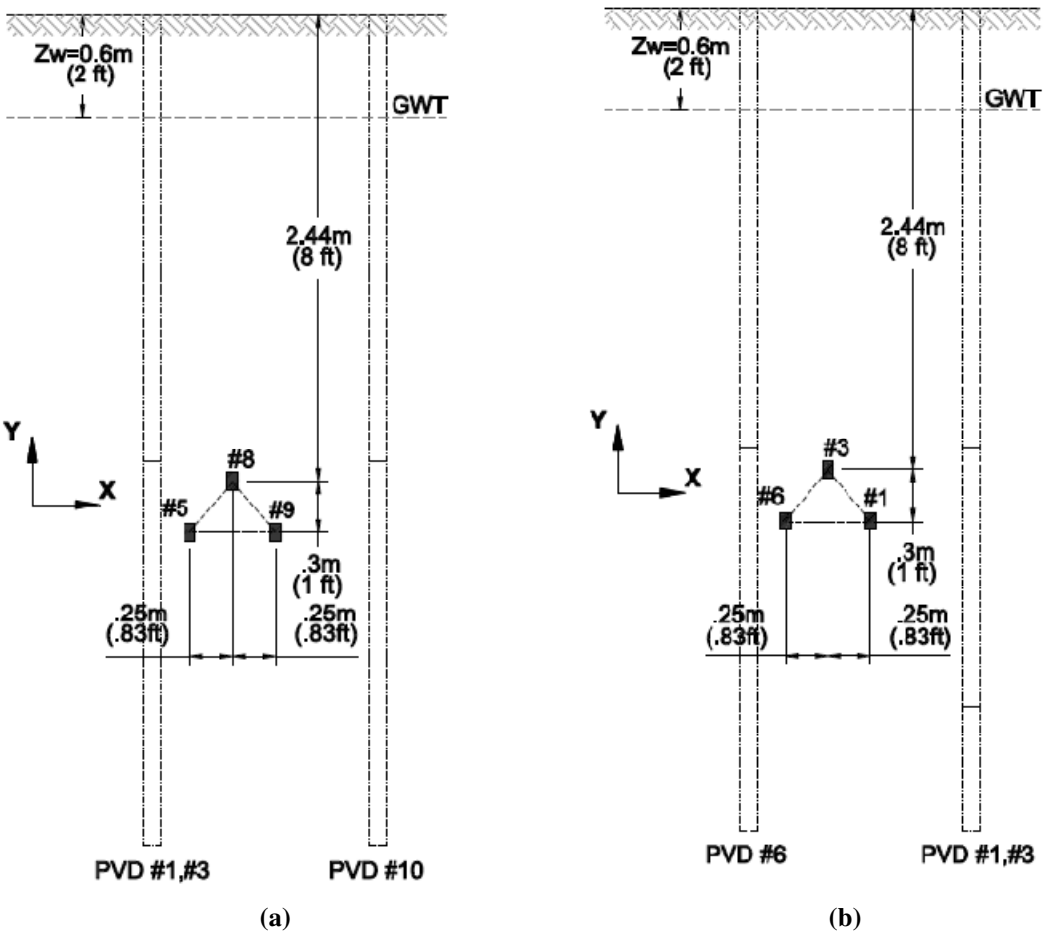

Figure 8.8 Treated Sensor Layout for (a) North and (b) South Triangular Arrays

In each case, node 1 is arbitrarily selected to be the origin such that $x_1=y_1=0$ and $y_2 = 0$. The area of the element is constant and can be expressed in terms of global coordinates as

Equation 8-6

$$A = {}^{1}/_{2} \cdot x_2 \cdot y_3$$

Substitution of Equation 8-5 into Equation 8-6 (where $x_1=y_1=0$ and $y_2 = 0$) yields the following shape function:

$$N_1 = \frac{x_2y_3 - y_3x + x_3y - x_2y}{2A} = \left(\frac{1}{x_2y_3}\right) \cdot x_2y_3 - y_3x + x_3y - x_2y,$$

Equation 8-7

$$N_2 = \frac{y_3x - x_3y}{2A} = \left(\frac{1}{x_2y_3}\right) \cdot x_2y_3 - y_3x + x_3y - x_2y,$$

$$\text{and } N_3 = \frac{x_2y}{2A} = \left(\frac{1}{x_2y_3}\right) \cdot x_2y_3 - y_3x + x_3y - x_2y$$

The global geometry from each of the sensor arrays used to solve for the shape functions are summarized in Table 8.1. Referring back to Equation 8-1, the stress field for the CST in 2 dimensions is defined as

Equation 8-8

$$\{\boldsymbol{d}\} = \begin{bmatrix} \boldsymbol{u_1} \\ \boldsymbol{v_1} \\ \boldsymbol{u_2} \\ \boldsymbol{v_2} \\ \boldsymbol{u_3} \\ \boldsymbol{v_3} \end{bmatrix}$$

Substitution of Equation 8-8 and the known shape function yields the following solution for the horizontal, vertical and shear strains.

Equation 8-9

$$\boldsymbol{\varepsilon_x \approx \frac{1}{2x_2y_3}(-y_3u_1 + y_3u_2 + 0)}$$

Equation 8-10

$$\boldsymbol{\varepsilon_y \approx \frac{1}{2x_2y_3}((x_3 - x_2)v_1 + c_2v_2 + c_3v_3)}$$

Equation 8-11

$$\boldsymbol{\gamma_{xy} \approx \frac{1}{2x_2y_3}(x_3 - x_2)u_1 + -y_3v_1 + -x_3u_2 + y_3v_2 + x_2u_3 + 0}$$

Table 8.1 Global Geometry of Sensor Elements

Node	Array Description	Sensor	$x_{i(Sensor)}$ (m)	$y_{i(Sensor)}$ (m)
1	Untreated Upper	5	$x_{1(5)} = 0$	$y_{1(5)} = 0$
	Untreated Lower	1	$x_{1(1)} = 0$	$y_{1(1)} = 0$
	Treated South	6	$x_{1(6)} = 0$	$y_{1(6)} = 0$
	Treated North	5	$x_{1(5)} = 0$	$y_{1(5)} = 0$
2	Untreated Upper	2	$x_{2(2)} = .51$	$y_{2(2)} = 0$
	Untreated Lower	8	$x_{2(8)} = .52$	$y_{2(8)} = 0$
	Treated South	1	$x_{2(1)} = .5$	$y_{2(1)} = 0$
	Treated North	9	$x_{2(9)} = .5$	$y_{2(9)} = 0$
3	Untreated Upper	4	$x_{3(4)} = .25$	$y_{3(4)} = .3$
	Untreated Lower	3	$x_{3(3)} = .25$	$y_{3(3)} = .3$
	Treated South	3	$x_{3(3)} = .25$	$y_{3(3)} = .3$
	Treated North	8	$x_{3(8)} = .25$	$y_{3(8)} = .3$

8.4. Signal Processing of Pore Pressure Records

Signal processing of the pore pressure responses from the field test was performed in the following sequence using the Mathworks Inc. MATLAB® software program:

1. Truncation and zero correction
2. Apply Low-Pass Filter and Decimation
3. Determine excess pore pressure ratios vs. time

8.4.1. Truncating, Zero Correction, and Filtering

Similar to the acceleration data, pore pressure data was selected to begin one second prior to shaking. It should be noted that in order to observe the behavior in dissipation after shaking, the data was retained until the end of the recording. Zero correction was done in the same manner as zero correction for the acceleration records.

The Fourier spectrum in Figure 8.9 shows that the signal was dominated by low frequencies and therefore, only a low-pass Butterworth filter was necessary. A 6^{th} order low pass Butterworth filter was applied to each of the pore pressure records with a corner frequency of 60 Hz. Figure 8.10 compares the excess pore pressure prior to filtering the data and after filtering. The response demonstrates the fact that the filter retains the transient pore pressures during shaking while removing erroneous signals due to noise. Similar to acceleration data, pore pressure data was decimated to every 10^{th} data point to reduce file size.

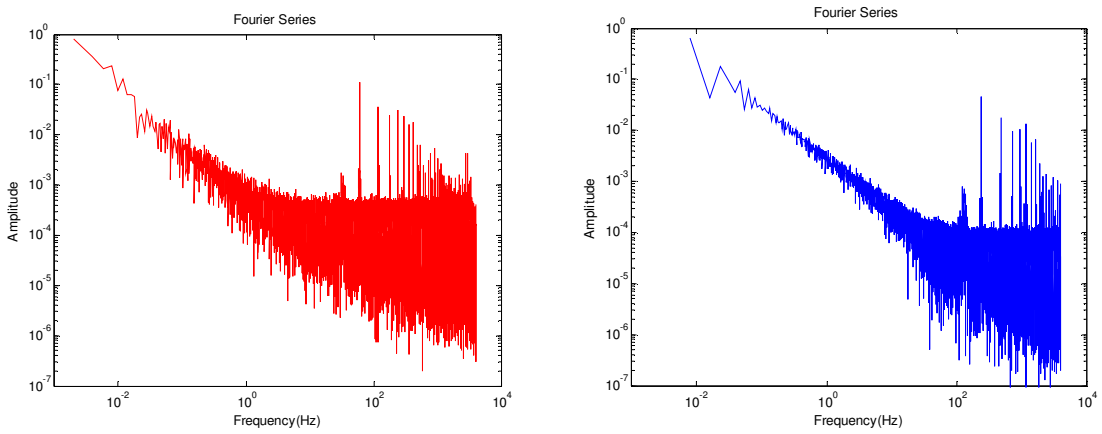

(a) **(b)**

Figure 8.9 Fourier Series for (a) Treated and (b) Untreated Pore Pressure Response

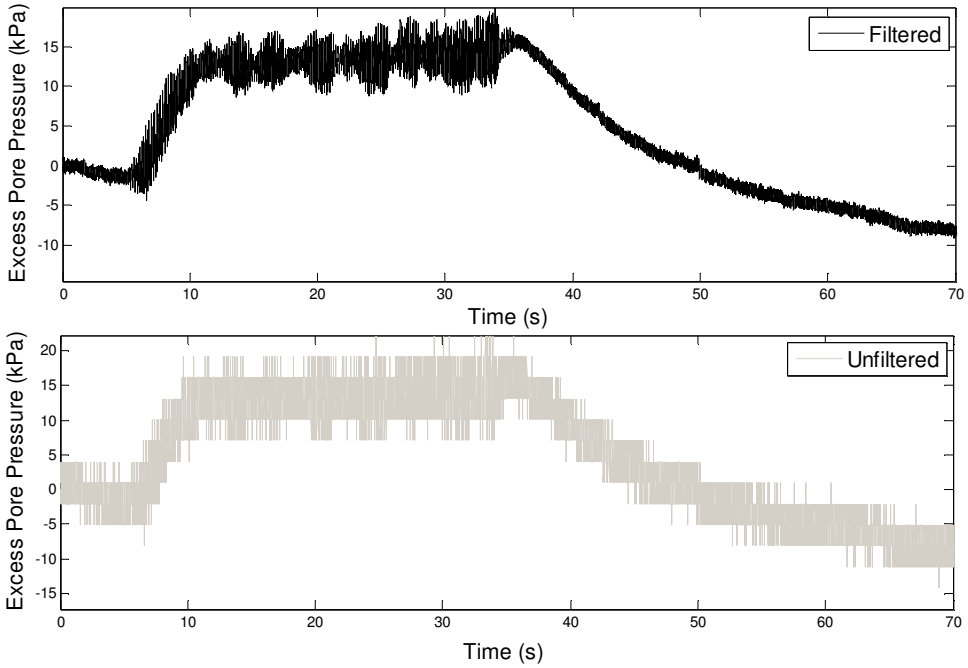

Figure 8.10 Filtered vs. Unfiltered Pore Pressure Response

8.4.2. Determination of Excess Pore Pressure Ratio

Excess pore pressure ratios were established throughout each shaking event by dividing the excess ratio recordings by effective stress. The effective stresses were determined at each of

the liquefaction sensor locations (Table 8.2). Well tests were carried out in the field to measure the depth of the groundwater table and was determined to be 0.61 m (2 ft). Soil unit weights were based upon site characterization data that was reported by the geotechnical contractor (S&ME, 2006). The wet and saturated unit weights were reported at 18.8 kN/m^3 (120 pcf) and 19.6 kN/m^3 (125pcf), respectively.

Table 8.2 Effective Stress Summary

Sensor	Description	Depth (m)	σ'_{vo} (kN/ft^2)
ACC1 and ACC8	Lower Untreated	3	47
ACC3	Lower Untreated	2.7	43
ACC2 and ACC5	Upper Untreated	2.1	34
ACC4	Upper Untreated	1.8	29
ACC5 and ACC9	North Treated	2.7	43
ACC8	North Treated	2.4	38
ACC1 and ACC6	South Treated	2.7	43
ACC3	South Treated	2.4	38
ACC2 and ACC4	Alone Treated	2.7	43

8.5. Cross-hole Testing

Pre and post shaking cross-hole tests were performed in the treated and untreated test locations to determine shear wave velocities. The cross-hole test involved generating a seismic wave by striking an impulse rod encapsulated by a steel tube inserted into the ground. Striking the impulse rod sends a compression wave coupled with soil as it travels down the length of the rod. In this way, body waves (e.g. P-waves and S-waves) are generated through the formation which are picked up through two adjacent liquefaction sensors monitoring accelerations. For generating the wave, a hammer was used to strike the cross-hole source rod and several recordings were performed for verification purposes.

The velocities of the waves were determined by a known travel distance and travel time. The travel distance was taken as the lateral distance between the liquefaction sensors. The travel time is determined as the difference in arrival times between the two liquefaction sensors. Typically, travel times for determining wave velocities are determined by identifying the arrival points of waves generated from the sensor data. However, in situ tests can be very sensitive to noise and therefore, signal processing techniques, such as filtering, can more accurately define travel times. As a result, lowpass and highpass filters were applied to the signal for baseline correction and noise removals. Travel times were then taken as the difference of first arrivals between each of the signals. It should be noted that arrival times were manually selected from the recordings, such as those illustrated in Figure 8.11.

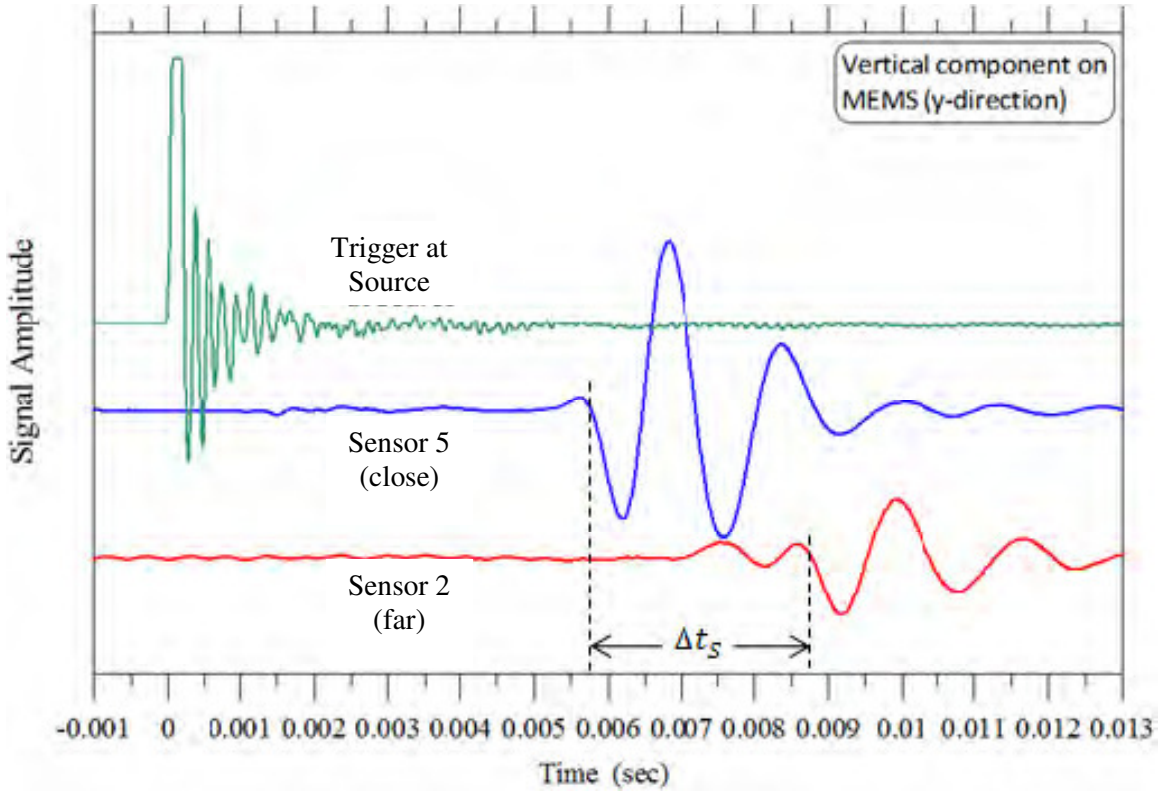

Figure 8.11 Cross-hole Test Recording for Untreated Test Area (Marinucci, 2010)

For the treated test area, cross hole testing was conducted using the standalone liquefaction sensors #2 and #4 at a depth of 2.7 m (9 ft). The source pipe was placed closest to sensor #2 at a lateral distance of 1.5 m (5 ft). For the untreated test area, the cross hole tests were conducted using the bases of the upper and lower triangular sensor arrays. In this way, cross-hole tests were performed at two different depths. From the lower triangular array, cross-hole testing was performed at a depth of 3 m (10 ft) using sensors #1 and # 8. The source pipe was placed closest to sensor #1 at a lateral distance of 3.9 m (12.8 ft). From the upper triangular array, cross-hole testing was performed at a depth of 2 m (7 ft) using sensors #2 and #5. The source pipe was placed closest to sensor #5 at a lateral distance of 2.7 m (8.75 ft) (Figure 7.18).

8.6. Cone Penetration Test Results

Results of the post-grouting CPT performed in the treated area and CPT performed in the untreated test area is presented in Figure 8.12. Overall, the tip stresses are about twice as high compared to that of the untreated area. Cone resistances in the upper third of the treatment zone are about 12 MPa (112 tsf) while cone resistances in the bottom third of the treatment zone is about 30 MPa (280 tsf). For depths of 2.4-2.7m (8-9 ft), cone resistances range from 5 MPa (47 tsf) to7 MPa (65 tsf). This is an indication that a weaker layer does exist at this depth range despite grouting. At about 3 m (10 ft), the cone resistance dramatically increases to almost 32 MPa (300 tsf). Readings of cone resistance are maxed out at this depth and at this point, the cone was extracted. The dramatic increase in cone resistance may be an indication of a preferential grout zone or the existence of a thin, gravel layer. As discussed in Chapter 7, more variability existed in the treated test area compared with the untreated test area. As a result, it is difficult to directly compare pre-grout and post-grouted data since CPTs were not performed in the exact location. Overall, the upper third and bottom third of the test area represent the upper limits of

the pre-grout test data while the data at depths of 2.4-2.7 m (8-9 ft) represent lower limits of the pre-grout test data . The CPT data presented in Figure 8.12 illustrate non-uniformity within the treatment area that may be the combined result of non-uniformity in the soil profile and non-uniformity in treatment coverage. Therefore, CPT test data in the field does not prove to be a reliable method to assess treatment unless the soil profile throughout the test area was uniform or the CPT tests were conducted in the exact same locations.

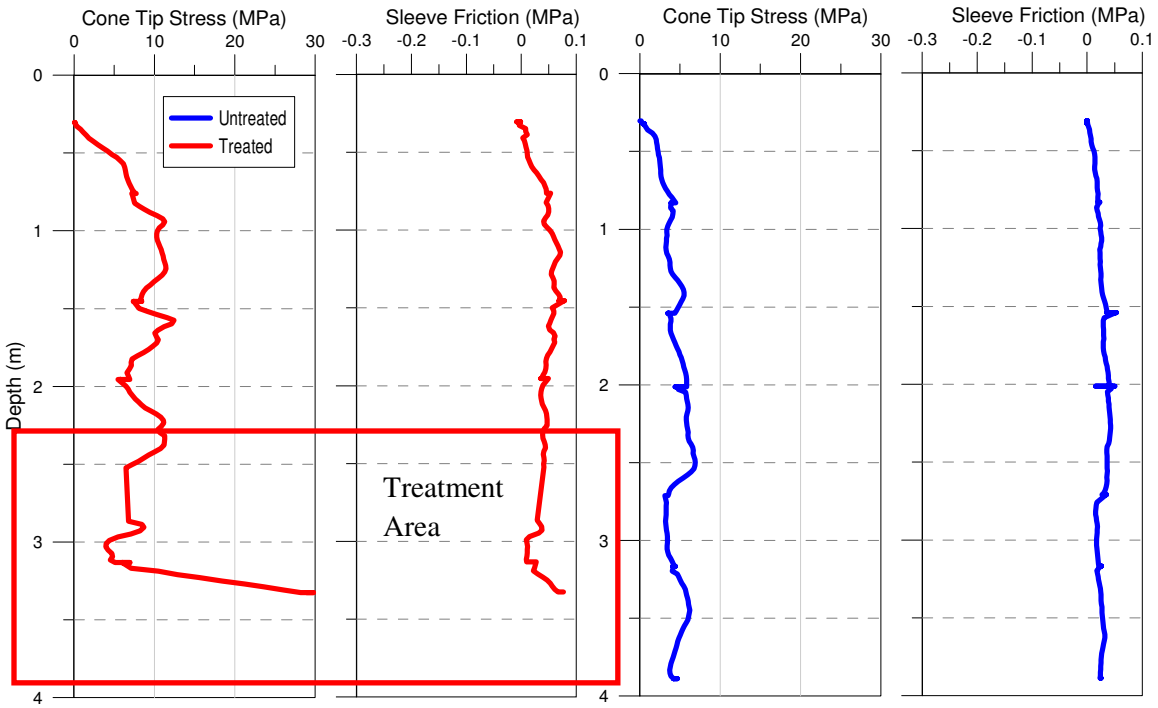

Figure 8.12 Treated and Untreated Cone Penetration Test Data

8.7. Cross-hole Testing Results

The results of the cross-hole tests are shown in Table 8.3. In general, the grouted soils show higher shear wave velocities for both pre and post-shaking measurements. After shaking, the reduction in shear wave velocity for the untreated area in the upper array shows a 42% decrease in V_S from the shaking event while the grouted area experiences a 25% decrease.

Table 8.3 Cross-hole test summary

Cross-hole Test	Location	Depth (ft)	Δt (sec)	Distance (ft)	Velocity (ft/s)	Velocity (m/s)	Shear Modulus, G (MPa)
Untreated Pre-Shake	S Wave Lower Array	10	0.0026	1.71	670	204	83
	S Wave Upper Array	7	0.0021	1.71	833	254	128
Untreated Post-Shake	S Wave Lower Array	10	0.0027	1.71	629	192	73
	S Wave Upper Array	7	0.00353	1.71	485	148	43
Treated Pre-Shake	S Wave	9	0.0027	2.63	987	301	180
Treated Post Shake	S Wave	9	0.0035	2.63	747	228	103

8.8. Acceleration Response

The acceleration response is based upon shaking events that occurred at various distances away from the liquefaction sensors. Prior to presenting the results, it should be noted that several sensors failed during the shaking sequence. The sensors that failed in the treated and untreated test areas are summarized in Table 8.4.

Table 8.4 Summary of Sensors that Failed during Testing

Motion	Sensor Failures	
	Treated	Untreated
1.5 m	AccY5, AccZ5	AccX4, AccY4, AccZ4
3 m	AccY5, AccZ5, AccZ2	AccX4, AccY4, AccZ5
4.6 m	AccY5, AccZ5	--
6.1 m	AccX9,AccX4, AccY4, AccY5, AccY9, AccZ5	--

Shaking began 6.1 m (20 ft) away from the liquefactions sensors and was incrementally increased such that the source motion became closer to liquefactions sensors. The purpose of this sequence was to gradually increase the induced PGA response. For each record, the average

PGA was calculated for the *x*,*y*, and *z* directions and is summarized in Table 8.5 and Table 8.6 for the untreated and treated areas, respectively.

Table 8.5 Average Peak Base Acceleration for Untreated Area

Motion (Untreated)	Upper Sensor (g)			Lower Sensor (g)		
	PGA_X	$GM\text{-}PGA_y$	$GM\text{-}PGA_z$	$GM\text{-}PGA_X$	$GM\text{-}PGA_y$	$GM\text{-}PGA_z$
1.5 m	0.42	0.55	0.30	1.71	1.17	0.90
3 m	0.21	0.13	0.10	0.29	0.24	0.27
4.6 m	0.14	0.21	0.12	0.07	0.11	0.07
6.1 m	0.07	0.12	0.11	0.06	0.12	0.07

Table 8.6 Average Peak Base Acceleration for Treated Area

Motion (Treated)	North Sensor (g)			South Sensor (g)		
	$GM\text{-}PGA_X$	$GM\text{-}PGA_y$	$GM\text{-}PGA_z$	$GM\text{-}PGA_X$	$GM\text{-}PGA_y$	$GM\text{-}PGA_z$
1.5 m	0.19	0.30	0.27	0.22	0.15	0.19
3 m	0.23	0.40	0.24	0.21	0.19	0.20
4.6 m	0.10	0.13	0.05	0.06	0.09	0.06
6.1 m	0.06	0.07	0.03	0.04	0.05	0.04

Figure 8.13 through Figure 8.28 show the acceleration response in the untreated and treated test areas for shaking motions that occurred 6.1 m (20 ft), 4.6 m (15ft), 3 m (10ft), and 1.5 m (5 ft) away from the measured response. At a distance of 6.1 m (20 ft) and 4.6 m (15ft), the acceleration records in the untreated and treated area indicate that the motion was predominately in the vertical (*y*) direction with similar values of PGA. As expected, the PGA values at a distance of 4.6 m (15 ft) are slightly greater for both test areas. For source distances of 1.5 m (5 ft) and 3 m (10 ft) the untreated area responds with further increases in PGA up to 1.2g. On the other hand, the acceleration response in the treated area is dramatically different from the untreated area. In both the 1.5 m(5 ft) and 3m (10 ft) shakes, the response can be described as a combination of minimal response and high-frequency acceleration spikes. The behavior can be

attributed to numerous factors that may or may not be related to CS treatment. First, if the soil adjacent to the mandrel liquefied during shaking, the measured response in the treated area could have been affected. Second, the CPT data prior to grouting indicates more variability in the treated test area compared with the untreated test area. The existence of thin, stiff soil layers between the mandrel and the sensors can preclude transmission of the strong seismic accelerations. Another possibility is that colloidal silica may have produced stiff zones in concentrated areas which may have also inhibited the transmission of the response.

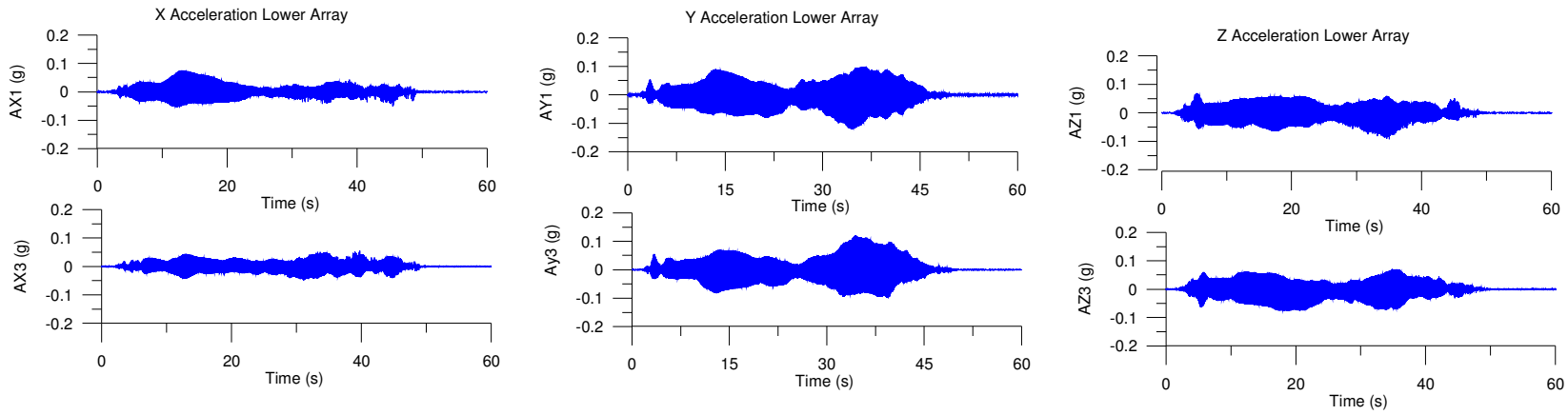

Figure 8.13 Untreated Lower Array for 6.1 m Shake

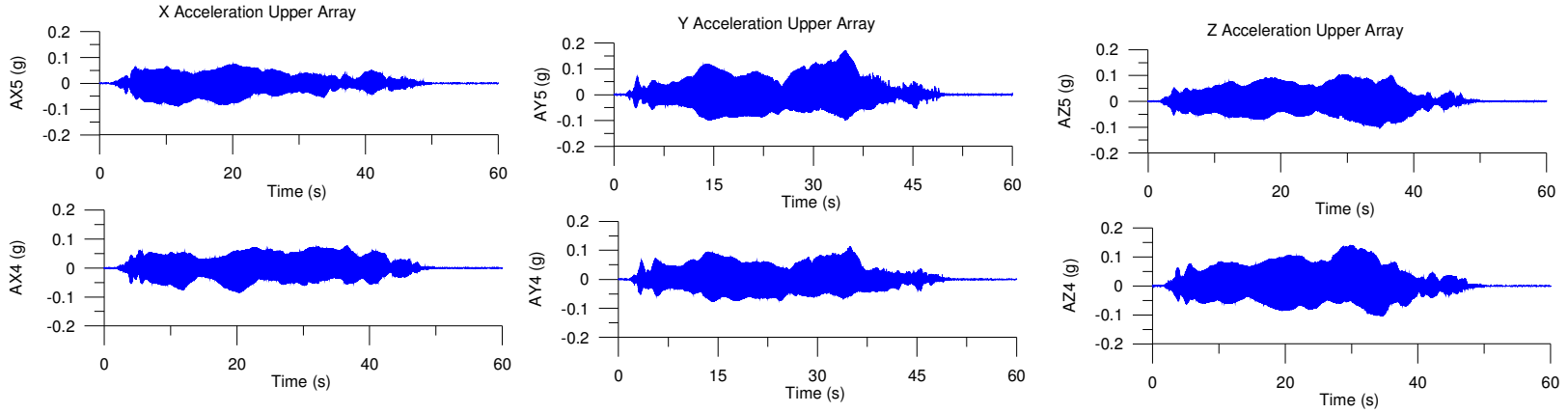

Figure 8.14 Untreated Upper Array for 6.1 m Shake

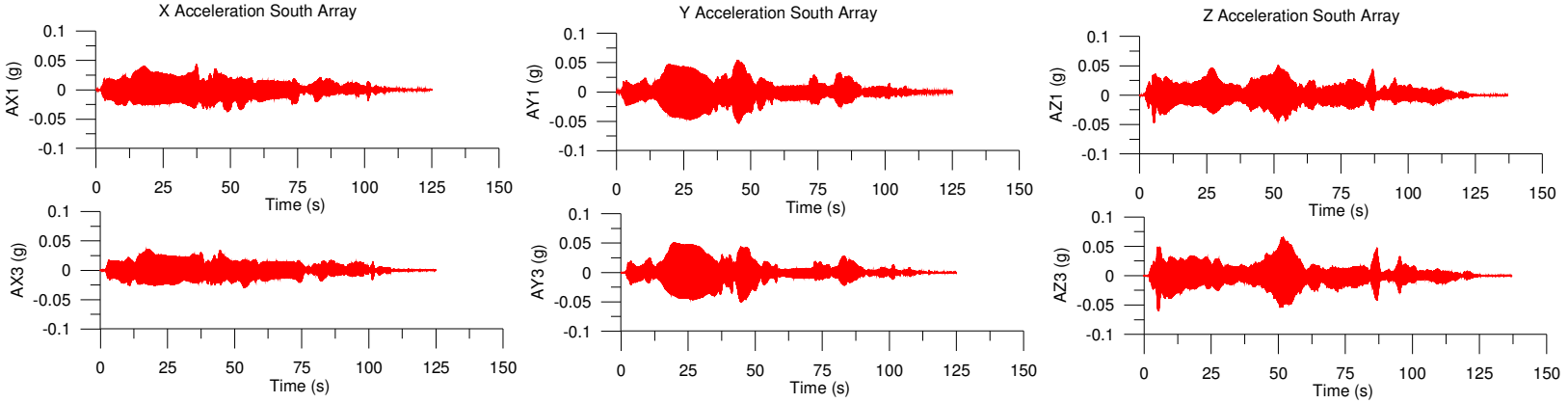

Figure 8.15 Treated South Array for 6.1 m Shake

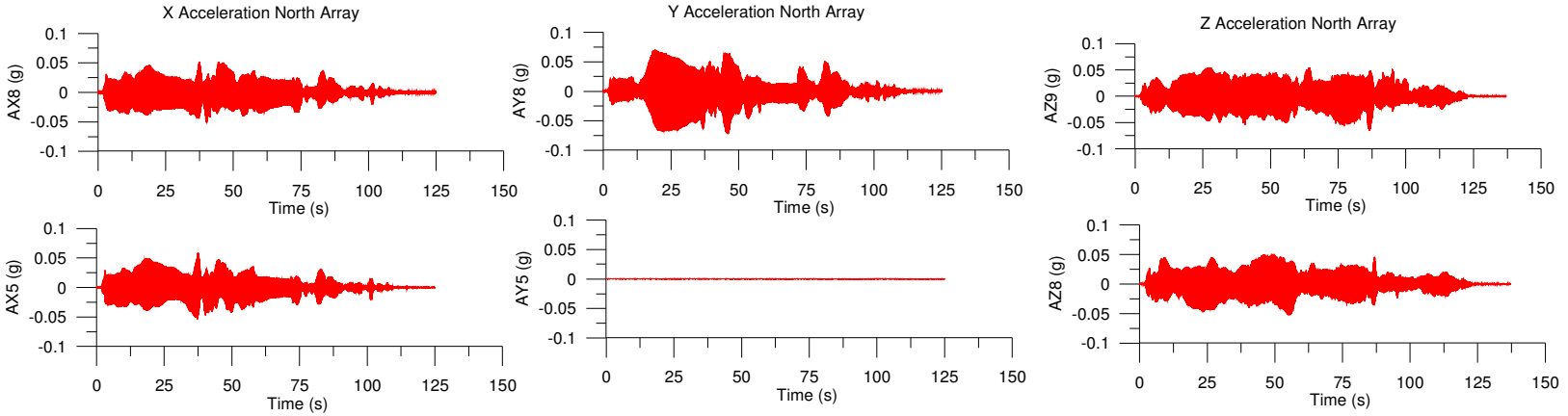

Figure 8.16 Treated North Array for 6.1 m Shake

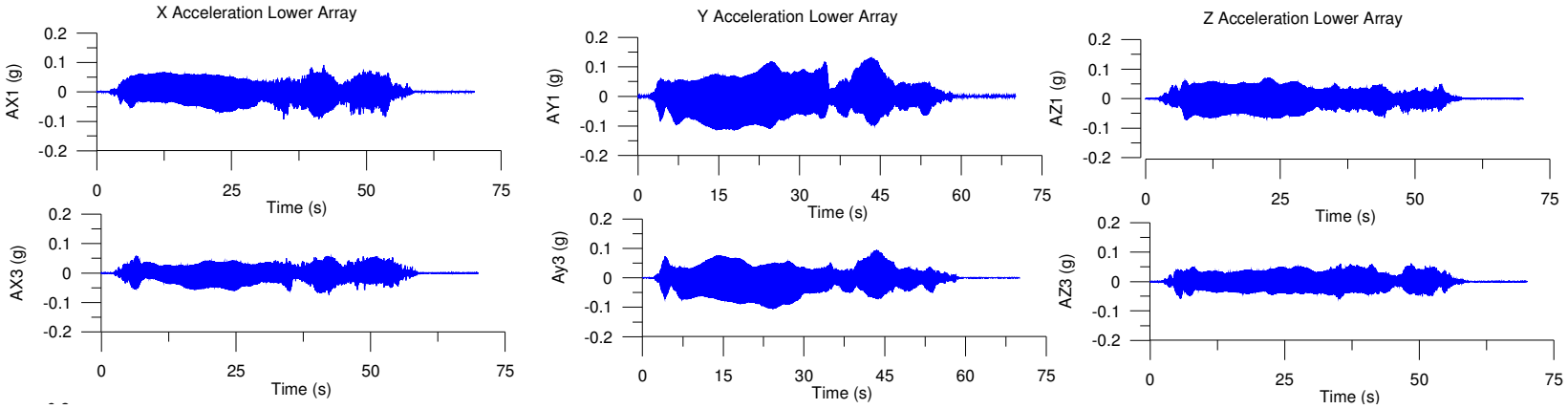

Figure 8.17 Untreated Lower Array for 4.5 m Shake

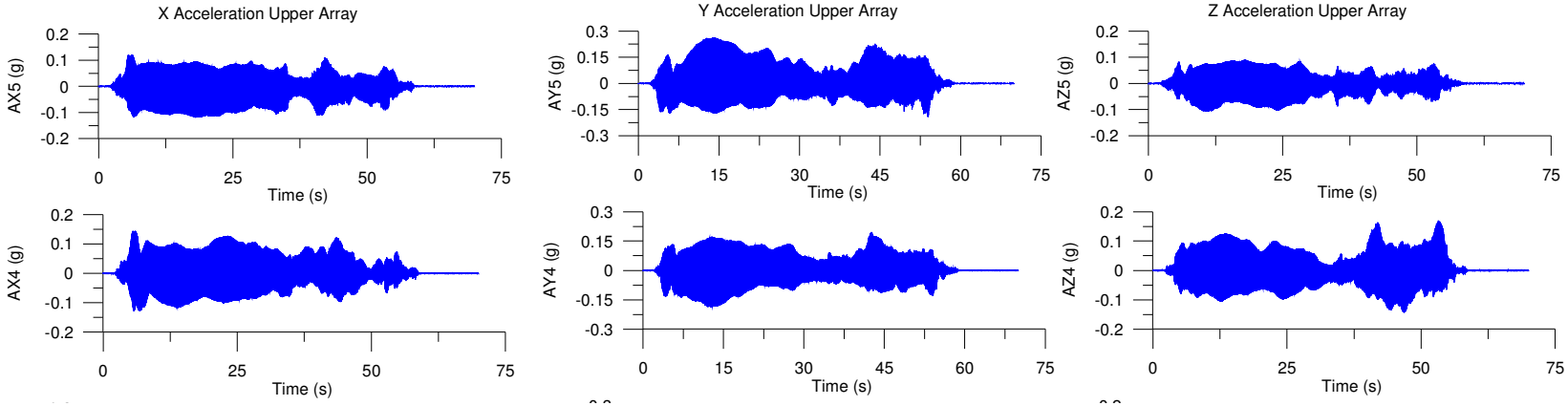

Figure 8.18 Untreated Upper Array for 4.5 m Shake

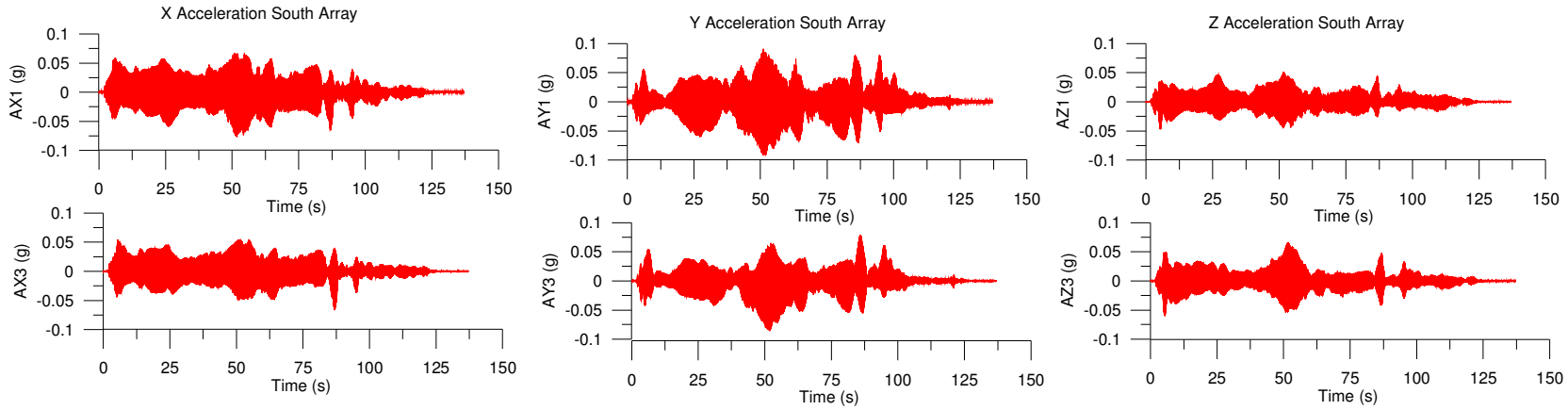

Figure 8.19 Treated South Array for 4.5 m Shake

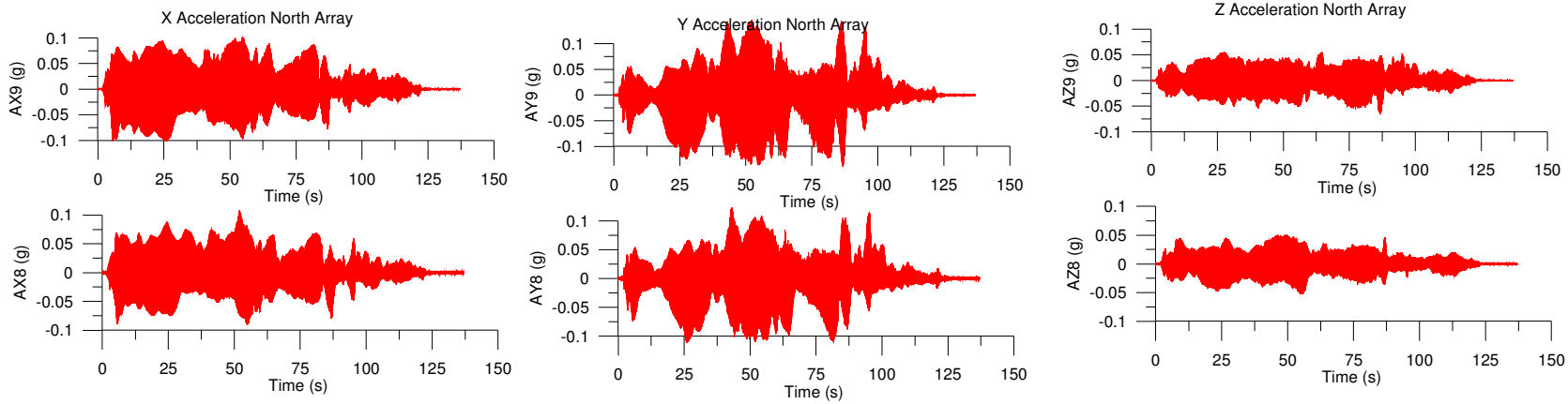

Figure 8.20 Treated North Array for 4.5 m Shake

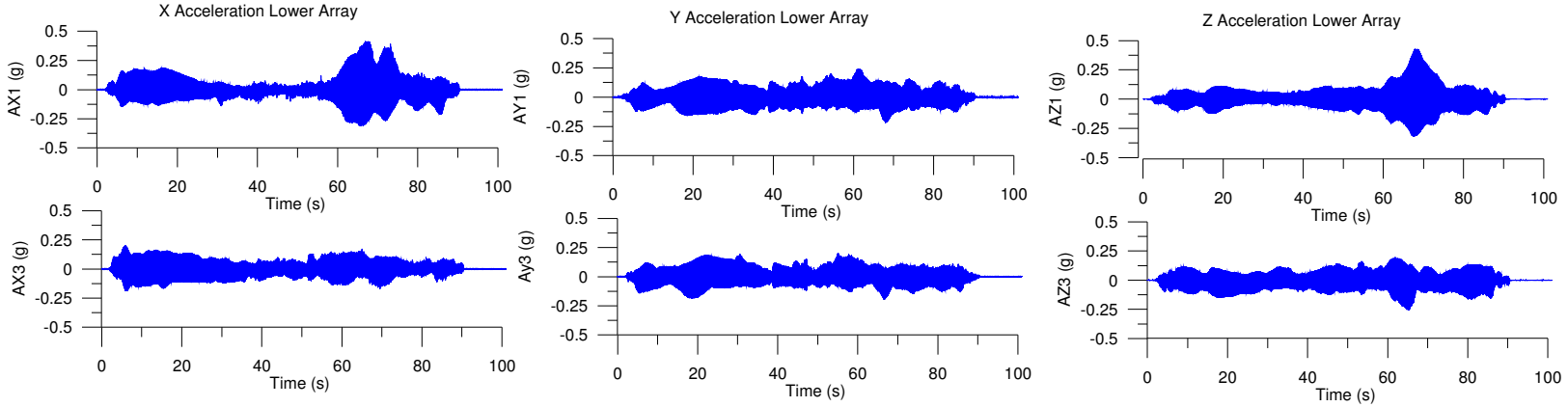

Figure 8.21 Untreated Lower Array for 3.0 m Shake

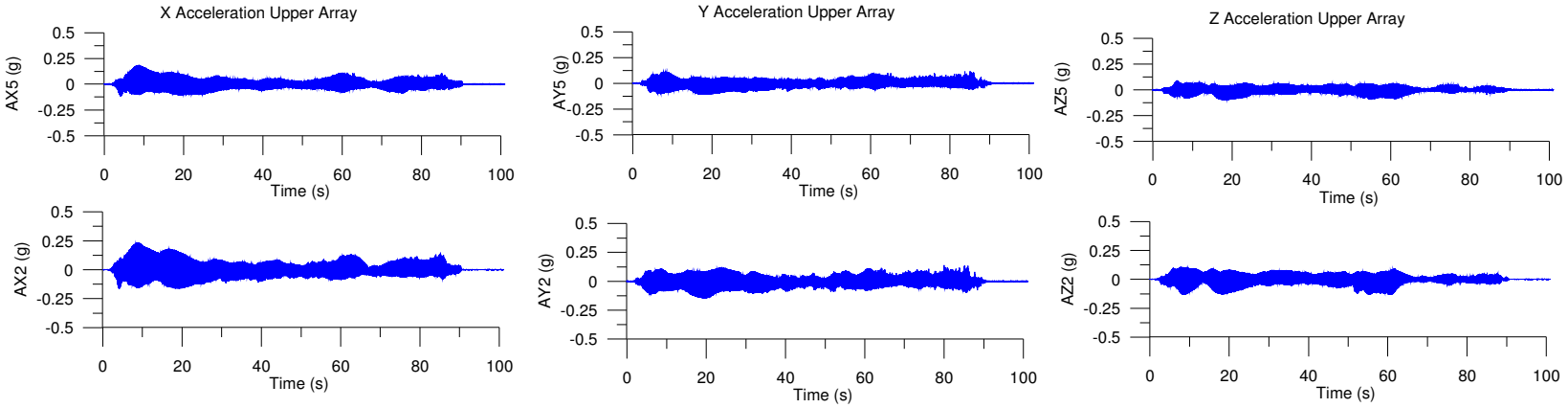

Figure 8.22 Untreated Upper Array for 3.0 m Shake

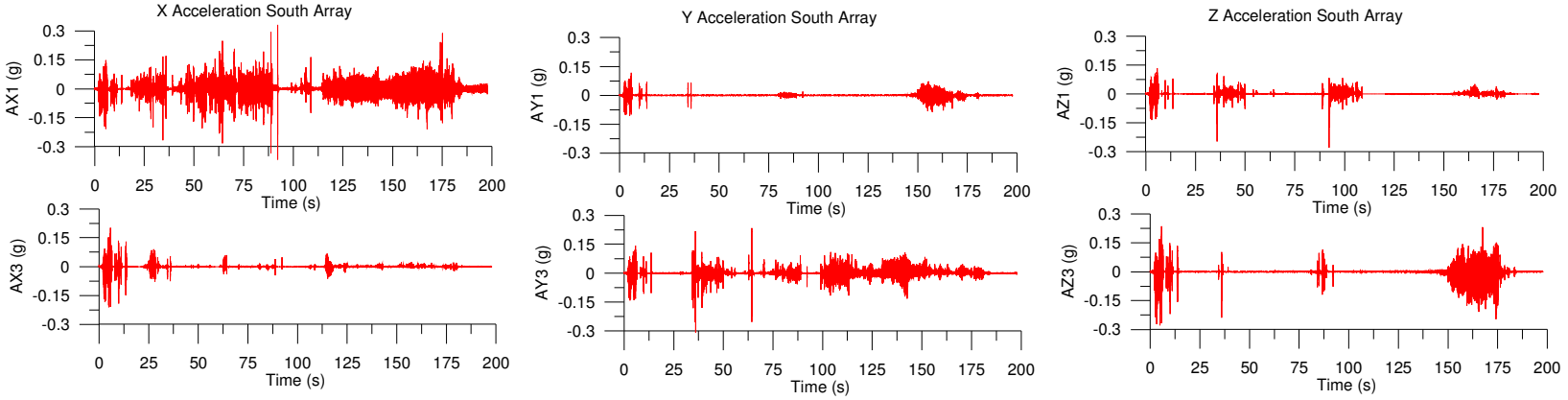

Figure 8.23 Treated South Array for 3.0 m Shake

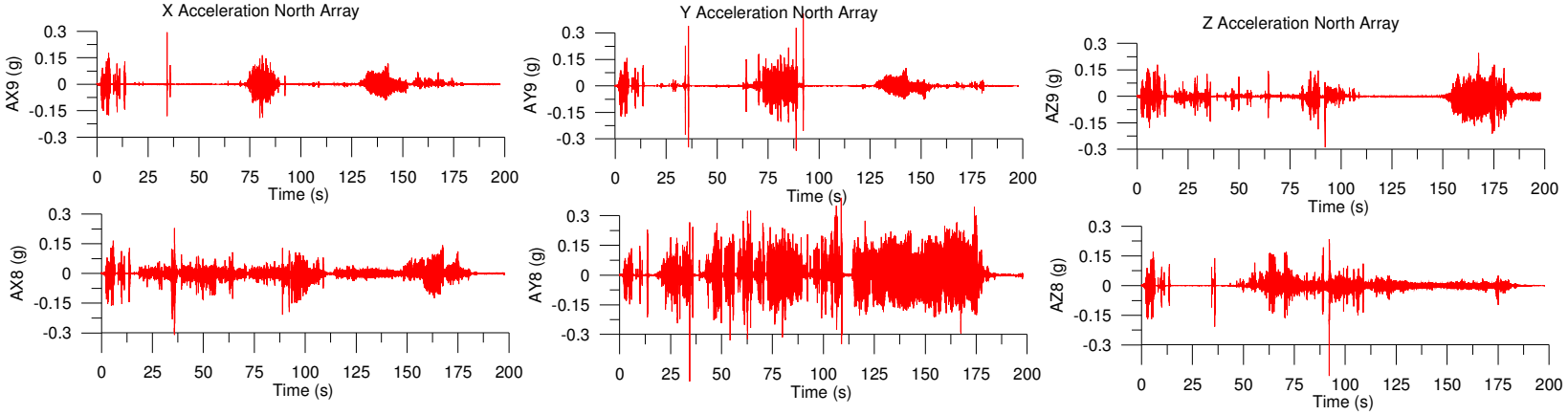

Figure 8.24 Treated North Array for 3.0 m Shake

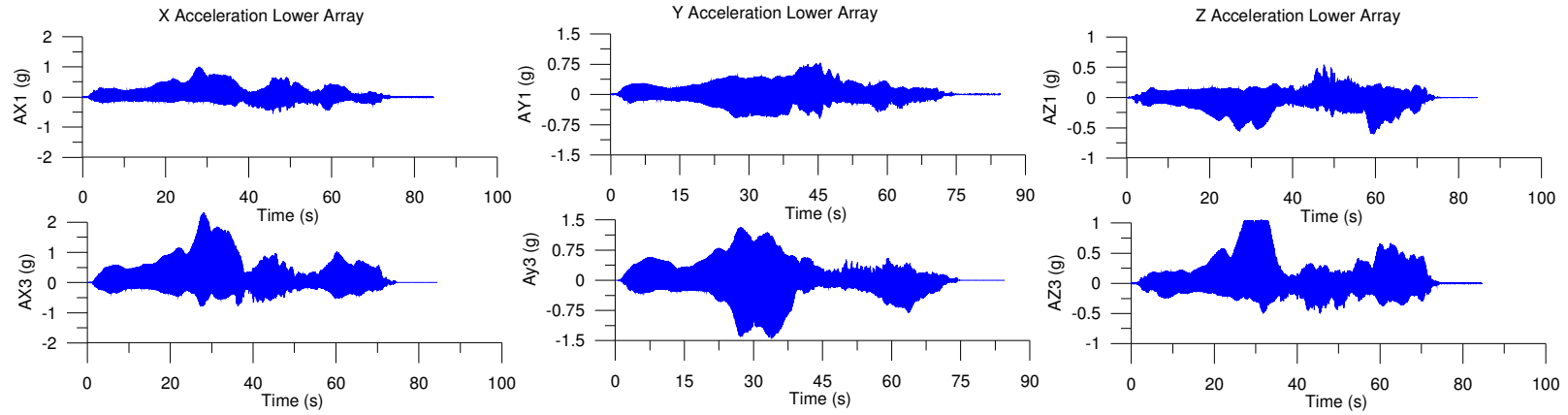

Figure 8.25 Untreated Lower Array for 3.0 m Shake

-

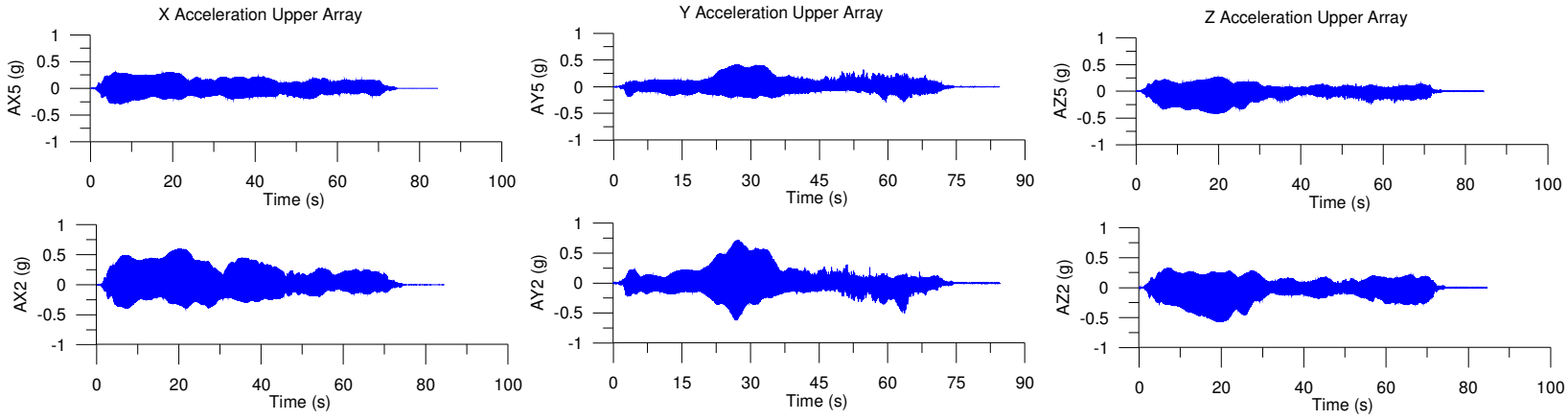

Figure 8.26 Untreated Upper Array for 3.0 m Shake

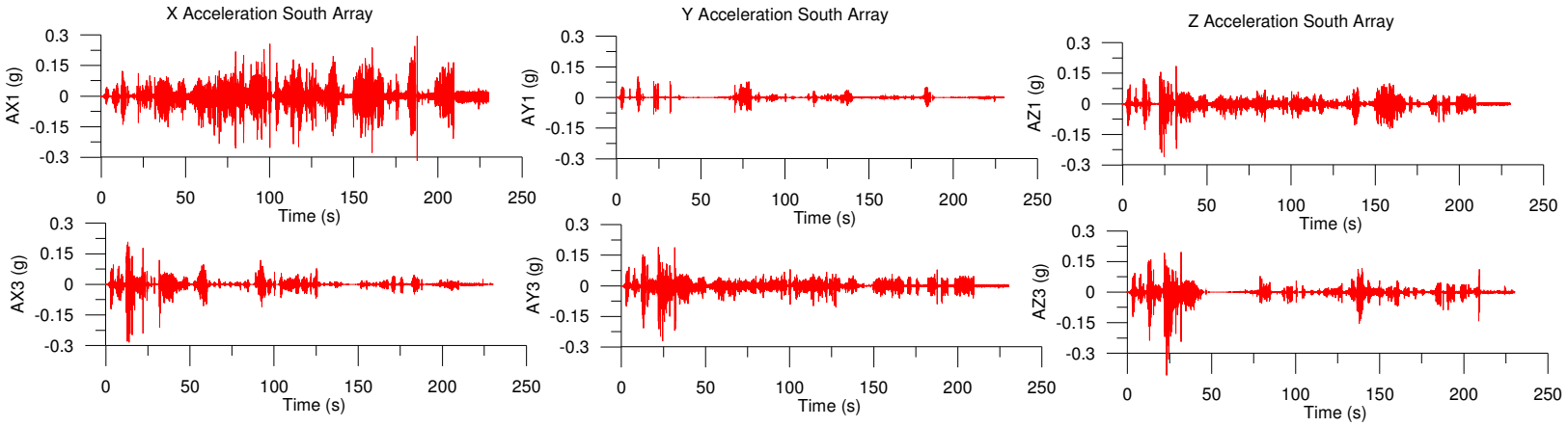

Figure 8.27 Treated South Array for 3.0 m Shake

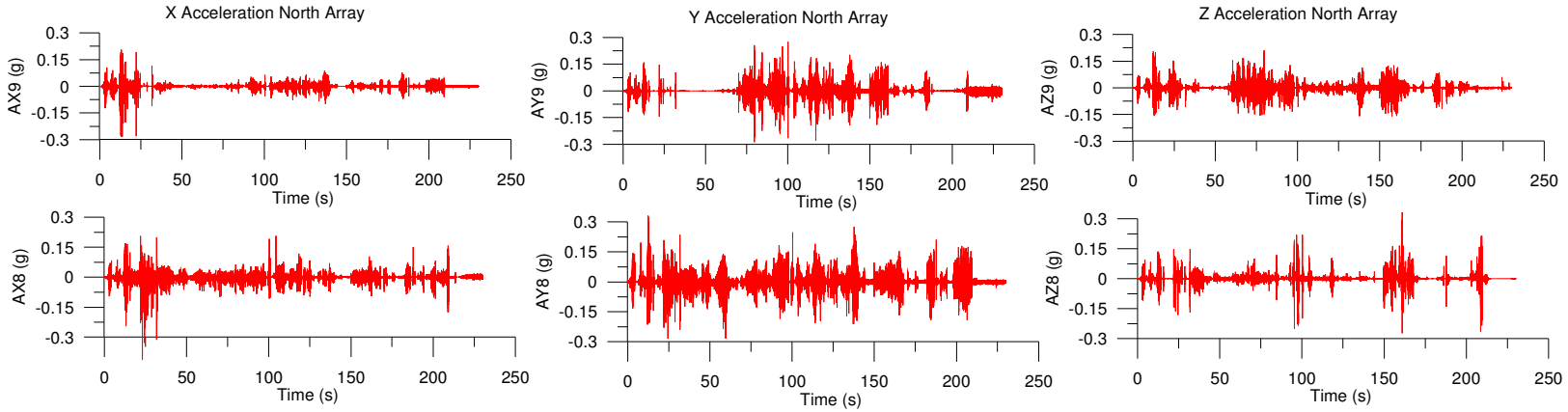

Figure 8.28 Treated North Array for 3.0 m Shake

8.9. Shear Strain Response

Shear stains were determined for each liquefaction sensor arrays in both the in-plane (*xy*) and cross-plane (*xz* and *yz*) directions. As previously discussed, finite element analysis techniques were used to compute the in-plane shear strain of a constant strain triangle from the triangular sensor arrays. The cross plane shear strains were computed by assuming linear variation between two nodal locations.

The results of the shear strains for each of the shakes are summarized in Table 8.7 and Table 8.8 in the untreated and treated areas, respectively and plotted in Figure 8.29 through Figure 8.32. Results show that the shear strains developed in the untreated and treated areas were predominately in the *xz* (cross plane) direction followed by the in-plane shear strains. For each shake, the figures demonstrate a clear reduction in shear strains in the treated versus untreated areas.

Table 8.7 In –plane and cross-plane shear strain summary for Untreated Test Area

Motion (Untreated)	γ_{xy} (%)		γ_{xz} (%)		γ_{yz} (%)			
	524(Upper)	183 (Lower)	5-2 (Upper)	1-8 (Lower)	5-4 (Upper)	2-4 (Upper)	1-3 (Lower)	8-3 (Lower)
1.5 m	--	0.121	0.005	0.055	--	--	0.106	0.089
3 m	--	0.072	0.009	0.034	--	--	0.114	0.142
4.6 m	0.005	0.003	0.004	0.002	0.008	0.005	0.007	0.007
6.1 m	0.004	0.004	0.004	0.002	0.005	0.004	0.029	0.027

Table 8.8 In –plane and cross-plane shear strain summary for Treated Test Area

Motion (Treated)	γ_{xy}(%)		γ_{xz}(%)		γ_{yz} (%)			
	589 (North)	136(South)	9-5 (North)	1-6 (South)	9-8 (North)	5-8 (North)	1-3 (South)	6-3 (South)
1.5 m	--	0.023	--	0.010	0.036	0.037	0.011	0.013
3 m	--	0.039	--	0.012	0.021	--	0.014	0.018
4.6 m	--	0.003	--	0.001	--	0.002	0.002	0.001
6.1 m	--	0.003	--	0.001	0.004	0.001	0.002	0.001

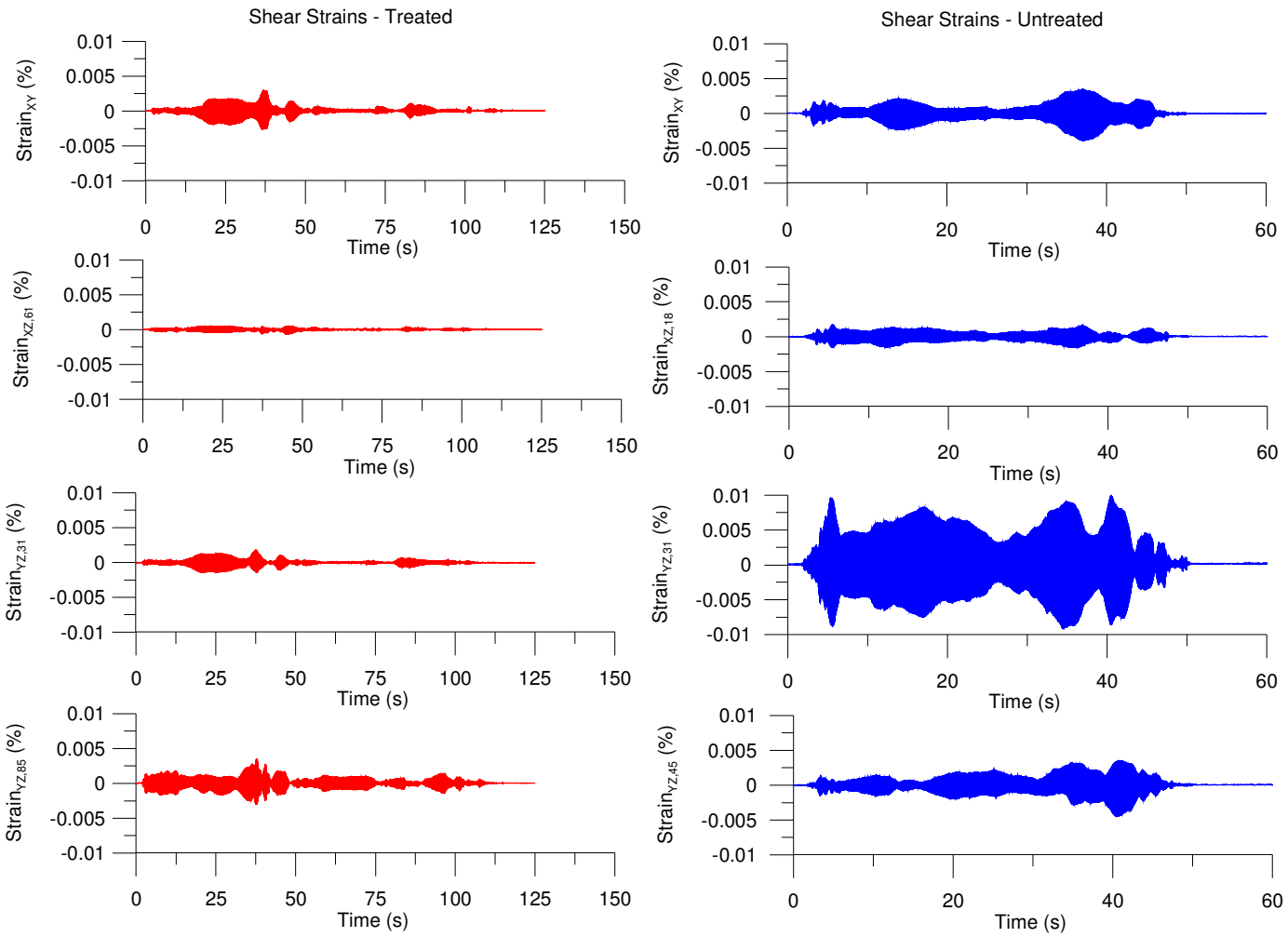

Figure 8.29 Shear Strain Response for (a)Treated and (b)Untreated area 6.1 m from source

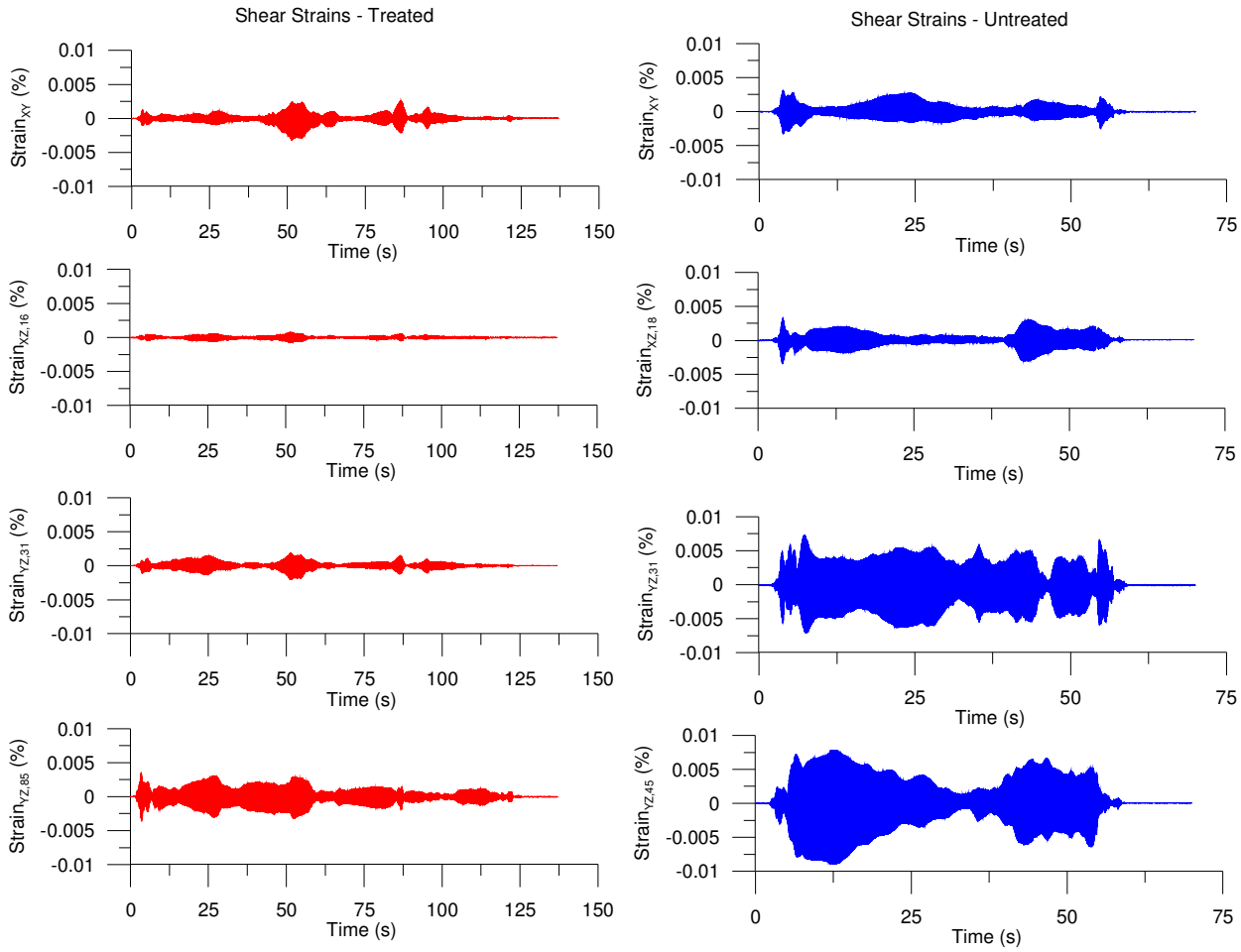

Figure 8.30 Shear Strain Response for (a)Treated and (b)Untreated area 4.6 m from source

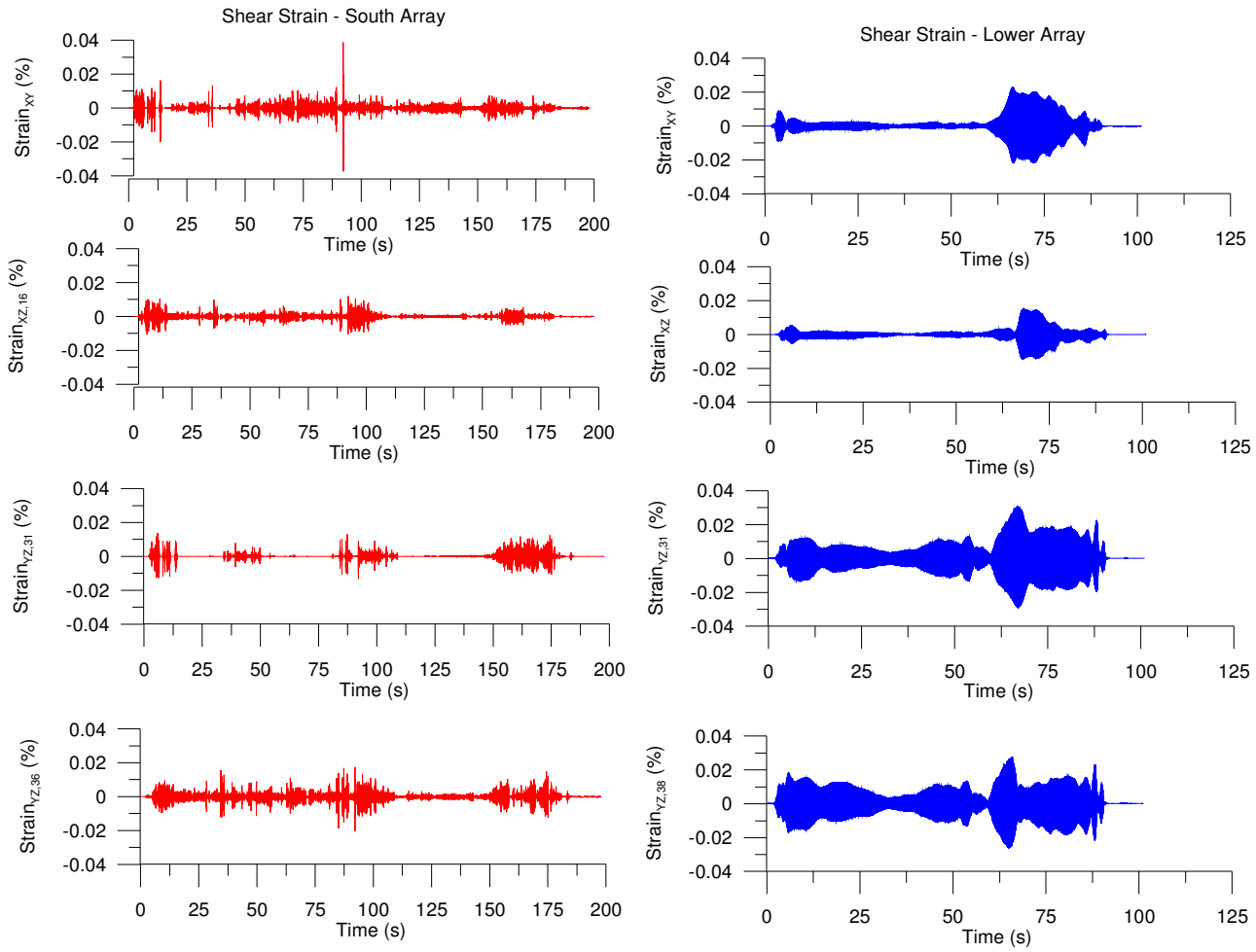

Figure 8.31 Shear Strain Response for (a)Treated and (b)Untreated area 3.0 m from source

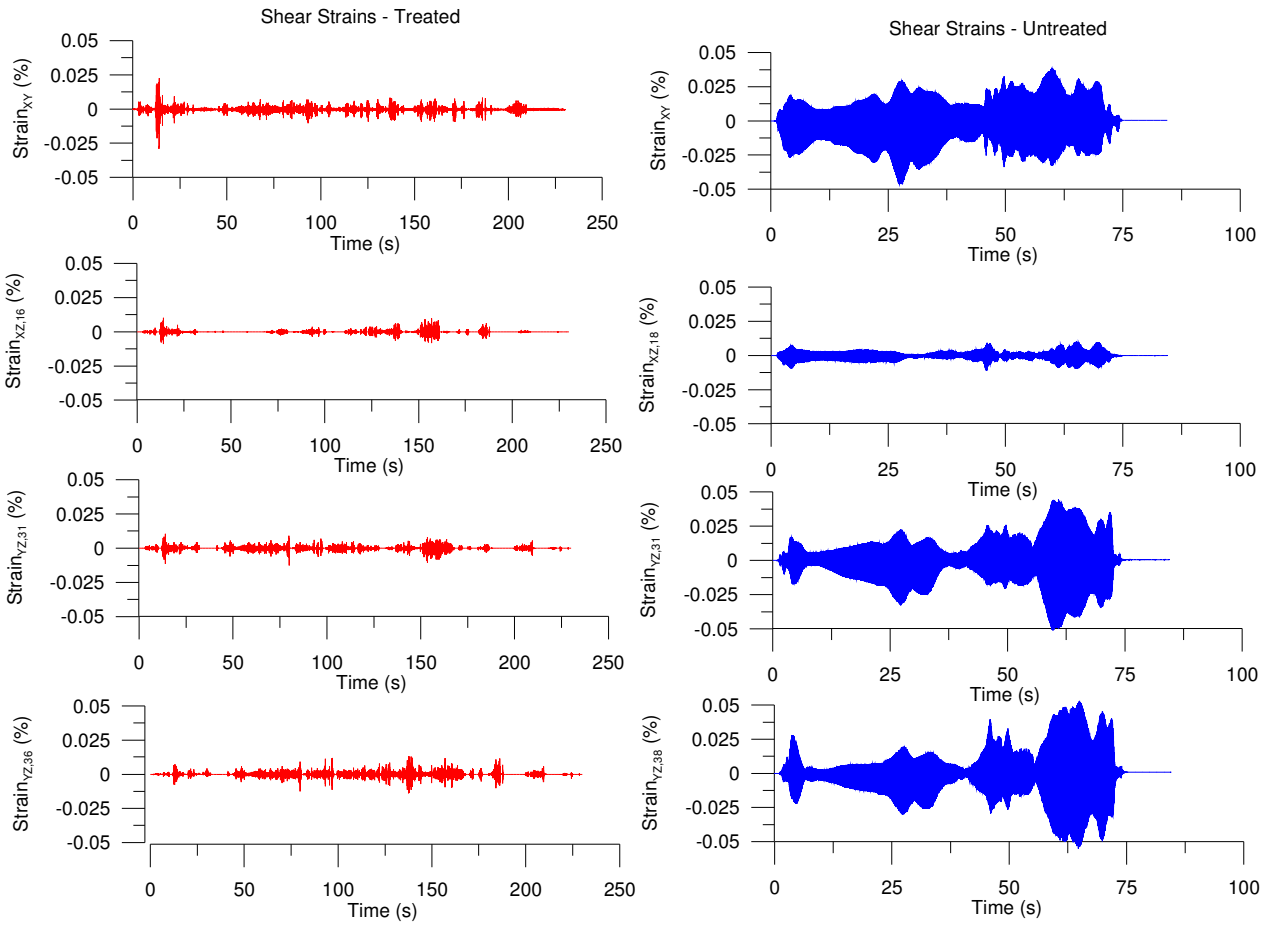

Figure 8.32 Shear Strain Response for (a) Treated and (b) Untreated area 1.5 m from source

8.10. Pore Pressure Response

For the treated sand, the change in pressure measured by a pore pressure transducer is believed to correspond to the change in normal stress that develops on the gel within the sand pores. Table 8.9 and Table 8.10 summarize the excess pore pressure ratios developed for the untreated and treated areas, respectively. Results of the pore pressure response in the untreated and treated areas suggests that liquefaction was initiated in the 1.5 m (5 ft) source motion event.

The response for each event is plotted in Figure 8.29 through Figure 8.36. The results show similar response of the treated and untreated behavior observed in the 4.6 m (15 ft) and 6.1 m (20 ft) shakes. For these events, little to no excess pore pressure is developed. This response is expected for smaller PGA values recorded at further distances from the source motions. For closer source shakes, there is an overall reduction in pore pressure response for the treated soils versus the untreated soils. This behavior is consistent with centrifuge model tests previously discussed.

Table 8.9 Summary of Ru values for the Untreated Test Area

Dist From Source Motion (Untreated)	Untreated					
	1 (Lower)	3 (Lower)	8 (Lower)	2 (Upper)	4 (Upper)	5 (Upper)
1.5 m	0.60	0.81	0.96	0.56	0.48	0.53
3.0 m	0.54	0.51	0.74	0.50	0.44	0.39
4.6 m	0.16	0.23	0.13	0.28	0.03	'--
6.1 m	0.04	0.04	0.04	0.08	0.03	0.12

Table 8.10 Summary of Ru values for the Treated Test Area

Dist From Source Motion (Treated)	Maximum Excess Pore Pressure Ratio							
	5 (North)	8 (North)	9 (North)	1 (South)	3 (South)	6 (South)	2 (Alone)	4 (Alone)
1.5 m	0.42	0.96	'--	0.20	0.20	0.42	0.49	0.25
3.0 m	0.16	0.20	0.58	0.05	0.15	0.17	0.11	0.14
4.6 m	0.09	0.09	0.43	0.03	0.12	0.12	0.04	0.08
6.1 m	0.84	0.45	0.01	0.03	0.12	0.13	0.90	0.01

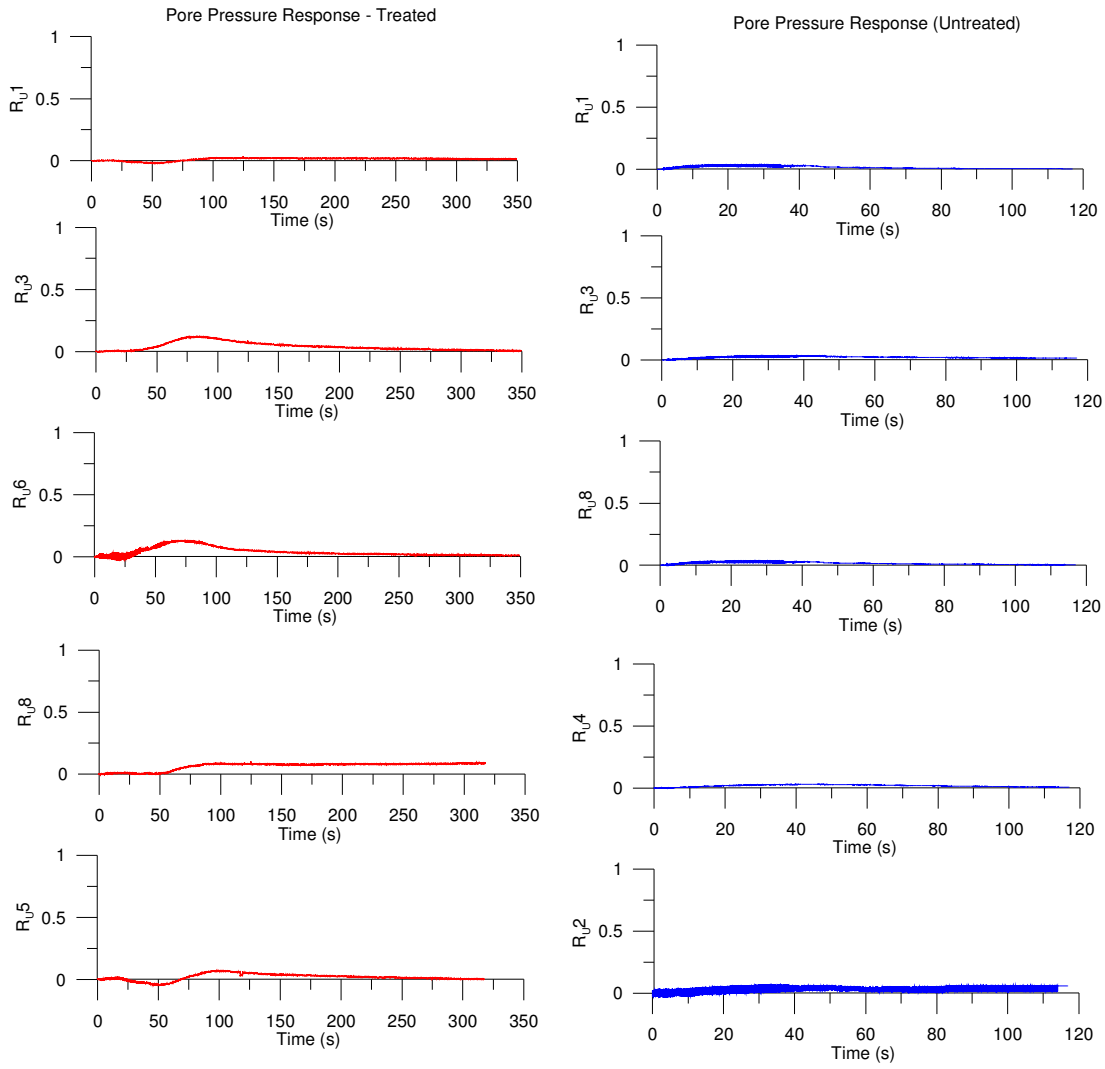

Figure 8.33 Excess Pore Pressure Ratio for Treated and Untreated 6.1 m from source motion

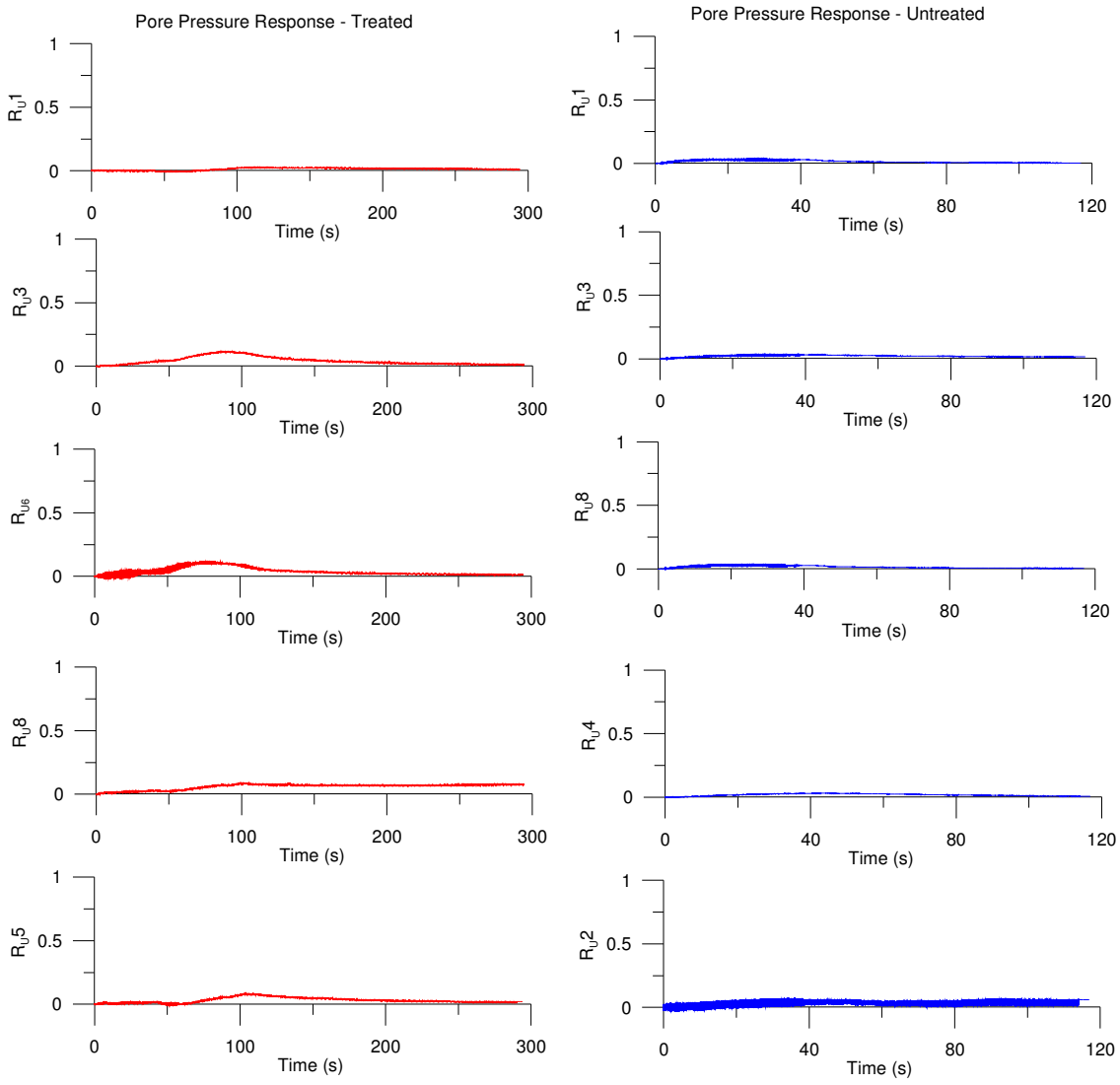

Figure 8.34 Excess Pore Pressure Ratio for Treated and Untreated 4.6 m from source motion

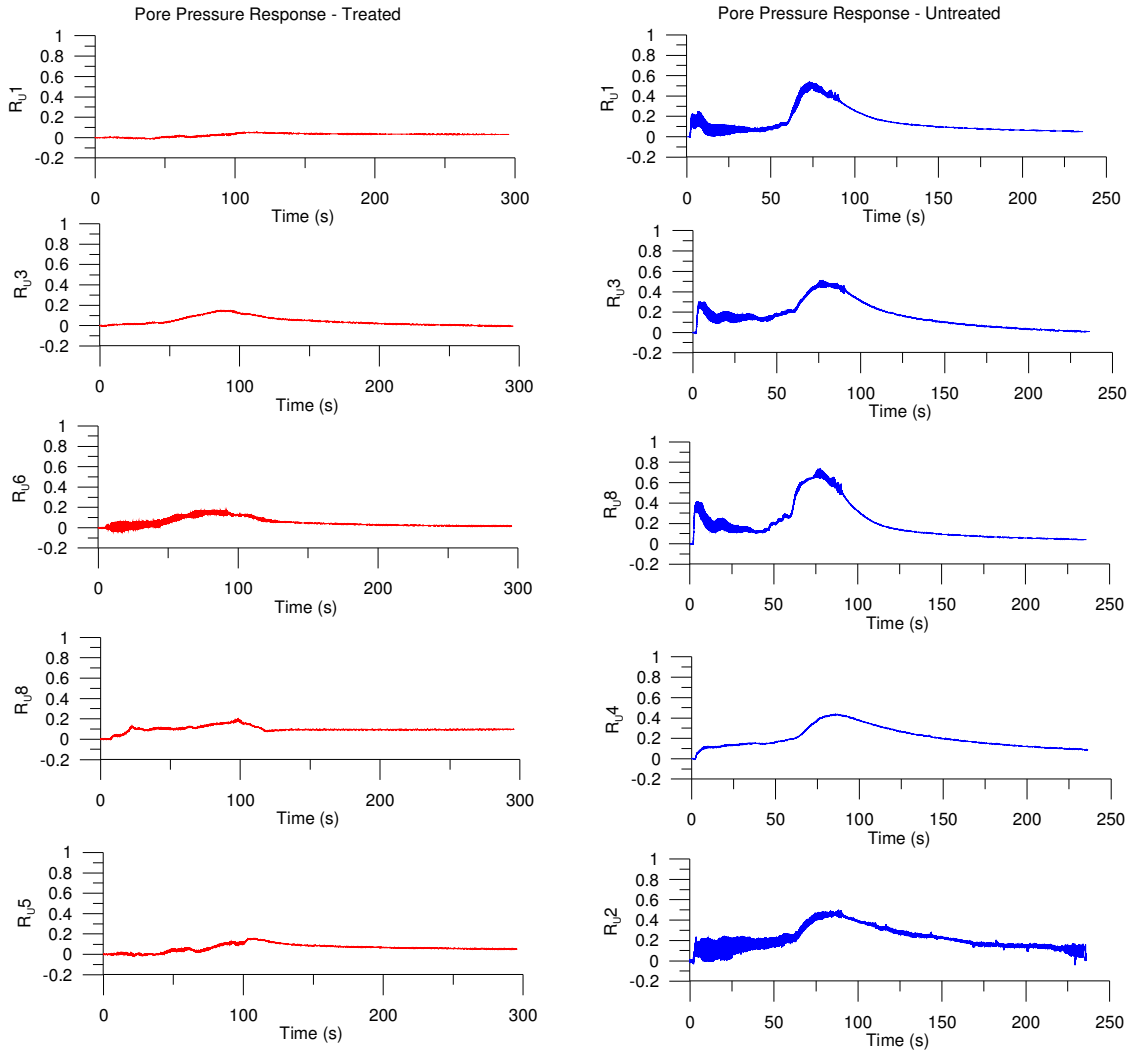

Figure 8.35 Excess Pore Pressure Ratio for Treated and Untreated 3.0 m from source motion

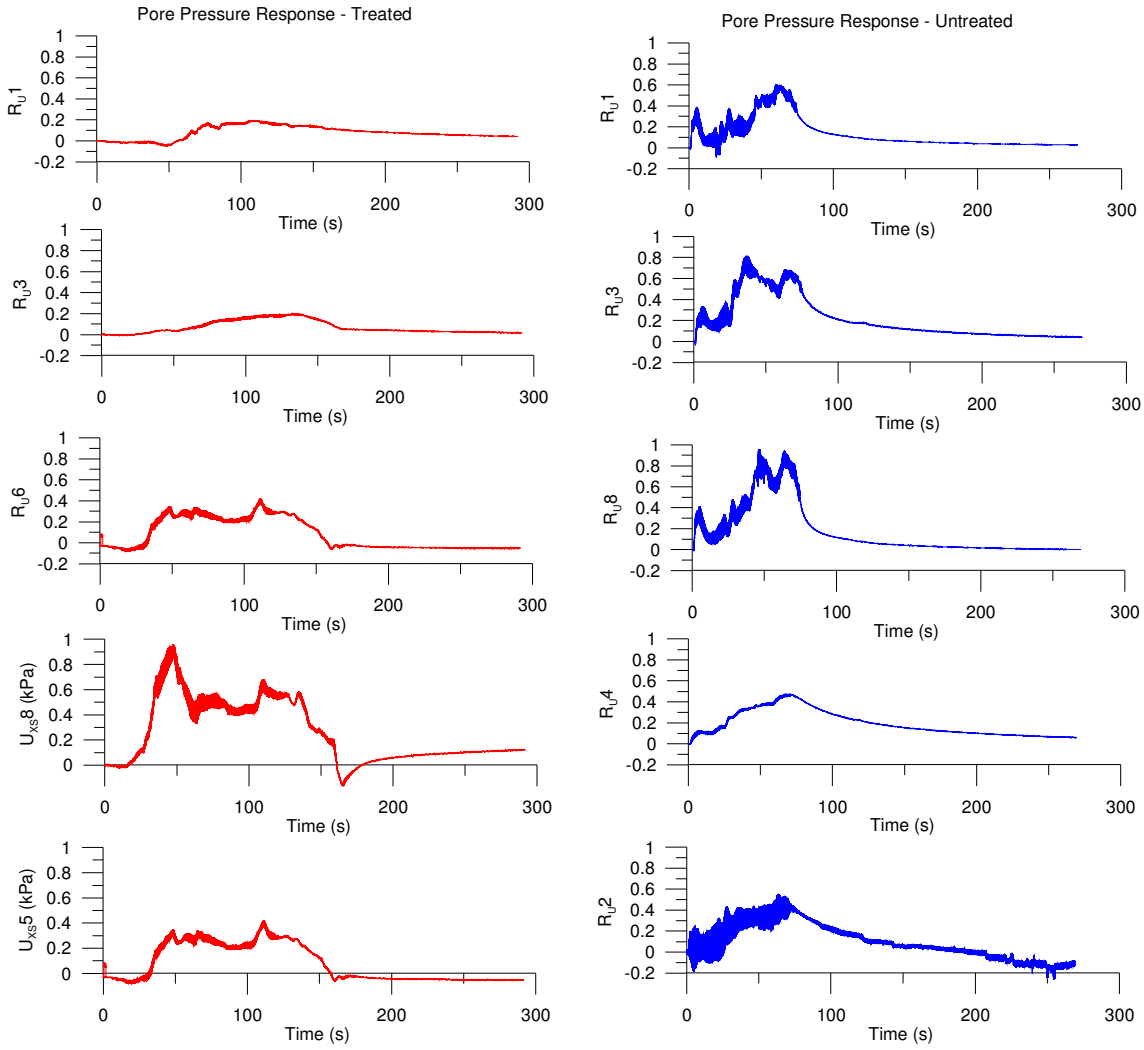

Figure 8.36 Excess Pore Pressure Ratio for Treated and Untreated 1.5 m from source motion

8.11. Post Shaking Analysis

Post shaking analysis consisted of standard penetration tests and split spoon samples which were collected at various depths to determine compressive strengths and confirm the quality of soil improvement. Borings B1 and B2 were located within the treatment area (denoted as SPT1 and SPT2 in Figure 7.16 while B3 was taken outside the treatment area (denoted as SPT3 in Figure 7.16) for purposes of comparison.

A summary of blowcounts and compressive strengths are summarized in Table 8.11. The results show blowcount data to be about twice as high for the treated area (53 and 36 blows/m [16 and 11 blows/ft]) versus the untreated area (16 blows /m [5 blows/ft]) for a depth interval of 3.4-4.0 m (11-13 ft). Blowcount data for the remaining depth intervals, on the other hand do not show dramatic differences.

The unconfined compressive strength on the north side of the array shows increases compared with the untreated test sample tested. Visual inspection of the samples also revealed the presence of grout in the sand. Results from UC tests from Hamderi (2010) shown in Table 8.12 suggest the north side was saturated with a 4% grout. The unconfined compressive strengths from the south side of the grouted area were not as high, but still showed an overall increase compared with the ungrouted samples after shaking. It should be noted that while extruding the Shelby tube samples for the UC tests, two of the samples from outside the treated area immediately collapsed and were unable to be tested.

Table 8.11 Post-shaking SPT data summary

Sample	Description	Depth (m)	N (blows/m)	q_U (kPa)
S1B1	Grouted (South)	2.1-2.7	13-13-13-13	--[1]
S2B1		2.7-3.4	10-3-3-7	5.0
S3B1		3.4-4.0	23-46-53-89	5.7
S1B2	Grouted (North)	2.1-2.7	13-13-20-20	11.2
S2B2		2.7-3.4	7-10-13-33	27.7
S3B2		3.4-4.0	23-30-49-39	22.8
S1B3	Ungrouted Area	2.1-2.7	10-13-16-23	--[1]
S2B3		2.7-3.4	13-13-16-23	0.6
S3B3		3.4-4.0	7-10-20-26	--[1]

Table 8.12 Unconfined Compressive Strengths for colloidal silica concnetrations (Hamderi, 2010)

% CS	q_U (kPa)
9	139.0
9	128.5
8	81.0
8	81.0
7	65.0
7	75.0
6	58.0
6	30.0
5	35.6
5	22.0
4	25.5
4	25.5
0	1.2

8.12. Field Test Limitations

Large-scale testing of colloidal silica soils posed many challenges due to several limitations that are worth mentioning. First, soil variability and stiff zones within the suspected liquefiable layer made it extremely difficult to establish treatment levels through post-grouting CPT data. Additionally, soil variability can preclude the transmission of seismic waves generated

during shaking and this was especially a concern when the source shaking motions were closest to the treated test area. Another factor was the limited control of dynamic loading with the mandrel. Unlike centrifuge model tests where the input motion is well defined, the input motion with the mandrel was unknown. As a result, comparisons between input motion and the recorded response could not be compared. Finally, there were a limited number of sensors installed in the treatment area and the response could only be measured at discreet locations.

8.13. Summary of Field Test Results

The field test fulfilled two general purposes: to complement the centrifuge model tests and to further investigate field procedures and QA/QC methods to improve future field tests. Similar to the centrifuge model tests, the pore pressure response was generally reduced in the treated test area compared with the untreated test area. Shear strains based on acceleration records were also reduced in the treated test area. Cone tip stresses did not prove to be a good indication of treatment levels in the field primarily due to the fact that there was a large degree of soil variability within the test area. In this case, it was difficult to distinguish between stiff soil layers and areas that were treated with colloidal silica. The post-grouting shear wave velocity was generally higher than the untreated test area. Again, soil variability makes it difficult to definitively determine whether this is due to CS treatment or the existence of stiff soil layers. Similar to centrifuge test findings, shear wave velocity and cone resistance are not strong indicators of treatment levels.

Another objective of the field test was to develop field procedures for grouting with colloidal silica. In terms of grouting equipment, the packer/well system proves to be a viable means of injecting the colloidal silica into the subsurface and isolating the target treatment depths. Less invasive methods for well installation are recommended. A significant amount of disturbance during well installation can create a preferential flow path to the surface and result in grout return. This was the greatest challenge in the field test because of the significant amount of

disturbance the mandrel caused during well installation. A more effective way would be to use a drill auger where disturbance is minimal.

As with most field tests, unexpected changes and problems arose in the field, which make it extremely important to solve problems quickly and efficiently. Prior to grouting, pre-defined gel time curves for various gel times and concentrations served as a valuable tool for formulating colloidal silica recipes quickly and efficiently. There were also several cases in which problems arose in the field and injection was delayed. In order to prevent premature gelation of the batches, several gallons of water were added to the mix in order to increase gel time. However, it is recommended that NaOH be used to delay gel times as an alternative method for two main reasons. First, NaOH alters the pH of the solution as opposed to diluting the CS. As previously mentioned, soil strength is directly related to CS grout concentration and diluting the CS could result in lower treatment levels. Another reason for using NaOH over water is that it is less labor intensive. For example, several gallons of water is required to achieve the same result in gel time that adding only several drops of NaOH would.

Several QA/QC methods were identified from the field test as well. During batching, chloride concentration monitoring ensured that proper proportions of CS, water, and NaCl were added to the mix. Collecting samples for each batch served as a check that the solution gelled within the target gel time. Similar to conventional grouting methods, injection pressures should be closely monitored to prevent uplift and fracture of the surrounding soil. A simple rule of thumb is to inject at pressures no greater than 1 psi per foot of injection depth. Additionally, monitoring injection rates and grout volumes during injection are recommended to prevent premature gelation of the batch mix and to make sure that a sufficient volume of grout has been injected in the target treatment area.

CHAPTER 9: CONCLUSIONS

9.1. Research Contributions

One of the major research contributions made in this study was experimentally determining the parameters required for cyclically loaded soil models for colloidal silica soils. For purposes of liquefaction remediation, it was desired to develop soil models for colloidal silica soils so that they can ultimately be implemented into numerical models that predict mechanical behavior under seismic loading. The most commonly used soil models for cyclically loaded soils include equivalent linear models and cyclic nonlinear models. One of the necessary requirements for both soil models is the shear modulus degradation (or backbone) curve, such as those developed by Vucetic and Dobry (1991) for sands and clays. From the centrifuge model tests, the shear modulus degradation curve was developed for colloidal silica soils under various strain levels ranging from about 0.01% up to 4%.

While equivalent linear models are the simplest and most commonly used soil models, they are limited in capturing aspects of dynamic soil behavior. Cyclic nonlinear models, on the other hand, can more accurately represent the dynamic response because they follow the actual path of the stress-strain loop during cyclic loading. One of the major advantages of cyclic nonlinear models is that they can be used to identify permanent strains induced after cyclic loading whereas equivalent linear models cannot. Cyclic nonlinear models require an appropriate pore pressure generation model where changes in effective stress during undrained cyclic loading can be represented. These models also require rules that govern unloading-reloading behavior and stiffness degradation. The centrifuge model tests presented in this research identify unique characteristics based on acceleration and pore pressure response of colloidal silica soils necessary for cyclic nonlinear models. Pore pressures proved useful for capturing behavior of the stress transmission between the colloidal silica gel and the sand at a macroscopic level. The

acceleration records revealed dilation responses for stonger shaking events similar to that observed for dense sands. Both pore pressure response and acceleration responses were able to capture the affects of strength increases and linearity with colloidal silica concentrations. Additionally, the actual hysteretic response was tracked during cyclic loading for various shaking levels such that the effects of colloidal silica concentration, soil stiffness, and permanent strains were identified. The hysteretic responses were found to be similar to that of dense sands, but with significantly more damping. The characteristic responses for all of these parameters studied in the centrifuge model tests define rules that govern loading-unloading behavior in cyclic nonlinear soil models for colloidal silica soils.

The centrifuge model test not only confirmed the ability of colloidal silica soils to reduce surface settlements, but it also shows that treatment of liquefiable soils underneath non-liquefiable sloped embankments can dramatically decrease the extent of lateral spreading. Mitigation of this kind of liquefaction damage can be relevant in port facilities where structures often rest on similar soil profiles.

Additionally, the use of commonly used geophysical testing parameters was assessed as a way to identify treatment levels. Among the geophysical methods studied include cone resistance and shear wave velocity. Although centrifuge models show colloidal silica soils to yield higher cone tip resistances and shear wave velocities, they may not always be a reliable indication of treatment levels, especially if treatment is performed in areas where soil variability is prevalent. In this way, stiffer soil layers can easily be misinterpreted as treated soils. The uncertainty of these geophysical parameters present the need for testing modifications and alternative methods to be explored in which colloidal silica soils and natural geologic materials can be easily distinguished.

Finally, the in situ test of colloidal silica for purposes of liquefaction mitigation reported in this research is the second known field test of its kind. Therefore, it allowed for in-situ

procedures to be further developed. Several recommendations have been made that will give improvement for future field tests.

9.2. Summary of Research Findings

Colloidal silica grout has been shown to stabilize soils and mitigate the effects associated with liquefaction-induced damage. Its advantage over other chemical grouts is primarily the ability to have a wide range of controllable gel times, its permanence, and its ability to continuously increase the strength of soils over time. In addition to being permanent, colloidal silica is biologically and chemically inert, which makes it a benign material to be used in the subsurface.

For purposes of liquefaction remediation, an understanding of the dynamic response of colloidal silica treated soils can make a significant contribution for implementing numerical models and ultimately achieving optimal improvement in large-scale field applications. Studies based on the dynamic behavior of colloidal silica grouted soils are focused primarily on laboratory scale soil specimens. This research utilized centrifuge testing to represent much larger prototypes and a full-scale field test to characterize the dynamic behavior of colloidal silica treated soils.

The first part of this research utilized centrifuge model tests to study the behavior of colloidal silica soils. Through centrifuge model testing, the dynamic response of these treated soils was studied for a much larger prototype scale compared with laboratory specimens. Several features of colloidal silica treated sands were identified by analysis of centrifuge test data. The tests provided comparisons of the response for untreated sands and sands treated with 4%, 5.25%, and 9% colloidal silica concentrations (by weight) subjected to a sequence of dynamic shaking events. To determine whether treatment could be identified through commonly used soil parameters, shear wave velocity readings and cone penetration tests were also conducted for each

of the soil types prior to shaking . For each shaking event, the dynamic response of colloidal silica soils was characterized using time histories of pore pressures, accelerations, and surface displacements. Hysteretic behavior along the liquefiable soil profile was also determined using integration and inverse analysis methods from acceleration time histories. Additionally, shear wave velocity measurements were taken in between subsequent shaking events to characterize effects of shear modulus for a series of dynamic loads.

Based on the centrifuge model tests, the following conclusions can be drawn regarding the behavior of colloidal silica soils:

- Settlements that occur as a result of liquefaction can be significantly reduced by treating liquefiable zones with colloidal silica.
- Colloidal silica treatment can dramatically reduce lateral spreading in sloped embankments resting on liquefiable soil layers.
- Pore pressure response of treated soils describes how stresses were transferred between the soil and the gel. Although pore pressure ratios reached 1.0 for the grouted soils, greater shaking accelerations were required to achieve this state. The occurrence of r_U=1.0 was directly related to grout concentration. Higher levels of shaking were required to reach r_U=1.0 for higher colloidal silica concentrations
- The acceleration and pore pressure response were found to be indications of how well the integrity of the soil/gel matrix was maintained. The high-frequency acceleration spikes observed for the treated soils correlated well with pore pressure response when r_U=1.0 is achieved.
- The acceleration response shows that the occurrence of soil dilation is more pronounced for lower concentrations of colloidal silica. Evidence of soil dilations is first observed in 4% colloidal silica soils whereas greater shaking accelerations were required for 9% colloidal silica soils.

- Pore pressure dissipation was observed in the treated soils, but occurred at a much slower rate. Considering scaling laws, dissipation took at least 3 hours verses a couple of minutes for water saturated soils.
- The stress-strain response of the treated sands exhibited cyclic mobility consistent with dens sands, but with greater hysteretic damping than untreated sands.
- The stress-strain behavior revealed a lower degree of cyclic degradation for higher concentrations of colloidal silica. The stiffness of the 5.25% colloidal silica soils continues to degrade during cyclic loading while the 9% colloidal silica treated soil was maintained up to peak base accelerations of 0.56g.
- The post-shaking shear wave velocities of colloidal silica soils progressively decreased as the peak base acceleration increased. The response can be attributed to two factors: (1) residual pore pressures induced on the gel from previous shaking events and (2) disruption of the sand/gel matrix.
- Colloidal silica treated sands yield higher cone tip and sleeve friction resistance than in water saturated sands. The cone tip resistances were still relatively low and would not necessarily be a strong indication of treatment levels.
- Colloidal silica sands result in a stronger and stiffer soil formation. However, the initial shear wave velocities were not sufficiently high relative to untreated sands. Therefore, shear wave velocity is not an obvious method for identifying treatment levels.

The next part of this research implemented a full-scale field test to complement the centrifuge model tests. The main objective of the field test was to study and compare the dynamic response of a 1.5 m (5 ft) thick layer of colloidal silica treated soil versus untreated soils in an adjacent test area. The dynamic response was characterized through time histories of accelerations, pore pressures, and finite element analysis methods for determining shear strains.

Prior to shaking, post-grouting CPT s were conducted to measure the cone resistance. Additionally, pre and post-shaking cross-hole tests were conducted to measure shear wave velocity of the treated and untreated soils. Based upon the field study, the following characteristics complementary to the centrifuge model tests are identified:

- Pore pressure response shows an overall reduction in excess pore pressures developed for the treated soils.
- Shear strains based on acceleration records were reduced in the colloidal silica soils.
- Cone tip stresses are not necessarily a good indication of treatment levels. This is especially true in areas with soil variability where stiffer soil layers can easily be misinterpreted as zones of treatment.
- Measured shear wave velocities from cross-hole tests show an overall increase in shear wave velocity in colloidal silica soils versus untreated soils. Soil variability, however, makes it difficult to definitively determine whether this is an effect of treatment or stiff soil zones.

The secondary objective of the field test was to develop field procedures such as colloidal silica batching, injection methods, and QA/QC measures. For in-situ field testing, the following recommendations have been developed:

- Unexpected changes in the field may require changes in gel times during batching. Obtaining gel time curves prior to batching serve as a valuable tool for formulating colloidal silica recipes quickly and efficiently.
- Chloride concentration monitoring and sample collection for each batch mixed are effective methods for verifying proper proportions of colloidal silica recipes and ensuring target gel times are achieved.
- When complications arise during injection, it becomes necessary to delay gel times and prevent premature gelation. It is recommended to use sodium hydroxide to delay gel times

instead of water because sodium hydroxide does not compromise the concentration of colloidal silica and therefore, does not alter potential strength gain for treatment. Adding several drops of sodium hydroxide versus several gallons of water is also less labor intensive and less time consuming.

- Similar to conventional grouting techniques, it is necessary to monitor injection pressures to prevent uplift and fracture of the surrounding soil. A simple rule of thumb in soil grouting is to inject at pressures no greater than 1psi per foot of injection depth.
- Monitoring injection rates and grout volumes during injection are also recommended to prevent premature gelation of the batch mix and ensure that a sufficient volume of grout has been injected into the target treatment area.
- The packer/well system proves to be a viable means of injecting the colloidal silica into the subsurface and isolating the target treatment depths. Minimally invasive methods for well-installation are strongly recommended to prevent grout return to the surface during injection.
- Cone tip resistance and shear wave velocity measurements are not strong indicators of treatment levels is situ especially in areas where soil variability is prevalent. Drilling and soil sampling continue to be the most reliable means for determining treatment.

9.3. Lessons Learned from the Research Program

Overall, the centrifuge model tests proved to be a valuable way of accomplishing many of the research objectives. The step-up shaking sequence allowed for colloidal silica soil properties to be identified under a wide range of shaking intensities. Dense, vertical sensor arrays were by far the most effective sensor configuration to have in the model because it provided the most amount of information. For example, the response could be identified at varying confining pressures and provided an overall picture of the soil profile. Dense vertical

sensor arrays also made it possible to calculate the hysteretic stress-strain behavior through the soil profile where strength and stiffness of the soil could be tracked during shaking.

Bender elements served as an extremely valuable tool for monitoring shear wave velocities. By measuring shear wave velocities in between varying shake levels, characteristics of shear modulus and soil stiffness were identified for a wide range of dynamic loads.

If additional centrifuge tests were to be performed, structural models to represent pile supported wharfs could be added to a similar geometry. In this way, soil-structure interaction could be assessed.

As with most large-scale field tests, numerous limitations were involved that made it more difficult to analyze data and characterize trends. From Chapter 8, one of the greatest challenges was the fact that soil variability and stiff zones existed within the suspected liquefiable layer. This made it extremely difficult to establish treatment levels. Soil variability can preclude the transmission of seismic waves generated during shaking and make it difficult to establish a characteristic dynamic response. It is therefore necessary that in situ tests be performed at a site where soils are relatively uniform. For example, areas that consist primarily of loose, artificial fill would be an ideal area for in situ testing of colloidal silica. Due to the fact that CPT tests and shear wave velocity were not a reliable means of detecting treatment in the field, it is also recommended that conductivity probes be used as a means for detecting treatment.

Another significant challenge during the field test was getting grout return between the injection well and the soil during injection. Although soil variability could have played a role in getting grout return, another factor was well installation using the mandrel. The mandrel was a largely invasive well installation technique that disturbed the surrounding soil. The high disturbance caused by the mandrel likely produced preferential flow paths up to the ground surface. It is therefore necessary to implement minimally invasive methods for well installation, such as using a drill auger.

9.4. Recommendations for Future Work

Research of colloidal silica for liquefaction mitigation purposes incorporates a broad spectrum of inter-disciplinary fields. Among them are geotechnical earthquake engineering, ground improvement, nano-technology, hydraulic engineering, and chemistry. This research study focused on geotechnical earthquake engineering and the overall dynamic response of colloidal silica soils. Ongoing research continues to show colloidal silica as a promising material for liquefaction mitigation.

Collaboration between the various disciplines just mentioned is highly encouraged regardless of the research focus. For example, a greater understanding of the dynamic behavior of colloidal silica soils could be achieved with research focus of colloidal silica soils at the microscopic scale. Additional research regarding the bonding mechanisms between colloidal silica and sand particles with an emphasis on the chemical and micro-mechanical aspects of colloidal silica soils is highly recommended.

As previously discussed, equivalent linear and cyclic nonlinear soil models are commonly used in geotechnical engineering to predict soil behavior under seismic loading. Additional parameters to be studied to develop colloidal silica soil models include damping ratio and development of further modulus reduction curves that incorporate additional factors governing unloading-reloading and stiffness degradation. Such factors may include confining stress and colloidal silica concentration higher than 9%. A greater understanding of pore pressure response may also be expanded. From a macroscopic scale, pore pressure response can provide insight as to the way in which stresses are transferred between the gel and soil under dynamic loading. Pore pressure response would be better studied using laboratory tests because few laboratory tests have been conducted in this area and laboratory testing also offers a more controlled environment versus large-scale testing. Since colloidal silica soils increase in strength

over time, long term tests beyond one year may be desired in order to determine limiting strength gain and ultimate shear modulus.

Further research may also include the effects of different model preparation methods for commonly used laboratory tests. Effects of specimen preparation may include surcharge loading, treatment on wet sands versus dry sands, and cyclic prestraining. Laboratory testing with chemical grouts, such as sodium silicate, have addressed these issues (i.e. Maher et al., 1993) but are not well-known for colloidal silica. Study of such effects may help to gain insight into results of commonly used laboratory tests and also give guidance in model preparation methods including centrifuge models.

Field testing for extent and control of target treatment areas requires extensive study. An expansion of this research may include the exploration of various grouting methods (i.e. injection and extraction well configurations) for controlling migration and reaching target areas in the subsurface. Another consideration may include the extent of coverage adequate to prevent structural damage at a particular site. Less invasive quality control methods may also be explored to assess the extent of grout coverage.

Finally, large-scale tests are time-consuming, labor intensive, and costly. Therefore, incorporating colloidal silica treatment into numerical models is an ideal method for both optimizing treatment in the field and predicting dynamic response of colloidal silica soils under seismic loading. Presently, investigations of numerical modeling with colloidal silica is limited. Linear equivalent and nonlinear equivalent models previously discussed can be used in numerical models and potentially address remaining issues in the future. Among these issues include the extent of treatment coverage necessary to prevent structural damage and the performance under different shaking events. Numerical models can also be used to optimize treatment coverage in situ and address remaining issues such as injection/extraction well configurations for greater control over grout migration. In order to make numerical models a viable way to study these aspects, a research program must be laid out in which the different numerical modeling programs

are identified and assessed. Once suitable modeling programs are selected, the necessary parameters required for implementation can be identified and studied.

List of References

Andrus, R.D. and Stokoe, K.H (2000). "Liquefaction Resistance of Soils from shear-wave velocity." *Journal of Geotechnical and Geoenvironmental Engineering.*

Andrus, R.D. and Stokoe II, K (1999). "A Liquefaction Evaluation Procedure Based on Shear Wave Velocity." *Proceedings of 31st Joint Meeting of Wind and Seismic Effects: U.S./Japan Natural Resources Development Program (UJNR).* Tskuba, Japan.

Andrus, R.D., Chung, R.M., Stokoe, K.H., Bay, J.A (1998). "Delineation of densified sand at Treasure Island by SASW testing." *Geotechnical Site Characterization Proceedings of the 1st International Conference on Site Characterization,* Atlanta, GA.

Arulnathan, R., Boulanger, R.W., and Riemer, M.F (1998). "Analysis of Bender Element Tests." *Geotechnical Testing Journal*, GTJODJ, Vol.21, No 2, June 1998, pp120-131

Ashford, S.A., Rollins, K.M., and Lane, J.D. (2004). "Blast-induced liquefaction for full-scale foundation testing." *J. of Geotech. and Geoenv. Engr.*, 130(8), 798-806.

Baker, W.H. (1982), "Planning and performing structural chemical grouting." *Proceedings of the ASCE Specialty Conference Grouting in Geotechnical Engineering.* ASCE, N.Y., 515-539.

Bennett, KE., Fitzjohn, J.L., Harmon, R.A., and Yates, PC., Jr (1998). K.E. Bennett, JL. Fitzjohn, R.A. Harmon, and P.C. Yates, Jr. "Colloidal Silica Based Fluid Diversion," U.S. Patent 4, 732, 213.

Berry, D (2006). "Soil Grouting – There's only One Way to View It." *Geotechnical News* ,

24(3), 39-46.

Boore, D.M., Bommer, J.J (2005). "Processing of strong-motion accelerograms: Needs, options and consequences." *Soil Dynamics and Earthquake Engineering,* 25(2), 93-115

Brachman, R.W.I., Martin, C.D, and Gilliss, S.A (2004). "Grout field trials in outwash sands." *Canadian Geotechnical Journal.* 41(1), 1-11.

Brennan, A.J., Thusyantan, N.I., Madabhushi, S.P.G (2005). "Evaluation in Shear Modulus and Damping in Dynamic Centrifuge Tests." *Journal of Geotechnical and Geoenvironmental Engineering*, 131(12), 1488-1497

Boulanger, R.W.and Idriss, I.M (2006). "Liquefaction Susceptibiity Criteria for Silts and Clays." *Journal of Geotechnical and Geoenvironmental Engineering,* ASCE, 132 (11), 1413-1425.

Brandenberg, S.J., Wilson, D.W, and Rashid, M.M (2009). "A Weighted Residual Numerical Differentiation Algorithm Applied to Experimental Bending Moment Data." *Journal of Geotechnical and Geoenvironmental Engineering,* Vol. accepted.

Brandenberg, S.J., Kutter, B.L., Wilson, D.W. (2008). "Fast Stacking and Phase Corrections of Shear Wave Signals in a Noisy Environment." *Journal of Geotechnical and Geoenvironmental Engineering*. August, 2008.

Brennan, A.J., Thusyanthan, N.I., and Madabhushi, S.P.G (2005). "Evaluation of shear modulus and damping in dynamic centrigfuge Tests." *Journal of Geotechnical and Geoenvironmental Engineering,* 131(12), 1488-1497.

Cook, R.D, Malkus, D.S., Plesha, M.E., and Witt, R.J (2002). *Concepts and applications of finite element analysis, 4th Edition.* John Wiley & Sons, New York, NY.

Cubrinovski, M and Ishihara, K (2001). "Correlation between penetration resistance and relative density of sandy soils." *1[5th] International Conference on Soil Mechanics and Geotechnical Engineering.* Istanbul, Turkey, 27-31.

Diaz-Rodriguez, J.A. and Antoniao-Izarraras, V.M (2004). "Mitigation of Liquefaction Risk using Colloidal Silica Stabilizer." *13th World Conference on Earthquake Engineering, Paper No 509.* Vancouver, B.C.

Dobry, R., Ladd, R.S., Yokel, F.Y., Chung, R.M., and Powell, D. (1982) Predictionof pore water pressure buildup and liquefaction of sands during earthquakes bythe cyclic strain method, *NBS Building Science Series 138,* National Bureau of Standards, Gaithersburg, MD, pp 150.

DuPont (1997). *Ludox Colloidal Silica: Properties, Uses, Storage, and Handling*. Product Information, DuPont, Wilmington, DE.

Drnevich, V. P. and Richart, F. E. Jr. (1970) Dynamic prestraining of dry sands, Journal of Soil Mechanics and Foundations Divisions, Proceedings of the American Society of Civil Engineers, Vol. 96, No. SM2, March, PP. 451- 469.

Ellington,S (2008). "Ellington Cross Geotechnical Contractors." <http://www.ellingtoncross.com/> (August, 2008).

Forero-Duenas, C.A (1998). "Shear Modulus-Time Variations of a Silica Gel." *3rd World Congress on Particle Technology.* Brighton, U.K.

Fritges, M.B., DeJong, J.T. and Nusslein, K (2006). "Biologically Induced Improvement of Loose Sand." *Proceedings of the 8th U.S. National Conference on Earthquake Engineering,* Paper No. 1691*,* San Francisco, CA.

Funeehag, J. and Fransson, A (2005). "Sealing narrow fractures with a Newtonian fluid: Model prediction for grouting verified by field study." *Tunneling and Underground Space Technology,* 21 (5), 492-498.

Gallagher, P.M., Conlee, C.T. and Rollins, K.M. (2007). "Full-Scale Field Testing of Colloidal Silica Grouting for Mitigation of Liquefaction Risk." *Journal of Geotechnical and Geoenvironmental Engineering,* 133(2):186.

Gallagher, P.M., Pamuk, A., Abdoun, T (2007). "Stabilization of Liquefiable Soils Using Colloidal Silica Grout." *Journal of Materials in Civil Engineering*, 19 (33).

Gallagher, P.M., and Lin, Y. (2005). "Column testing to determine colloidal silica transport mechanisms." *Innovations in Grouting and Soil Improvement, GSP No. 136,* Proc. of the Sessions of the Geo-Frontiers Congress (2005), Texas, USA, 162(15).

Gallagher, P.M., and Koch, A.J. (2003). "Model testing of passive site stabilization: a new grouting technique." *Proc., 3rd Int. Conf. on Grouting and Ground Treatment*, Vol. 2, 1478-1479.

Gallagher P.M., and Mitchell, J.K. (2002). "Influence of colloidal silica grout on liquefaction potential and cyclic undrained behavior of loose sand." *Soil Dynamics and Earthquake Engineering*, 22(2002) 1017-1026.

Gallagher, P.M. (2000). "Passive Site Remediation for Mitigation of Liquefaction Risk." PhD Dissertation, Virginia Polytechnic Institute and State University, Blacksburg VA.

Hall, L., Bodare, A (2000). "Analysis of the cross-hole method for determining shear wave velocities and damping ratios." *Soil Dynamics and Earthquake Engineering,* 20(1-4), 167-175.

Hamderi, M (2010). "Pilot-Scale Modeling of Colloidal Silica Delivery to Liquefiable Sands." PhD Dissertation, Drexel University, Philadelphia, PA.

Iler, R.K. (1979). *The Chemistry of Silica: Solubility, Polymerization, Colloid and Surface Properties, and Biochemistry*, John Wiley & Sons, New York.

Jurinak, J.J., Summers, L.E. and Bennett, K.E. (1989). "Oilfield application of colloidal silica gel." *Society of Petroleum Engineers International Symposium on Oil Field Chemistry*, Houston, TX, 406-412.

Kamai, R. and Boulanger, R.W (2010). "Characterizing localization processes during liquefaction using inverse analyses of instrumentation arrays." *Meso-Scale Shear Physics in Earthquake and Landslide Mechanics.* Y.H. Hatzor, J. Sulem, and I. Vardoulakis, eds. Leiden: CRC Press, 219-238.

Karol, R.H. (2003). *Chemical Grouting and Soil Stabilization 3rd Edition*, CRC, 584.

Karol, R.H. (1990). *Chemical Grouting 2nd Edition, Revised and Expanded.* Marcel Dekker, Inc. New York.

Kodaka, T., Oka, F., Ohno, Y., Takyu, T., and Yamasaki, N (2005). "Modeling of Cyclic Deformation and Strength Charachteristics of Silica Treated Sand." *Geomecahnics: Testing, Modeling, and Simulation*, ASCE, GSP 143, 205-216

Kutter, B.L., and Wilson, D.W. (1999) "De-liquefaction shock waves." 7th U.S. – Japan Workshop on Earthquake Resistant Design of Lifeline Facilities and Countermeasures Against Liquefaction, Seattle Washington, Technical Report MCEER-99-0019 (O'Rourke, Bardet, and Hamada eds.), pp. 295-310.

Lee, J. and Santamarina, C. (2005). "Bender Elements: Performance and Signal Interpretation." Journal *of Geotechnical and Geoenvironmental Engineering*. Sept, 2005.

Lindblom, U.E. and Jansson, I (2004). "Novel Ground Improvement Techniques based on Colloidal Silica." *Proceedings of the 5th International Conference on Ground Improvement Techniques,* Kuala Lumpur, Malaysia.

Maher, M.H., Ro, K.S., and Welsh, J.P (1994). "High strain dynamic modulus and damping of chemically grouted sand." *Soil Dynamics and Earthquake Engineering,* 13 (2), 131-138

Maher, M.H., Ro, K.S., and Welsh, J.P (1994)"Cyclic Undrained Behavior and Liquefaction Potential of Sand Treated with Chemical Grouts and Microfine Cement (MC-500)." *Geotechnical Testing Journal*, 17(2), 159-170.

Mollova, G. (2006) "Effects of Digital Filtering in Data Processing of Seismic Acceleration Records." *EURASIP Journal on Advances in Signal Processing ,* 2007

Moridis, G.J., Apps, J., Persoff, P., Myer, L., Muller, S., Yen, P. and Pruess, K. (1996). "A field test of a waste containment technology using a new generation of injectable barrier liquids." *Spectrum '96*, Seattle WA.

nees@utexas, George E. Brown, Jr. Network for Earthquake Engineering Simulation" <http://nees.utexas.edu/Home.shtml> (August 2008).

Marinucci, Antonio (2010). "Effect of Prefabricated Vertical Drains on Pore Water Pressure Generation and Dissipation in Liquefiable Sand." PhD Dissertation, The University of Texas at Austin.

Noll, M.R., Epps, D.E., Bartlett, C.L. and Chen, P.J. (1993). "Pilot field application of a colloidal silica gel technology for in situ hot spot stabilization and horizontal grouting." *Proc., 7th National Outdoor Action Conference*, National Ground Water Association, Las Vegas, NV, 207-219.

Noll, M.R., Epps, D.E., Bartlett, C.L. and Chen, P.J. (1993). "Pilot field application of a colloidal silica gel technology for in situ hot spot stabilization and horizontal grouting." *Proceedings of the 7th National Outdoor Action Conference*, National Ground Water Association, Las Vegas, NV, 207-219.

Ozgurel, H.G., and Vipulanandan, C. (2005). "Effect of grain size and distribution on permeability and mechanical behavior of acrylamide grouted sands." *Journal of Geotechnical and Geoenvironmental Engineering.,* 131(12), 1457-1465.

Pamuk, A., Gallagher, P.M. and Zimmie, T. (2007). "Remediation of pile foundations against lateral spreading by passive site stabilization technique." Submitted to *Soil Dynamics and Earthquake Engineering*, December 2005.

Persoff, P., Moridis, G.J., Apps, J., Pruess, K., and Muller, S.J. (1994). "Designing injectable colloidal silica barriers for waste isolation at the Hanford site." *In Situ Remediation: Scientific Basis for Current and Future Technologies, Proceedings of the 33rd Hanford Symposium on Health and the Environment*, Pasco, WA, 1, 87-101.

Persoff, P., Apps, J., Moridis, G. and Whang, J.M. (1999). "Effect of dilution and contaminants on strength and hydraulic conductivity of sand grouted with colloidal silica gel." *J. of Geotech. and Geoenv. Engr.*, 125(6), 461-469.

Persoff, P., Finsterle, S. Moridis, G.J., Apps, J., Pruess, K., and Muller, S.J. (1995). "Injectable Barriers for Waste Isolation." *Proceedings of the 1995 National Heat Transfer Conference,* Portland, OR.

Robertson, P.K., and Wride, C.E. (1997), "Cyclic Liquefaction and its Evaluation on the SPT and CPT", MCEER Workshop on Evaluation of Liquefaction Resistance of Soils, Technical Report MCEER-97-0022, Youd, T.L., and Idriss, I.M., Editors, January 4-5 1996, Salt Lake City, Utah.

Robertson, P.K. (1990). "Soil classification using the cone penetration test." *Canadian geotechnical journal, 27(1), 151-158.*

Rollins, K.M. (2004). "Liquefaction Mitigation using Vertical Composite Drains: Full Scale Testing." *NCHRP-IDEA Program Project Final Repo*rt, TRB, 107.

Silco International. (2005). "Colloidal Silica Technical Information." Silco International, LLC, Portland, OR, http://www.silco-intl.com/technical/index.html.

Spencer, L.M., Rix, G.J., and Gallagher, P.M. (2008). "Colloidal Silica Gel and Sand Mixture Dynamic Properties." *Proceedings of the conference of Geotechnical Earthquake Engineering and Soil Dynamics IV,* GSP181, Sacramento, CA.

Stokoe, K.H., II, Menq, F.Y., Wood, S.L., Park, K., Rosenblad, B. and Cox, B.R. (2008). "Experience with nees@UTexas large-scale mobile shakers in earthquake engineering studies," *Third International Conference on Site Characteristic,* Taipei, Taiwan.

Stokoe II, K.H., Woods, R.D (1972). "In situ shear wave velocity by cross-hole method." *Journal of the Soil Mechanics and Foundation Division,* 98(SM5), 443-460.

S&ME < http://www.smeinc.com/> (September, 2009).

Taboada, V. M., (1995). "Centrifuge modeling of earthquake-induced lateral spreading in sand using a laminar box." *Ph.D. Thesis*, Dept. of Civil Engineering, Rensselaer Polytechnic Institute, Troy, NY.

USA Corps of Engineers (1997). "Grouting of Sands and Gravels", *Technical Memorandum No. 3-408* R.J. Essex, Editor.

Vucetic, M., and Dobry, R. (1991): "Effect of Soil Plasticity on Cyclic Response," Journal of the Geoechnical Engineering Division, ASCE, Vol 117, No. 1, pp.89-107.

Welch and Smith (2001) "Saline water intrusion adjacent to the Fraser River, Richmond, British Columbia." *Canadian Geotechnical Journal,* 38, 67-82.

Whang, J.M. (1995). "Section 9 – Chemical-based barrier materials." *Assessment of Barrier Containment Technologies for Environmental Remediation Applications*, R. R. Rumer and J.K. Mitchell, eds., NTIS, Springfield, VA, 211-247.

Wride, C.E., Robertson, P.K., Biggar, K.W., Campanella, R.G., Hofmann, B.A., Hughes, J.M.G., Kuppper, A., and Woeller, D.J. (2000). "Interpretation of in-situ test results from the CANLEX sites." *Canadian Geotechnical Journal*, NRC, 37, 505-529.

Youd, T.L. and Idriss, I.M. "Liquefaction Resistance of Soils: Summary Report from the 1996 NCEER and 1998 NCEER/NSF Workshops on Evaluation of Liquefaction Resistance of Soils." *Journal of Geotechnical and Geoenvironmental Engineering,* 127(10), 297-313.

Zhou, Y., Chen, Y., Chen, R (2009). "Evaluation of Ground Improvement for Liquefiable Deposits using Shear Wave Velocity." *Proc of the 2009 US-China Workshop on Ground Improvement Technologies, GSP 188.*

Vita

Carolyn T. Conlee was born in Denville, NJ on May 6, 1981 as the only child of Jeanne Clements and Bernard Conlee. In 1999 she graduated with honors from Parsippany Hills High School in Parsippany, NJ and attended Villanova University in September, 1999. She spent her second year of college as a Chemical Engineering student and in her third year decided to switch her major to Civil Engineering. She received her Bachelor's of Science in Civil and Environmental Engineering in 2004 as a member of the Chi Epsilon Honor Society. As a Villanova Engineering student, she participated in Habitat for Humanity and assistend in the structural design of a school and performed land surveying at a boys' orphanage in Honduras. In September, 2004 she enrolled in the Masters/PhD program at Drexel University in Philadelphia, PA. During her 6-years as a Drexel University graduate student, she received her Master's of Science in Civil and Environmental Engineering in 2006. She received several scholarships and fellowships including the Koerner Family Fellowship, Stenven Giegrerich Memorial Scholarship, East Asia Pacific Summer Institute Grant, and Graduate Assistance in Areas of National Need Fellowship. She also received several awards including the Graduate Student Research Award, Dean Fellowship Award, and Graduate Honorable Mention for Eighth Annual Research Day. Additionally, she attended Tokyo University in Japan and University of California, Davis as a visiting researcher. Finally, she also published several conference papers and journal papers including the *Journal of Geotechnical and Geoenvironmental Engineering* and the *Geotechnical Earthquake of Engineering and Soil Dynamics Journal.*